Quasiparticle formation and induced correlations in strongly coupled Bose-Fermi mixtures

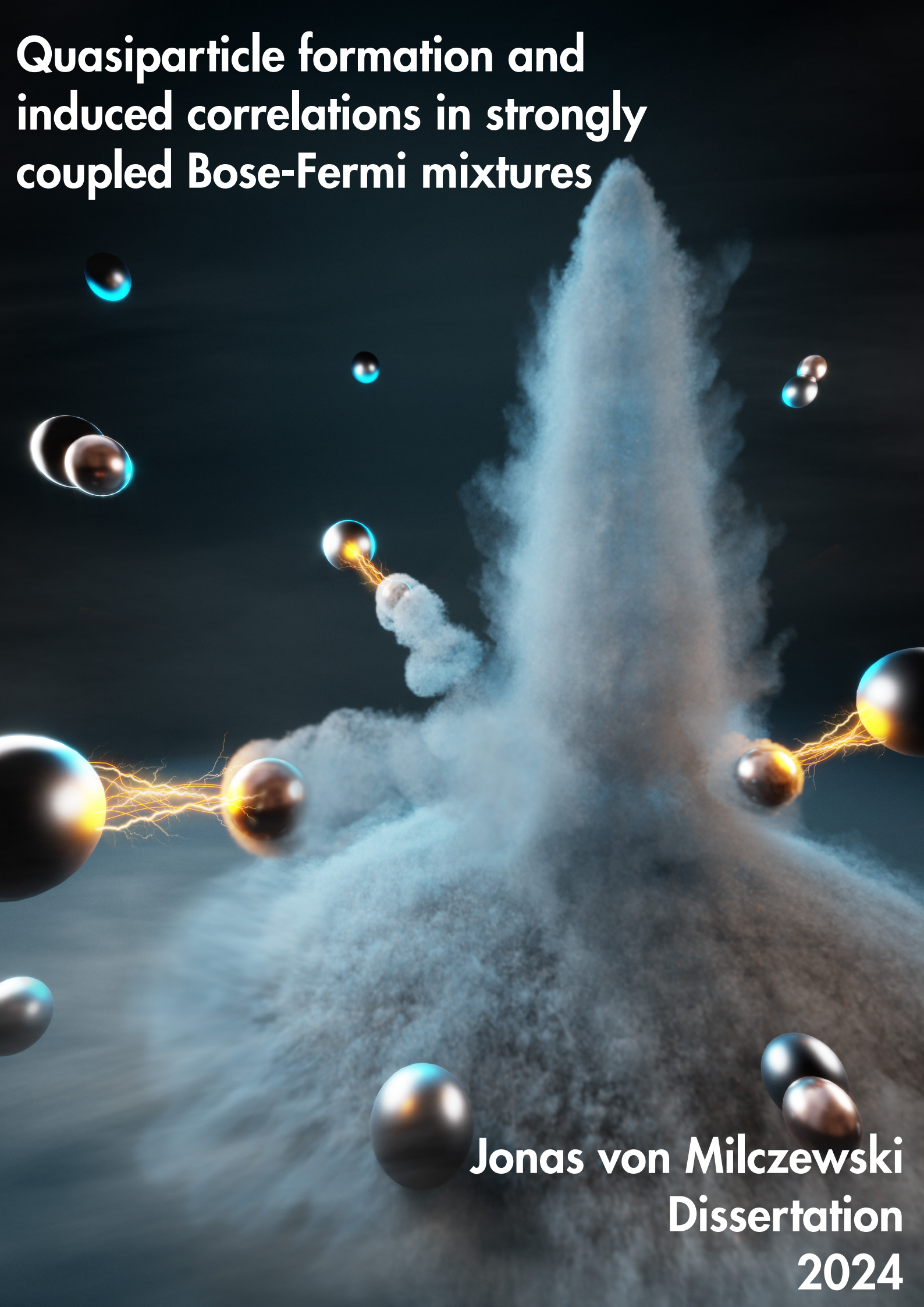

Jonas von Milczewski

Dissertation

2024

Cover illustration by Christoph Hohmann/MQCST

Dissertation

submitted to the

Combined Faculty of Natural Sciences and Mathematics

of Heidelberg University, Germany

for the degree of

Doctor of Natural Sciences

Put forward by

Jonas von Milczewski

born in: Bonn Bad-Godesberg

Oral examination: 08-02-2024

Quasiparticle formation and induced correlations in strongly coupled Bose-Fermi mixtures

Referees: Prof. Dr. Richard Schmidt

Prof. Dr. Tilman Enss

Abstract

In this thesis, field theoretical and variational methods are applied to few- and many-body problems of strongly interacting ultracold atomic gases and atomically-thin semiconductors. In strongly interacting mixtures of particles, the renormalizing effect of one species upon another is investigated to study the competition between the formation of different quasiparticles and the associated quantum phases related to the appearance of such particles. Tracing back to the Fermi polaron problem in which an impurity interacts attractively with a bath of fermionic particles, a majority of the work presented in this thesis may be understood in the context of a transition between the molecule state, in which a bath particle binds tightly to the impurity, and a quasiparticle best described as an impurity dressed by a cloud of bath particles. Going from a few to many impurities, due to the small energy gap between these quasiparticles, insights obtained in the Fermi polaron problem are leveraged to study the phase diagram of Fermi-Fermi and Bose-Fermi mixtures. First, the phase diagram of two- and three-dimensional Bose-Fermi mixtures is studied using the functional renormalization group (fRG). Three-body correlations are considered, and the approach is suited to treat finite-density populations of both bosons and fermions to study the molecular phase. Concurrently, experimental data are analyzed to characterize the superfluid-to-normal transition encountered in three-dimensional Bose-Fermi mixtures. A self-consistent, frequency- and momentum-resolved fRG approach is used to predict the transition point. This fRG method is then improved leveraging its analytical structure to obtain Greens functions at arbitrary complex frequencies using exact analytical continuation at a reduced computational cost. This is used to study the momentum-dependent decay rates of low-lying excited states, and predictions for Ramsey and Raman measurements are made. A stochastic variational approach is used to study bound-state formation in few-body problems. Precursors of the physics of the Fermi polaron problem are observed, and we find that finite interaction ranges, along with confinement, can greatly enhance trimer formation, relating to superfluid p-wave pairing. Finally, insights obtained in the study of strongly coupled Bose-Fermi mixtures are leveraged to study superconductivity in two-dimensional heterostructures of transition metal dichalcogenides. Here, capturing the strong-coupling physics of Bose-Fermi mixtures, boson-induced correlations are studied as a means to induce/enhance superfluid pairing with high critical temperatures.

Zusammenfassung

In dieser Dissertation werden feldtheoretische und variationelle Methoden auf Wenig- und Vielteilchenprobleme in stark wechselwirkenden ultrakalten atomaren Quantengasen und atomar dünnen Halbleitern angewandt. In stark wechselwirkenden Teilchenmischungen wird der renormierende Effekt, den eine Teilchenspezies auf eine andere ausübt, untersucht, um den Wettbewerb zwischen der Bildung verschiedener Quasiteilchen und der mit ihrem Auftreten assoziierten Quantenphasen zu untersuchen. Zurückgehend auf das Fermi Polaron Problem, in dem ein Störteilchen attraktiv mit einem Bad fermionischer Teilchen wechselwirkt, kann ein Großteil der Ergebnisse dieser Dissertation verstanden werden im Kontext eines Übergangs zwischen einem Molekülzustand, in dem ein Badteilchen eng an das Störteilchen gebunden wird, und eines Quasiteilchens, das man als ein von einer Wolke von Badteilchen umgebenes Störteilchen beschreiben kann. Wird die Anzahl der Störteilchen von wenigen auf viele erhöht, so lassen sich, aufgrund der kleinen Energielücke zwischen diesen Teilchen, im Fermi Polaron Problem gewonnene Erkenntnisse auf Untersuchungen das Phasendiagrams von Fermi-Fermi und Bose-Fermi Mischungen übertragen. Zunächst untersuchen wir mithilfe der funktionellen Renormierungsgruppe (fRG) das Phasendiagramm zwei- und drei-dimensionaler Bose-Fermi Mischungen. Dreiteilchenkorrelationen werden berücksichtigt und mit dieser Herangehensweise können endliche Boson- and Fermiondichten behandelt werden, um die auftretende Molekülphase zu untersuchen. Im Zuge dieser Untersuchung werden experimentelle Daten analysiert, um den Übergang zwischen superfluidem und normalfluidem Verhalten in einer dreidimensionalen Bose-Fermi Mischung zu charakterisieren. Wir nutzen eine selbstkonsistente, frequenz- und impuls-aufgelöste fRG, um den Übergangspunkt vorherzusagen. Diese fRG-Methode wird anschließend unter Ausnutzung ihrer analytischen Struktur verbessert, um Greensche Funktionen bei beliebig komplexer Frequenz unter Nutzung einer exakten analytischer Fortsetzung bei stark reduziertem Rechenaufwand zu erhalten. Dies wird genutzt, um frequenzabhängige Zerfallsraten tiefliegender Anregungszustände zu untersuchen, um Vorhersagen für Ramsey und Raman Messungen zu tätigen. Eine stochastisch-variationelle Methode wird anschließend genutzt, um die Bildung gebundener Zustände in Wenigteilchensystemen zu untersuchen. Vorläufer der aus dem Fermi Polaron Problem bekannten Physik werden hierbei beobachtet und wir finden, dass endliche Wechselwirkungsreichweiten und räumliche Einschränkung die Bildung von Trimeren verstärken können, was Auswirkungen auf superfluide p-Wellen Paarungen hat.

Anschließend werden in der Untersuchung stark gebundener Bose-Fermi Mischungen gewonnene Erkenntnisse genutzt, um Supraleitung in zwei-dimensionalen Heterostrukturen von Übergangsmetalldichalkogeniden zu untersuchen. Hierzu werden, unter Berücksichtigung der starken Bindungsphysik in Bose-Fermi Mischungen, bosoninduzierte Korrelationen als ein Mechanismus zur Erzeugung und Verstärkung superfluider Bindungen bei hohen kritischen Temperaturen untersucht.

Publications

This work is based on the following articles, ordered by appearance in this thesis. The last three publications are not subject of this dissertation.

[1] J. von Milczewski, F. Rose, and R. Schmidt, *Functional-renormalization-group approach to strongly coupled Bose-Fermi mixtures in two dimensions*, Phys. Rev. A **105**, 013317 (2022).

[2] M. Duda, X.-Y. Chen, A. Schindewolf, R. Bause, J. von Milczewski, R. Schmidt, I. Bloch, and X.-Y. Luo, *Transition from a polaronic condensate to a degenerate fermi gas of heteronuclear molecules*, Nature Physics **19**, 720–725 (2023).

[3] R. Li*, J. von Milczewski*, A. Imamoglu, R. Odziejewski, and R. Schmidt, *Impurity-induced pairing in two-dimensional fermi gases*, Phys. Rev. B **107**, 155135 (2023).

[4] J. von Milczewski, X. Chen, A. Imamoglu, and R. Schmidt, *Superconductivity induced by strong electron-exciton coupling in doped atomically thin semiconductor heterostructures*, arXiv: 2310.10726, (2023).

[5] J. von Milczewski and R. Schmidt, *Momentum-dependent quasiparticle properties of the fermi polaron from the functional renormalization group*, arXiv: 2312.05318, (2023).

[6] J. von Milczewski and J. R. Tolsma, *Dispersion forces between weakly disordered van der waals crystals*, Phys. Rev. B **104**, 125111 (2021).

[7] A. Nikolaenko, J. von Milczewski, D. G. Joshi, and S. Sachdev, *Spin density wave, fermi liquid, and fractionalized phases in a theory of antiferromagnetic metals using paramagnons and bosonic spinons*, Phys. Rev. B **108**, 045123 (2023).

[8] O. K. Diessel, J. von Milczewski, A. Christianen, and R. Schmidt, *Probing molecular spectral functions and unconventional pairing using raman spectroscopy*, arXiv:2209.11758, (2022).

[9] G. Ness, C. Shkedrov, Y. Florshaim, O. K. Diessel, J. von Milczewski, R. Schmidt, and Y. Sagi, *Observation of a Smooth Polaron-Molecule Transition in a Degenerate Fermi Gas*, Phys. Rev. X **10**, 041019 (2020).

Contents

Abstract v

Zusammenfassung vii

Publications ix

Contents xi

1 Introduction 1
- 1.1 Ultracold quantum gases . . . 2
- 1.2 Transition metal dichalcogenides . . . 4
- 1.3 Scattering physics . . . 5
- 1.4 Feshbach resonances . . . 8
- 1.5 Two-channel and single-channel models . . . 11
- 1.6 Regularization of the two-channel model and the single-channel model . 12
  - 1.6.1 Two-body limit in two dimensions . . . 16
- 1.7 The Fermi polaron problem . . . 17
- 1.8 Fermi polaron problem in ultracold atoms and atomically thin semiconductors . . . 23
- 1.9 Effective action and functional renormalization group (fRG) formalism 23

2 Strongly coupled Bose-Fermi mixtures 29
- 2.1 Introduction . . . 29
- 2.2 Degenerate three-dimensional Bose-Fermi mixtures in the density-matched regime . . . 33
  - 2.2.1 Phase diagram . . . 33
    - 2.2.1.1 Quantum phase transition from a polaronic phase to a molecular phase . . . 34
  - 2.2.2 Review of theoretical treatments of the quantum phase transition 36
    - 2.2.2.1 Theoretical treatment by Ludwig et al. (2011) . . . 36
    - 2.2.2.2 Theoretical treatment by Guidini et al. (2015) . . . 40
    - 2.2.2.3 Calculation using a functional renormalization group (fRG) approach and its comparison to the non-self-consistent T-matrix approach . . . 43
  - 2.2.3 Experimental setup and probe of the QPT . . . 45
    - 2.2.3.1 Reversal of the phase transition . . . 49

2.2.3.2 Projection of polaronic states onto deeply bound molecules 50
2.2.4 Degenerate Fermi gas of NaK Feshbach molecules 51
2.2.5 Conclusion on strongly coupled three-dimensional Bose-Fermi mixtures 52
2.3 Strongly coupled Bose-Fermi mixtures in two dimensions 54
2.3.1 Introduction 54
2.3.2 Model 56
2.3.2.1 fRG formalism and effective action 57
2.3.2.2 Truncation schemes 58
2.3.2.3 Regulators 61
2.3.2.4 Vertex projections and gradient expansion parameters 61
2.3.2.5 Flow Equations 62
2.3.2.6 RG initial conditions 63
2.3.2.7 Chemical potentials and distinction of phases 64
2.3.3 Quantum impurity limit: single boson in a Fermi sea 66
2.3.3.1 Quasiparticle energies 66
2.3.3.2 Vertex functions 68
2.3.3.3 The polaron energy within the gradient expansion scheme 71
2.3.4 Bose-Fermi mixture at finite boson density 73
2.3.4.1 Phase diagram as a function of chemical potential . . . 74
2.3.4.2 Phase diagram as a function of density 76
2.3.4.3 Mean-field model 79
2.3.5 Quasiparticle properties of polarons and molecules in the quantum impurity limit from a frequency- and momentum-resolved scheme (FMR) 80
2.3.5.1 Frequency- and momentum-resolved flow equations . . 81
2.3.5.2 Equivalence to a non-self-consistent T-matrix resummation 82
2.3.5.3 Results 83
2.3.6 Conclusion on strongly coupled two-dimensional Bose-Fermi mixtures 89

3 Impurity-induced pairing in two-dimensional Fermi gases 93
3.1 Introduction 94
3.2 Model 96
3.3 Method 97
3.3.1 Algorithm and Sampling 98
3.3.2 The Hamiltonian in the ECG basis 101
3.3.3 Angular Momentum in the ECG basis 103
3.4 Ground state transition between a dimer and a trimer state 104
3.4.1 Two-body problem without confinement 105
3.4.2 Non-interacting fermions 105
3.4.3 Coulomb interaction 112
3.4.4 Deviation from the asymptotic result $\alpha_c \approx 3.34$ 115

3.5 Polaron-to-molecule transition within a few-body system . . . 118
3.5.1 Triggering a polaron-to-molecule transition by tuning the potential depth . . . 118
3.5.2 Spatial wavefunction analysis of the polaron and the molecule . 122
3.5.3 Angular momentum expectation values $\langle \mathbf{L}^2_{\mathrm{tot}} \rangle$, $\langle \mathbf{L}^2_I \rangle$ and $\langle \mathbf{L}^2_F \rangle$ of the non-interacting ground state . . . 124
3.5.4 Could the polaron be the trimer? Comparison of the simplified Ansatz in Eq. (3.9) in the polaron-to-molecule transition . . . 127
3.6 Discussion . . . 128

4 Superconductivity induced by strong electron-exciton coupling in doped atomically thin semiconductor heterostructures 131
4.1 Introduction . . . 131
4.2 Model . . . 133
4.3 Method . . . 135
4.4 Analytical expressions and practical computation . . . 137
4.4.1 Trion self-energy . . . 138
4.4.2 Renormalized Green's functions . . . 138
4.4.3 Exciton self-energy . . . 139
4.4.4 Fermion number equation . . . 140
4.4.5 Computation of electron-trion scattering vertex . . . 140
4.4.6 Solving for the chemical potentials and determining the critical pairing temperature . . . 140
4.5 Results: critical pairing temperature . . . 142
4.5.1 Determining the boundary of the BCS regime from the bipolaron binding energy . . . 143
4.5.2 Approximation of the BKT transition temperature . . . 145
4.5.3 BCS-BEC crossover . . . 146
4.6 Conclusion . . . 146
4.7 RG analysis of the extended Fröhlich model in the few-body limit . . . 148
4.7.1 Flow of coupling constants in two dimensions . . . 149
4.7.2 Flow of coupling constants in three dimensions . . . 151
4.7.3 Discussion . . . 151

5 Momentum-dependent quasiparticle properties of the Fermi polaron from the functional renormalization group 153
5.1 Introduction . . . 154
5.2 Model . . . 156
5.2.1 fRG equations . . . 157
5.3 Exact Matsubara integration . . . 158
5.3.1 Analytical structure of zero-density propagators and the residue theorem . . . 160
5.4 Solution of the coupled flow equations . . . 163
5.4.1 Parametrization of inverse retarded Green's functions . . . 163

5.4.2 Initial conditions of the flow . . . 164
5.5 Results . . . 165
5.5.1 Energies and lifetimes at zero momentum in 3D . . . 166
5.5.2 Decay width of the excited state molecule from Fermi liquid theory . . . 170
5.5.3 Momentum-dependent energies and decay widths . . . 172
5.5.4 Decay of the ground state attractive polaron at finite momentum from Fermi liquid theory . . . 177
5.6 Conclusion . . . 179

6 Dispersion forces between weakly disordered van der Waals crystals 181
6.1 Introduction . . . 181
6.2 Induced dispersion forces in bilayer systems . . . 183
6.2.1 Derivation of ground state energy and force per layer from the fRG . . . 186
6.2.2 Numerical Results . . . 189
6.3 Impact of disorder on VdW forces: The 'Diffuson' . . . 191
6.4 Quantum interference effects on VdW forces: The 'Cooperon' . . . 196
6.5 Summary And Discussion . . . 198

7 Conclusion and Outlook 201

A Bose-Bose-Fermi coupling in the three-body limit and at finite density 205

B Explicit flow equations for the functional renormalization group analysis of a strongly-coupled two-dimensional Bose-Fermi mixture 207
B.1 Boson renormalization . . . 207
B.2 Molecule renormalization . . . 208
B.3 Three-body renormalization . . . 208
B.3.1 Bubble . . . 208
B.3.2 Triangle . . . 208
B.3.3 Square . . . 209
B.3.4 Total . . . 209
B.4 Fermion renormalization . . . 209
B.5 Effective potential . . . 209

C Two-body problem with confinement from the SVM 211

D Convergence Analysis of SVM method 213
D.1 Convergence analysis of the number of basis states N . . . 215
D.2 Convergence analysis of the number of sampling steps . . . 216

Bibliography 219

Acknowledgements 247

Chapter 1

Introduction

The realm of quantum mechanics brings with itself many instances of physical behavior that even a professional quantum physicist may deem counter-intuitive, to say the least. As a quick query in the search engine of one's choice may easily confirm, in the past decades many, many technological advances have been the fruit of quantum physics research, both in spite and because of the complications it brings with it.

While virtually all physical properties of the objects we interact with in our daily life draw their properties from quantum mechanics, some of which with very useful properties, their basic ingredients come as nature provides them and sometimes this means that they do not hold the properties we would like them to hold. Now, of course, there are many ways in which one can change the quantum mechanical properties of an object without having to resort to quantum mechanics, let alone have heard of it. However if that does not then prove successful then one way to change or engineer quantum mechanical properties is to manufacture a quantum system from ground up in a way that holds the properties you are looking for. You may even go the opposite way and build a quantum system in which you study the conditions under which it holds certain properties.

Depending on the insight one is after, such a pursuit may go many ways; one might aim to build a device that holds the properties one is looking for without caring too much about the microscopic processes that lie underneath. However, if one is after a property that has so far remained elusive to experimental implementation, then a microscopic understanding of the system might go a long way. One might even go as far as modeling a system that one is interested in by implementing it in an utterly different system that is easier to study and drawing conclusions about the original system from that.

This is where the systems studied in this thesis come into play, ultracold atom systems and two-dimensional semiconductor structures. Not only do these systems offer controlled environments that show truly quantum mechanical behavior, they also offer various possibilities to tune their properties externally and to probe the system to learn more about it. Most importantly, these systems master the difficult balancing act between (i) having microscopic ingredients that are simple enough to be susceptible to the description in effective theoretical models and experimental implementations, and

(ii) interesting enough to host a rich variety of universal many-body physics arising from these simple ingredients.

As these systems offer strong interparticle interactions, most physical properties can be studied along the lines of the quasiparticles, or *collective excitations*, arising from these interactions, which may look rather different from the microscopic ingredients. Throughout this thesis we will repeatedly study the quasiparticle formation arising from strongly coupled mixtures of bosons and fermions, which are in the quantum-degenerate regime. In the present chapter, we will provide an overview of the systems hosting the processes we study, their coupling processes, how they might be modeled and finally, we will introduce the Fermi polaron problem, which against all odds seems to be a reoccurring paradigm in our work.

1.1 Ultracold quantum gases

In ultracold quantum gas systems, a dilute alkali-metal vapor is trapped within a magnetic or optical trap and cooled using a variety of cooling techniques such as evaporative and laser cooling [10, 11]. Due to a careful interplay of different length scales, these systems are rather stable and can be cooled to be in the quantum degenerate regime in which the system particles exhibits quantum statistics. As such, the first experimental realization of a Bose-Einstein condensate (BEC) in 1995 [12–14], the subsequent realization of a degenerate Fermi gas a few years later [15–17], and the realization of Feshbach resonances [18, 19] have paved the way for a myriad of research directions, which are facilitated by a high degree of experimental control and tunability. In the following, we shall review the length scales governing cold atoms to gain an understanding of how these systems may be modeled.

Due to the loading of the trap and the ensuing harmonic oscillator potential, a number of atoms is confined to a region of space. The resulting density profile of atoms is determined by the trapping, and by using different trapping frequencies for different spatial directions, the effective dimensionality of the system may be tuned. These traps are rather shallow in energy and thus the atoms need to have low kinetic energies to avoid single-particle losses. Another key source of loss occurs when atoms collide and transition to lower-lying states, releasing large amounts of kinetic energy. To avoid such losses, ultracold gases are kept dilute, that is, at low densities where the distance between particles d is large compared to their interaction range. At the same time, the gas may not be too dilute, since for extremely low densities the cooling can no longer compete with technical sources of heating and loss [11].

In order for the ultracold quantum gas to be in the quantum-degenerate, also referred to as *ultracold*, regime the thermal de Broglie wavelength

$$\lambda_{th} = \sqrt{\frac{2\pi\hbar^2}{mk_BT}} \tag{1.1}$$

needs to be on the order of or larger than the interparticle distance d, where T is the temperature, m the atom mass and k_B the Boltzmann constant. This is enabled due

to the advanced cooling techniques which allow for temperatures in the nanokelvin range [20].

While the atoms are neutral in charge, usually they still interact with each other. At length scales comparable to the physical extent of the atom, the electron clouds of the atoms overlap, and due to Pauli exclusion, there is strong repulsion between the atoms. At larger distances, the electron clouds of the atoms may polarize to form dipoles, resulting in mutual attraction. This attraction at large distances may be captured in the effective van der Waals potential [20].

$$V_l(r) = -\frac{C_6}{r^6} + \frac{\hbar^2}{2\mu}\frac{l(l+1)}{r^2}, \tag{1.2}$$

where r denotes the distance between the atoms, C_6 is a constant, l denotes the relative angular momentum of the two atoms atoms and μ is their reduced mass. The latter part is the angular momentum barrier that arises in the radial part of the Schrödinger equation. Comparing the two terms, one may define the van der Waals length

$$l_{vdW} = \frac{1}{2}\left(\frac{2\mu C_6}{\hbar^2}\right), \tag{1.3}$$

as a range length scale of the potential. This length scale is typically significantly larger than the distance where strong Pauli repulsion becomes relevant, but importantly it is usually much smaller than the interparticle distance $l_{vdW} \ll d$. As a result, for the low-energy collisions studied in ultracold systems, s-wave scattering ($l = 0$) is the dominant collision process as higher momentum states ($l > 0$) reflect from the centrifugal barrier without seeing the attractive potential within Eq. (1.2). Furthermore, as the interparticle distance is much larger than the interaction length scale, the microscopic details of the interatomic interaction potential do not need to be resolved, but rather the culmination of the sum of microscopic details into a single (or sometimes a few) parameter which describes the effect of the scattering at length scales of the interparticle distances suffices. The most important parameter is called the s-wave scattering length a, which we will introduce in Section 1.3.

The precise form of the interatomic potentials depends on the species of quantum gases used and also on the internal state of the scattering atoms. Apart from that, however, they cannot really be modified. The use of Feshbach resonances between different interaction channels, however, has enabled access to ultra-strong coupling physics in ultracold quantum gases and allows for tunable interaction parameters.

Thus, ultracold quantum gases have been at the forefront of studies of strongly coupled many-body systems, as they allow to enter the quantum degenerate regime in a controlled way where due to the tunability of interactions, a rich variety of exciting physics awaits. At the same time, the microscopic ingredients are rather well understood, since due to the length scales mentioned in this section the constituent particles may be approximated as point-like particles that interact through an s-wave potential, which can be parametrized by few coefficients.

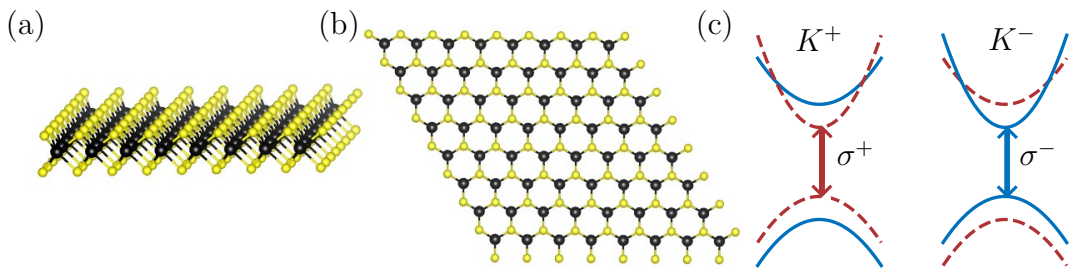

Figure 1.1. Schematic diagrams of monolayer TMD. Side (a) and top view (b) of a single layer of TMD, where the transition metals are shown in black, and the chalcogen atoms are shown in yellow. In (b) the hexagonal lattice structure becomes visible which has a three-fold rotational symmetry around the atoms. A schematic band structure near the K^+ and K^- points is shown in (c) which features a direct band gap. Here, spin-orbit coupling lifts the degeneracy between the different electron spin states (red and blue). Due to selection rules, the optical transition is highly selective of spin and valley index, resulting in separate addressability based on the polarization, σ^+ and σ^-, of light. Figure adapted from [21].

1.2 Transition metal dichalcogenides

The second type of physical system studied in this thesis are so-called transition metal dichalcogenides (TMD), which are a class of layered materials. For a detailed account of TMD, we refer to Ref. [22]. Here, we provide a brief introduction to TMD systems. The fundamental building blocks of TMDs are two-dimensional crystalline sheets of transition metals and chalcogenides which are each only one atomic layer thick (see Fig. 1.1). A sheet of transition metal is sandwiched between two chalcogenide sheets, making up a single layer of transition metal dichalcogenide. TMDs exist in nature in bulk form containing many layers of TMD. While bulk TMDs have been studied for a long time, more recently, newly developed exfoliation techniques have enabled atomically thin structures of few to only a single layer of TMD, where the electrons are effectively confined to two dimensions. These techniques were originally developed to produce graphene from graphite, but have recently been also in heavy use for the study of TMDs.

The band structure of graphene is remarkable: It does not have a band gap and at the Dirac points the conduction and valence bands touch [23]. As a result, one can not only tune the electron density through gating, so that graphene may continuously be tuned from a hole gas into an electron gas. Furthermore, at the Dirac point, the electrons and holes fulfill a massless Dirac equation with a dispersion relation that is linear in momentum. Although TMDs have been studied for decades, they have made a comeback into scientific interest, as the advances made in the study of graphene have enabled better sample preparation, manipulation and detection in few-layer TMD systems. As a result, TMD can now be manufactured in single- to few-layer configurations. While molybdenum disulfide (MoS_2), a common TMD, in its bulk form has an indirect band gap, with decreasing layer number, it transitions towards a direct band gap, and finally in single-layer form it possesses, in contrast

to single-layer graphene, a direct band gap [24, 25]. The presence of a direct band gap facilitates optical excitations across the band gap, which in itself already has interesting applications [26–29].

In addition, MoS_2 belongs to a group of semiconducting dichalcogenides in which the band extrema (where conduction and valence band are closest in energy) are not located at the center of the Brillouin zone, but rather at finite momentum at the K^+ and K^- points (similar to graphene). Due to the selection rules at these points, the optical transitions require specific polarizations of light, which differ for the K^+ and K^- points (see Fig. 1.1). As optical transitions they do not require momentum transfer and additionally they can be selectively excited based on the polarization of the used light [30, 31]. When exciting across the band gap, the created (conduction-band) electron and the (valence-band) hole experience mutual Coulomb attraction and may form a bound state, called exciton, with binding energies of several 100 meV (for comparison, the energy scale of room temperature is 26 meV). Thus excitons play an important role not only at extremely cold temperatures but also at room temperature. This tight binding is enabled by the unique combination of almost ideal in-plane confinement of particles in TMD and the thinness of the material layers which greatly reduces the dielectric screening that usually weakens Coulomb interactions in three-dimensional bulk materials.

Although the exciton is a neutral particle, due to its spatial extent of a few lattice sites (in single-layer systems), in the presence of a charge it may develop a dipole moment that may interact attractively with an electron or hole to form a negatively or positively charged three-particle state, called trion [22]. These states typically have a binding energy of roughly 10% of the exciton binding energy [32] and therefore may play a role even at room temperature. While TMD systems appear very different from the ultracold quantum gas systems discussed in the previous section, they also realize strong coupling, not only between electrons and holes but also between excitons and electrons/holes. It is thus not surprising that both the Bose polaron and the Fermi polaron problem (which we will discuss in Section 1.7), have not only been studied within ultracold atoms but also within TMDs [33, 34] and qualitatively similar physics can be found in both systems.

Today, excitons may be created not only within single layers of TMD but also an electron and a hole living in two different layers of TMD may bind and form a so-called *interlayer* exciton [35–39]. Due to the ensuing spatial alignment of the exciton (and the ensuing dipole), this thus enables much stronger exciton-electron interactions leading to stronger trion formation, as we will discuss in the context of exciton-induced superconductivity in Chapter 4.

1.3 Scattering physics

Having familiarized ourselves in Section 1.1 with the concept of ultracold atoms and their length scales, let us briefly recall the low-energy scattering theory which we will use to describe most of the interactions throughout this thesis.

As mentioned before, in the ultracold atom systems we consider, the range of the interatomic interaction potential is usually quite a bit smaller than the average interparticle distance and the thermal de Broglie wavelength, so that the main scattering contributions come from vanishing angular momentum $l = 0$. Moreover, the microscopic structure of the interaction usually does not need to be resolved, since we are only interested in its effect far beyond its interaction range. Here, the solution of the two-body problem takes on the form of the free-space solution of two free particles. Thus, the microscopic structure of the interaction potential has two effects: First, inside the interaction range it may strongly modify the two-body wavefunction, which secondly provides the boundary conditions for the solution outside the interaction range.

The resulting two-body wavefunction can then be compared to standard results from two-body scattering theory [20, 40, 41]. Let us consider two atoms in their center of mass frame colliding with momenta $\mathbf{k}$ and $-\mathbf{k}$ and a reduced mass of μ_{cd}. At large distances from the origin, the two-body wavefunction of a planar wave $|\mathbf{k}| = k$ in z-direction, scattering at the origin into a spherical wave at large distances, is written as

$$\psi(r, \theta) \sim e^{ikz} + \frac{f(\theta)}{r} e^{ikr}, \tag{1.4}$$

defining the angle-dependent scattering amplitude f. Here we have assumed a spherically symmetric potential, such that f depends only on the polar angle θ. Rather than being explicit with respect to the normalization constant, we choose to suppress the normalization constant.

The incoming plane wave has a representation in terms of angular momentum

$$e^{ikz} = e^{ikr\cos(\theta)} = \sum_{l=0}^{\infty} i^l (2l+1) J_l(kr) P_l(\cos(\theta)), \tag{1.5}$$

where J_l is the l-th Bessel functions of the first kind and P_l is the l-th Legendre polynomial. At large distance this expression simplifies to

$$e^{ikr\cos(\theta)} \approx \sum_{l=0}^{\infty} \frac{2l+1}{ikr} (e^{ikr} - (-1)^l e^{-ikr}) P_l(\cos(\theta)), \tag{1.6}$$

and it is clear that the incoming wave has many different angular momentum contributions (and so may the scattered spherical wave). As we are merely interested in s-wave ($l = 0$) scattering, we now limit our attention to the corresponding wavefunctions. As mentioned before, at large interparticle distances, the microscopic details of the interatomic potential provide boundary conditions to the asymptotic solution and as a result the two-body wavefunction at momentum k and large distances may be written as

$$\psi(r) \sim e^{i\delta} \frac{\sin(kr + \delta(k))}{kr}, \tag{1.7}$$

where the microscopic details of the interatomic potential $U(r)$ have culminated in a mere phase shift δ. The additional phase $e^{i\delta}$ is retained to keep up with notation frequently used in literature.

Matching factors of e^{ikr} in Eqs. (1.4) and (1.7), for s-wave scattering one thus obtains

$$f(k,\theta) = f(k) = \frac{e^{2i\delta} - 1}{2ik} = \frac{1}{k\cot(\delta) - ik}, \tag{1.8}$$

relating the scattering amplitude to the phase shift.

When solving the Laplace equation which was used to obtain Eq. (1.7), in the radial component of the wavefunction, it is useful to define an auxiliary function u, such that the radial component of ψ is captured by $u(r)/r$. Thus, from the corresponding Laplace equation

$$\left(\frac{d^2}{dr^2} + k^2 - 2\mu_{cd}U(r) - \frac{l(l+1)}{r^2}\right) u_l(r) = 0 \tag{1.9}$$

one can see that for $l = 0$ at low energy ($k \to 0$) the second derivative of $u_0(r)$,

$$\frac{d^2}{dr^2}u_0(r) \to 0 \text{ for } k \to 0 \tag{1.10}$$

vanishes. As a result, for small values of k and with the aim of comparing to Eq. (1.7), we may write u_0 as

$$u_0(r) = c(r - a), \tag{1.11}$$

where c and a are constants. Given that we have neglected normalization, we may either boldly identify u_0 from the expression in Eq. (1.7) or, as is commonly done, we may compute a dimensionless logarithmic derivative, which takes care of normalization factors. This may be defined as

$$r\frac{u_0'(r)}{u_0(r)} = \frac{(r\psi(r))'}{\psi(r)}. \tag{1.12}$$

Thus, matching Eqs. (1.7) and (1.11) using Eq. (1.12), for $k \to 0$ we obtain the condition that

$$\frac{r}{r-a} = \lim_{k\to 0} kr\cot(kr + \delta(k)), \tag{1.13}$$

which can be interpreted as a low energy boundary condition. For completeness, we have included a momentum dependence for the phase shift. We may use this equation to define the scattering length a as

$$-\frac{1}{a} = \lim_{k\to 0} k\cot(\delta(k)), \tag{1.14}$$

which by virtue of Eq. (1.11) has the geometrical interpretation that it is the node of $u_0(r)$ of the wavefunction outside of the interatomic interaction range. Similarly, we note that the low-energy scattering amplitude is given by

$$\lim_{k\to 0} f(k) = -a. \tag{1.15}$$

Considering scattering at small but finite energies, one may expand Eq. (1.14) to higher orders in k

$$k\cot(\delta(k)) \approx -\frac{1}{a} + \frac{1}{2}r_0 k^2, \tag{1.16}$$

where r_0 is called the effective range, such that

$$f(k) \approx \frac{1}{-\frac{1}{a} + \frac{1}{2}r_0 k^2 - ik}. \tag{1.17}$$

Importantly, attractive microscopic interactions may lead to both positive and negative scattering lengths. For positive scattering lengths, it can be shown that an attractive bound state of energy

$$E_B = -\frac{\hbar^2}{2\mu_{cd}a^2} \tag{1.18}$$

exists, where μ_{cd} is the reduced mass of the two particles and we assumed that $r_0 = 0$.

1.4 Feshbach resonances

Having discussed basic scattering physics and how microscopic interatomic interactions may lead to observable phase shifts and scattering lengths, let us discuss how interactions may be tuned in ultracold atoms using so-called Feshbach resonances [20]. The effective interatomic interaction potential between two atoms ($i = 1, 2$) depends on their internal state, as different combinations of spin $\mathbf{S}_i$, angular momentum $\mathbf{L}_i$ and nuclear spin $\mathbf{I}_i$ all lead to different effective interactions between atoms.

Let us consider two atoms with internal states K_1 and K_2 (in a state $|K_1, K_2\rangle$ to respect (anti)-symmetrization) scattering off each other at low energy. After these atoms have scattered, they may now have different internal states K_1' and K_2'. If these internal states lie lower in energy, then to conserve energy, the atoms must have picked up kinetic energy. On the other hand, if the scattering happens at sufficiently low energy, then the final states may not lie higher in internal energy, as energy must be conserved. The former case is referred to as an inelastic collision, and within ultracold atoms this often leads to atoms being ejected from the trap. As a result, we will focus on collisions where the final internal states are the same as the initial internal states.

In the absence of external manipulation, the scattering of the two atoms with internal states K_1 and K_2 due to their interatomic potential V_{open} is not tunable and may very often be rather weak in the sense that they provide only a small phase shift. However, by means of a so-called Feshbach resonance, it may be tuned. The two atoms in K_1 and K_2 have an energy E that, due to their low kinetic energy, is slightly above the scattering threshold of the $|K_1, K_2\rangle$ state. Consider now a different scattering channel between atoms in H_1 and H_2 which interact with an interatomic potential V_{closed} whose scattering threshold lies higher in energy than E (see Fig. 1.2).

As mentioned above, one may not scatter into an asymptotic state of $|H_1, H_2\rangle$ because of energy conservation, and thus we refer to such a scattering channel as

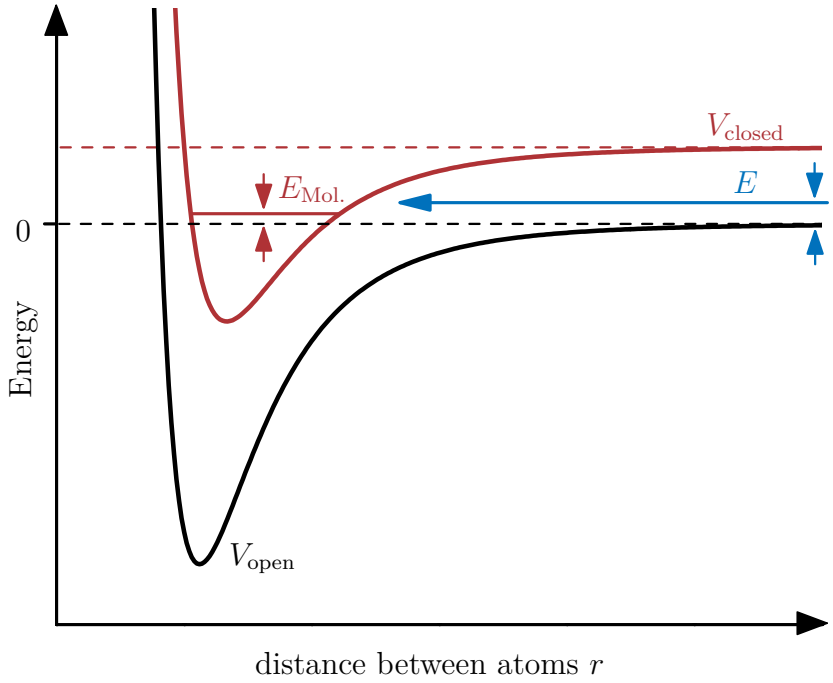

Figure 1.2. Schematic diagram of a Feshbach resonance in a two-channel model. Two atoms with energy E in the open channel interact via the open channel potential V_{open} (solid, black). They may virtually scatter into a closed channel where they interact via the closed channel potential V_{closed} (solid, red); however, they may not asymptotically scatter into that channel, as the closed channel scattering threshold (dashed, red) lies higher in energy. If the closed channel supports a bound state of energy $E_{\text{Mol.}}$, using magnetic field tuning, this state may be brought into resonance with the closed channel scattering threshold (dashed, black), significantly increasing the scattering cross section between atoms in the open channel. Figure adapted from Ref. [20].

closed (in the same way a channel is *open* if it is allowed energetically). However, we may very well scatter into such a state virtually before eventually scattering back, especially at a shorter distance where V_{closed} may lie below the scattering threshold of the open channel. If the closed-channel potential V_{closed} supports a state confined at small distances, which we refer to as a bound state or a molecule, then this can increase the scattering cross section between atoms in the open channel, as atoms can virtually couple into the closed channel and back into the open channel. The strength of this induced interaction depends not only on the scattering rate between the open and closed channels, but also on the energy difference $E_{\text{Mol.}}$ between the bound state and the scattering threshold of the open channel.

If the open channel ($|K_1, K_2\rangle$) and the closed channel ($|H_1, H_2\rangle$) have different magnetic moments, μ_K, μ_H, then tuning an external magnetic field in a suitable way, the relative energy shift $E_{\text{Mol.}}$ may be tuned and may eventually vanish. This may significantly enhance the scattering in the open channel. The resulting scattering

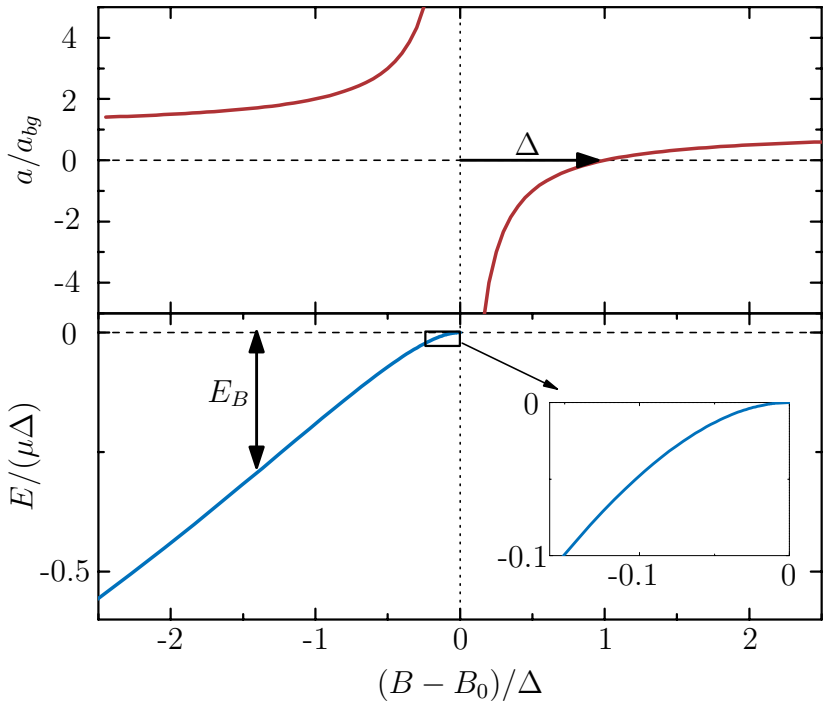

Figure 1.3. Scattering properties near a Feshbach resonance. The scattering length a according to Eq. (1.19) (top) and the ensuing closed channel binding energy E_B (bottom) are shown as a function of magnetic field B near a Feshbach resonance at B_0. As discussed in the text, away from the resonance E_B varies linearly with B, while close to the resonance in the universal regime the scattering length is large. For large, positive scattering length the binding energy is given by Eq. (1.20). Figure adapted from Ref. [20].

length in dependence of the magnetic field may be written as [20]

$$a(B) = a_{bg}\left(1 - \frac{\Delta}{B - B_0}\right) = a_{bg} - \frac{2}{r^*\mu(B - B_0)}, \tag{1.19}$$

where $\mu = \mu_H - \mu_K$, B_0 is the magnetic field at which the scattering length diverges and a_{bg} is the scattering length within the open channel, when couplings to other channels are not relevant. Note that B_0 is different from $B_c = E_{\text{Mol.}}/\mu$ as the molecule energy $E_{\text{Mol.}}$ is an asymptotic energy, which itself is modified when both channels are brought close to resonance. The parameter r^* is related to the width of the resonance and microscopically it originates from the scattering matrix between the open and the closed channel. It is related to the effective range as $r_0 = -2r^*$. Similarly, the parameter Δ relates to the magnetic width of the Feshbach resonance and incorporates both the scattering between open and closed channels as well as the difference in magnet moment.

The physics of a Feshbach resonance is akin to an avoided crossing, and as such the eigenstates near the resonance are admixtures of the open- and closed-channel asymptotic eigenstates. Similar to the two-body collisions discussed in Section 1.3, for positive values of $a(B)$ a bound state emerges whose energy vanishes at the resonance. Away from the resonance, the energy of this bound state is given by the energy of

the unperturbed closed channel bound state, which varies linearly with the magnetic field B with a slope given by μ [20]. Closer to the resonance, the bound state is an admixture between the open and closed channels, which is increasingly dominated by the open channel as the resonance is approached. Near the resonance, for large positive values of $a(B)$ the molecule state has an energy given by [20]

$$E_B = -\frac{\hbar^2}{2\mu_{cd} a(B)^2}, \tag{1.20}$$

analogous to Eq. (1.18). This is illustrated in Fig. 1.3.

The parameter Δ controls the width of the magnetic field range in which the effective scattering range $a(B)$ differs from the background scattering length a_{bg}. One may see the difference between these two as a measure for the degree of admixture between the open and closed channels, and thus Δ also controls the range in which the molecule energy is given by Eq. (1.20) before it begins to be linear with magnetic field strength. To quantify this, it is useful to define a dimensionless resonance strength parameter [20]

$$s_{res} = \frac{\bar{a}}{r^*}, \tag{1.21}$$

where $\bar{a}$ denotes the mean scattering length which is defined in terms of the van der Waals length l_{vdW} as $\bar{a} \approx 0.955978\ l_{vdW}$. Resonances with $s_{res} \gg 1$ are thus referred to as *open-channel dominated* and resonances with $s_{res} \ll 1$ are referred to as *closed-channel dominated*.

1.5 Two-channel and single-channel models

In the following, let us consider an ultracold mixture of two species of atoms which interact near a Feshbach resonance. For example, these may be different Zeeman states of ^{40}K interacting with each other, it may be different Zeeman states of ^{40}K and ^{23}Na interacting with each other, but also other combinations are possible. In Ref. [20] a characterization of common Feshbach resonances is given. In its simplest form, when there is only a single bound state in the closed channel that is relevant, such a system may be modeled by the following *two-channel* Hamiltonian [20, 42–48]

$$\hat{H} = \sum_{\mathbf{p}} \varepsilon^c_{\mathbf{p}} \hat{c}^\dagger_{\mathbf{p}} \hat{c}_{\mathbf{p}} + \sum_{\mathbf{p}} \varepsilon^d_{\mathbf{p}} \hat{d}^\dagger_{\mathbf{p}} \hat{d}_{\mathbf{p}} + \sum_{\mathbf{p}} (\xi_{\mathbf{p}} + \nu)\, \hat{m}^\dagger_{\mathbf{p}} \hat{m}_{\mathbf{p}} + \frac{h}{\sqrt{V}} \sum_{\mathbf{l},\mathbf{p}} \left(\hat{m}^\dagger_{\mathbf{p}} \hat{c}_{\mathbf{l}} \hat{d}_{\mathbf{p}-\mathbf{l}} + \hat{d}^\dagger_{\mathbf{p}-\mathbf{l}} \hat{c}^\dagger_{\mathbf{l}} \hat{m}_{\mathbf{p}} \right). \tag{1.22}$$

Here, the $\hat{c}^\dagger$ and $\hat{d}^\dagger$ are the creation operators of the two species in the open channel. The $\hat{m}^\dagger$ are the creation operators of the corresponding bound state in the closed

channel. Setting $\hbar = 1$, their dispersion relations are given by

$$\varepsilon_{\mathbf{p}}^{c} = \frac{\mathbf{p}^2}{2M_c} \tag{1.23}$$

$$\varepsilon_{\mathbf{p}}^{d} = \frac{\mathbf{p}^2}{2M_d} \tag{1.24}$$

$$\xi_{\mathbf{p}} = \frac{\mathbf{p}^2}{2(M_c + M_d)}, \tag{1.25}$$

where M_c and M_d are the masses of the two species and ν denotes the magnetically tuned detuning of the unperturbed closed channel bound state energy with respect to the scattering threshold of the open channel. The last term in Eq. (1.22) couples the open and closed channels due to the scattering between these states with a rate of h (which should not be confused with the Planck constant). While Eq. (1.19) contains a background scattering length a_{bg}, which would correspond to a term $\sim \hat{d}^\dagger_{-\mathbf{l}'+\mathbf{p}} \hat{c}^\dagger_{\mathbf{l}'} \hat{c}_{\mathbf{l}} \hat{d}_{-\mathbf{l}+\mathbf{p}}$ in Eq. (1.22), in practice the background scattering is often so weak that it may be disregarded altogether. In the following sections, we will see how the macroscopic parameters ν and h may be related to the observable parameters of scattering length a and effective range r_0. Note that the bare molecule which is created using the $\hat{m}^\dagger$ operators should not be confused with the dressed molecule bound state which may appear in the spectrum of the Hamiltonian in Eq. (1.22).

In an open channel-dominated Feshbach resonance ($r^* \to 0$), the bound state in the spectrum has little admixture from closed channel molecules and as we will see, this corresponds to $h \to \infty$, where $\nu \sim h^2$. As a result, the dynamics of the bare closed channel molecule will not be relevant and the particle may be integrated out to yield the single-channel Hamiltonian

$$\hat{H} = \sum_{\mathbf{p}} \varepsilon_{\mathbf{p}}^{c} \hat{c}^\dagger_{\mathbf{p}} \hat{c}_{\mathbf{p}} + \sum_{\mathbf{p}} \varepsilon_{\mathbf{p}}^{d} \hat{d}^\dagger_{\mathbf{p}} \hat{d}_{\mathbf{p}} + \frac{g}{V} \sum_{\mathbf{p},\mathbf{p}',\mathbf{q}} \hat{c}^\dagger_{\mathbf{p}+\mathbf{q}} \hat{c}_{\mathbf{p}} \hat{d}^\dagger_{\mathbf{p}'-\mathbf{q}} \hat{d}_{\mathbf{p}'}, \tag{1.26}$$

which is equivalent to Eq. (1.22), provided that $g = -h^2/\nu$ and $h \to \infty$ [49, 50]. This Hamiltonian only takes into account the open-channel scattering between c and d particles and its coupling constant g is tuned to the scattering length a which originally stems from interactions with the closed channel. As we will see, the effective range r_0 of this Hamiltonian vanishes.

1.6 Regularization of the two-channel model and the single-channel model

After having introduced the two-channel model, let us relate its parameters to physical observables. There are different ways one may start such a quest. Using a variational wavefunction Ansatz, one may describe the two-body bound state and relate this to the scattering function f. Alternatively, one may use quantum field theory to compute the effective scattering vertex, which one can also relate to f. One may even use the functional renormalization group to solve this problem. In this case, we will use

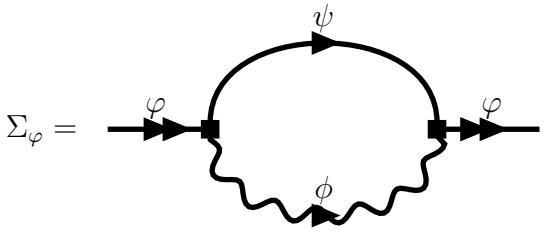

Figure 1.4. Self-energy of the molecule φ. Straight lines denote ψ particle propagators, while curly lines and lines with two arrows denote ϕ and φ particles, respectively. The square blocks, denote the Yukawa coupling $\sim h$.

quantum field theory. In Section 1.7 we will use variational wavefunctions to solve the Fermi polaron problem, from which one may also deduce the corresponding two-body solution. Finally, in Section 1.9 we will also introduce the functional renormalization group and use it to solve a similar two-body problem in Section 4.7.

To begin, let us define an action corresponding to the two channel model of Eq. (1.22) as

$$\begin{aligned} S = \int_{\mathbf{p},\omega} \left\{ \psi_P^* \left(-i\omega + \varepsilon_{\mathbf{p}}^c - \mu_\psi \right) \psi_P + \phi_P^* \left(-i\omega + \varepsilon_{\mathbf{p}}^d - \mu_\phi \right) \phi_P + \varphi_P^* \left(-i\omega + \xi_{\mathbf{p}} + \nu \right) \varphi_P \right\} \\ + h \int_x \left\{ \psi_x^* \phi_x^* \varphi_x + \varphi_x^* \phi_x \psi_x \right\} \ , \end{aligned} \tag{1.27}$$

where the fields ψ, ϕ and φ, correspond to the operators $\hat{c}, \hat{d}$, and $\hat{m}$; μ_ψ and μ_ϕ are chemical potentials, $P = (\mathbf{p}, \omega)$ comprises the momentum $\mathbf{p}$ and the Matsubara frequency ω, $\int_x \equiv \int_0^{1/T} d\tau \int d^3\mathbf{r}$ and $\int_{\mathbf{p},\omega} \equiv \int d^3\mathbf{p} d\omega$.

To operate in the two-body limit, we set both chemical potentials to vanish, $\mu_\psi = \mu_\phi = 0$, such that due to the locations of the poles in the propagators of the ψ and ϕ particles, their densities vanish [51, 52]. In fact, only the φ particles experience quantum fluctuations in the two-body limit. As a result, we can compute the molecule self-energy Σ_φ^σ (see Fig. 1.4) as

$$\begin{aligned} \Sigma_\varphi(\mathbf{p}, \omega) &= h^2 \int_{\mathbf{q},\nu} G^0_{\psi_\sigma^* \psi_\sigma}(\mathbf{p} - \mathbf{q}, \omega - \nu) G^0_{\phi^* \phi}\ (\mathbf{q}, \nu) \\ &= \frac{h^2}{(2\pi)^4} \int d\mathbf{q} d\nu \frac{1}{[-i(\omega - \nu) + \varepsilon^c_{\mathbf{p}-\mathbf{q}}][-i\nu + \varepsilon^d_{\mathbf{q}}]} \\ &= \frac{h^2}{(2\pi)^3} \int d\mathbf{q} \frac{1}{\left[-i\omega + \frac{(\mathbf{p}-\mathbf{q})^2}{2M_c} + \frac{\mathbf{q}^2}{2M_d}\right]}. \end{aligned} \tag{1.28}$$

Shifting $\mathbf{q} \to \mathbf{q} + \mathbf{p}M_d/(M_c + M_d)$ and introducing an upper momentum cutoff, we thus obtain

$$\begin{aligned} &= \frac{4\pi h^2}{(2\pi)^3} \int_0^\Lambda dq q^2 \frac{1}{-i\omega + \frac{1}{2(M_c+M_d)}\mathbf{p}^2 + \frac{M_c+M_d}{2M_cM_d}\mathbf{q}^2} \\ &= \frac{4\pi h^2}{(2\pi)^3} \left(\frac{2M_cM_d}{M_c+M_d}\Lambda - \frac{\sqrt{-i\omega + \frac{\mathbf{p}^2}{2(M_c+M_d)}}}{\left(\frac{M_c+M_d}{2M_cM_d}\right)^{3/2}} \tan^{-1}\left(\frac{\sqrt{\frac{M_c+M_d}{2M_cM_d}}\Lambda}{\sqrt{-i\omega + \frac{\mathbf{p}^2}{2(M_c+M_d)}}} \right) \right), \end{aligned} \tag{1.29}$$

where we can identify the reduced mass μ_{cd} of M_d, M_c such that we arrive at

$$\Sigma_\varphi(\mathbf{p},\omega) = \frac{h^2}{2\pi^2}\left(2\mu_{cd}\Lambda - (2\mu_{cd})^{3/2}\sqrt{-i\omega + \frac{\mathbf{p}^2}{2(M_c+M_d)}}\tan^{-1}\left(\frac{\sqrt{\frac{M_c+M_d}{2M_cM_d}}\Lambda}{\sqrt{-i\omega + \frac{\mathbf{p}^2}{2(M_c+M_d)}}} \right) \right). \tag{1.30}$$

Finally, we can compute the renormalized inverse molecule Green's function

$$G_\varphi^{-1}(\mathbf{p},\omega) = -i\omega + \xi_{\mathbf{p}} + \nu - \Sigma_\varphi(\mathbf{p},\omega), \tag{1.31}$$

which in turn is related to the T-matrix as

$$T(\mathbf{p},\omega) = -\frac{h^2}{G_\varphi^{-1}(\mathbf{p},\omega)}. \tag{1.32}$$

Now, we can proceed to compare the T-matrix to the scattering amplitude to relate ν and h to a and r_0. To do this, we must evaluate the T-matrix in the center-of-mass frame of the two colliding particles, setting $\mathbf{p} = 0$, at the energy of the two particles of opposite momenta $\mathbf{q}$ and $-\mathbf{q}$, which is achieved by continuing $i\omega \to \Omega = \mathbf{q}^2/2M_c + \mathbf{q}^2/2M_d + i0^+ = q^2/2\mu_{cd} + i0^+$. Then

$$\begin{aligned} f(q) &\stackrel{!}{=} -\frac{\mu_{cd}}{2\pi}T(\mathbf{0}, -i\Omega) = \frac{h^2\mu_{cd}}{2\pi G_\varphi^{-1}(\mathbf{0},-i\Omega)} \\ &= \frac{h^2\mu_{cd}}{2\pi}\frac{1}{-\frac{q^2}{2\mu_{cd}} - i0^+ + \nu - \Sigma_\varphi(0,-i\Omega)}, \end{aligned} \tag{1.33}$$

where

$$\Sigma_\varphi(0,-i\Omega) = \frac{h^2}{2\pi^2}\left(2\mu_{cd}\Lambda - (2\mu_{cd})^{3/2}\sqrt{-\frac{q^2}{2\mu_{cd}} - i0^+}\tan^{-1}\left(\frac{\Lambda}{\sqrt{2\mu_{cd}}\sqrt{-\frac{q^2}{2\mu_{cd}} - i0^+}} \right) \right). \tag{1.34}$$

Considering Eq. (1.17) and taking $q \to 0$, we have

$$\lim_{q\to 0} 1/f(q) = -\frac{1}{a} \stackrel{!}{=} \lim_{q\to 0}\frac{2\pi G_\varphi^{-1}(\mathbf{0},-i\Omega)}{h^2\mu_{cd}} = \frac{2\pi}{h^2\mu_{cd}}\left(\nu - \frac{h^2}{2\pi^2}2\mu_{cd}\Lambda \right) \tag{1.35}$$

such that

$$\nu = h^2\left(-\frac{\mu_{cd}}{2\pi a} + \frac{\mu_{cd}\Lambda}{\pi^2} \right) \tag{1.36}$$

and noting that

$$h^2\frac{\mu_{cd}\Lambda}{\pi^2} = h^2\int\frac{d\mathbf{q}}{(2\pi)^3}\frac{1}{\varepsilon^c_{\mathbf{q}}+\varepsilon^d_{\mathbf{q}}}, \tag{1.37}$$

we obtain the fixing condition for ν

$$\nu = h^2\left(-\frac{\mu_{cd}}{2\pi a}+\int\frac{d\mathbf{q}}{(2\pi)^3}\frac{1}{\varepsilon^c_{\mathbf{q}}+\varepsilon^d_{\mathbf{q}}}\right). \tag{1.38}$$

Ideally, one would now go back and using the fixing condition for ν, one would compute the combination $\nu-\Sigma_\varphi(\mathbf{p},\omega)$, in which the divergences cancel. However, one can also read off that the divergences cancel, and taking the limit $\Lambda\to\infty$, we arrive at

$$G^{-1}_\varphi(\mathbf{p},\omega) = -i\omega+\xi_{\mathbf{p}}-\frac{\mu_{cd}h^2}{2\pi a}+\frac{h^2}{4\pi}(2\mu_{cd})^{3/2}\sqrt{-i\omega+\frac{\mathbf{p}^2}{2(M_c+M_d)}}. \tag{1.39}$$

Considering

$$\begin{aligned}\lim_{q\to0}\frac{1}{f(q)q} = -i \overset{!}{=} \lim_{q\to0}\frac{1}{q}\frac{2\pi G^{-1}_\varphi(\mathbf{0},-i\Omega)}{h^2\mu_{cd}} &= \lim_{q\to0}\frac{1}{q}\frac{2\pi}{h^2\mu_{cd}}\frac{h^2}{4\pi}(2\mu_{cd})^{3/2}\sqrt{-\frac{q^2}{2\mu_{cd}}-i0^+}\\ &= -i,\end{aligned} \tag{1.40}$$

is a sanity check of our result. Finally, we can compute

$$\lim_{q\to0}\frac{1}{f(q)q^2} = \frac{r_0}{2} \overset{!}{=} \lim_{q\to0}\frac{1}{q^2}\frac{2\pi G^{-1}_\varphi(\mathbf{0},-i\Omega)}{h^2\mu_{cd}} = -\frac{\pi}{h^2\mu^2_{cd}}, \tag{1.41}$$

which can be used to fix h by the effective range r_0 (or equivalently r^*).

From Eq. (1.39) one may obtain a retarded propagator by continuing $i\omega\to z$ onto the upper half of the complex plane

$$G^{-1,R}_\varphi(\mathbf{p},z) = -z+\xi_{\mathbf{p}}-\frac{\mu_{cd}h^2}{2\pi a}+\frac{h^2}{4\pi}(2\mu_{cd})^{3/2}\sqrt{-z+\frac{\mathbf{p}^2}{2(M_c+M_d)}}. \tag{1.42}$$

As Eq. (1.39) is valid for both $\omega>0$ and $\omega<0$, the same procedure may be carried out in the lower half of the complex plane for the advanced propagator. Due to the appearing square-root the retarded Green's function is analytic for $\mathrm{Re}(-z+\mathbf{p}^2/2(M_c+M_d))>0$. As a result, Eq. (1.42) is an analytic continuation onto the whole complex plane, except for $z\in\mathbb{R}, z>\mathbf{p}^2/2(M_c+M_d)$, where the propagator has a branch cut. Finally, we note that the resulting molecule propagator has poles if and only if $a>0$, in which case the poles are given by

$$z = \xi_{\mathbf{p}}-\frac{\mu_{cd}h^2}{2\pi a}-\frac{1}{2}\left(\frac{h^2}{4\pi}(2\mu_{cd})^{3/2}\right)^2+\frac{1}{2}\sqrt{\left(\frac{h^2}{4\pi}(2\mu_{cd})^{3/2}\right)^4+4\left(\frac{h^2}{4\pi}(2\mu_{cd})^{3/2}\right)^2\frac{\mu_{cd}h^2}{2\pi a}}, \tag{1.43}$$

giving the energy of the molecule.

In the single-channel model, a similar calculation may be carried out. Alternatively, from Eq. (1.38) one may obtain a fixing condition for $g = -h^2/\nu$, which does not depend on h. More generally, when computing a quantity in the two-channel model which has an equivalent quantity in the single-channel model, the single channel result can be obtained simply by sending $h \to \infty$, while ensuring that all h-dependencies are explicit.

1.6.1 Two-body limit in two dimensions

In two dimensions, renormalizing the coupling constant works slightly differently. For a sufficiently short-ranged attractive interaction, the molecular bound state always exists in two dimensions [53], such that we may use its binding energy $\epsilon_B = \hbar^2/(2\mu_{cd}a_B^2)$ (where we have introduced a change in notation from E_B to ϵ_B)to fix the microscopic coupling constant.

On a technical level, the calculations work in a similar fashion as in three dimensions, however the fixing conditions are slightly different. Furthermore, while we carry out the calculation in a two-channel model, we will take the single-channel limit, as in the context of our work effective range corrections are less relevant in two dimensions.

Once again, our starting point is the vacuum two-body limit, where we set both chemical potentials to negative values, such that the corresponding densities vanish, $\mu_\psi, \mu_\phi < 0$. To fix the binding energy of the molecule, the location of the pole of the renormalized molecule Green's function Ω_{mol} must lie an amount of ϵ_B below the combined energy of the ϕ and ψ particles such that we have

$$G_\varphi^{-1,R}(\mathbf{0}, \Omega_{mol}) = 0 \tag{1.44}$$

$$\Omega_{mol} + \mu_\phi + \mu_\psi = -\epsilon_B. \tag{1.45}$$

Thus, we choose chemical potentials with $\mu_\phi + \mu_\psi = -\epsilon_B$ and $\mu_\psi, \mu_\phi < 0$, such that $\Omega_{mol} \overset{!}{=} 0$. Tracing the steps of the calculation in three dimensions, we thus have

$$\begin{aligned}
\Sigma_\varphi(\mathbf{p}, \omega) &= h^2 \int_{\mathbf{q},\nu} G^0_{\psi_\sigma^* \psi_\sigma}(\mathbf{p}-\mathbf{q}, \omega-\nu) G^0_{\phi^*\phi}(\mathbf{q}, \nu) \\
&= \frac{2\pi h^2}{(2\pi)^2} \int_0^\Lambda dq q \frac{1}{-i\omega + \frac{1}{2(M_c+M_d)}\mathbf{p}^2 + \frac{M_c+M_d}{2M_cM_d}\mathbf{q}^2 + \epsilon_B} \\
&= \frac{h^2\mu_{cd}}{2\pi}\left[\log\left(\epsilon_B - i\omega + \xi_{\mathbf{p}} + \frac{\Lambda^2}{2\mu_{cd}}\right) - \log\left(\epsilon_B - i\omega + \xi_{\mathbf{p}}\right)\right]
\end{aligned} \tag{1.46}$$

and using the fixing condition Eq. (1.44) one finds that

$$\nu = \frac{h^2\mu_{cd}}{2\pi}\log\left(1 + \frac{\Lambda^2}{2\mu_{cd}\epsilon_B}\right) = \frac{h^2}{(2\pi)^2}\int_{|\mathbf{q}|<\Lambda} d\mathbf{q} \frac{1}{\varepsilon^c_{\mathbf{q}} + \varepsilon^d_{\mathbf{q}} + \epsilon_B}. \tag{1.47}$$

With this renormalization, we can safely compute the renormalized molecule Green's function for $\omega > 0$ as

$$G_\varphi^{-1}(\mathbf{p}, \omega) = -i\omega + \xi_{\mathbf{p}} - \frac{h^2\mu_{cd}}{2\pi}\log\left(\frac{\epsilon_B}{\epsilon_B + \xi_{\mathbf{p}} - i\omega}\right). \tag{1.48}$$

After going to the single-channel limit we thus have

$$\frac{1}{g} = -\frac{1}{(2\pi)^2}\int_{|\mathbf{q}|<\Lambda} d\mathbf{q}\frac{1}{\varepsilon^c_{\mathbf{q}} + \varepsilon^d_{\mathbf{q}} + \epsilon_B}, \tag{1.49}$$

$$T(\mathbf{p},\omega) = \frac{2\pi}{\mu_{cd}}\frac{1}{\log\left(\frac{\epsilon_B}{\epsilon_B + \xi_{\mathbf{p}} - i\omega}\right)}. \tag{1.50}$$

1.7 The Fermi polaron problem

Having discussed the scattering of two different particles with each other, an important milestone in understanding strongly coupled two-component mixtures is the so-called *Fermi polaron problem*. It describes a strongly population-imbalanced mixture of a Fermi gas (called a *bath*) of density n_F interacting with a single particle of another species (referred to as an *impurity*).

The Fermi polaron problem has been realized experimentally both in ultracold atom and in TMD experiments. Most of its physical observables can be explained using a simple variational Ansatz, which we will review in the following. Like its natural counterpart, the *Bose polaron problem* of a Bose gas of density n_B interacting with a single particle of another species, these extremely population-imbalanced cases of strongly interacting mixture systems capture significant aspects of the scattering physics observed in balanced mixtures. We will see in Section 2.2 that a description of the Fermi polaron problem can make meaningful predictions even in an almost density-matched regime, which came as a surprise at the time. Similarly, in Chapter 4 we will use a theory that connects to both polaron problems to describe induced coupling processes in strongly coupled Bose-Fermi mixtures. This connection to both polaron problems will be used to argue that the strong-coupling physics has been treated appropriately.

In Sections 1.3 and 1.4, we reviewed the two-body scattering near a Feshbach resonance and found that in three dimensions a bound state exists between these two particles for positive scattering lengths, while in two dimensions it always exists. In both cases, the interaction parameters $1/a$ and ϵ_B determine the bound state energy (or the lack thereof) and in the Fermi polaron problem they are complemented by the length and energy scales of the Fermi gas to obtain dimensionless interaction parameters $1/k_F a$ and ϵ_B/ϵ_F. Here k_F is the Fermi wavevector and ϵ_F is the Fermi energy of the Fermi gas, which in three dimensions is related to the fermion density through $\epsilon_F = \hbar^2(6\pi^2 n_F)^{2/3}/2M_c = \hbar^2 k_F^2/2M_c$, where M_c is the fermion mass.

The physics of the Fermi polaron can be understood qualitatively from a tuning of the dimensionless interaction parameters. The tuning of $1/k_F a$ from $-\infty$ to $+\infty$ may be regarded as going from (vanishingly) weak to strong interactions. This can be appreciated from the underlying two-body bound state energy, where for $1/k_F a < 0$ the interaction is too weak to feature a bound state. For $1/k_F a > 0$ the bound state energy begins to increase and eventually diverges for $1/k_F a \to +\infty$. In the absence of interactions, the ground state of the system is given by an unperturbed Fermi sea along with an impurity in a zero-momentum state. We call this state the *non-interacting*

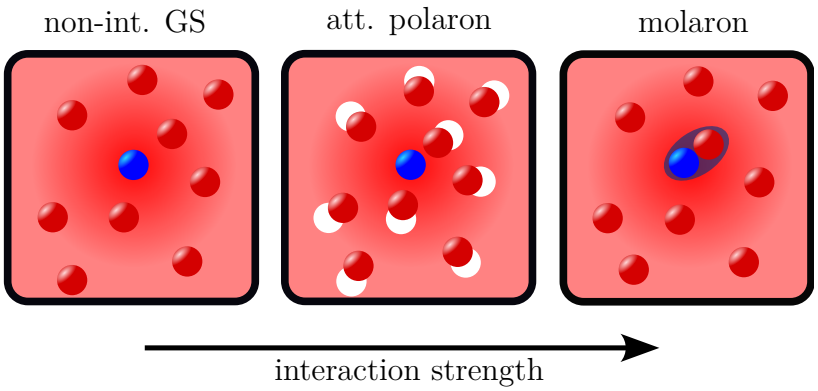

Figure 1.5. Schematic picture of the physics of the Fermi polaron problem. For vanishing impurity-bath interactions, the ground state is given by an unperturbed Fermi sea (red particles) along with an impurity in a well-defined momentum state (left). As interactions increase, the impurity may scatter with particles near the Fermi surface and due to the attractive nature of the interaction the bath particles are pulled slightly towards the impurity. In this attractive polaron state (middle), the impurity is dressed due to the bath particles and its quasiparticle properties such as its effective mass begin to change, as bath particles are dragged along. Once the interaction strength is strong enough, a molaron (right) forms in which a bath particle binds closely to the impurity. The molaron still experiences dressing due to the Fermi sea. Another polaron state, the repulsive polaron exists as an excited state in which bath particles are pushed away from the impurity rather than being attracted to it.

ground state, as interactions increase in strength, the impurity may interact with the Fermi sea and a superposition of the non-interacting state along with particle-hole excitations around the Fermi sea may form (see Fig. 1.5). This state which is adiabatically connected to the noninteracting ground state is commonly referred to as the Fermi polaron and for reasons that will become clear in the course of this section, we refer to it as the *attractive polaron*. In the opposite limit of near-infinitely strong interactions ($1/k_F a \to +\infty$), the average interfermion distance $\sim 1/k_F$ is much larger than the binding length of the two-body bound state $\sim a$ and as a result, the ground state will be a two-body bound state on top of a Fermi sea. Of course, the Pauli blocking of the Fermi sea will affect this state, but in the limit $1/k_F a \to +\infty$ the Pauli blocking becomes negligible. We refer to this state as the *molecule state*. Moving towards unitarity, this state will experience dressing due to the Fermi sea and the effect of Pauli blocking will become more noticable. The resulting state, which connects to the molecule state for $1/k_F a \to +\infty$, is commonly referred to as the *molaron* to indicate its dressing due to the Fermi sea, however in an abuse of notation it is often referred to as the *molecule*.

Between these limits, both types of states experience significant modifications of their quasiparticle properties due to the fermionic dressing, and the ground state of the system changes from the polaron to the molaron. In the Fermi polaron problem, the polaron and the molaron are orthogonal, and as a result at a critical interac-

tion strength there is a transition between these states which is referred to as the *polaron-to-molecule transition*. In the Bose polaron this is a crossover, as the presence of a condensate of bosons hybridizes polarons and molecules. Importantly, both the molaron and the attractive polaron exist as quasiparticles in the whole range of interaction strengths, even though the underlying two-body molecule state exists only for positive scattering lengths. Interestingly, a second polaron state exists above the attractive polaron, which we will refer to as the *repulsive polaron*. It is a well-defined quasiparticle only for $1/k_F a \gtrsim 0$.

In Chapter 5 we will treat the Fermi polaron problem using a self-consistent functional renormalization group method, however to familiarize ourselves with the concept, in the following we will treat it using a variational wave function Ansatz, which we will then relate to an equivalent diagrammatic approach. Within the single-channel model Eq. (1.26), both polaron states can be captured using a variational wavefunction commonly referred to as the Chevy Ansatz [54, 55]

$$|\psi_P^{\mathbf{p}}\rangle = \alpha_0^{\mathbf{p}} \hat{d}_{\mathbf{p}}^\dagger |\mathrm{FS}_N\rangle + \sum_{\mathbf{k},\mathbf{q}}{}' \alpha_{\mathbf{k},\mathbf{q}}^{\mathbf{p}} \hat{d}_{\mathbf{p}+\mathbf{q}-\mathbf{k}}^\dagger \hat{c}_{\mathbf{k}}^\dagger \hat{c}_{\mathbf{q}} |\mathrm{FS}_N\rangle \,, \tag{1.51}$$

where $\mathbf{p}$ denotes the momentum of the state, $|\mathrm{FS}_N\rangle$ a Fermi sea of N particles, the sums are for $|\mathbf{q}| < k_F, |\mathbf{k}| > k_F$ and the $\alpha_0^{\mathbf{p}}, \alpha_{\mathbf{k},\mathbf{q}}^{\mathbf{p}}$ are variational parameters. Similarly, the molaron state can be captured using the following Ansatz [55–57]

$$|\psi_M^{\mathbf{p}}\rangle = \sum_{\mathbf{k}}{}' \beta_{\mathbf{k}}^{\mathbf{p}} \hat{c}_{-\mathbf{k}}^\dagger \hat{d}_{\mathbf{k}+\mathbf{p}}^\dagger |\mathrm{FS}_{N-1}\rangle \;, \tag{1.52}$$

where to preserve particle number between both wavefunctions, $|\mathrm{FS}_{N-1}\rangle$ denotes a Fermi sea of $N-1$ particles. Near a narrow Feshbach resonance, both Ansätze may be extended to also feature molecule operators and be treated in the two-channel Hamiltonian Eq. (1.22). For $h \to \infty$ the results reduce to those obtained using Eqs. (1.51) and (1.52) within a single-channel Hamiltonian.

For a given $\mathbf{p}$, minimizing the energy functional $\langle \psi_{P/M}^{\mathbf{p}} | \hat{H} - E | \psi_{P/M}^{\mathbf{p}} \rangle$ with respect to the variational parameters

$$\begin{aligned} \frac{\delta}{\delta \alpha_0^{\mathbf{p}}} \langle \psi_{P/M}^{\mathbf{p}} | \hat{H} - E | \psi_{P/M}^{\mathbf{p}} \rangle &\stackrel{!}{=} 0 \\ \frac{\delta}{\delta \alpha_{\mathbf{k},\mathbf{q}}^{\mathbf{p}}} \langle \psi_{P/M}^{\mathbf{p}} | \hat{H} - E | \psi_{P/M}^{\mathbf{p}} \rangle &\stackrel{!}{=} 0 \quad \forall |\mathbf{q}| < k_F, |\mathbf{k}| > k_F, \end{aligned} \tag{1.53}$$

the ensuing equation systems admit two solutions for the Chevy Ansatz (1.51) and one solution for the molaron Ansatz (1.52). The quasiparticle weight/residue $Z_{\mathbf{p}} = |\alpha_0^{\mathbf{p}}|^2$ gives the overlap of the polaron state with the non-interacting ground state. Furthermore, it quantifies the occupation probability of finding the impurity in the $\mathbf{p}$-state, which, as we shall see in Section 2.2, connects to the condensate fraction in a nearly balanced Bose-Fermi mixture. Furthermore, it quantifies the residue of the corresponding pole in the retarded Green's function.

The resulting energies of both polaron states and the molaron state are shown in Fig. 1.6. Furthermore, the quasiparticle weights are shown. As can be seen, the

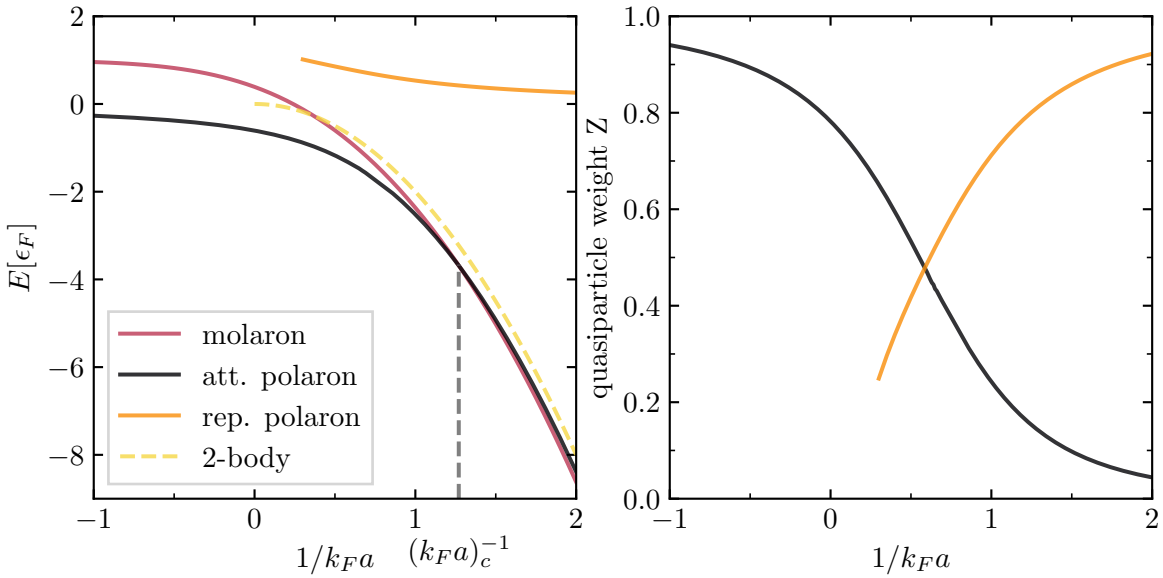

Figure 1.6. Quasiparticle energy and weight of different quasiparticles in the Fermi polaron problem as obtained from the Ansätze in Eqs. (1.51) and (1.52). The energies (left) and quasiparticle weights (right) of the molaron (red), the attractive polaron (black) and the repulsive polaron (orange) are shown as a function of $1/k_Fa$. Energies are shown in units of the Fermi energy. Furthermore, the energy of the two-body bound state (yellow, dashed) is shown for comparison.

attractive polaron and molaron energies cross at the polaron-to-molecule transition $(k_Fa)_c$. At small, positive values of $1/k_Fa$ the repulsive polaron begins to exist as an excited state and its energy asymptotically tends to zero for $1/k_Fa \to +\infty$. The molaron exists for all interaction strengths. With increasing values of $1/k_Fa$, the molaron energy turns from positive to negative and eventually crosses the attractive polaron energy. Asymptotically, both the attractive polaron and the molaron energy lie within a range of ϵ_F around the two-body binding energy. The quasiparticle weight of the attractive polaron is near unity for small values of $1/k_Fa$, decreases with increasing $1/k_Fa$ and vanishes asymptotically for $1/k_Fa \to \infty$. The quasiparticle weight of the attractive polaron is slowly transferred to the repulsive polaron, which increases with increasing $1/k_Fa$ and approaches unity for $1/k_Fa \to \infty$. The attribute *attractive* and *repulsive* for the polaron stem from its energy lying above or below the energy of a non-interacting system and also have corresponding effects on the spatial configuration of the fermion dressing cloud [58].

The treatment within the variational Ansatz of up to one particle-hole excitation is equivalent [59] to a diagrammatic Ansatz (see Fig. 1.7), in which the T-matrix is computed as

$$\begin{aligned}\frac{1}{T(\mathbf{p},\omega)} &= \left(\frac{\mu_{cd}}{2\pi a} - \int \frac{d\mathbf{k}}{(2\pi)^3}\frac{1}{\varepsilon^c_{\mathbf{k}}+\varepsilon^d_{\mathbf{k}}} + \int_{\mathbf{k},\nu} G^0_{\psi^*_\sigma\psi_\sigma}(\mathbf{p}-\mathbf{k},\omega-\nu)G^0_{\phi^*\phi}(\mathbf{k},\nu)\right) \\ &= \frac{\mu_{cd}}{2\pi a} + \int \frac{d\mathbf{k}}{(2\pi)^3}\left(\frac{n_F(\epsilon_F-\varepsilon^c_{\mathbf{p}-\mathbf{k}})}{-i\omega+\varepsilon^c_{\mathbf{p}-\mathbf{k}}+\varepsilon^d_{\mathbf{k}}-\epsilon_F-\mu_\phi} - \frac{1}{\varepsilon^c_{\mathbf{k}}+\varepsilon^d_{\mathbf{k}}}\right) \end{aligned} \tag{1.54}$$

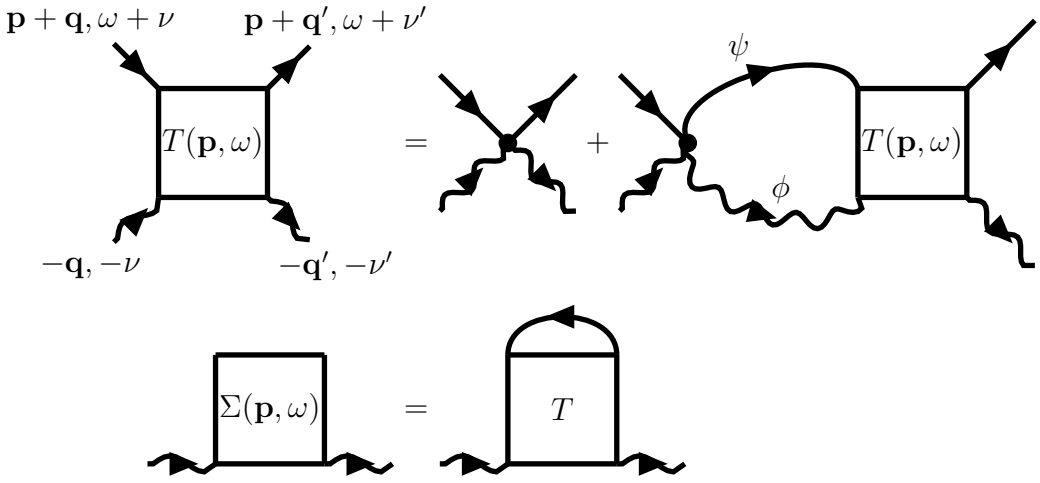

Figure 1.7. Feynman diagrams of the T-matrix (Eq. (1.54)) and the impurity self-energy (Eq. (1.55)) within the non-selfconsistent T-matrix approach. The same notation as in Fig. 1.4 is used, and the dots denote the four-body vertex $\sim g$.

while the self-energy of the impurities is computed as

$$\Sigma_\phi(\mathbf{p}, \omega) = -\int \frac{d\mathbf{q}}{(2\pi)^3} n_F(\varepsilon^c_{\mathbf{q}} - \epsilon_F) T(\mathbf{p}+\mathbf{q}, \omega - i(\varepsilon^c_{\mathbf{q}} - \epsilon_F)) \tag{1.55}$$

such that the renormalized inverse impurity Green's function is given by

$$G^{-1}_\phi(\mathbf{p}, \omega) = -i\omega + \varepsilon^d_{\mathbf{p}} - \mu_\phi - \Sigma_\phi(\mathbf{p}, \omega). \tag{1.56}$$

To set the density of the Fermi gas to n_F, we have set its chemical potential as $\mu_\phi = \epsilon_F$. The scattering matrix T can be interpreted as the Green's function of the molecule operator, and thus its spectrum contains the molaron. Similarly, the impurity Green's function contains the polaron.

Continuing both T and G_ϕ to the complex plane $i\omega \to z$, we find that the retarded impurity propagator G^R_ϕ has two poles, corresponding to the two polaron states, and T^R has one, corresponding to the molaron state. From the location of the poles $z = \Omega - i\gamma$, the energy E and the decay width Γ of the corresponding particles can be determined as

$$\begin{aligned} E &= \Omega + \mu_\phi \\ \Gamma &= \gamma. \end{aligned} \tag{1.57}$$

Being able to relate the variational Ansätze to an equivalent treatment within field theory has the key advantage that properties such as the quasiparticle spectral function of the different operators can be computed in a natural way. Defining the impurity $\mathcal{A}_\phi$ and molecule spectral functions $\mathcal{A}_\varphi$ as

$$\begin{aligned} \mathcal{A}_\phi(\Omega, \mathbf{p}) &= 2\,\mathrm{Im}\, G^R_\phi(\Omega + i0^+, \mathbf{p}) \\ \mathcal{A}_\varphi(\Omega, \mathbf{p}) &= 2\,\mathrm{Im}\, T^R(\Omega + i0^+, \mathbf{p}), \end{aligned} \tag{1.58}$$

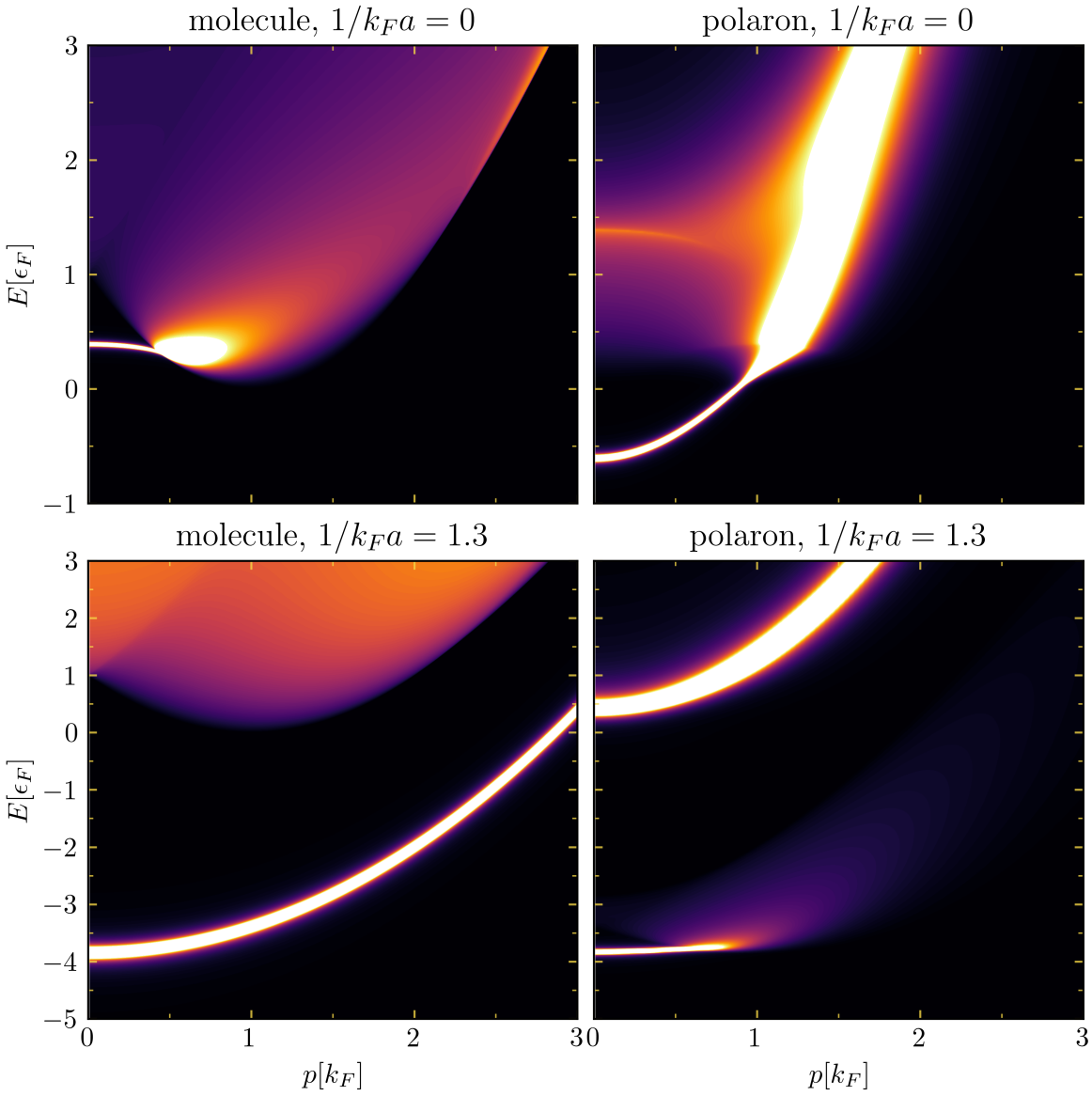

Figure 1.8. Spectral functions as obtained from the non-selfconsistent T-matrix approach. The molecule (left) and impurity (right) spectral functions, $\mathcal{A}_\varphi$ and $\mathcal{A}_\phi$, are shown as a function of momentum and p (in units of k_F) and energy E (in units of ϵ_F, see Eq. (1.57)) for $1/k_Fa = 0$ (top) and $1/k_Fa = 1.3$ (bottom).

we are able to study their excitation spectra[1]. In Fig. 1.8, both spectral functions from Eq. (1.58) are shown at unitarity and near the transition at $1/k_Fa = 1.3$. In the impurity spectral functions the attractive and repulsive polaron can be seen along with particle-hole continua. At unitarity the repulsive polaron lies within the particle-hole continuum, thus it is not a well-defined quasiparticle, evidenced also by its low quasiparticle weight. The molaron is visible in both spectra, tough near unitarity it eventually joins the continuum at intermediate momenta, which it does not do at

[1]Note that the impurity spectral function is sometimes referred to as a polaron spectral function, because it contains the polaron states. Strictly speaking, however, a spectral function describes the response of a system due to an excitation by a bare operator, so the name impurity spectral function is more precise.

$1/k_F a = 1.3$. Spectra and quasiparticle properties obtained from a functional renormalization group approach are shown in Chapter 5. Furthermore, in Section 2.3.5.2 we will show how the results obtained for the diagrammatic non-selfconsistent T-matrix approach shown in this section may also be obtained using the functional renormalization group (fRG) formalism which we will introduce in Section 1.9.

1.8 Fermi polaron problem in ultracold atoms and atomically thin semiconductors

As we have seen in the previous section, the nature of the ground state of the Fermi polaron problem universally depends on the ratio of the two relevant energy scales of the problem: the kinetic energy, represented by ϵ_F, and the interaction energy, set by ϵ_B in two dimensions and the scattering length a in three dimensions. While ϵ_F/ϵ_B can, in theory, be tuned by either adjusting ϵ_F or ϵ_B, in experiments it depends on the physical system which parameter is accessible for easy tunability.

As discussed in Sections 1.1 and 1.2 two major systems in which strongly coupled Bose-Fermi mixtures can be realized today are ultracold atoms and TMD. To support the following discussion, in Table 1.1 we summarize key parameters and quantities describing the universal connection between these systems.

In monolayer TMD, ϵ_B represents the trion binding energy that is typically fixed [33, 60–63]. However, by electrostatically doping the system with charge carriers, the Fermi energy ϵ_F is easily adjusted and thus ϵ_F/ϵ_B can be tuned. In cold atoms the situation is reversed. Here, the binding energy ϵ_B (or the scattering length in three dimensions) can be tuned using Feshbach resonances, while adjusting the Fermi energy over a wide range of values is challenging. As a result, in cold atoms, the Fermi energy ϵ_F is the natural unit and, correspondingly, the spectrum of the system is expressed as a function of the dimensionless energy E/ϵ_F and the interaction strength ϵ_B/ϵ_F. In contrast, in TMD the binding energy ϵ_B provides the appropriate unit, and the spectrum is expressed as a function of E/ϵ_B and ϵ_F/ϵ_B.

Of course, physics does not depend on the chosen units. It is, however, still instructive to compare spectra for both sets of units, as the choice of units reflects the experimental protocols employed to observe the physics of Fermi polarons: in TMD using gate-doping of ϵ_F and in cold atoms interaction tuning of ϵ_B exploiting Feshbach resonances.

1.9 Effective action and functional renormalization group (fRG) formalism

Throughout this thesis, we will make use not only of conventional diagrammatic methods in field theory, but also of functional renormalization group (fRG) methods, which are a momentum space implementation of Wilson's renormalization group idea. The fRG has been successfully applied to the study of strongly coupled systems in a broad

	2D semiconductors (TMD)	cold atoms
fermions	electron/hole	atom
charge	negative/positive	neutral
size	pointlike	$\sim a_0$
bosons	exciton	atom
charge	neutral	neutral
size	$\sim$ 1nm	$\sim a_0$
composite fermion	trion	molecule
charge	charged	neutral
size	$\sim$ 2nm (fixed)	$\sim 1000a_0$ (tunable)
typical Fermi energy $\sim \epsilon_F$	$0 - 50$meV $\widehat{=}$ 0 - 10THz	50peV $\widehat{=}$ 10kHz
tune?	tunable: gate doping	$\sim$fixed
typical int. energy $\sim \epsilon_B$	30meV $\widehat{=}$ 10THz	$0 - 50$peV $\widehat{=}$ $0 - 10$kHz
tune?	fixed	tunable: Feshbach resonances
dimension	2D	1D, 2D, 3D
Fermi temperature T/T_F	mK $-$ 300K: $T/T_F \sim 0 - 2$	5nK $-$ μK: $T/T_F \sim 0.05 - 2$
Bose-Fermi potential	short-ranged polar. int. $\sim 1/r^4$	short-ranged, vdW/Feshbach int.
Fermi-Fermi separation	$>$ 1nm (tunable)	$\sim 1000a_0$ ($\sim$ fixed)
int. strength ϵ_B/ϵ_F	$\sim$ 1, strong coupling	$\sim$ 1, strong coupling

Table 1.1. Comparison of key properties of physical systems in which two-dimensional Bose-Fermi mixtures can be realized in a universal way: two-dimensional semiconductors hosted in atomically thin transition metal dichalcogenides (TMD) and confined, quasi-two-dimensional gases of ultracold atoms interacting via Feshbach resonances. The constant $a_0 = 0.529$Å denotes the Bohr radius.

range of areas [64–67], spanning from the asymptotic safety of quantum gravity [68–70] to high-energy [71, 72], statistical [73–75] and condensed matter physics [76–80]. Compared to conventional quantum field theory approaches, it displays several advantages. First, it usually provides for a fully self-consistent treatment that naturally includes high-order quantum fluctuations and incorporates these on equal footing. Second, the fRG includes quantum fluctuations in a coarse-grained fashion —momentum-by-momentum shell— which makes it ideally suited to treat competing ordering instabilities. Third, similar to variational techniques, the fRG can be improved systematically by using increasingly refined truncations of the underlying quantum effective action. Finally, it offers easier access to spectral and dynamical response functions compared to Monte Carlo approaches, where the analytic continuation of noisy data is required. In the following, we briefly provide an introduction to the effective action functional and then give a brief introduction into the principle ideas and equations concerning the fRG. For a detailed discussion, we refer to Refs. [64–66, 79].

Being presented with a Hamiltonian $\hat{H}$ such as the one in Eq. (1.22), the corresponding grand canonical partition function is given by

$$\mathcal{Z} = \mathrm{Tr}\, e^{-\beta(\hat{H}-\mu\hat{N})}, \tag{1.59}$$

where $\beta = 1/T$ is the inverse temperature, μ denotes different chemical potentials and $\hat{N}$ the particle number operator corresponding to these chemical potentials. Using the Matsubara frequency formalism this can be reformulated in terms of quantum fields (for details see e.g. [52, 81]) and field integrals over them

$$\mathcal{Z} = \int \mathcal{D}\phi e^{-S[\phi]}, \tag{1.60}$$

where ϕ denotes the quantum fields corresponding to the operators in $\hat{H} - \mu\hat{N}$, $\mathcal{D}\phi$ is the measure for the field integration and S is the corresponding classical action. To give an intuition in the following, we will proceed for the simplest case of real, bosonic fields. Of course, these expressions can also be generalized to hold for more complicated fields. Note, however, that the fields may still have many field indices and should thus be treated analogous to vectors.

To be able to obtain observables from the partition function, one may add a source term to the exponent such that expectation values may be obtained using suitable functional derivatives

$$\mathcal{Z}[J] = \int \mathcal{D}\phi e^{-S[\phi]+J\phi}, \tag{1.61}$$

such that

$$\langle \phi^n \rangle_J = \frac{1}{\mathcal{Z}} \frac{\delta^n}{\delta J^n} \mathcal{Z}[J]. \tag{1.62}$$

Note that in this definition $\langle \phi^n \rangle$ is dependent on the source term J and the physical expectation value is computed for $J = 0$. The functional $\mathcal{Z}$ generates correlation functions, while one can show that in a similar way $W[J] = \log \mathcal{Z}[J]$ is the generator of connected correlation functions.

Defining a Legendre transform of W, we can then introduce an effective action as

$$\Gamma[\varphi] = J[\varphi]\varphi - W[J(\varphi)], \tag{1.63}$$

where $J[\varphi]$ is implicitly defined using the relation

$$\varphi = \frac{\delta}{\delta J} W[J] \bigg|_{J=J[\varphi]}, \tag{1.64}$$

such that one can show that

$$\varphi = \langle \phi \rangle_{J[\varphi]} \tag{1.65}$$

$$\frac{\delta}{\delta \varphi} \Gamma[\varphi] = J[\varphi] \tag{1.66}$$

$$\frac{\delta^2}{\delta \varphi^2} \Gamma = \left(\frac{\delta^2}{\delta J^2} W \right)^{-1}, \tag{1.67}$$

where Eq. (1.67) should be understood in the sense of a matrix inverse of a Hesse matrix in the case of fields and source terms with more than one entry. The quantum effective action Γ can be related to the W functional by noting that the equilibrium field configuration $\varphi_{eq} = \langle\phi\rangle_{J=0}$ is obtained for $J[\varphi_{eq}] = 0$ such that

$$\Gamma[\varphi_{eq}] = -W[J=0], \tag{1.68}$$

and

$$\mathcal{Z} = e^{-\Gamma[\varphi_{eq}]}, \tag{1.69}$$

where due to Eq. (1.66) we have that

$$0 = \frac{\delta}{\delta\varphi}\Gamma[\varphi]\bigg|_{\varphi=\varphi_{eq}}. \tag{1.70}$$

Thus, from obtaining the quantum effective action Γ all physical observables can be deduced from it as it is the generating functional of one-particle irreducible (1PI) correlation functions. While the classical action S contains no quantum fluctuations, all quantum fluctuations are contained within Γ and thus the quantum fluctuations contained within $\mathcal{Z}[J]$ may equally be described by considering classical physics of a hypothetical classical action described by the effective action Γ.

The fRG is a method to obtain an approximation of the effective action. The idea behind the fRG is to build a family of theories indexed by a momentum scale k such that only quantum fluctuations above that scale are taken into account. Thus rather than treating fluctuations at all scales at once, one iteratively integrates out modes from high to low energies by smoothly lowering k from the microscopic UV scale Λ down to $k = 0$. In practice this is done by adding to the classical action $S[\phi]$ an infrared regulator term

$$\Delta S_k[\phi] = \frac{1}{2}\phi R_k \phi, \tag{1.71}$$

which penalizes low-energy fluctuations, such that only high-energy modes contribute to the field integral.

Starting from the sum of S and ΔS_k one then defines a scale-dependent partition function

$$\mathcal{Z}_k[J] = e^{W_k[J]} = \int \mathcal{D}\phi e^{-S[\phi]-\Delta S_k[\phi]+J\phi}, \tag{1.72}$$

as well as a scale-dependent effective action

$$\Gamma_k[\varphi] = J[\varphi]\varphi - W_k[J(\varphi)] - \Delta S_k[\varphi] \tag{1.73}$$

through a (modified) Legendre transform of the free energy $\log \mathcal{Z}_k$, which is required to respect Eq. (1.64) for W_k. One can then show that

$$\begin{aligned}\partial_k W_k[J] = -\frac{1}{2}\langle\phi\partial_k R_k\phi\rangle &= -\frac{1}{2}\frac{\delta}{\delta J}(\partial_k R)\frac{\delta}{\delta J}W - \frac{1}{2}\frac{\delta W}{\delta J}(\partial_k R)\frac{\delta W}{\delta J} \\ &= -\frac{1}{2}\operatorname{Tr}\left((\partial_k R_k)\frac{\delta^2 W[J]}{\delta J^2}\right) - \frac{1}{2}\langle\phi\rangle\,\partial_k R\,\langle\phi\rangle\,.\end{aligned} \tag{1.74}$$

To avoid confusion, we now make the field indices explicit to show that

$$\left(\frac{\delta^2}{\delta\varphi^2}\left(\Gamma[\varphi]+\Delta S_k[\varphi]\right)\right)_{\alpha\beta}=\frac{\delta^2}{\delta\varphi_\alpha\delta\varphi_\beta}\left(\Gamma[\varphi]+\Delta S_k[\varphi]\right)=\frac{\delta J_\beta[\varphi]}{\delta\varphi_\alpha}, \tag{1.75}$$

while

$$\left(\frac{\delta^2}{\delta J^2}W[J]\Big|_{J=J[\varphi]}\right)_{\alpha\beta}=\frac{\delta^2}{\delta J_\alpha\delta J_\beta}W[J[\varphi]]=\frac{\delta\varphi_\beta[\varphi]}{\delta J_\alpha}, \tag{1.76}$$

such that we obtain

$$\begin{aligned}\partial_k\Gamma_k[\varphi]&=-\partial_k W_k[J[\varphi]]-\frac{1}{2}\varphi(\partial_k R_k)\varphi\\&=\frac{1}{2}\,\mathrm{Tr}\left((\partial_k R_k)\frac{\delta^2 W[J]}{\delta J^2}\right)\\&=\frac{1}{2}\,\mathrm{Tr}\left((\partial_k R_k)\left(\frac{\delta^2}{\delta\varphi^2}\left(\Gamma[\varphi]+\Delta S_k[\varphi]\right)\right)^{-1}\right).\end{aligned} \tag{1.77}$$

Generalizing this result to include fermionic fields, the evolution or 'flow' of the effective action as the scale k is lowered is then given by the Wetterich equation [82],

$$\partial_k\Gamma_k=\frac{1}{2}\,\mathrm{STr}\left[\left(\Gamma_k^{(2)}+R_k\right)^{-1}\partial_k R_k\right]. \tag{1.78}$$

In the above expression, the supertrace STr denotes a summation over all momenta and frequencies, as well as the different fields, including a minus sign for fermions. Moreover, $\Gamma_k^{(2)}$ and R_k represent the matrices of second functional derivatives of Γ_k and ΔS_k, respectively, with respect to the quantum fields. From now on we use the same symbol for the fields in the action S and in the flowing effective action Γ_k.

Provided $R_{k=\Lambda}=\infty$[2] at $k=\Lambda$ all fluctuations are suppressed and $\Gamma_{k=\Lambda}=S+const.$ [65, 66]. On the other hand, for $R_{k=0}=0$ one recovers at $k=0$ the effective action of the original model, $\Gamma_{k=0}=\Gamma$. Crucially, the effective action Γ (Gibbs free energy) is the generating functional of all one-particle irreducible vertices. It thus contains all information about the exact solution of the theory, and hence its determination corresponds to solving the non-relativistic, many-body Schrödinger equation.

In Chapters 2 and 5 we will make use of rather advanced fRG methods. An analysis of coupling constants which may serve as a first introduction to RG flows is provided in Section 4.7.

[2] In practice $R_{k=\Lambda}\simeq\Lambda^2$ is sufficient.

Chapter 2

Strongly coupled Bose-Fermi mixtures

This chapter is based on the following publications:

[1] **J. von Milczewski**, F. Rose, R. Schmidt,
Functional-renormalization-group approach to strongly coupled Bose-Fermi mixtures in two dimensions,

Physical Review A 105, 013317 (2022).

[2] M. Duda, X.-Y. Chen, A. Schindewolf, R. Bause, **J. von Milczewski**, R. Schmidt, I. Bloch, X.-Y. Luo,
Transition from a polaronic condensate to a degenerate Fermi gas of heteronuclear molecules,

Nature Physics 19, 720-725 (2023).

In this chapter we study the phase diagram of strongly coupled Bose-Fermi mixtures both in two and three dimensions. The discussions in this chapter are based on the work presented in Ref. [1] along with our contributions to Ref. [2] where we provided a theoretical explanation of the experimental observations.

2.1 Introduction

Ever since the theoretical explanation of conventional superconductivity as arising from the effective attraction between electrons mediated by phonons [83, 84], Bose-Fermi mixtures have been the subject of intense research. As they combine systems of different quantum statistics, their many-body behavior can be vastly different from that of the underlying bosonic or fermionic subsystems alone. Consequently, they can feature rich many-body physics ranging from superconductivity to the formation of composite bosonic or fermionic bound states similar to mesons and baryons in particle physics.

In solid-state physics, bosons typically appear as collective degrees of freedom. These may be, for instance, phonon excitations of an underlying crystalline lattice or collective excitations of the electronic system itself in the form of, e.g., magnons or plasmons. While electron-phonon coupling is captured by Fröhlich or Holstein models, developments in ultracold atoms [20] and van-der-Waals materials [33] now make it possible to realize Bose-Fermi mixtures that are governed by beyond-Fröhlich physics. Here bosons and fermions can bind to fermionic molecules [85–90] reaching the quantum-degenerate regime [91]. The competition between this novel bound state physics and mediated interactions leads to an enriched phase diagram potentially featuring supersolidity and charge-density-wave phases [92–95], molecular Fermi liquids [1, 96–100], and unconventional boson-induced superconductivity [101, 102].

Crucially, direct pairing between bosons and fermions is a new essential ingredient in these mixtures. Recently, it was shown [103] that for such strongly coupled Bose-Fermi mixtures a description in terms of Fröhlich or Holstein models [104, 105], in which fermions couple linearly to the bosonic degrees of freedom, fails. In addition, the coupling to bosons at quadratic order becomes relevant, which has to be accounted for in an *extended* Fröhlich Hamiltonian [103], giving rise to qualitatively new physics recently observed in experiments in cold gases [106–108] and Rydberg systems [109].

Various aspects of atomic, three-dimensional Bose-Fermi mixtures have been investigated theoretically using the Fröhlich model —thus disregarding the crucial quartic interaction term. This revealed a rich structure of the phase diagram ranging from polaron formation [110–112] and boson-induced p-wave superfluidity [101], to phonon softening and phase separation [92].

Similarly, the phase diagram of *two-dimensional* Bose-Fermi mixtures has been explored using the Fröhlich model. These studies were motivated in particular by exciton-electron mixtures in semiconductors, and, following initial work by Ginzburg [113], it was predicted that the system may turn superconducting [102, 114, 115], while other works proposed a transition to supersolidity [93, 94], or that the formation of both phases might be intertwined [95].

Due to the shortcomings of the Fröhlich model and mean-field inspired approaches that neglect pairing [116–121], these initial studies missed the fact that the microscopic interaction between atoms in ultracold gases and between excitons and electrons in semiconductors is fundamentally attractive. While in cold gases interactions arise from long-range van der Waals forces, the polarization of charge-neutral excitons by electrons gives rise to attractive forces in semiconductors. Crucially, in both cases the interactions support bound states between the fermionic and bosonic particles. Consequently, as the strongly coupled regime is entered, one has to consider the *extended* Fröhlich Hamiltonian in order to account for the pairing to fermionic Feshbach molecules in cold atoms and exciton-electron bound states, called trions, in semiconductors.

The presence of this novel bound state physics renders the description of strongly coupled Bose-Fermi mixtures an outstanding theoretical challenge. This is reflected by the fact that until now —except for initial studies in three dimensions [96, 98–100, 122–125]— the phase diagram of strongly coupled Bose-Fermi mixtures as function of

the density of bosons n_B and fermions n_F, schematically shown in Fig. 2.1, remains unexplored. With the discovery of atomically thin transition-metal-dichalcogenides, the semiconducting class of layered van der Waals materials, the exploration of this phase diagram in two dimensions becomes particularly urgent. This is not only due to the potential of layered materials for technological applications, but also due to the possibility of realizing long-lived, stable exciton-electron mixtures that feature a striking similarity to cold atomic mixtures [61, 62, 126]. This universal connection, detailed by the comparison of typical scales in both systems shown in Table 1.1, opens the possibility to explore emerging phases in strongly interacting systems in two complementary and seemingly disparate systems, that while playing on vastly different energy and length scales, are governed by the same dimensionless system parameters. Furthermore, applications such as inducing superconductivity between electrons via the exchange of excitons come within reach of experimental realization, and theoretical efforts to describe these systems require foundational work in the describing their phase diagram.

In three-dimensional ultracold atom experiments, the phase diagram of Bose-Fermi mixtures has primarily been explored in the regime of large population imbalance where one species acts as a dilute, thermal gas of impurities dressed by its environment. Bose polarons were recently observed in the limit of fermionic impurities in a bosonic bath [106–108], while the existence of a transition from Fermi polarons to molecules has by now been firmly established for impurities immersed in a Fermi sea [9, 128–130]. However, so far it has remained unclear how the transition from atoms to molecules proceeds when the impurities are degenerate, in particular when bosons and fermions of comparable density dress each other mutually and drastically modify their respective behavior. Importantly, this regime of matched particle density is promising for the association of heteronuclear molecules at high phase space density, which finds wide-ranging applications in quantum chemistry and the exploration of dipolar quantum many-body systems [131, 132]. At the same time, reaching this regime is notoriously difficult in double-degenerate mixtures due to the enhanced density of the bosonic condensate. The excess density of the Bose-Einstein condensate (BEC) causes fast interspecies loss, which remains the key bottleneck for reaching quantum degeneracy in heteronuclear molecules and for the study of strongly correlated Bose-Fermi mixtures.

This chapter of the thesis, consisting of studies in two and three dimensions, is structured as follows:

In the next section, after reviewing existing literature on the phase diagram of strongly coupled three-dimensional Bose-Fermi mixtures and performing related fRG calculations, experimental data obtained in three-dimensional strongly interacting Bose-Fermi mixtures with comparable densities are analyzed and interpreted. The data suggest that in the low temperature regime where the bosonic impurities condense, strong boson-fermion interactions induce a phase transition from a polaronic condensate to a molecular Fermi gas, connecting to an underlying quantum phase transition (QPT) at $T = 0$ [98]. Using a novel density-decompression technique which mitigates atomic loss, a double-degenerate Bose-Fermi mixture of ^{23}Na and ^{40}K with

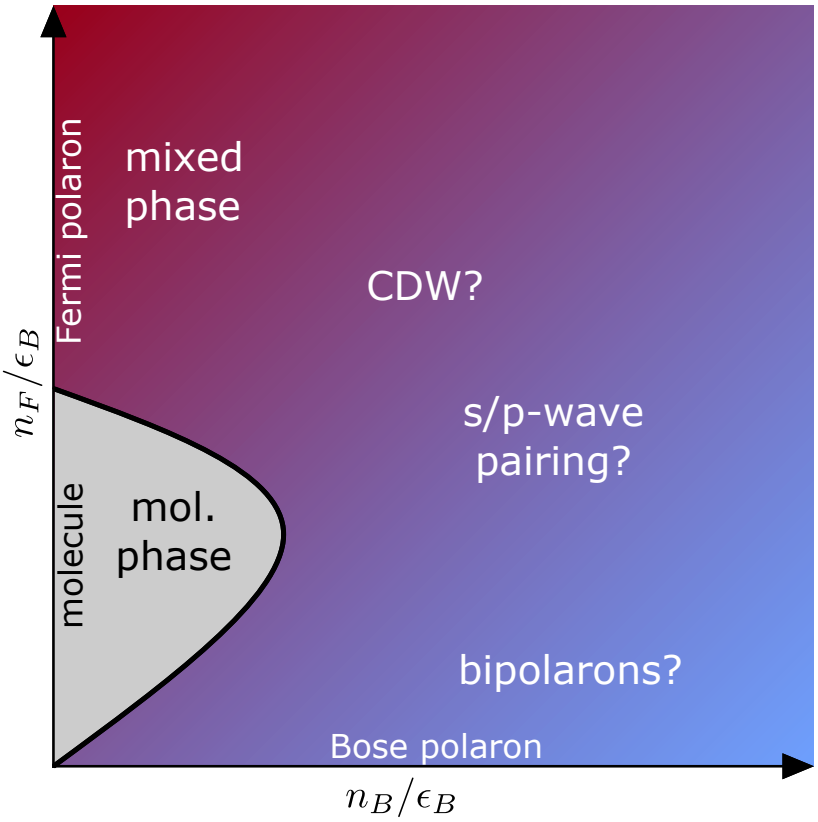

Figure 2.1. Schematic phase diagram of two-dimensional Bose-Fermi mixtures as a function of the density of either species. At strong coupling, the system is described by the extended Fröhlich model that accounts for the formation of a two-body bound state between fermions and bosons of energy ϵ_B. The limit $n_B = 0$ (along the y-axis) defines the Fermi polaron problem, discussed in Section 2.3.3, where a single bosonic impurity interacts with a fermionic bath. In this limit the impurity can either bind with a fermion into a molecule or remain unbound as a Fermi polaron. At finite boson density, discussed in Section 2.3.4, a transition from a molecular phase which hosts a Fermi sea of bound molecules (light gray) to a mixed phase in which a condensate of bosons hybridizes fermionic and molecular degrees of freedom (red/dark shading) is found. With the exception of the extreme limit $n_F = 0$ that corresponds to the Bose polaron problem (along the x-axis), as the boson density is increased beyond the regime $n_B \ll n_F$ (red/dark to blue/light shading), the phase diagram remains largely unexplored. Starting with the possibility of bipolaron formation [127], various competing phases can be conjectured based on studies of the simpler weak-coupling Fröhlich model, ranging from supersolid charge density wave states [94, 95] to boson-mediated s/p-wave fermion pairing [92, 101, 102, 114].

matched density was produced which reveals signatures of this QPT. Starting from a weakly interacting mixture, increased attractive interactions dress the bosonic condensate polaronically. By continuously tuning the interaction strength, the polaronic condensate is depleted, and a transition into a phase of quantum-degenerate fermionic molecules is observed. Driving the underlying QPT enhances the association efficiency

of Feshbach molecules to near unity. This enables the subsequent creation of ground-state ^{23}Na^{40}K molecules with a large molecular-frame dipole moment of 2.7 Debye in the quantum-degenerate regime. Section 2.2 ends with a conclusion on the works presented in that section.

In the following section, the phase diagram of strongly coupled two-dimensional Bose-Fermi mixtures is studied theoretically as a function of the boson and fermion densities. A key theoretical challenge is that the pairing between bosons and fermions gives rise to *fermionic* composite particles. Due to their fermionic nature, these particles evade conventional mean-field approaches and are thus much harder to describe than their bosonic counterparts in Fermi mixtures, where they emerge as Cooper pairs or bosonic molecules. Moreover, the existence of such fermionic composites implies a phase diagram that is richer in possible phase transitions compared to the simpler Fröhlich model. In two dimensions, however, the emergence of such fermionic composites is more challenging to capture than in three dimensions, as will be explained in Section 2.3. In that section, this challenge is tackled by developing first steps towards a comprehensive functional renormalization group approach that allows access to the full phase diagram of Bose-Fermi mixtures in two dimensions. Our approach accounts for the bound state physics arising from the extended Fröhlich Hamiltonian and can be systematically extended to describe the plethora of competing phases illustrated in Fig. 2.1. Section 2.3 ends with a conclusion on the work presented in that section.

2.2 Degenerate three-dimensional Bose-Fermi mixtures in the density-matched regime

2.2.1 Phase diagram

A simplified phase diagram of strongly coupled three-dimensional Bose-Fermi mixtures is illustrated in Fig. 2.2 as a function of the ratio of boson to fermion density n_B/n_F and the dimensionless interaction strength $1/k_i a_{BF}$. Here, a_{BF} denotes the boson-fermion scattering length and the wave vector k_i is determined by the interparticle spacing of the majority species $k_i = (6\pi^2 n_i)^{1/3}$ where we denote B(F) for $n_B > n_F$ ($n_B < n_F$). Phases involving bound states of more than one boson are ignored as these are intrinsically unstable due to fast recombination loss.

Qualitatively, the phase diagram in Fig. 2.2 can then be divided into two regimes. In the limit of vanishing Bose-Fermi attraction, $(k_i a_{BF})^{-1} \to -\infty$, bosons and fermions decouple and form a BEC along with a Fermi sea. As attractive interactions are switched on, fermions and bosons modify each other's properties, leading to quasiparticle formation. Due to the polaronic character of this interaction, the resulting phase is denoted as the *Polaronic phase*. In the opposite limit of strong attraction, realized at $(k_i a_{BF})^{-1} \to \infty$, for $n_B \leq n_F$ binding of all bosons to fermions leads to a Fermi sea of molecules coexisting with an atomic Fermi sea; denoted as the *Molecular phase*. For $n_B \leq n_F$ the Polaronic and Molecular phase are predicted to be either separated by a first-order QPT with phase separation or by a second-order QPT [96, 98–100,

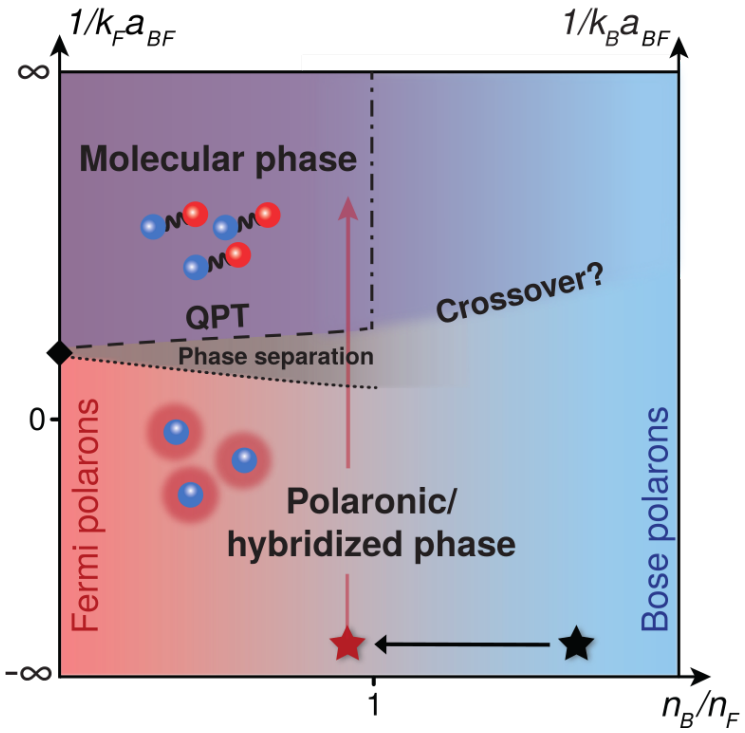

Figure 2.2. Simplified phase diagram of degenerate Bose-Fermi mixtures as a function of the density ratio n_B/n_F and the dimensionless interaction strength $(k_i a_{BF})^{-1}$. For $n_B/n_F \to 0$ one attains the Fermi polaron limit featuring a polaron-to-molecule transition (black diamond), while for $n_B/n_F \to \infty$ the Bose polaron limit with a smooth crossover is reached. For $n_B < n_F$ a QPT between a Polaronic and a Molecular phase of either first-order with phase separation or second-order is expected. The long-dashed line marks the complete depletion of the condensate $(k_F a_{BF})_c^{-1}$ and, in the case of phase separation, the dotted line marks its onset at $(k_F a_{BF})_{\mathrm{ps}}^{-1}$. The dash-dotted line marks a possible further QPT of unknown order.

124, 133]. When tuning the density ratio across $n_B/n_F \approx 1$ in the regime of strong attraction, an additional phase transition, where a condensate reappears, is predicted to occur [96]. This phase featuring molecules and an excess condensate is predicted to cross over into the Polaronic phase for $n_B/n_F \gtrsim 1$ [96]. Most experiments have been carried out in the impurity limits either on the far left- or the far right-hand side of the phase diagram [9, 106, 108, 128–130].

2.2.1.1 Quantum phase transition from a polaronic phase to a molecular phase

In the regime where $n_B \leq n_F$, theory at low temperature predicts a transition from a phase where a BEC coexists with a Fermi gas to a liquid where all bosons are bound into molecules [96, 98–100, 124, 133]. By tuning the interactions from weak to strong coupling, the boson-fermion interaction gradually depletes the BEC until the condensate fraction, representing the order parameter of the transition, vanishes

at the critical interaction parameter $(k_F a_{BF})_c^{-1}$ resulting in a phase transition. At this interaction strength for $T = 0$ a quantum phase transition, possibly masked by a phase-separation regime [99, 124, 133], occurs. This is a distinct feature in Bose-Fermi mixtures that is absent for the BEC-BCS crossover in spin-balanced fermionic mixtures where no symmetry-breaking pattern is changed as the interaction strength is varied across the Feshbach resonance [134]. Furthermore, in contrast to the BEC-BCS phase, the *Molecular phase* is more robust with respect to temperature [98, 135, 136]. In both cases pairing is required, which is not affected by small temperature fluctuations, as pairing occurs with binding energies on the order of several Fermi energies. In the BEC-BCS phase, however, molecules are additionally required to condense, whereas in Bose-Fermi mixtures they merely need to form a Fermi sea.

The order of the transition depends on the Bose-Bose repulsion a_{BB} and the density ratio n_B/n_F [99, 124, 133]. The transition is predicted to be of first order in a large parameter regime, and only beyond a threshold do stronger Bose-Bose repulsion and lower n_B/n_F favor a second order transition [99, 124]. Tuning the Bose-Fermi interaction strength $(k_F a_{BF})^{-1}$ from weak to strong interactions at a fixed density ratio $n_B/n_F < 1$, the condensate density decreases smoothly and vanishes beyond a critical interaction parameter $(k_F a_{BF})_c^{-1}$ for a second-order phase transition. For a first-order transition, on the other hand, the homogeneous system passes through a *phase separation* region. Upon reaching the lower boundary $(k_F a_{BF})_{\mathrm{ps}}^{-1}$ the system enters a phase-separated state (see Fig. 2.2, where the *local* condensate density drops to zero discontinuously in some parts of the system while it remains finite in others. Tuning the interactions further, the mixing ratio between the two phases shifts towards the *Molecular phase* and, once $(k_F a_{BF})_c^{-1}$ is reached, all parts of the system have transitioned to the Molecular phase. Importantly, however, the *globally averaged* condensate density is expected to decrease smoothly and to vanish continuously at $(k_F a_{BF})_c^{-1}$ in both cases. This effect is enhanced by the harmonic trap (see Fig. 2.9 and it makes distinguishing between the two cases challenging.

Within the condensed Polaronic phase it is predicted that the depletion of the condensate depends weakly on the boson-fermion density ratio which, remarkably, extends all the way to the Fermi polaron limit, $n_B/n_F \to 0$ [100, 130]. In the extreme limit of a single bosonic impurity in a Fermi gas, the phase transition connects to a polaron-to-molecule transition and the condensate fraction reduces to the impurity quasiparticle weight (for a detailed explanation see Ref. [100]). A computational, self-consistent functional renormalization group (fRG) technique that takes into account an infinite number of particle-hole excitations of the Fermi sea [137] predicts this transition to occur at $(k_F a_{BF})^{-1} = 1.16$ (see Fig. 2.7, Section 2.2.2.3). This transition point is expected to shift to larger values as temperature and boson-density increase [9, 100, 138].

2.2.2 Review of theoretical treatments of the quantum phase transition

In order to understand how the conclusions about the phase diagram described in Section 2.2.1 are reached, it is instructive to understand the methods used to obtain them. In this regard, the theory presented in Ref. [99] acts as a natural starting point to understand the statements made regarding the order of the phase transition. Next, to understand the physical properties of the polaronic and the molecular phase, the theory presented in Ref. [100] proves useful.

2.2.2.1 Theoretical treatment by Ludwig et al. (2011)

In Ref. [99], an atomic mixture of a Bose gas ϕ with a Fermi gas ψ is considered in a two-channel model in the limit of an infinitely broad Feshbach resonance ($h \to \infty$) (see Section 1.5). They include a Bose-Bose repulsion λ and an attractive Bose-Fermi interaction featuring a bound state molecule ξ. The resulting action can be written as

$$\begin{aligned} S = \int_x & \phi^*(x) G_B^{-1,0}(x)\phi(x) + \psi^*(x) G_F^{-1,0}(x)\psi(x) + \xi^*(x) G_\xi^{-1,0}(x)\xi(x) \\ & + \frac{\lambda}{2}[\phi^*(x)\phi(x)]^2 - h\left[\psi^*(x)\phi^*(x)\xi(x) + \text{h.c}\right], \end{aligned} \tag{2.1}$$

where $G_B^{-1,0}$, $G_F^{-1,0}$ and $G_\xi^{-1,0}$ denote the bare Green's functions of the bosons, fermions and molecules, which contain the chemical potentials μ_B and μ_F. To obtain an expression for the grand canonical potential Ω_G, the effective potential $U(\bar{\rho})$ is computed where $\bar{\rho}$ is the condensate density of the bosonic field, related to ϕ via $\sqrt{\bar{\rho}} = \langle\phi\rangle$. To this end, the path integral associated with the canonical distribution function $\mathcal{Z}$ (see Section 1.9) is solved in the following way. After expanding the action in Eq. (2.1) to second order in the bosonic and fermionic fields around their respective expectation values $\langle\phi\rangle = \sqrt{\bar{\rho}}$ and $\langle\psi\rangle = 0$ these fields can be integrated out. From this one obtains an effective action S_{eff} in terms of molecules and the condensate density

$$e^{-S_{\text{eff}}[\xi,\bar{\rho}]} = \int \mathcal{D}\phi\mathcal{D}\psi e^{-S[\phi,\psi,\xi]}. \tag{2.2}$$

After expanding S_{eff} to second order in ξ around its expectation value $\bar{\xi}$, the effective action can be computed by integrating ξ

$$e^{-\Gamma[\bar{\xi},\bar{\rho}]} = \int \mathcal{D}\xi e^{-S_{\text{eff}}[\xi,\bar{\rho}]} = \mathcal{Z}. \tag{2.3}$$

The effective potential $U(\bar{\rho}) = \Gamma[0,\bar{\rho}]T/V$ is obtained by setting $\bar{\xi}$ to its physical value, 0. The effective potential thus reads explicitly [99]

$$U(\bar{\rho}) = \frac{\lambda}{2}\bar{\rho}^2 - \mu_\phi\bar{\rho} + \frac{1}{2}\int_p \ln\left[\det G_B^{-1}\right] - \int_p \ln G_F^{-1,0} - \int_p \ln G_\xi^{-1}, \tag{2.4}$$

where the term containing G_B^{-1} originates from purely bosonic fluctuations which are ignored for simplicity. The first two terms are equally found in a repulsive Bose

gas ($\lambda > 0$), that does not interact with another species: for $\mu_\phi > 0$ the system is stable only due to the repulsive term and possesses a minimum at $\bar{\rho} > 0$. The fourth term describes the energy density due to populating a Fermi sea of free fermions. Finally, the last term accounts for the Bose-Fermi interactions, which modify the physical properties of bosons, fermions and molecules. As a result, this term accounts for the population of molecules and may lead to condensation of the bosonic field ($\bar{\rho} > 0$) even when the bosonic field is gapped at the bare level ($\mu_\phi < 0$). The self-energy contribution contained within G_ξ is fully equivalent to those contained within a standard non-self-consistent T-matrix approach Section 2.2.2.2 for $\bar{\rho} = 0$ and thus the strong Bose-Fermi coupling physics is captured.

For a vanishing Bose-Bose repulsion the system is unstable towards collapse as the fermions mediate an attractive force between the bosons. This is evident as the effective potential diverges as

$$U(\bar{\rho}) \propto -\bar{\rho}^{\kappa} \quad \text{for } \bar{\rho} \to \infty,\ \lambda = 0, \tag{2.5}$$

where $\kappa \approx 1.6$, which thus describes a thermodynamically unstable system. This term is balanced by the quadratic contributions from the Bose-Bose repulsion which render the system stable.

The effective potential $U(\bar{\rho})$ takes as input the fermionic and bosonic chemical potentials, μ_F and μ_B, along with the two scattering lengths a_{BF} and a_{BB} and is a function of the condensate density. For given chemical potentials and scattering lengths, the ground state of the system is found at the minimum of the effective potential with respect to the condensate density. From the effective potential at the minimum one can then compute the resulting fermionic and bosonic densities by differentiating with respect to the chemical potentials

$$n_F = -\frac{\partial U(\bar{\rho})}{\partial \mu_F} \tag{2.6}$$

$$n_B = -\frac{\partial U(\bar{\rho})}{\partial \mu_B}. \tag{2.7}$$

Unlike the bosonic and the fermionic chemical potential, the bosonic and fermionic densities are physical observables in ultracold quantum gases. In two-dimensional semiconductor systems, on the other hand, the chemical potential is a physical observable in the form of gate doping.

For $1/k_F a_{BF} \to \infty$ and arbitrarily small Bose-Bose repulsion, the bosonic condensate is fully depleted and the system is in the normal phase where the condensate density vanishes $\rho = 0$. Here, for $n_B < n_F$ all bosons are bound into molecules at $T = 0$, resulting in the name molecular phase, used before. Tuning the interaction strength and approaching the quantum phase transition from the normal phase, there are two different scenarios in which one can enter a phase with a finite condensate density (i.e. the minimum of the effective potential is at a finite condensate density). These are shown in Fig. 2.3. On the right a parameter is tuned and at a critical value a minimum away from zero forms, however the location of that minimum starts at 0 and then continuously moves away. In contrast on the left, the potential has a

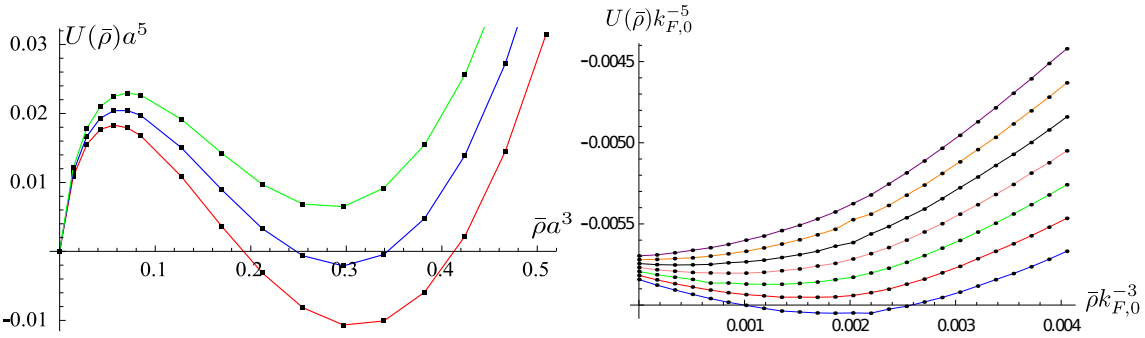

Figure 2.3. Effective potential for the Bose-Fermi mixture as a function of $\bar{\rho}$, illustrating a first (left) and a second (right) order phase transition. In both cases from bottom to top, the curves correspond to increasing values of $1/k_F a_{BF}$. On the left, one can see how the minimum jumps from $\bar{\rho} = 0$ to $\bar{\rho} > 0$, while on the left the minimum continuously moves away from $\bar{\rho} = 0$ once a critical value of $1/k_F a_{BF}$ is reached. Figure adapted from Ref. [99].

dip, and once that dip becomes the global minimum the condensate density jumps. The former case describes a continuous, second order transition while the latter is a discontinuous, first order transition. Depending on the Bose-Bose repulsion both first- and second-order transitions are found where weaker repulsion favors first-order and strong repulsion favours a second-order quantum phase transition.

The jump in condensate density upon crossing a first-order phase transition implies that also the densities carry a discontinuity. As a result, when considering a phase diagram that maps out densities, some regions may be skipped over and are thus not realizable. Forcing the system into such a forbidden region leads to phase separation, where the system locally realizes bubbles of different phases and mixes these bubbles accordingly. This phase separation, however can not be described in a quantum field theory. The forbidden region, however, can be seen in a phase diagram because no combination of chemical potentials and scattering lengths can realize it.

In Fig. 2.4 a first order transition with a forbidden region is visible. This diagram is given in terms of computed densities and the first-order transition curves are shown in red. Were this phase diagram given in terms of fundamental quantities (chemical potentials and scattering lengths) instead then no forbidden regions would appear. The jump in density when approaching the phase transition from both sides leads to these lines separating a region in between that is only realizable by mixing separated phase bubbles. The full circles denote a point in a fundamental phase diagram approached from within two different phases.

While a first-order quantum phase transition may occur when tuning a parameter, there may be a large potential barrier between the two states, corresponding to distinct local minima at $\rho = 0$ and $\rho > 0$. This barrier may suppress the transition to the new ground state [99]. In an experiment, one may thus enter a metastable state which only decays to the true ground state if the experimental timescales are larger than the timescales of decay to the ground state. Tuning further beyond the transition point, this potential barrier in the effective potential eventually ceases to exist and

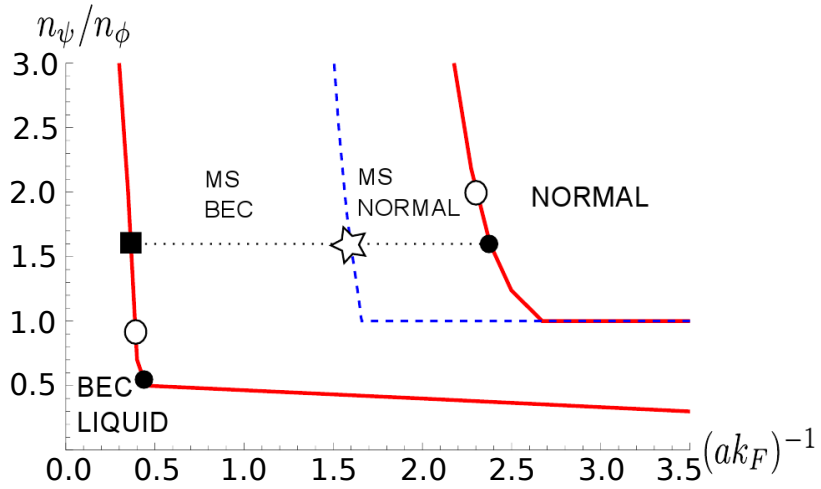

Figure 2.4. Illustration of the phase diagram as a function of the ratio of fermion to boson density n_ψ/n_ϕ and interaction parameter $1/(k_F a)$, including a small Bose-Bose repulsion of $\tilde{a}_B = a_B/a = 0.17$. transition separates The symmetry broken phase ($\rho > 0$, BEC-LIQUID) and the normal phase ($\rho = 0$, NORMAL) are separated by a first-order transition. The region between the two solid red lines corresponds to a mixed state where the two phases coexist due to phase separation. In this regime the second order phase transition line (blue dashed) separates the metastable (MS) normal and BEC phases. Figure adapted from Ref. [99].

the effective potential no longer holds a local minimum at $\bar{\rho} = 0$ such that a second-order phase transition is reached. In Fig. 2.4 this transition between two metastable states inside of the forbidden region is shown.

To study the second-order transition between a metastable polaronic and a molecular phase, a full solution of the effective potential is not necessary and rather its behavior near $\bar{\rho} = 0$ is sufficient. Such a transition point is characterized by the Thouless criterion [139] which states that the renormalized bosonic propagator becomes gapless,

$$-\mu_B + \Sigma_B = 0, \tag{2.8}$$

leading to condensation of the boson mode. Here, Σ_ϕ denotes the self-energy corrections to the bosonic propagator and this criterion is related to the derivative of the effective potential

$$-\mu_B + \Sigma_B \propto \frac{\partial U(\bar{\rho})}{\partial \bar{\rho}}\Big|_{\bar{\rho}=0}. \tag{2.9}$$

More generally, the relation between the gap of the bosonic propagator and the derivative of the effective potential can also be used for $\bar{\rho} > 0$ to determine local minima of the effective potential, from which the phases can be described. However, to determine whether the phase is stable or metastable, i.e. whether a found local minimum is also a global minimum the full effective potential needs to be determined.

In such a study, the Bose-Bose repulsion may be disregarded safely: the repulsion ensures thermodynamic stability of the system at large condensate densities, however

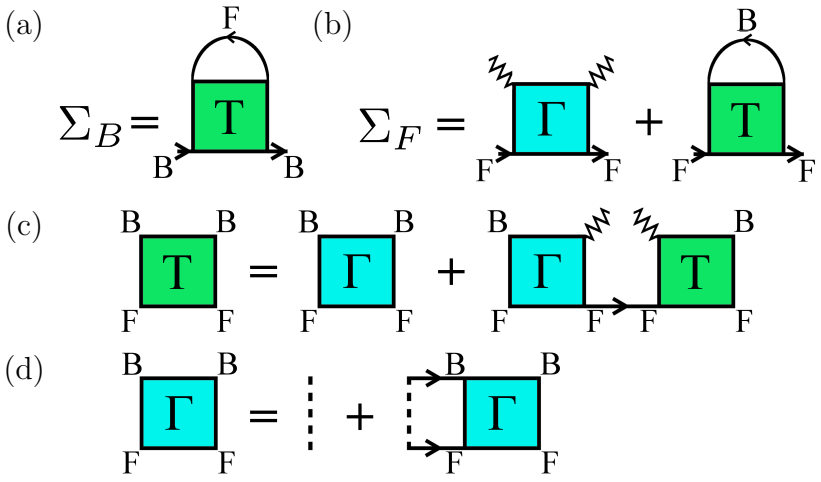

Figure 2.5. Feynman diagrams for the boson self-energy Σ_B (a), the fermion self-energy Σ_F (b) , along with the T-matrix (c) and the scattering vertex Γ (d). Full lines correspond to bare boson (B) and fermion (F) Green's functions $G_\phi^{-1,0}$ and $G_\psi^{-1,0}$, dashed lines to the regularised Bose-Fermi interaction g, zig-zag lines to condensate insertions $\sqrt{\rho}$. Dotted lines corresponds to interaction vertices. Figure adapted from Ref. [100].

when considering only local minima at small condensate densities no stability needs to be ensured. Furthermore, as the Bose-Bose repulsion in ultracold atom systems is typically very weak, the effect at small condensate densities is usually negligible [20].

2.2.2.2 Theoretical treatment by Guidini et al. (2015)

In Ref. [100], a theoretical description of the polaronic phase and its transition into a molecular phase is provided. The system is described using a diagrammatic Ansatz involving the use of Feynman diagrams. As mentioned before, this treatment is thus not suitable to determine the order of the transition, however it provides valuable predictions about the physical properties of the polaronic phase, independent of whether it is stable or merely metastable. While Bose-Bose repulsion is included in the study carried out in Ref. [100], its effects are almost negligible and thus for simplicity we review their methods omitting the Bose-Bose repulsion.

Rather than working in a two-channel model, they work in a single-channel model

$$\begin{aligned} S = &\int_x \phi^*(x) G_B^{-1,0}(x)\phi(x) + \psi^*(x) G_F^{-1,0}(x)\psi(x) \\ &+ g\int_x \psi^*(x)\phi^*(x)\phi(x)\psi(x), \end{aligned} \tag{2.10}$$

where g is renormalized to reproduce the s-wave scattering length a_{BF}. They employ a non self-consistent T-matrix approach to renormalize the Bose-Fermi coupling vertex which they then use to compute self-energy corrections. The corresponding Feynman diagrams are shown in Fig. 2.5. The diagram shown Fig. 2.5d) is the same type of ladder resummation done for the Fermi polaron problem discussed in Section 1.7. When considering a phase in which the bosons condense $\langle\phi\rangle = \sqrt{\rho}$, additional terms

in the T-matrix arise from condensate insertions denoted as wiggly lines in Fig. 2.5c). This ladder resummation Γ and the T-matrix are then used in self-energy contributions to the bosonic and the fermionic propagator. The self-energy contributions are again similar to those seen in Fermi polaron in Section 1.7. Additionally, the fermionic self-energy obtains contributions from condensate insertions.

While the diagrammatics are quite challenging to derive in a single-channel framework, they arise naturally in a two-channel framework. This diagrammatics will be used in Chapter 4 and a derivation in terms of the two-channel model can be found there and the renormalization to vertices in the effective action holds a simple form. The complicated structure in Eq. (2.10) arises when to obtain the propagator G the inverse propagator G^{-1} is inverted, which is given by second derivatives of the effective action

$$G^{-1}_{\sigma,\sigma'} \propto \frac{\delta^2\Gamma}{\delta\sigma\delta\sigma'} \tag{2.11}$$

with respect to the fields. Note that in Eq. (2.11), Γ denotes the effective action and not the scattering vertex seen in Fig. 2.5(d) From these diagrammatics the renormalized Green's functions are obtained as

$$G_B^{-1} = G_B^{-1,0} - \Sigma_B \tag{2.12}$$
$$G_F^{-1} = G_F^{-1,0} - \Sigma_F \tag{2.13}$$

and a local minimum of the effective potential is enforced using the Hugenholtz-Pines relation [140]

$$-\mu_B + \Sigma_B = 0, \tag{2.14}$$

to obtain the condensate density ρ. This is the same Thouless criterion as in Eq. (2.8). Finally, for given Bose-Fermi scattering length a_{BF} and chemical potentials, μ_B and μ_F, the boson and fermion density are obtained as

$$n_B = \rho - \int \frac{d\mathbf{k}}{(2\pi)^3} \int \frac{d\omega}{2\pi} G_B(\mathbf{k},\omega) e^{i\omega 0^+} \tag{2.15}$$
$$n_F = \int \frac{d\mathbf{k}}{(2\pi)^3} \int \frac{d\omega}{2\pi} G_F(\mathbf{k},\omega) e^{i\omega 0^+}, \tag{2.16}$$

which is used to define the Fermi wave vector k_F as $k_F \equiv (6\pi^2 n_F)^{1/3}$ and the Fermi energy as $\epsilon_F = k_F^2/2m_F$. Here $(\mathbf{k},\omega)$ denote the momentum and a Matsubara frequency.

In Fig. 2.6 simultaneous solutions of the Hugenholtz-Pines relation in Eq. (2.14) and the number equations in Eqs. (2.15) and (2.16) are shown for the bosonic chemical potential μ_B the fermionic chemical potential μ_F and the condensate density for different density ratios n_B/n_F. The data are obtained for different mass ration $m_B/m_F = 1$, 5 and 23/40. As it can be seen, the chemical potential of the bosons lies below the two-body binding energy ϵ_B and decreases with increasing interaction strength. The bosonic chemical potential has only a weak dependence on the density ratio n_B/n_F

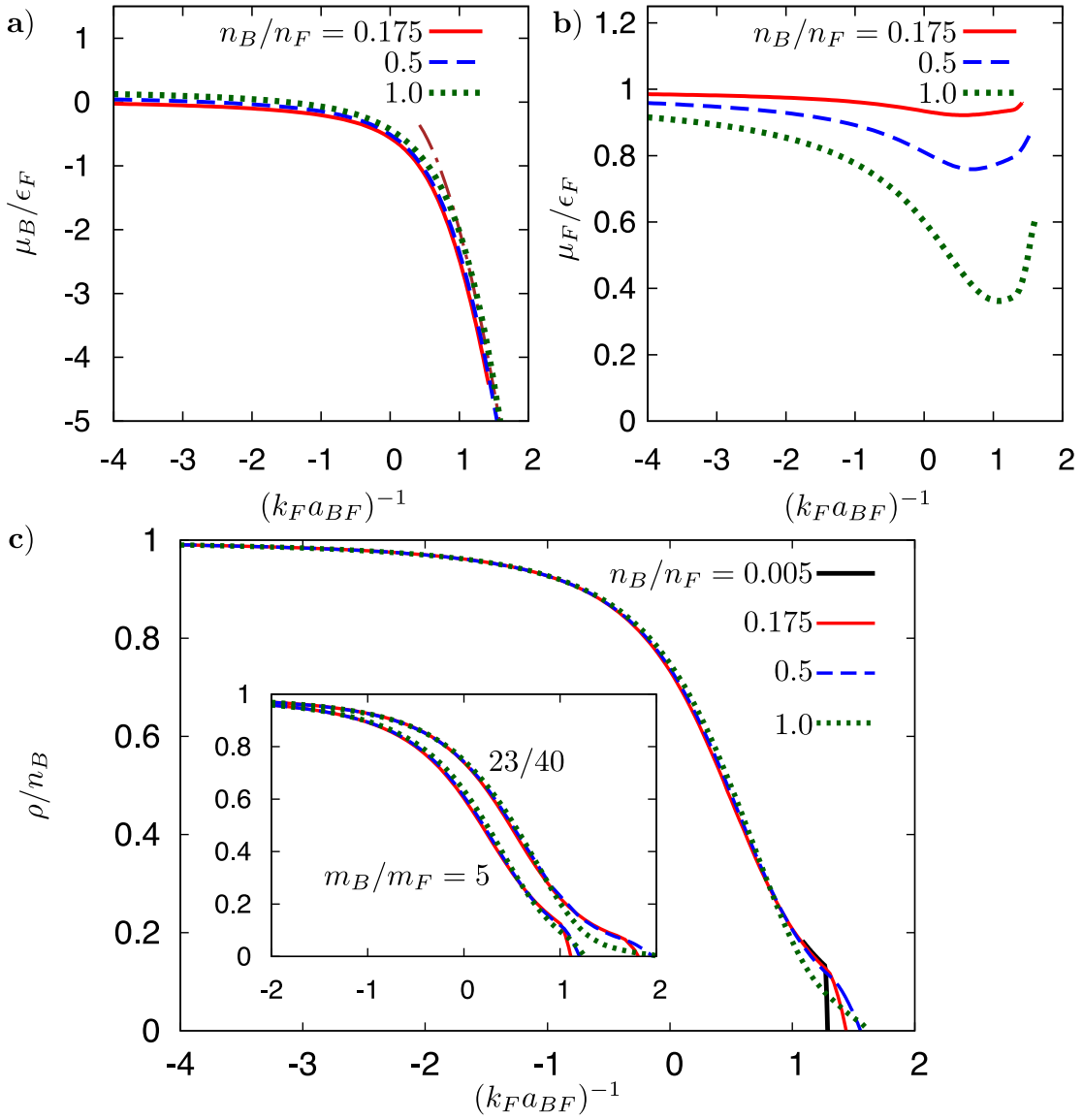

Figure 2.6. Bosonic chemical potential μ_B (**a**)), fermionic chemical potential μ_F (**b**)) and condensate fraction ρ/n_B (**c**)) as a function of the interaction strength $(k_F a_{BF})^{-1}$ for different values of n_B/n_F. These are simultaneous solutions of the Hugenholtz-Pines relation in Eq. (2.14) and the number equations in Eqs. (2.15) and (2.16). The dashed-dotted line in **a**) denotes the two-body binding energy $-\epsilon_B = -\frac{2}{a_{BF}^2}\left(\frac{1}{m_B} + \frac{1}{m_F}\right)$. The data in the main plots is for $m_B = m_F$, while the inset in **c**) shows data for $m_B/m_F = 5$ and 23/40. Figure adapted from Ref. [100].

and since the bosonic chemical potential connects to the Fermi polaron energy in the limit $n_B/n_F \to 0$ this is a first hint towards a universal behavior in terms of the Fermi polaron. The chemical potential of the fermions shows a much stronger dependence with respect to the density ratio n_B/n_F and approaches the Fermi energy $\mu_F \to \epsilon_F$ for $n_B/n_F \to 0$.

Finally, the condensate fraction shows the behavior described in the introduction. At weak interactions ($1/k_F a_{BF} \to -\infty$), all the bosons are within the condensate. For increasing $(k_F a_{BF})^{-1}$ the condensate fraction begins to decrease and eventually

vanishes completely. The curves show a striking universality with respect to the density ratio n_B/n_F in that for a large range of $(k_F a_{BF})^{-1}$ the condensate fraction is insensitive to the density ratio n_B/n_F. This shows a close correspondence between the condensate fraction ρ/n_B and the quasiparticle weight Z encountered in the Fermi polaron problem (see Section 1.7 and Chapter 5), which is noted in Ref. [100] and will also be discussed further in the context of the fRG calculations we undertook in studying this phase transition. Interestingly, because the diagrammatics used in Ref. [100] reduces to the diagrammatics of the polaron-to-molecule transition in the Chevy Ansatz, the condensate fraction obtained in Ref. [100] reduces exactly to the quasiparticle weight Z obtained in the polaron-to-molecule transition of the Fermi polaron within the Chevy Ansatz.

In the impurity limit $n_B/n_F \to 0$ the condensate fraction suddenly drops to 0 upon reaching the polaron-to-molecule transition. For increasing density ratios the condensate fraction follows the quasiparticle weight until it reaches approximately the polaron-to-molecule transition, the condensate fraction then quickly drops to zero and with increasing density ratio, the critical $(k_F a_{BF})_c^{-1}$ at which the condensate fraction vanishes increases. From this a physically intuitive picture in terms of the Fermi polaron problem arises: the system behaves as if it was occupying the polaron and molecule quasiparticle spectrum of the Fermi polaron impurity problem. For a given density ratio, the bosons form a condensate of Fermi polarons. Beyond the polaron-to-molecule transition the lower-lying molecule dispersion is populated with a Fermi sea of molecules. While the energy difference between the bottom of the molecule and the polaron band is small, the Fermi energy of the molecules is located at the energy of the lowest-lying polaron mode and the remaining bosons condense in the polaron mode. Eventually, the energy gap between molecules and polarons is so big, that all bosons can be accommodated for within the Fermi sea of molecules and thus the Fermi energy of the molecules lies below the bottom of the polaron band. As this point, no more bosons condense withing the polaron band and the condensate fraction vanishes. With increasing bosons density n_B a larger energy gap is necessary, which in turn leads to an increase in $(k_F a_{BF})_c^{-1}$ as seen in Fig. 2.6.

2.2.2.3 Calculation using a functional renormalization group (fRG) approach and its comparison to the non-self-consistent T-matrix approach

The non-self-consistent T-matrix (NSCT) approach in Section 2.2.2.2, from which a condensate depletion at equal density can be obtained, predicts the polaron-to-molecule transition to occur at $(k_F a_{BF})^{-1} = 1.60$ [100] for a mass ratio of 23/40. For finite boson densities it predicts the phase transition between the polaronic condensate and the molecular phase to take place beyond this value as the boson concentration increases, i.e. $(k_F a_{BF})_c^{-1} > 1.60$. Specifically, for the case of balanced densities, $n_B = n_F$, it predicts $(k_F a_{BF})_c^{-1} = 2.02$.

The NSCT approach, however, only takes into account single particle-hole excitations of the Fermi sea [141] and underestimates the modification of the binding energy of molecules inside the many-body environment. Indeed, when applying the

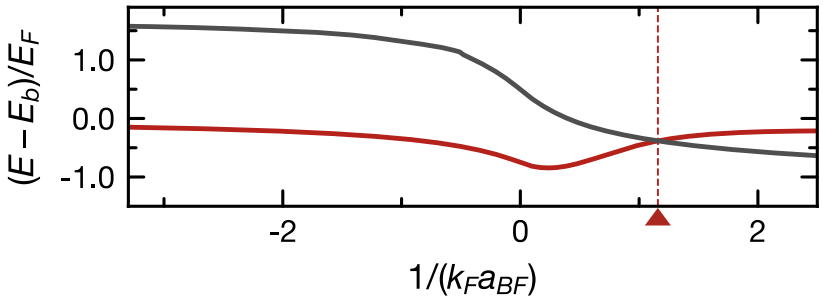

Figure 2.7. Energy spectrum of the zero-momentum Fermi polaron (red line) and the zero-momentum molecule (gray line) for a single bosonic impurity obtained from a self-consistent functional renormalization group (fRG) calculation at a mass imbalance of 23/40. The energies cross at the polaron-to-molecule transition at $(k_F a_{BF})_c^{-1} = 1.16$ (red dashed line). For $a_{BF} > 0$, the binding energy $E_b = -\hbar^2/2\mu a_{BF}^2$ is subtracted where μ is the reduced mass.

NSCT approach [100] to the Fermi polaron problem at mass balance one finds the polaron-to-molecule transition to occur at $(k_F a_{BF})_c^{-1} = 1.27$ [56], while techniques that include higher-order correlations such as functional renormalization group (fRG) [137] and state-of-the-art diagrammatic Monte Carlo (QMC) [142, 143] predict a value of $(k_F a_{BF})_c^{-1} = 0.90$.

Thus, in order to obtain a more accurate description of the critical interaction strength for the heteronuclear case considered in this work, an fRG scheme which takes into account an infinite number of particle-hole excitations in the Fermi sea [137] is employed. The scheme is described in detail in Chapter 5 and although it uses a different method to solve the self-consistent fRG equations it is in principle equivalent to the calculations carried out in [137], albeit for a different mass ratio of 23/40.

The resulting polaron and molecule energies are shown in Fig. 2.7, yielding a polaron-to-molecule transition at $(k_F a_{BF})^{-1} = 1.16$. The polaron quasiparticle weight is shown in Fig. 2.8 and we see that the polaron quasiparticle weight obtained in the impurity limit already describes the condensate fraction well except for its discontinuity at the polaron-to-molecule transition. From investigations of two-component Fermi gases it is expected that this discontinuity will be smoothed out due to finite boson density, temperature or combinations thereof [9, 138]. Moreover, as explicitly shown in [1, 9, 100, 138] and suggested by mean-field arguments [1], one expects the transition to shift to larger values of $(k_F a_{BF})^{-1}$ as the boson density increases. Hence, the value of $(k_F a_{BF})^{-1} = 1.16$ obtained from the fRG in the impurity limit can be regarded as a lower bound on the actual location of the quantum phase transition at $(k_F a_{BF})_c$.

We note that the polaron and molecule energies cross at a rather shallow angle as can be seen in Fig. 2.7. As a result, the underestimation of the molecule energy is the main reason for the difference in the predicted location of the polaron-to-molecule transition in the NSCT and fRG calculations. The quasiparticle weight is, in contrast, less affected and, as shown in Fig. 2.8, both approaches yield similar results for the

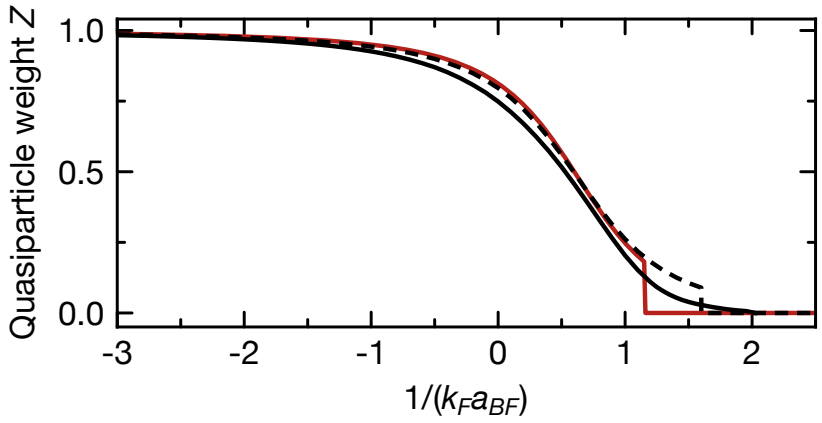

Figure 2.8. Impurity quasiparticle weight in the Fermi polaron problem for $\alpha = 23/40$. The quasiparticle weight of the impurity as a function of the interaction strength is shown as obtained from the fRG (red, solid) and the NSCT approach (black, dashed). While both methods yield similar results they differ in the prediction of the point where the polaron-to-molecule transitions occurs, beyond which the occupied quasiparticle weight drops to zero. To indicate the effect of finite boson density, the condensate fraction of the mixture computed in NSCT is shown for $n_B = n_F$ (black solid, also shown in Fig. 2.11).

quasiparticle weight of a bosonic impurity. Based on this finding, NSCT theory can be expected to give a reliable prediction for the condensate fraction also at finite boson density [100].

2.2.3 Experimental setup and probe of the QPT

A natural way to investigate the phase diagram away from the impurity limits starts from producing a double-degenerate Bose-Fermi mixture. Especially the regime of matched densities is of interest where the system becomes strongly correlated and neither of the atomic species can be regarded as a quantum impurity. To access this novel regime, in Ref. [2] a species-dependent dipole trap at 785 nm was employed, which was near-detuned to the D-lines of the K atoms. This trap provides a weaker confinement of the Na compared to the K atoms, lowering the density of the Na BEC and increasing overlap between the species (see Fig. 2.9, right). As a consequence, the detrimental loss resulting from collisions of Na atoms in the BEC with NaK* Feshbach molecules is dramatically reduced. In contrast, for a typical trap setup where the trapping effect is similar for both atomic species, the peak density of the BEC is considerably larger than that of the Fermi gas (see Fig. 2.9, left). The latter trap setup results in an entirely different physical regime related to the Bose polaron problem with a low molecule association efficiency when starting from the BEC.

In the following, experimental probes of signatures of this QPT are described. The experiment described in Ref. [2] typically starts with 2.3×10^5 ^{40}K atoms at a temperature $T = 80\,\mathrm{nK}$ (corresponding to $T/T_F \sim 0.2$) and 0.8×10^5 ^{23}Na atoms with a condensate fraction of 60% at a magnetic field of 81 G. A single magnetic

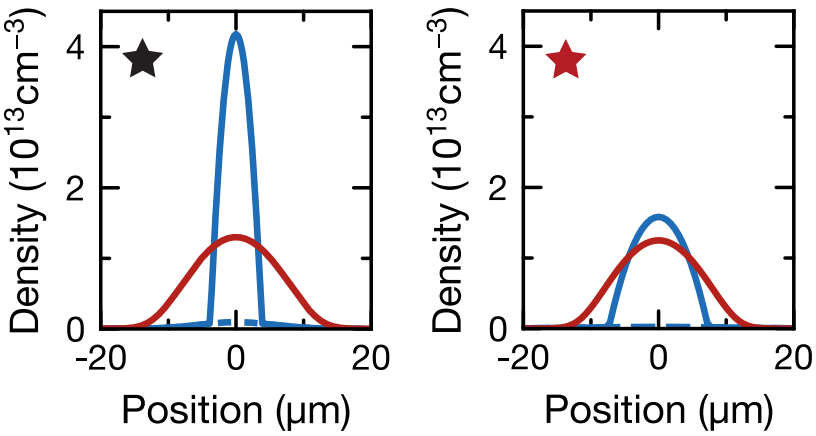

Figure 2.9. Calculated in-trap density profiles. Calculated in-situ density profiles of bosons (blue) and fermions (red) in the species-dependent 785-nm dipole trap (right), and in a far-detuned trap (left). The dashed blue line gives the thermal boson fraction, showing a lack of thermal bosons in regions where bosons and fermions overlap. The black and the red star indicate different ratios of boson to fermion density shown in Fig. 2.2.

field ramp with a speed of 3.5 G/ms is employed that is terminated at the desired magnetic field close to a Feshbach resonance at 78.3 G [144, 145], corresponding to different interaction strengths $(k_F a_{BF})^{-1}$ while the Bose-Bose interaction remains at $a_{BB} = 53\,a_0$ [144]. Due to the small effective-range parameter $k_F R^* = 0.08$ of this broad Feshbach resonance, the Bose-Fermi interactions are characterized by the single parameter $(k_F a_{BF})^{-1}$ [144].

Theory [99, 123, 133, 146] and early experiments [147, 148] suggest that for strong interactions, especially close to unitarity, the Bose-Fermi mixture might undergo collapse. However, the timescale for the collapse to occur is on the order of the trapping period. In this experiment the strongly interacting regime is ramped through on a time scale shorter than the trapping period, prohibiting the collapse to occur. Indeed, the observations show that the Bose-Fermi mixture remains in a metastable state on such experimental time scales, which in turn allows the physics of the phase diagram shown in Fig. 2.2 to be explored. Specifically, the density increase in a collapse scenario would lead to enhanced interspecies loss, which is not observed. As a further instability one might also consider immiscibility of the mixture leading to a separation of bosonic and fermionic atoms. Such immiscibility is expected to occur for repulsive interactions between bosons and fermions. However in this experiment the attractive interaction branch of the system is followed and, given the efficient molecule formation observed, immiscibility, which would be characterized by poor spatial overlap, can be excluded.

Furthermore, it was ensured that the depletion of the BEC is independent of the ramp speed for the sufficiently slow ramp used there. This indicates that the system stays close to a local equilibrium state until near the critical point. Then the magnetic field is quenched to 72.3 G. This projects the system onto free atoms

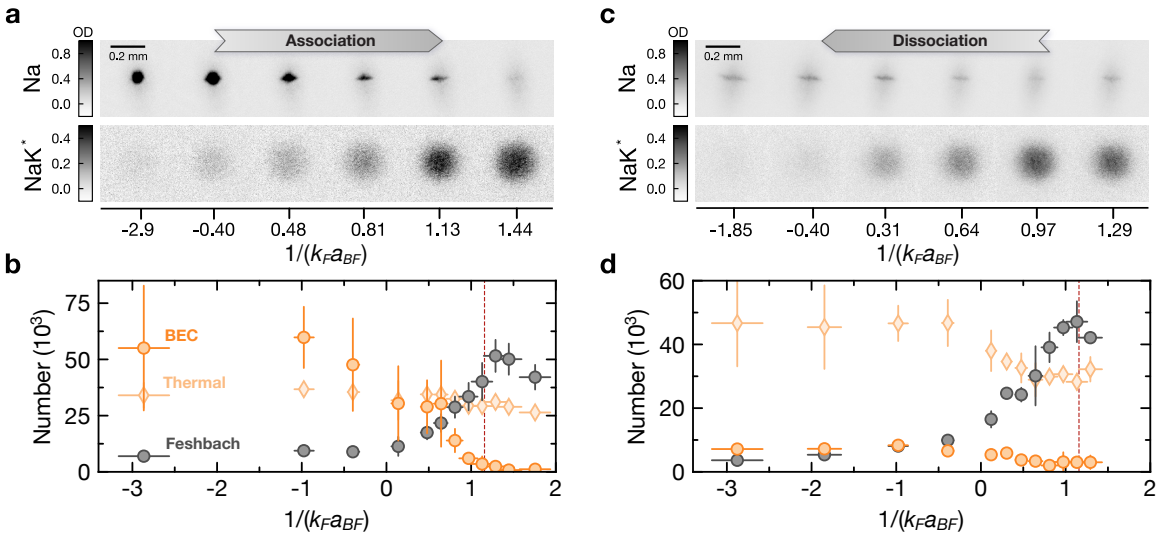

Figure 2.10. Association and dissociation process of degenerate Feshbach molecules. (a) Absorption images of Na atoms (Na) and Feshbach molecules (NaK*) after 18 ms time of flight during the association ramp from the polaronic BEC to the Molecular phase. (b) Production of Feshbach molecules. Numbers of condensed Na atoms (dark orange points), thermal Na atoms (bright orange diamonds) and Feshbach molecules (gray points) are shown as a function of $(k_F a_{BF})^{-1}$ for $\bar{n}_B/\bar{n}_F = 0.7$. The red line indicates the polaron-to-molecule transition at $(k_F a_{BF})^{-1} = 1.16$ in the Fermi polaron problem. (c) Absorption images during the dissociation ramp with 18 ms time of flight. (d) Dissociation of Feshbach molecules. Condensed Na atom (dark orange points), thermal Na atom (bright orange diamonds) and Feshbach molecule (gray points) numbers are shown as a function of $(k_F a_{BF})^{-1}$ for $\bar{n}_B/\bar{n}_F = 0.7$.

and deeply bound molecules which are subsequently imaged in time of flight after Stern-Gerlach separation as shown in Fig. 2.10a, b.

To characterize the phase transition quantitatively, the normalized order parameter $\phi = N_{\mathrm{BEC}}/(N_{\mathrm{m}} + N_{\mathrm{BEC}})$ is defined. Here N_{BEC} and N_{m} represent the number of condensed Na atoms and those associated to molecules, respectively. The order parameter ϕ describes the depletion of the condensate fraction due to the excitation of bosons to finite-momentum states by quantum fluctuations. These quantum fluctuations are dominated by the build-up of pairing correlations, measured by the projection onto molecules. Note, in the definition of ϕ thermal Na atoms are disregarded as the condensate fraction in the center of the trap is described: First, the spatial extension of thermal bosons (see Fig. 2.9, right) is much larger than that of the BEC and the fermions, both of which are concentrated in the center of the trap. Here the density of thermal bosons is more than twenty times smaller than that of the BEC. Second, on the time scales of the experiment thermal bosons do not play a significant role in the molecule formation due to their weak spatial overlap with the fermions. Molecules are thus formed predominantly from BEC atoms.

The temperature of bosons in the center of the trap where most of the boson-fermion collisions take place is thus effectively much lower than suggested by the

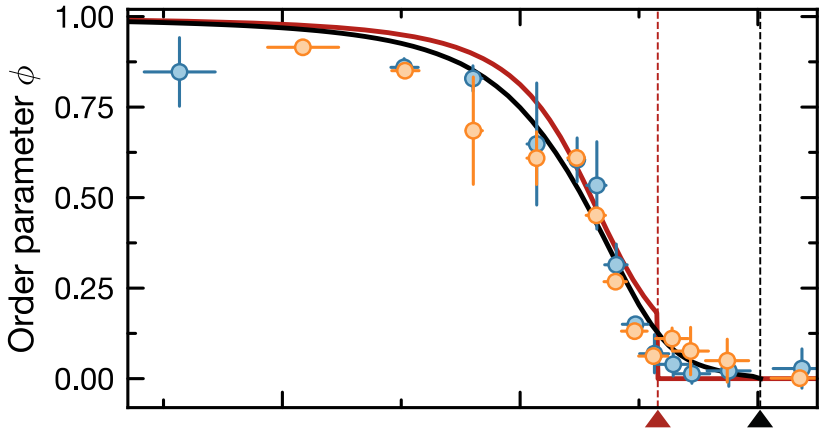

Figure 2.11. Quantum phase transition in a density-matched Bose-Fermi mixture. Order parameter ϕ as a function of $(k_F a_{BF})^{-1}$ for the boson-fermion average-density ratio $\bar{n}_B/\bar{n}_F = 0.4$ (orange points) and $\bar{n}_B/\bar{n}_F = 0.7$ (blue points). The black solid line shows the order parameter from zero-temperature theory in Ref. [100] predicting the QPT to occur at $(k_F a_{BF})_c^{-1} = 2.02$ (black triangle) for ideal bosons interacting with a Fermi gas at $n_B/n_F = 1$. The red solid line shows the polaron quasiparticle weight of a bosonic impurity in a Fermi gas obtained from a self-consistent functional renormalization group (fRG) calculation that predicts the polaron-to-molecule transition to occur at $(k_F a_{BF})_c^{-1} = 1.16$ (red triangle).

equilibrium temperature, allowing for a direct comparison of the findings with zero-temperature theory. Specifically, in Fig. 2.11 comparison is made with the quasiparticle weight of a bosonic impurity calculated from a self-consistent fRG approach (see Section 2.2.2.3, red dashed line) and predictions of the condensate fraction from a non-self-consistent T-matrix (NSCT) theory (see Section 2.2.2.2 and Ref. [100], black solid line) for $n_B = n_F$ which neglects multiple particle-hole excitations in the Fermi sea.

In Fig. 2.11, the measured order parameter ϕ is shown as a function of $(k_F a_{BF})^{-1}$ for $\bar{n}_B/\bar{n}_F = 0.4$ and 0.7 where $\bar{n}_B/\bar{n}_F$ denotes the ratio of the average boson and fermion density in parts of the trap with a finite condensate fraction in the weakly interacting regime. As the interaction strength increases, ϕ reduces slowly for negative values of the interaction parameter $(k_F a_{BF})^{-1} < 0$. However, once the scattering length becomes positive, ϕ decreases rapidly and vanishes in the regime beyond $(k_F a_{BF})^{-1} = 1.44(15)$ $(\bar{n}_B/\bar{n}_F = 0.7)$ and $(k_F a_{BF})^{-1} = 1.75(18)$ $(\bar{n}_B/\bar{n}_F = 0.4)$ where the residual condensate fraction is comparable to the uncertainty of the measurement. The experimental measurements agree well with the predicted condensate fraction from the NSCT approach throughout the entire interaction regime. Importantly, both data sets overlap within error bars, providing support for the predicted universality of the condensate depletion with respect to varying n_B/n_F [100, 130]. This, in turn, justifies comparing the in-trap experiment with predictions for a homogeneous system. The data also show a remarkable agreement with the quasiparticle weight of a single impurity in most of the interaction regime except close to the phase transition. This indicates that, despite having a large boson density, the system can

be well described as a condensate of polaronically dressed bosons. In contrast, however, at the transition the order parameter vanishes smoothly compared to a jump predicted in the impurity limit.

To estimate the transition point independently from the slowly varying order parameter, we consider the projected Feshbach molecule number shown in Fig. 2.10b as a measure of existing boson-fermion pairing correlations (see Section 2.2.3.2). As $(k_F a_{BF})^{-1}$ increases, so do the pairing correlations (including potential mixing between fermions and molecules [96]) until they saturate when the bosons are fully bound into molecules. The resulting transition point $(k_F a_{BF})^{-1} = 1.29(14)$ extracted from the measured Feshbach molecule number is consistent with the transition point obtained through the vanishing of the order parameter.

Driving through the transition provides an efficient method to create molecules. The data show that a striking conversion efficiency of around 80% of the Na atoms in the BEC into Feshbach molecules can be achieved. Accounting for the residual density mismatch and the resulting interspecies loss from the excess bosons, the experimental data suggest that the entirety of the BEC could be converted into molecules for perfectly matched density conditions. In contrast, the highest conversion efficiency from a BEC previously reported was less than 50% in KRb, where the density of bosons in the center of the trap was ten times higher than that of the fermions, which was possible only because of the ten-fold lower interspecies loss coefficients compared to NaK [91, 145, 149].

2.2.3.1 Reversal of the phase transition

Following the drive through the phase transition, the reversal of the phase transition can be investigated. After the association ramp reaches $(k_F a_{BF})^{-1} = 1.3$, in Ref. [2] the magnetic field was ramped back to dissociate the molecules. The dissociation ramp was followed by a magnetic field quench to 72.3 G for detection. As can be seen from the time-of-flight images in Fig. 2.10c, the number of projected Feshbach molecules decreases, while a finite BEC fraction is recovered. In particular, it is shown that the number of Na atoms in the BEC can be increased from $3(2) \times 10^3$ to $8(1) \times 10^3$ (see Fig. 2.10d). Heating is evident after the dissociation in the form of an increase of thermal Na atoms which is attributed to the non-adiabatic nature of the magnetic field ramps near the transition point. Due to the changing number of Na atoms in the thermal wings, the reversal of the phase transition thus cannot be characterized with the order parameter ϕ as done in the association ramp. Nonetheless, the partial restoration of the BEC highlights the coherence preserved in the experiment and is a striking example of how bosons that were bound into fermionic molecules in finite-momentum states are converted back into their motional ground state. Thus, the Fermi degeneracy of the molecules and the partial restoration of the BEC underline the low entropy of the observed molecular clouds.

2.2.3.2 Projection of polaronic states onto deeply bound molecules

As evident from Fig. 2.10b, a finite number of Feshbach molecules is detected already before the phase transition. This can be understood from the fact that the rapid ramp to 72.3 G projects the system onto deeply bound molecules. As a result, short-distance pairing correlations between bosons and fermions are effectively measured before the phase transition. However, once the phase transition is crossed in the initial magnetic-field ramp, all bosons are bound into weakly bound molecules in an adiabatic fashion. In that case, the weakly bound Feshbach molecules are transferred into deeply bound states by the subsequent rapid magnetic field ramp.

In the following, it is demonstrated that a simple Fermi polaron wavefunction indeed overlaps with deeply bound molecules when a projection measurement is performed. Similar to the calculations performed in Ref. [150] one can define the molecule number operator as

$$\hat{N}_{\mathrm{Mol}} = \sum_{\mathbf{mlk}} \hat{c}^{\dagger}_{\mathbf{m+k}} \hat{d}^{\dagger}_{-\mathbf{k}} \phi_{\mathbf{m}}(\mathbf{k}) \phi^{*}_{\mathbf{m}}(\mathbf{l}) \hat{d}_{-\mathbf{l}} \hat{c}_{\mathbf{m+k}} \ . \tag{2.17}$$

Here, $d_{\mathbf{q}}$ and $c_{\mathbf{q}}$ are the fermionic and bosonic annihilation operators, respectively, while $\phi_{\mathbf{p}}(\mathbf{k})$ denotes the wavefunction of the molecule in vacuum at center-of-mass momentum $\mathbf{p}$. It is approximated with the form valid for an attractive contact interaction potential,

$$\tilde{\phi}_{\mathbf{p}}(\mathbf{k}) = \frac{1}{E_b + \frac{\alpha+1}{2m_F\alpha}\left(\mathbf{k} + \frac{\alpha}{1+\alpha}\mathbf{p}\right)^2}, \tag{2.18}$$

$$\phi_{\mathbf{p}}(\mathbf{k}) = \frac{\tilde{\phi}_{\mathbf{p}}(\mathbf{k})}{\sqrt{\sum_{\mathbf{l}} \left|\tilde{\phi}_{\mathbf{p}}(\mathbf{l})\right|^2}}. \tag{2.19}$$

Here, E_b denotes the energy of the molecule at $\mathbf{p} = \mathbf{0}$, m_F denotes the mass of the fermions, and $\alpha = 23/40$ is given by the ratio of the bosonic m_B and the fermionic mass m_F.

The operator $\hat{N}_{\mathrm{Mol}}$ measures the number of projected molecules with respect to the Chevy Ansatz [54] for the Fermi polaron (see also Section 1.7)

$$|\mathrm{Pol}\rangle = \alpha_0 \hat{d}^{\dagger}_{\mathbf{0}} |\mathrm{FS}_N\rangle + \sum_{\mathbf{kq}} \alpha_{\mathbf{kq}} \hat{d}^{\dagger}_{\mathbf{q-k}} \hat{c}^{\dagger}_{\mathbf{k}} \hat{c}_{\mathbf{q}} |\mathrm{FS}_N\rangle \tag{2.20}$$

as $N_{\mathrm{Mol}} = \langle \mathrm{Pol}| \hat{N}_{\mathrm{Mol}} |\mathrm{Pol}\rangle$. Here, α_0 and $\alpha_{\mathbf{kq}}$ denote variational parameters and $|\mathrm{FS}_N\rangle$ denotes a Fermi sea containing N fermions.

The resulting fractions are shown in Fig. 2.12 for a mass ratio of $\alpha = 23/40$ and different values of E_b. For the binding energies shown, it can be seen that with increasing $(k_F a_{BF})^{-1}$ the molecule fraction increases, with the fraction getting smaller as E_b increases. This shows that, although the polaron is by no means a molecular state, it still features pairing correlations that will lead to a finite overlap with deeply bound molecules. Note that when the transition to the molecular phase is reached, in the experimental procedure described before the associated weakly bound molecules will

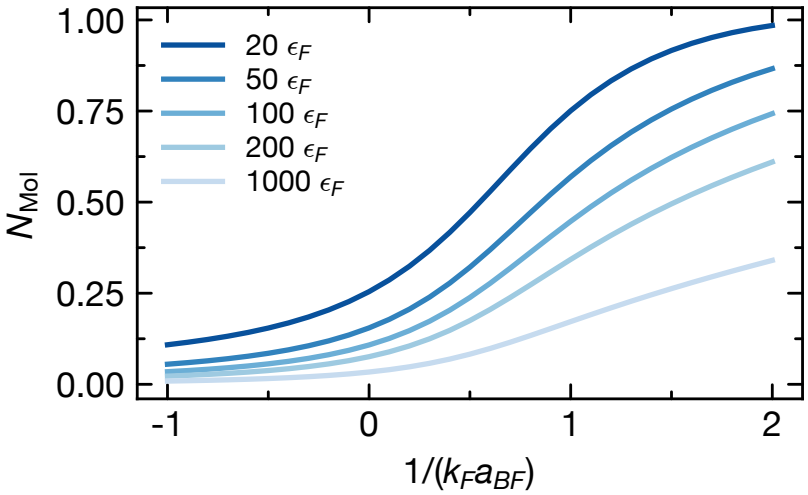

Figure 2.12. Number of projected molecules. The projected molecule fraction N_{Mol} obtained from the Fermi polaron state within the Chevy Ansatz [54] is shown as a function of the interaction parameter $(k_F a_{BF})^{-1}$ for different binding energies of the deeply bound molecule.

be transferred nearly adiabatically to the more deeply bound molecules approximately described by Eq. (2.18). Thus the number of observed molecules would approximately saturate (in absence of losses). Since during the final part of the initial ramp, however, excess bosons undergo lossy collisions with the molecules, the number of molecules will be further reduced, and it is thus expected that the number of observed molecules will in fact be maximized at the transition using the experimental procedure described before.

2.2.4 Degenerate Fermi gas of NaK Feshbach molecules

After the preparation 5×10^4 of Feshbach molecules at a temperature of 100 nK by ramping across the QPT, these can be converted to more deeply bound states by quenching the magnetic field to 75 G. At this magnetic field, a strong gradient is turned on to levitate the molecules and remove any residual atoms from the trap. Inelastic collisions between molecules are strongly suppressed by Pauli blocking, leading to a second-long lifetime. The quantum degeneracy of the molecular gas after association is determined by time-of-flight imaging after holding the molecules for 100 ms (see Fig. 2.13), ensuring that collective oscillations induced by the magnetic field ramps of the molecular cloud are dampened out. The momentum distribution of the molecules is well described by a Fermi-Dirac distribution [91] with a temperature of $T = 0.28(1)\ T_F$, while a thermal Gaussian fit, which unlike the Fermi-Dirac distribution does not include Pauli blocking, overestimates the occupation of lower momentum modes. This highlights the quantum-degeneracy of the Feshbach molecules.

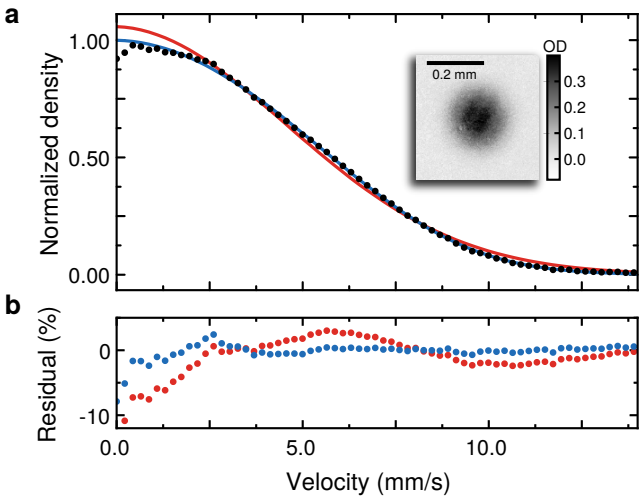

Figure 2.13. Quantum degeneracy of Feshbach molecules. (a) Velocity distribution of Feshbach molecules. The angular integral (black points) of an average of fifteen images with a time of flight of 15 ms (shown in the inset) was fitted with a Fermi-Dirac (blue line) and a Gaussian distribution (red line). While the Gaussian fit overestimates the occupation at lower velocities, the data are well described by a Fermi-Dirac distribution, which accounts for the Pauli blocking. The fit of the Fermi-Dirac distribution results in a $T/T_F = 0.28(1)$. (b) Angular integral of the residuals.

2.2.5 Conclusion on strongly coupled three-dimensional Bose-Fermi mixtures

Using a species-dependent decompression technique of atomic clouds, signatures of a QPT in Bose-Fermi mixtures between a phase featuring condensation and a molecular Fermi gas were observed in excellent quantitative agreement with theory. By driving the system through this phase transition, a gas of quantum-degenerate Feshbach molecules was produced with a record efficiency. The characterized phase transition represents a new phenomenon complementary to the paradigmatic BEC-BCS crossover observed in Fermi systems [134] and the atomic-to-molecular BEC crossover in Bose systems [151]. It is a first step in the exploration of strong-correlation physics in degenerate Bose-Fermi systems and provides a benchmark for their theoretical understanding. The investigation of the order of the transition is an intriguing venue for future research such as an observation of hysteresis [99] and quantum critical dynamics [152] or the exploration of solid state systems where chemical potentials can be readily tuned [33]. This method can be extended to other Bose-Fermi mixtures to produce large degenerate samples of fermionic molecules and may help achieve a heteronuclear molecular BEC from Bose-Bose mixtures that suffer even more severe losses when both bosonic species condense [153–158]. Ultimately this technique allows to produce a gas of nonreactive ground-state molecules in the quantum-degenerate regime with five times stronger molecular-frame dipole moments than the first degenerate polar molecules of KRb and provides excellent conditions for evaporative cooling of ground-state molecules as demonstrated for KRb [159, 160] and recently also for NaK

[161]. This opens up exciting opportunities to study strongly correlated dipolar quantum systems [162] ranging from the collapse of dipolar Fermi gases [163] to extended Heisenberg XXZ models [164] and extended Fermi-Hubbard models [165] in optical lattices.

2.3 Strongly coupled Bose-Fermi mixtures in two dimensions

2.3.1 Introduction

In order to explore the phase diagram of two-dimensional Bose-Fermi mixtures at strong coupling, shown in Fig. 2.1, it is crucial to start from limits that allow for a controlled understanding of the physics involved. One such limit is found at extreme population imbalance where just a single boson is immersed in a fermionic bath. This so-called Fermi polaron problem already displays rich physics that has been studied extensively in three dimensions [50, 54, 56, 57, 59, 137, 138, 141, 142, 166–169]. As discussed in Section 1.7, one finds that as the interaction between the impurity and the bath is tuned, the system undergoes a sharp transition from a polaronic to a molecular state. While in the polaron state the impurity is essentially weakly dressed by bath excitations, in the molecular state the impurity binds tightly to one fermion of the surrounding environment giving rise to a state that, close to the transition [137, 167], is orthogonal to the polaron state.

The two-dimensional case has received attention over the last decade [170–176] as well. It turns out that this case is more challenging to describe due to the increased significance of quantum fluctuations in reduced dimensions. While early works based on simple variational wavefunctions found no polaron-to-molecule transition [170], later studies showed that this finding was in fact an artifact caused by the neglect of three-body correlations. Including these, one indeed recovers a polaron-to-molecule transition in two dimensions [171, 174], a result supported by subsequent studies using a variety of Quantum Monte-Carlo (QMC) techniques [173, 175, 176].

As the preceding discussion shows, there are strong constraints on any approach that aims to reliably describe strongly-coupled Bose-Fermi mixtures in two dimensions even on a qualitative level. First, in order to address the strong-coupling character of the problem correctly, it must be based on the extended Fröhlich model. Second, it must go beyond perturbation theory in order to describe the formation of fermionic bound states. Third, at vanishing boson density it must correctly reproduce the quantum impurity limit, which necessitates the incorporation of three-body correlations. Fourth, in order to describe the phase diagram at finite boson density n_B, the approach must be able to deal with the fermionic nature of the composite particles that will experience Pauli blocking at finite density similar to baryons in atomic nuclei.

Unfortunately, the approaches used in the previous section to describe the phase diagram at fermion-dominated density ratios ($n_B < n_F$) quite reliably, cannot be applied to the two-dimensional problem: In two dimensions, the non-self consistent T-matrix approach discussed in Section 2.2.2.2 does not feature a polaron-to-molecule transition and as a result cannot capture the transition into a molecular phase. The same goes for the effective potential approach discussed in Section 2.2.2.1 which features very similar self-energies.

As mentioned in Section 1.9, these requirements are met by the functional renormalization group (fRG). In addition to addressing the aforementioned constraints im-

posed by the two-dimensional polaron problem, the fRG technique developed in this section displays several other advantages. First, in contrast to variational approaches based on particle-hole excitation expansions, it provides a fully self-consistent approach that naturally includes high-order quantum fluctuations and treats polaron and molecular states on equal footing. Second, by including quantum fluctuations in a coarse-grained fashion, momentum-by-momentum shell, unlike conventional quantum field theory approaches the fRG may treat competing instabilities in an unbiased way. Third, by using increasingly refined truncations of the underlying quantum effective action one may improve the fRG improved systematically. Finally, it offers an easier access to spectral and dynamical response functions compared to Monte Carlo approaches where the analytic continuation of noisy data is required.

We demonstrate the applicability of our approach by focusing on the case where the size a_B of the fermionic bound state is small compared to the average distance $d \sim n_B^{-1/2}$ between bosons. Since for sufficiently short-ranged attraction this bound state always exists in two dimensions [53], its binding energy $\epsilon_B = \hbar^2/(2\mu a_B^2)$ (with μ the reduced mass) is the relevant interaction scale, i.e. we work in the limit $(\hbar^2/2\mu)n_B/\epsilon_B \ll 1$.

By including the full feedback of three-body correlations on the renormalization group flow, we demonstrate the correct description of the polaron-to-molecule transition in the single boson limit. In particular we predict the transition to occur at a critical dimensionless interaction strength $(\epsilon_F/\epsilon_B)^* = 1/18.78$ in excellent agreement with state-of-the-art variational [171, 174] and diagrammatic MC approaches [173, 175, 176].

Having thus established the limiting case of the phase diagram, we extend the renormalization group (RG) flow to finite boson density. At small dimensionless Fermi energies ϵ_F/ϵ_B, we find that fermionic composites build up a well-defined Fermi surface, leading to the formation of a trion liquid in the case of semiconductors and a Fermi sea of dressed Feshbach molecules in the case of ultracold atoms. As the boson density is increased, the effective energy gap of the composites decreases, leading to a transition into a strongly-correlated phase where fermions are hybridized with molecular degrees of freedom. This extension of a single boson framework does not take into account the formation of higher-order bound states including more than one boson [177–179]. While this description might thus be missing some of the phases and states at play, recent theoretical and experimental results suggest that this simplified treatment may, however, still be sufficient to describe the physics relevant on experimental times scales [2, 100].

Adapting the fRG approach to account for the full frequency-dependence of self-energies, we predict the spectral properties of the model. We find that the inclusion of three-body correlations has a strong impact on the effective masses of polarons and molecules (trions) which can be observed using state-of-the-art experimental techniques recently developed in ultracold atoms [9, 180, 181].

This section is structured as follows: in Section 2.3.2 we introduce the strong-coupling model of Bose-Fermi mixtures and discuss the effective action formalism. Here we also introduce our fRG approach, derive the corresponding renormalization

group equations and discuss how the various phases discussed in this work can be distinguished. As this section contains a detailed discussion of the used technique, readers mainly interested in the predictions of our work may proceed from the introduction to Section 2.3.3 and the sections thereafter. In Section 2.3.3 we discuss the universal connection between strongly-coupled Bose-Fermi mixtures in atomically thin semiconductors and ultracold atoms. We benchmark our approach on the limiting case of a single boson embedded in a fermionic environment, obtain the ground state energy of the system and study the evolution of correlation functions in dependence on the fermion density and interaction strength. In Section 2.3.4 we turn to the case of finite boson density. We determine the phase diagram both as a function of the chemical potential and density of both species. In Section 2.3.5 we adapt the fRG scheme to describe the spectral functions of the model and we predict the properties of quasiparticles emerging in the theory. We conclude in Section 2.3.6, discuss perspectives for possible experimental realizations and provide an overview of open questions and promising extensions of the fRG approach introduced in the present chapter.

2.3.2 Model

Let us consider a two-dimensional Bose-Fermi mixture consisting of a fermionic species ψ into which bosonic particles ϕ are embedded. The system is described by the microscopic action

$$S = \int_x \psi_x^* \left(\partial_\tau - \frac{\boldsymbol{\nabla}^2}{2m_F} - \mu_\psi\right)\psi_x + \int_x \phi_x^* \left(\partial_\tau - \frac{\boldsymbol{\nabla}^2}{2m_B} - \mu_\phi\right)\phi_x + g\int_x \psi_x^*\phi_x^*\phi_x\psi_x \tag{2.21}$$

where $x = (\mathbf{r}, \tau)$ denotes the coordinate $\mathbf{r}$ and imaginary time $\tau \in [0, 1/T]$; moreover, $\int_x = \int_0^{1/T} d\tau \int d^2\mathbf{r}$. In the following, we consider zero temperature, $T = 0$, and assume that bosons and fermions have the same mass $m = m_F = m_B$. We work in units $\hbar = k_\mathrm{B} = 1$, and set $2m = 1$ unless indicated otherwise. The fields ψ and ϕ are of fermionic Grassmann and complex boson nature, respectively. The two species interact by means of an attractive contact potential of strength $g < 0$. The model is regularized in the ultraviolet (UV) by a momentum cutoff Λ.

The densities of both species are set by the chemical potentials $\mu_{\psi/\phi}$. At a finite fermion density n_ψ (set by a chemical potential $\mu_\psi > 0$), tuning the boson chemical potential μ_ϕ at fixed μ_ψ and g, triggers a transition at a critical chemical potential μ_ϕ^c between a vacuum phase of bosons ($\mu_\phi < \mu_\phi^c$) with vanishing boson density to a phase of finite boson density $n_B > 0$ ($\mu_\phi > \mu_\phi^c$).

For strongly-coupled Bose-Fermi mixtures it is crucial to allow for the possibility of the pairing of the bosons and fermions to a composite fermionic molecular (trion) state. In order to describe this bound state, it is essential to resolve the pole structure of the scattering vertex sufficiently well [59, 182]. In order to achieve this in an efficient way, rather than considering the action in Eq. (2.21), we study a two-channel model where the interspecies interaction is mediated by a molecule field t, that describes a

composite fermionic particle of mass $2m$ [43, 44, 47, 48]. The action is given by

$$\begin{aligned} S = \int_{\mathbf{p},\omega} \Big\{ & \psi_P^* \left(-i\omega + \mathbf{p}^2 - \mu_\psi\right) \psi_P \\ & + \phi_P^* \left(-i\omega + \mathbf{p}^2 - \mu_\phi\right) \phi_P + t_P^* \left(-i\omega + \frac{\mathbf{p}^2}{2} + m_t\right) t_P \Big\} \\ & + h \int_x \left\{\psi_x^* \phi_x^* t_x + t_x^* \phi_x \psi_x\right\} \ . \end{aligned} \tag{2.22}$$

Here, a boson and a fermion can be converted into the molecule (trion) t with a conversion Yukawa coupling h, and m_t is the detuning energy of the molecule. In Eq. (2.22) we give the action in Fourier space where $P = (\mathbf{p}, \omega)$ comprises the momentum $\mathbf{p}$ and the Matsubara frequency ω, and $\int_{\mathbf{p},\omega} \equiv \int d^2\mathbf{p} d\omega$. We operate in the limit where $h \to \infty$ which universally describes both open-channel dominated Feshbach resonances in cold atoms [20] as well as electron-exciton scattering in atomically thin transition metal dichalcogenides [61]. In this limit, t becomes a purely auxiliary Hubbard-Stratonovich field, i.e. it can be integrated out to yield back the original action (2.21) when $h^2/m_t = -g$ is fulfilled [49, 50].

In two dimensions, a bound state exists for any attractive interaction strength $g < 0$ [53]. Using a sharp UV cutoff in the Lippmann-Schwinger equation, the binding energy ϵ_B is related to the parameters of the microscopic model through [53, 170, 183]

$$m_t = \frac{h^2}{8\pi} \log\left(1 + \frac{2\Lambda^2}{\epsilon_B}\right) . \tag{2.23}$$

Thus, rather than using the microscopic coupling g (or equivalently h and m_t) we can parametrize the interaction strength in terms of the experimentally measurable binding energy ϵ_B of the molecule (in the case of cold atoms) or trion (in the case of 2D semiconductors), respectively. Note, in the following we will often use the terms trion and molecule interchangeably.

2.3.2.1 fRG formalism and effective action

As introduced in Section 1.9, the fRG is a momentum space implementation of Wilson's renormalization group. To introduce a scale-dependent partition function $\mathcal{Z}_k$ as well as a scale-dependent effective action Γ_k through a modified Legendre transform of the free energy $\ln \mathcal{Z}_k$ (see Section 1.9), we add to the action (2.22) an infrared regulator term

$$\begin{aligned} \Delta S_k = \int_{\mathbf{p},\omega} \Big\{ & \psi_P^* R_{\psi,k}(P) \psi_P + \phi_P^* R_{\phi,k}(P) \phi_P \\ & + t_P^* R_{t,k}(P) t_P \Big\} \end{aligned} \tag{2.24}$$

which penalizes low-energy fluctuations, such that only high-energy modes contribute to the field integral.

For bosons and fermions at vanishing density the low-energy modes are located at small momenta. Thus the cutoff function $R_{\sigma,k}(P)$ ($\sigma = \psi, \phi, t$) is set to be large (wrt.

k^2) for $|\mathbf{p}| \ll k$ and negligible for $|\mathbf{p}| \gg k$. In this way, low-momentum fluctuations are suppressed while high-momentum ones are left unaffected. For fermions at a finite density, the low-energy modes are located around the Fermi surface. Accordingly, in this case $R_{\sigma,k}$ is chosen to suppress fluctuations of modes inside a momentum shell of width $\sim 2k$ around the Fermi surface.

After specifying a regulator on may thus compute the flow of the effective action Γ_k from the UV regime down to the infrared regime at $k = 0$ to obtain the quantum effective action Γ using the Wetterich equation

$$\partial_k \Gamma_k = \frac{1}{2} \mathrm{STr} \left[\left(\Gamma_k^{(2)} + R_k \right)^{-1} \partial_k R_k \right] \tag{2.25}$$

introduced in Section 1.9.

2.3.2.2 Truncation schemes

While the Wetterich flow equation (1.78) is exact, it is, in most practical cases, impossible to solve without resorting to approximations. A standard strategy is to propose an *Ansatz* for the flowing effective action Γ_k. When dealing with fermions, it is customary to expand in the powers of the fields in a so-called vertex expansion [79]. Following this strategy we choose the *Ansatz* for the field-dependent part of the effective action

$$\begin{aligned} \Gamma_{2,k} = \int_{\mathbf{p},\omega} \Big\{ & \psi_P^* G_{\psi,k}^{-1}(P) \psi_P + \phi_P^* G_{\phi,k}^{-1}(P) \phi_P \\ & + t_P^* G_{t,k}^{-1}(P) t_P \Big\} + h_k \int_x (\psi_x^* \phi_x^* t_x + t_x^* \phi_x \psi_x) \ . \end{aligned} \tag{2.26}$$

We perform an additional gradient expansion by neglecting a possibly emerging momentum dependence of the Yukawa coupling h_k via vertex corrections. Each field $\sigma = \psi, \phi, t$ carries renormalized flowing single-particle Green's functions whose momentum dependence is approximated within the gradient expansion as

$$G_{\psi,k}^{-1}(\mathbf{p}, \omega) = A_{\psi,k} \left(-i\omega + \mathbf{p}^2 - \mu_\psi \right) + m_{\psi,k} \ , \tag{2.27}$$

$$G_{\phi,k}^{-1}(\mathbf{p}, \omega) = A_{\phi,k} \left(-i\omega + \mathbf{p}^2 \right) + m_{\phi,k} \ , \tag{2.28}$$

$$G_{t,k}^{-1}(\mathbf{p}, \omega) = A_{t,k} \left(-i\omega + \mathbf{p}^2/2 \right) + m_{t,k} \ , \tag{2.29}$$

parametrized by inverse quasiparticle weights $A_{\sigma,k}$ and detunings $m_{\sigma,k}$. Note that for the boson field ϕ we have absorbed the dependence on the chemical potential μ_ϕ into the definition of the detuning $m_{\phi,k}$ for convenience. The *Ansatz* (2.26) incorporates in detail two-body correlations between the bosons and fermions. In particular, it describes well the pairing correlations between the particles which is essential to enter the strong-coupling regime. As a short-hand we refer to the effective flowing action (2.26) as the *'two-body truncation'*.

The two-body truncation has been used successfully to study the Fermi polaron problem in three space dimensions [137, 184, 185]. In two space dimensions, however, quantum fluctuations are stronger and previous works [170, 171] have established that

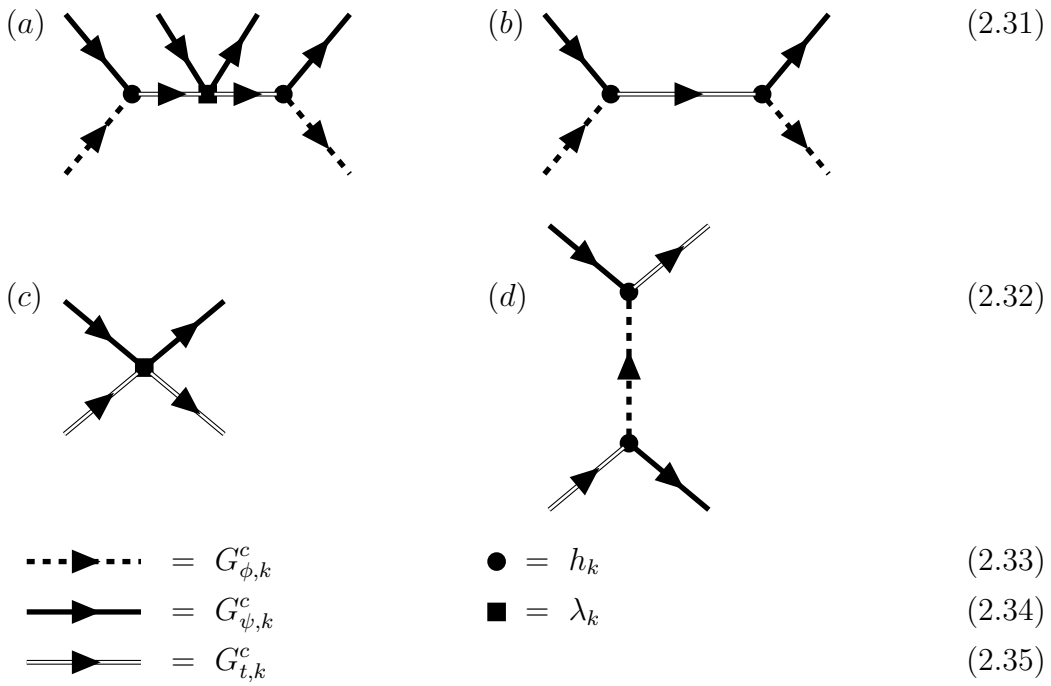

Figure 2.14. (a) Tree-level diagram generated from the effective action that leads to the emergence of three-body correlations in the system. (b) Exchange tree-level diagram giving rise to the Bose-Fermi scattering T-matrix. (c), (d) Tree-level diagrams contributing to the overall atom-molecule scattering amplitude. The dashed, solid and double lines denote the boson, fermion and molecule Green's functions $G_{\phi/\psi/t,k=0}$, respectively, while the dots and squares denote $h_{k=0}$ and $\lambda_{k=0}$, all evaluated at $k = 0$.

higher-order correlations must be taken into account to describe the ground state of the system. Indeed, as we shall see in Section 2.3.3, the two-body truncation is not sufficient to describe the polaron–to–molecule transition.

Consequently, we extend the *Ansatz* for the effective action to a *'three-body truncation'*. To this end we add a term to the two-body truncation that accounts for the build up of three-body correlations during the RG flow:

$$\Gamma_{3,k} = \Gamma_{2,k} + \lambda_k \int_x \psi_x^* t_x^* t_x \psi_x \ . \tag{2.30}$$

The additional term proportional to the contact coupling λ_k describes the scattering between composite molecules and fermions, and thus, by virtue of the tree-level diagram depicted in Fig. 2.14(a), it accounts effectively for the emergence of three-body correlations in the system.

Let us briefly comment on the validity of the gradient expansion used for both truncations (2.26) and (2.30). In the single-boson limit, we expect the low-energy excitations of the boson ϕ and the composite particle t to be at small momenta and we may thus expand the momentum-dependence of their propagators in a power series about $\mathbf{p} = 0$, $\omega = 0$. For the fermions, on the other hand, we expect the most relevant

excitations to lie around the Fermi surface. We thus expand their propagator about $\mathbf{p}^2 = \epsilon_F$, $\omega = 0$.

As we extend our calculation to a finite boson density we retain the expansion around $\mathbf{p} = 0$ for the molecules as we will find that their phase appears in a regime of the phase diagram where $n_B \ll n_F$. Thus the Fermi energy of molecules always remains small. Moreover, we employ a gradient expansion that neglects effective mass corrections as these are not expected to be crucial to correctly capture the qualitative physics of the phase diagram (except for large mass ratios $m_F \ll m_B$ [186], a regime we have not considered in our work).

In the quantum impurity limit, the vanishing of the boson density implies that the properties of the fermionic Green's function are not affected by interactions; i.e. the propagator in Eq. (2.27) with $A_{\psi,k} = 1$ and $m_{\psi,k} = 0$ is *exact*. This can also be verified explicitly from the flow equations derived further below [cf. Eqs. (2.42) to (2.46)]. At finite boson density we neglect the renormalization of the fermionic propagators since throughout this section we will remain in the regime of density ratios $n_B \ll n_F$.

While the truncation in Eq. (2.30) can be improved systematically, e.g., by considering higher-order correlations or a more involved momentum dependence of the propagators or the vertices, the model in Eq. (2.30) is sufficient to accurately describe the intricate quantum impurity limit, as shown in Section 2.3.3. In particular, even though h_k and λ_k have no momentum dependence, the Bose-Fermi scattering T-matrix, as described by the exchange tree-level diagram shown in Fig. 2.14(b), acquires a momentum dependence due to the dynamic field t that is sufficient to describe accurately the Bose-Fermi scattering at the relevant energy scales.

We note that at finite boson density our truncation does not account for the possible formation of bound states between two or more bosons and a single fermion [177–179]. In a realistic experimental setting, where the system will be prepared adiabatically, the formation of these higher-order bound states requires several bosons to be located in the close vicinity of the fermions. Since we focus here, however, on the regime where the boson density is significantly smaller than the fermion density, $n_B \ll n_F$, the probability to find such configurations will be small. As a result, compared to the time scale of Fermi polaron or molecule formation, the formation of higher-order bound states will be suppressed, enabling the observation of the phase diagram studied in this section on transient time scales. Nevertheless, while recent results suggest that this treatment is appropriate [2, 100], the framework used in this section can be extended to feature bound states between two bosons and a fermion; both in the vacuum limit as well as at finite density (for details see Appendix A). This highlights that this study provides only an initial step in the exploration of this phase diagram which, given sufficiently stable bound states, may feature an even richer structure.

2.3.2.3 Regulators

For the regulators $R_{\sigma,k}$ we use sharp cutoff functions [79], defined so that the *regulated* inverse flowing propagators

$$(G^c_{\sigma,k})^{-1} = (G_{\sigma,k})^{-1} + R_{\sigma,k} \tag{2.36}$$

appearing on the rhs. of the flow equation (1.78) acquire the simple form

$$G^c_{\psi,k}(\mathbf{p},\omega) = G_{\psi,k}(\mathbf{p},\omega)\Theta(|\mathbf{p}^2 - \epsilon_{F,k}| - k^2) \ , \tag{2.37}$$
$$G^c_{\phi,k}(\mathbf{p},\omega) = G_{\phi,k}(\mathbf{p},\omega)\Theta(|\mathbf{p}| - k) \ , \tag{2.38}$$
$$G^c_{t,k}(\mathbf{p},\omega) = G_{t,k}(\mathbf{p},\omega)\Theta(|\mathbf{p}| - k) \ . \tag{2.39}$$

Here,

$$\epsilon_{F,k} = \mu_\psi - m_{\psi,k}/A_{\psi,k} \tag{2.40}$$

is the Fermi energy of the fermionic species ψ. For the fermions ψ the regulator suppresses fluctuations at momenta in a shell of width $2k$ around the, in principle, flowing Fermi-surface of the bath [187]. Even though the molecule is a fermion as well and thus may develop a Fermi surface at finite boson density, we regulate it about zero momentum as all phases considered in this section appear in the regime $n_B \ll n_F$.

The choice of sharp cutoff functions has several advantages (For a detailed discussion of regulator dependence in this model in three dimensions see Ref. [185]). Foremost, it allows for an analytic derivation of the flow equations. In addition, it facilitates the comparison to previous FRG studies [137, 184, 185] as well as to self-consistent diagrammatic approximations that display a similar mathematical structure [103].

2.3.2.4 Vertex projections and gradient expansion parameters

To be able to compute a flow equation of one of the n-point functions contained in the Ansatz for the effective action in Eqs. (2.26) and (2.30), they need to be obtained using suitable functional field derivatives. The n-point functions considered here are obtained from the effective flowing action Γ_k using the following projections:

$$\begin{aligned}
G^{-1}_{\psi,k}(\mathbf{p},\omega) &= \frac{\delta}{\delta\psi(\mathbf{p},\omega)}\frac{\delta}{\delta\psi^*(\mathbf{p},\omega)}\Gamma_k \ , \\
G^{-1}_{\phi,k}(\mathbf{p},\omega) &= \frac{\delta}{\delta\phi(\mathbf{p},\omega)}\frac{\delta}{\delta\phi^*(\mathbf{p},\omega)}\Gamma_k \ , \\
G^{-1}_{t,k}(\mathbf{p},\omega) &= \frac{\delta}{\delta t(\mathbf{p},\omega)}\frac{\delta}{\delta t^*(\mathbf{p},\omega)}\Gamma_k \ , \\
\frac{h_k}{(2\pi)^{3/2}} &= \frac{\delta}{\delta t(\mathbf{0},0)}\frac{\delta}{\delta\phi^*(\mathbf{0},0)}\frac{\delta}{\delta\psi^*(\mathbf{0},0)}\Gamma_k \ , \\
\frac{\lambda_k}{(2\pi)^3} &= \frac{\delta}{\delta\psi(\mathbf{0},0)}\frac{\delta}{\delta t(\mathbf{0},0)}\frac{\delta}{\delta t^*(\mathbf{0},0)}\frac{\delta}{\delta\psi^*(\mathbf{0},0)}\Gamma_k \ .
\end{aligned} \tag{2.41}$$

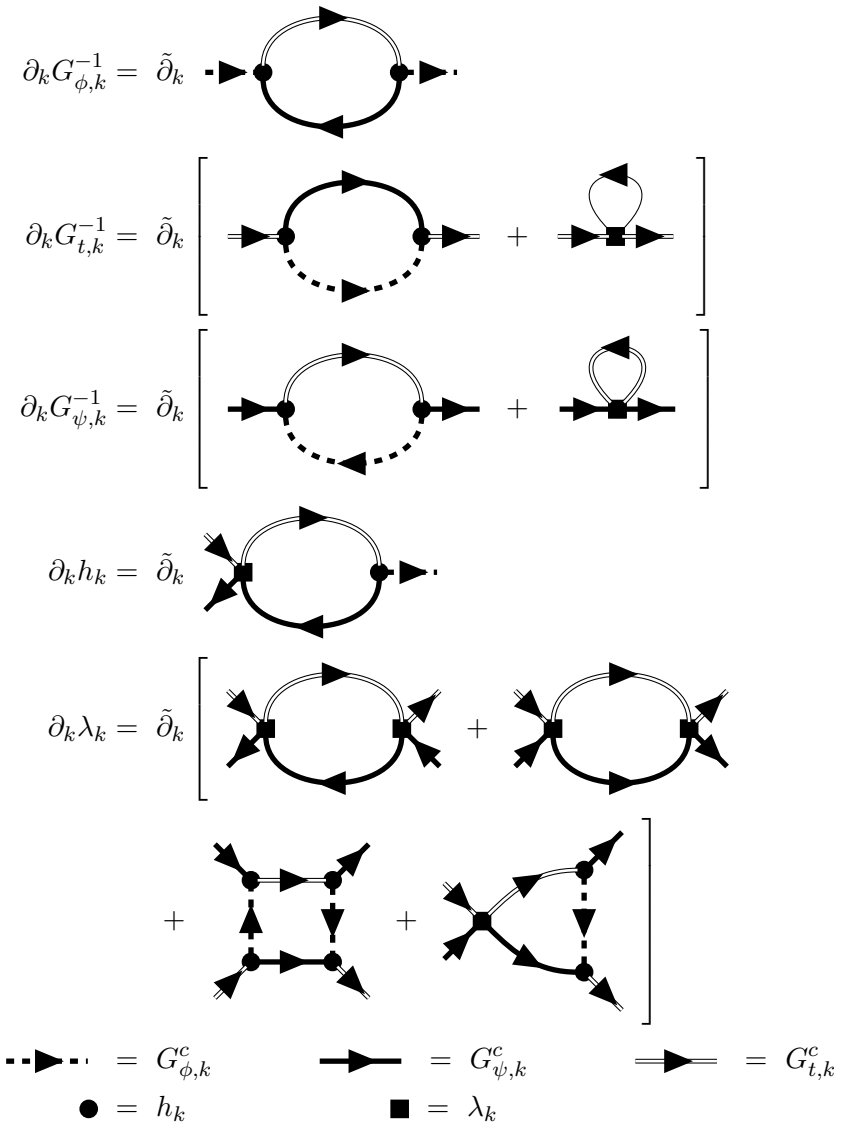

Figure 2.15. Diagrammatic representation of the fRG flow equations Eqs. (2.42) to (2.46). Lines represent the full scale-dependent propagators, including the regulators, and the dots denote interaction vertices.

2.3.2.5 Flow Equations

We now turn to the explicit derivation of the RG equations [188, 189] of all running coupling constants. For the three-body truncation $\Gamma_{3,k}$ ($\Gamma_{2,k}$ is a subset obtained by setting $\lambda_k \equiv 0$ in all flow equations) all vertices can be expressed in terms of the six running couplings $A_{\sigma,k}$, $m_{\sigma,k}$, h_k and λ_k. Following the prescription detailed in Section 2.3.2.4, the flow equations are obtained from appropriate functional derivatives of the Wetterich equation. Their diagrammatic representation is shown in Fig. 2.15

and in terms of the flowing Green's functions they read

$$\partial_k G^{-1}_{\phi,k}(P) = h_k^2 \tilde{\partial}_k \int_Q G^c_{t,k}(P+Q) G^c_{\psi,k}(Q) \ , \tag{2.42}$$

$$\partial_k G^{-1}_{\psi,k}(P) = -h_k^2 \tilde{\partial}_k \int_Q \left[G^c_{t,k}(P+Q) G^c_{\phi,k}(Q) + \frac{\lambda_k}{h_k^2} G^c_{t,k}(Q) \right] , \tag{2.43}$$

$$\partial_k G^{-1}_{t,k}(P) = -h_k^2 \tilde{\partial}_k \int_Q \left[G^c_{\phi,k}(P-Q) G^c_{\psi,k}(Q) + \frac{\lambda}{h_k^2} G^c_{\psi,k}(Q) \right] , \tag{2.44}$$

and

$$\partial_k h_k = -\frac{\lambda_k}{h_k} \partial_k G^{-1}_{\phi,k}(0) \ , \tag{2.45}$$

$$\begin{aligned} \partial_k \lambda_k = & -\lambda_k^2 \tilde{\partial}_k \int_Q G^c_{t,k}(Q) \left[G^c_{\psi,k}(Q) + G^c_{\psi,k}(-Q) \right] \\ & - h_k^4 \tilde{\partial}_k \int_Q G^c_{t,k}(Q) G^c_{\phi,k}(Q)^2 G^c_{\psi,k}(-Q) \\ & - 2h_k^2 \lambda_k \tilde{\partial}_k \int_Q G^c_{t,k}(Q) G^c_{\phi,k}(Q) G^c_{\psi,k}(-Q) \ . \end{aligned} \tag{2.46}$$

In these expressions $\tilde{\partial}_k$ stands for the derivative with respect to the k dependence of the regulator only, i.e. $\tilde{\partial}_k = (\partial_k R_k)\partial_{R_k}$ and $\int_P \equiv (2\pi)^{-3} \int d^2\mathbf{p} d\omega$. From Eqs. (2.42) to (2.44) the flow equations of the couplings $A_{\sigma,k}$, $m_{\sigma,k}$ are obtained by projection onto the momentum dependencies given in Eqs. (2.27) to (2.29). The parameters of the gradient expansion of the two-point functions $G^{-1}_{\phi,\psi,t,k}$ are thus given by

$$\begin{aligned} m_\psi &= G^{-1}_{\psi,k}(\mathbf{p},\omega)|_{\mathbf{p}^2=\epsilon_F,\omega=0} \ , \\ A_\psi &= \partial_{-i\omega} G^{-1}_{\psi,k}(\mathbf{p},\omega)|_{\mathbf{p}^2=\epsilon_F,\omega=0} \ , \\ m_\phi &= G^{-1}_{\phi,k}(\mathbf{p},\omega)|_{\mathbf{p}=\mathbf{0},\omega=0} \ , \\ A_\phi &= \partial_{-i\omega} G^{-1}_{\phi,k}(\mathbf{p},\omega)|_{\mathbf{p}=\mathbf{0},\omega=0} \ , \\ m_t &= G^{-1}_{t,k}(\mathbf{p},\omega)|_{\mathbf{p}=\mathbf{0},\omega=0} \ , \\ A_t &= \partial_{-i\omega} G^{-1}_{t}(\mathbf{p},\omega)|_{\mathbf{p}=\mathbf{0},\omega=0} \ . \end{aligned} \tag{2.47}$$

In Appendix B we provide the explicit form of the flow equations.

2.3.2.6 RG initial conditions

The initial conditions for the flows are obtained by setting $\Gamma_{k=\Lambda} = S + const.$ First, we discuss the UV initial conditions for m_t and A_t which are obtained from the physical renormalization condition that in the two-body problem a bound state of energy ϵ_B forms between the boson and the fermion species. This two-body problem of a single boson scattering with a single fermion can be solved exactly and as a result it can also be solved exactly in an fRG framework and the resulting initial condition for $m_{t,k=\Lambda}$ is given by Eq. (2.23).

To arrive at this expression one may recognize that in the two-body problem the molecule is the ground state. As such it has to be a gapless degree of freedom in the infrared, i.e. $m_{t,k=0} = 0$. Moreover, μ_ψ and μ_ϕ must be set to negative values

μ_ψ^{vac} and μ_ϕ^{vac} to yield a vanishing density of either species and the molecule has to remain gapped $m_{t,k} \geq 0$ throughout the flow. In addition, $\mu_\psi^{\text{vac}} + \mu_\phi^{\text{vac}} = -\epsilon_B$ has to be fulfilled to ensure that the energy cost to create two particles from the vacuum to form a bound state is given by the molecular binding energy ϵ_B. These conditions guarantee that the chemical potentials are tuned correctly to the boundary between the vacuum state and the state comprised of a molecule submersed in vacuum.

The flow of the three-body vertex does not have to be taken into account, since λ_k does not feed back into the solution of the two-body problem. Similarly, in the two-body problem the flow equations of $G_{\psi,k}^{-1}(P)$ and $G_{\phi,k}^{-1}(P)$ evaluate to zero because the poles of their propagators in Eqs. (2.42) and (2.43) lie in the same half of the complex plane and thus their frequency contour integrals evaluate to zero. Physically, this is because neither of the particle species has a finite density which would be required to generate a renormalization of the particle self-energies by particle-hole fluctuations. The molecule on the other hand is renormalized by a particle-particle diagram and thus does not require a finite density of bosons or fermions.

As the three body-vertex is not relevant in the two-body problem, the Yukawa term h does not renormalize. After evaluation and projection of Eq. (2.44), the flow equations of $m_{t,k}$ and $A_{t,k}$ in the two-body limit are therefore given by

$$\partial_k m_{t,k} = \frac{h^2 k}{2\pi} \frac{1}{2k^2 - \mu_\phi - \mu_\psi} \tag{2.48}$$

and

$$\partial_k A_{t,k} = -\frac{h^2 k}{2\pi} \frac{1}{(2k^2 - \mu_\phi - \mu_\psi)^2} \ . \tag{2.49}$$

Using $m_{t,k=\Lambda} = m_{t,k=0} + \int_0^\Lambda dk (\partial_k m_{t,k})$ and $m_{t,k=0} = 0$ this yields Eq. (2.23). Note that since in this few-body calculation no Fermi surfaces are present, the regulators are proportional to $\Theta(|\mathbf{p}| - k)$ for all particles involved.

We work in the limit of large $h_{k=\Lambda}$ which ensures t to be purely an auxiliary field and we use $A_{t,k=\Lambda} = 1$. Furthermore, we set $\lambda_{k=\Lambda} = 0$ as it does not appear in the classical action in Eq. (2.22).

The initial condition for the field renormalization of the boson field is naturally given by $A_{\phi,\Lambda} = 1$, and the UV value of its detuning is set by the boson chemical potential, $m_{\phi,\Lambda} = -\mu_\phi$. Finally, since we will only study phases at small ratios $n_B \ll n_F$ we can assume that the fermion field is not renormalized, i.e. $A_{\psi,k} = 1$ and $m_{\psi,k} = 0$ throughout the RG flow.

2.3.2.7 Chemical potentials and distinction of phases

The numerical integration of the flow equations yields the physical value of the propagators and interaction vertices at the infrared scale $k = 0$. Depending on their properties we can distinguish various states and phases of the strongly-coupled Bose-Fermi mixture, summarized in Table 2.1.

In the single-boson limit, yet at finite fermion density, we distinguish two *states*: a *molecular state* in which the boson is paired into a composite particle, and a *polaron*

n_t	n_ϕ	μ_ϕ	$m_{t,0}$	$m_{\phi,0}$	state/phase	# bosons
$=0$	$=0$	$<\mu_\phi^c$	>0	>0	boson-vacuum	0
$=0$	$=0$	$=\mu_\phi^c$	$=0$	>0	molecular state	1
$=0$	$=0$	$=\mu_\phi^c$	>0	$=0$	polaron state	1
>0	$=0$	$>\mu_\phi^c$	<0	>0	molecular phase	$\gg 1$
>0	>0	$>\mu_\phi^c$	$\in\mathbb{R}$	$=0$	mixed phase	$\gg 1$

Table 2.1. Characterization of different ground states and phases of strongly-coupled Bose-Fermi mixtures discussed in this chapter.

state where the boson is dressed by fluctuations of majority fermion particles. At finite boson density, we distinguish two *phases*: a *molecular phase*, where all bosons are paired into fermionic molecules, $n_t > 0$ and $n_\phi = 0$, and a *mixed phase* where molecules and unpaired polarons coexist [96]. In the mixed phase, $n_\phi > 0$, so that the condensate of bosons creates a bilinear coupling in the effective action $\sim h\sqrt{n_\phi}(t^*\psi + \text{c.c.})$ leading to a hybridization of the fermions with the molecular degree of freedom. This means that no purely polaronic phase with $n_t = 0$ and $n_\phi > 0$ is possible. In the limit of $n_B \to 0$ the mixed phase connects to the polaron state, whereas the molecular phase connects to the molecular state.

Note, that the phases referred to in this section as the *mixed phase* and the *polaronic phase* from Section 2.2 are equivalent phases (albeit described in different dimensions). As the work presented in this section only describes the transition into the mixed phase but not its physical properties within the phase, we refrain from referring to it as the polaronic phase: While in three dimensions it is now known that the polaronic phase behaves very similar to the Fermi polaron (see Section 2.2), in two dimensions this connection has not been made and is merely a conjecture.

In order to differentiate between these states and phases we consider the different densities defined by integrals proportional to $\int_{\mathbf{p},\omega} G_{\sigma,k=0}(\mathbf{p},\omega)$. These densities are nonzero only when poles of $G_{\sigma,k=0}(\mathbf{p},\omega)$ lie in the upper half of the complex ω-frequency plane. Hence, from the location of poles, manifest in the energy gaps of the particle in the infrared, we can determine whether the corresponding densities vanish.

Specifically, the boson vacuum corresponds to a finite excitation gap for both the boson and the molecule, $m_{\phi,k=0}$, $m_{t,k=0} > 0$. Likewise, in the single-boson limit the ground state has to be gapless while the excited state is gapped since this limit marks the boundary between the boson vacuum and the many-boson regime.

At finite boson density, the molecular phase corresponds to $m_{\phi,k=0} > 0$ and $m_{t,k=0} < 0$, i.e. molecules feature a Fermi surface determined by their Fermi energy $-m_{t,k=0}/A_{t,k=0}$. For the mixed phase, the situation is more subtle. Our *Ansatz* does not allow for the description of a condensate at finite boson density that could be accounted for, e.g., by shifting the ϕ-field expectation value by a coherent state transformation. However, it is still possible to predict whether a boson condensate forms. Indeed, a necessary condition for the existence of a ϕ-condensate is that for

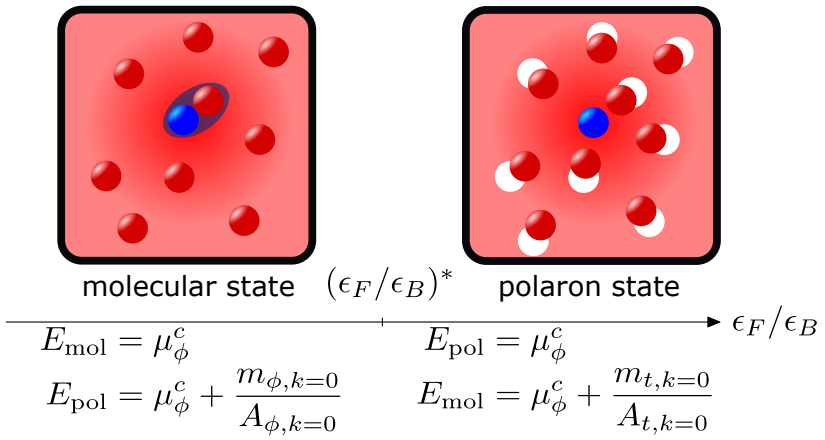

Figure 2.16. Schematic characterization of the relevant states in the Fermi polaron problem. In the molecular state the impurity binds to a single fermion while in the polaron state it is collectively dressed by the environment. For each state, we give the expressions for the energies $E_{\rm pol}$ and $E_{\rm mol}$ of the polaron and the molecule.

some $0 \leq k \leq \Lambda$ the boson gap $m_{\phi,k}$ vanishes [1]. In that case, even though we are unable to further pursue the RG flow, we identify the phase to be the mixed phase.

In this mixed phase the bilinear term mentioned above leads to a mixing of the fermionic and the molecular propagators. Consequently, these propagators share the same pole structure and the corresponding species are thus populated simultaneously. As a result all three particle species are present in this phase. This implies that in our model a regime populated exclusively by majority fermions and condensed minority bosons is only possible in the single-boson limit at $n_B = 0$.

2.3.3 Quantum impurity limit: single boson in a Fermi sea

We first apply our approach to the limiting case of the Bose-Fermi phase diagram where an individual boson is immersed in a bath of fermions. This limit defines the so-called Fermi polaron problem, and its solution determines the phase diagram along the y-axis of Fig. 2.1. In order to reach this single-boson limit, the boson chemical potential is tuned to the critical value $\mu_\phi = \mu_\phi^c$ that separates the boson vacuum ($\mu_\phi < \mu_\phi^c$) from the phase of a finite boson density ($\mu_\phi > \mu_\phi^c$); see Table 2.1.

2.3.3.1 Quasiparticle energies

In order to obtain the spectrum of the Fermi polaron problem we first determine the ground state energy of the system, set by μ_ϕ^c, the critical energy needed to bring a boson from the vacuum. The procedure is summarized in Fig. 2.16: when the polaron is the ground state, $m_{\phi,k=0} = 0$, and the polaron energy is given by $E_{\rm pol} = \mu_\phi^c$. In this *'polaron regime'* the molecular state is an excited state whose energy is determined

[1] When the condensate appears at finite RG scale $k > 0$ it could, of course, again vanish at smaller RG scales due to the effect of quantum or thermal fluctuations.

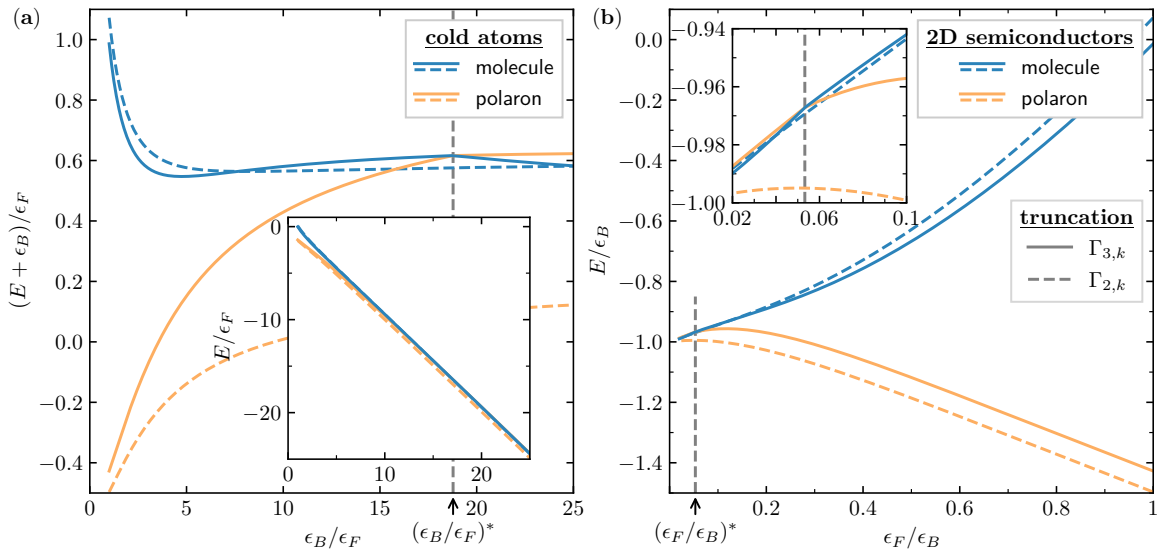

Figure 2.17. Polaron and molecule energies, $E_{\rm pol}$ (orange) and $E_{\rm mol}$ (blue), obtained using the two- and three-body truncations $\Gamma_{2,k}$ (dashed lines) and $\Gamma_{3,k}$ (solid lines). (a) Energy spectrum expressed in units most suitable for cold atom experiments where ϵ_B is the tunable parameter whereas ϵ_F is fixed. As all particle energies are approximately proportional to ϵ_B, the energies $E_{\rm pol/mol}$ are shifted by ϵ_B to enhance visibility. The inset shows the energies without the shift. (b) Energy spectrum expressed in units most suitable for 2D semiconductor experiments. Here ϵ_B is fixed and ϵ_F is varied using gate-doping. Despite the different appearance, both panels show the same data. The polaron-to-molecule transition is marked by the vertical, dashed gray line. The results are obtained for $h^2_{k=\Lambda} = 10^8\epsilon_F$ and $\Lambda^2 = 2.5\times10^5\epsilon_F$ which ensures that the two-channel model reduces to a model of contact interactions between fermions and bosons.

from the pole of its Green's function which yields $E_{\rm mol} = E_{\rm pol} + m_{t,k=0}/A_{t,k=0}$. In turn, in the *'molecular regime'* the molecule is the ground state. Here, $m_{t,k=0} = 0$, and the molecule energy is given by $E_{\rm mol} = \mu^c_\phi$, while the polaron is an excited state with an energy gap $E_{\rm pol} = E_{\rm mol} + m_{\phi,k=0}/A_{\phi,k=0}$.

In Fig. 2.17 we show the polaron and the molecular energy as obtained from the two- and three-body truncations. The spectrum of the Fermi polaron problem is shown both in units convenient for cold atoms [Fig. 2.17(a)] as well as 2D materials [Fig. 2.17(b)]. The comparison of (a) and (b) demonstrates that despite the fact that both panels contain fully redundant information, they yet represent seemingly different behavior which is, however, solely due to the different choice of units.

In Fig. 2.17 the results obtained from the two-body truncation (2.26) are shown as dashed lines. This truncation takes into account a similar set of diagrams as a non-self-consistent T-matrix approach [172] which, in turn, is equivalent to a variational Chevy approach [59, 170]. By contrast to the aforementioned approaches our fRG is self-consistent. As expected from these approaches, we find that the two-body truncation is not sufficient to generate a polaron-to-molecule transition.

Instead we find that the inclusion of irreducible three-body correlations is crucial, which is consistent with diagrammatic MC [175] and higher-order variational approaches [171, 174]. We find that the inclusion of the three-body vertex $\Gamma_{3,k}$ lowers the molecular energy while increasing the polaron energy. As a result, taking into account the RG flow of the irreducible atom-molecule scattering vertex λ_k (solid lines in Fig. 2.17) we find a transition at a dimensionless interaction strength $(\epsilon_B/\epsilon_F)^* = 18.78$ which is in excellent agreement with MC and variational results. A comparison of our result for $(\epsilon_B/\epsilon_F)^*$ with literature is provided in Table 2.2.

Similar to previous field-theoretical or variational approaches [170–172, 174], we do not include all possible two-body correlations and focus on the effect of pairing correlations. Further two-body correlations can, for instance, be generated by the re-emergence of the four-point vertex $\sim \gamma\psi^*\psi\phi^*\phi$. One may justify the exclusion of this vertex by an analogy to BEC superconductivity. There the vertex γ accounts for induced interactions in the particle-hole channel, leading to a contribution similar to the Gorkov corrections to BCS superconductivity [190–192]. In the BCS case, it leads to an effective shift of the inverse dimensionless interaction strength that appears in the gap equation determining T_c/T_F. Based on this analogy, we expect that such terms will not establish a new polaron-to-molecule transition, but rather only shift the location of an already present transition. Thus we concur with previous studies that it is three-body correlations that are essential to establish the formation of a phase of trions in strongly-coupled Bose-Fermi mixtures [2].

We note that at low Fermi energies, we find a weak non-monotonous behavior of the polaron energy in the dependence on ϵ_F/ϵ_B. Such a behavior is not present in works using variational [170–172, 174] or MC approaches [175, 176]. As we will discuss in Section 2.3.3.3, we attribute this effect to the limited resolution of the frequency- and momentum-dependence of the vertex functions in both our truncations. This effect is, however, not relevant for our study of the Bose-Fermi phase diagram which only depends on the relative energy gaps between the polaron and molecular state and not on their respective absolute values.

2.3.3.2 Vertex functions

The FRG approach allows one to analyze the two- and three-body vertices that determine the emergent effective interactions and correlations in the system. In Fig. 2.18, the dimensionless, renormalized atom-molecule scattering vertex

$$\tilde{\lambda} \equiv \lambda_{k=0}\epsilon_F/h^2_{k=0} \tag{2.50}$$

and molecular gap

$$\tilde{m}_t \equiv m_{t,k=0}/h^2_{k=0} \tag{2.51}$$

[2] In this argument we disregard the Coulomb repulsion between the excess charge carriers in 2D semiconductors that might further reduce the interaction range over which trions can build a stable phase.

Theoretical approach	$(\epsilon_B/\epsilon_F)^*$	η_c
fRG (present work)	18.78	-1.12
Basic variational [171]	9.9	-0.8
High-order variational [174]	14	-0.97
Diag. MC [175]	18.1 ± 7.2	-1.1 ± 0.2
Diag. MC [176]	13.4 ± 4	-0.95 ± 0.15
Diffusion MC [173]	≈ 15	≈ -1
Experiment [129, 193]	11.6 ± 4.6	-0.88 ± 0.2

Table 2.2. Comparison of the critical ratio $(\epsilon_B/\epsilon_F)^*$ and the interaction parameter $\eta_c = -\log(\epsilon_B/2\epsilon_F)/2 = \log(k_F a_{2D})$ (that relates the 2D scattering length to the binding energy) obtained from our approach (fRG, first line) with that found by previous theoretical calculations based on Monte-Carlo techniques, variational Ansätze and experiment.

are shown as function of ϵ_F/ϵ_B. We have scaled both vertices by powers of h that reflect the scaling of the vertices with the molecular wavefunction renormalization $A^{-1}_{t,k=0}$ yielding results independent of h in the contact-interaction limit at $h \to \infty$.

Atom-molecule scattering The vertex λ_k describes the scattering between the composite fermionic molecules and the excess fermions in the system. During the RG flow, λ_k evolves from $\lambda_{k=\Lambda} = 0$ in the UV to a negative value in the infrared at $k = 0$. Thus $\tilde{\lambda}$ yields an attractive contribution, shown in Fig. 2.14(c), to the overall atom-molecule scattering amplitude that has an additional, significant contribution from the tree-level ϕ-exchange diagram depicted in Fig. 2.14(d).

Fig. 2.18 shows the absolute value of the scattering vertex in the three-body limit (dashed orange line) where it takes the value

$$\tilde{\lambda} = \tilde{\lambda}^{(3B)} = -\epsilon_F/\epsilon_B, \tag{2.52}$$

as we will show towards the end of this subsection. Thus the vertex scales proportional to the square of the size of the molecular bound state $a_B \propto \sqrt{1/\epsilon_B}$. The solid orange line shows the result for $\tilde{\lambda}$ in the polaron problem. At small fermion density the molecule is the ground state. In this *'molecular regime'* the density of fermions is so low that the average inter-fermion spacing greatly exceeds the molecular size a_B. Thus the atom-molecular scattering vertex is essentially unaffected by the presence of the fermionic medium, and $\tilde{\lambda}$ follows the three-body result $\tilde{\lambda}^{(3B)}$.

As ϵ_F/ϵ_B is increased we observe a suppression of the atom-molecule scattering vertex. We attribute this effect to two contributing factors. First, the molecule becomes an excited state beyond the critical interaction $(\epsilon_F/\epsilon_B)^*$. In this case the molecule is gapped and within our FRG approach which projects vertex functions on vanishing external vertex frequencies and momenta (see Section 2.3.2.5), $\tilde{\lambda}$ is thus suppressed by the molecular energy gap. More importantly, however, as the Fermi energy becomes larger than ϵ_B, $\epsilon_F/\epsilon_B > 1$, the size of the bound state starts to exceed

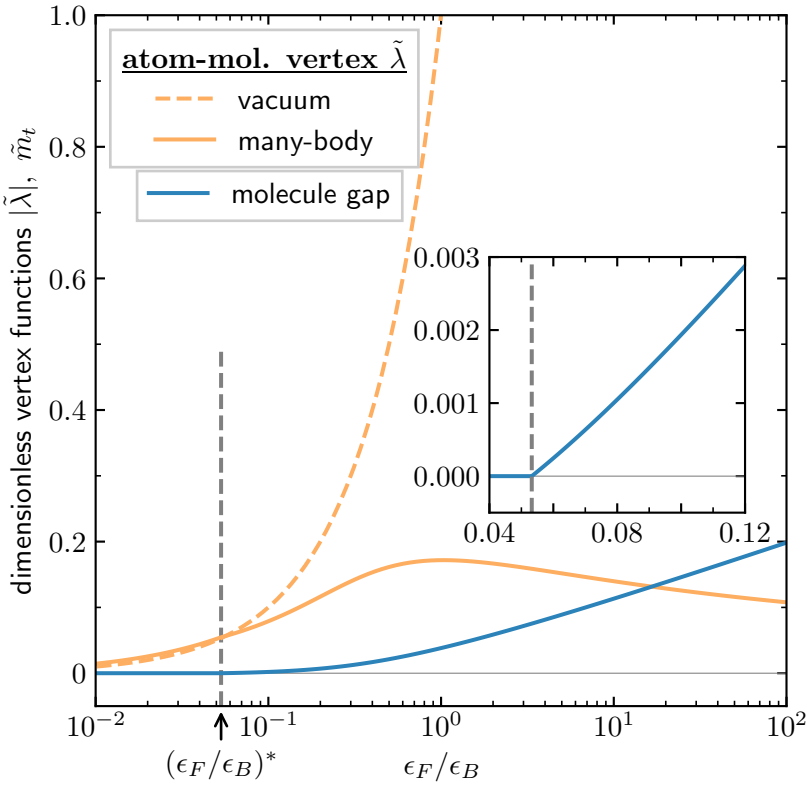

Figure 2.18. Renormalized dimensionless three-body vertex $|\tilde{\lambda}| = |\lambda_{k=0}\epsilon_F/h^2_{k=0}|$ (orange, solid) and renormalized dimensionless molecular gap $\tilde{m}_t = m_{t,k=0}/h^2_{k=0}$ (blue, solid) obtained within the three-body truncation $\Gamma_{3,k}$ as a function of ϵ_F/ϵ_B. The dashed orange line shows the value of the atom-molecule scattering vertex in the three-body (vacuum) limit where $\tilde{\lambda} \to \tilde{\lambda}^{(3B)} = -\epsilon_F/\epsilon_B$. Deep in the strong-binding or, equivalently, low fermion doping regime $\epsilon_F/\epsilon_B \ll 1$, $\tilde{\lambda}$ approaches the three-body result. Starting at around the scale $\epsilon_F \approx \epsilon_B$, medium corrections to the atom-molecule scattering lead to a pronounced suppression effect. The inset shows that close to the polaron-to-molecule transition the molecular gap $\tilde{m}_t$ vanishes linearly as $(\epsilon_F/\epsilon_B) - (\epsilon_F/\epsilon_B)^*$. In the two-body truncation $\lambda_k \equiv 0$, and $\tilde{m}_t$ remains positive for all ϵ_F/ϵ_B, since no polaron-to-molecule transition exists at this level of approximation. The results are obtained for $\Lambda^2 = 2.5 \times 10^5 \epsilon_F$ and $h^2_{k=\Lambda} = 10^8 \epsilon_F$.

the typical inter-fermion distance. As a consequence, in-medium effects come into play leading to significant modifications of $\tilde{\lambda}$. Indeed, these corrections become so strong that $\tilde{\lambda}$ starts to decrease at even larger values of ϵ_F/ϵ_B.

Molecular gap The dimensionless molecular gap $\tilde{m}_t = m_{t,k=0}/h^2_{k=0}$ is shown as a blue line in Fig. 2.18. For interaction strengths $\epsilon_F/\epsilon_B < (\epsilon_F/\epsilon_B)^*$ where the molecule is the ground state, the molecule is gapless, $\tilde{m}_t = 0$. Beyond the transition the molecule becomes an excited state and we find that its gap vanishes linearly as $m_t \sim (\epsilon_F/\epsilon_B) - (\epsilon_F/\epsilon_B)^*$ towards the transition.

The corresponding crossing of the molecular and the polaron state can also be interpreted as leading to an effective Feshbach resonance in the polaron-fermion scattering where the tree-level diagram shown in Fig. 2.14(b), evaluated on-mass-shell, diverges. The associated polaron-fermion scattering length changes sign at the transition, with a positive value signaling the existence of a fermionic bound state.

In turn, within a single-channel theory that is formulated purely in terms of the 'atomic fields' ψ and ϕ, the divergence of the effective polaron-fermion scattering vertex $\sim h^2/P_t$ signals the instability towards a phase of fermionic bound states. In this language, entering this phase at finite boson density would necessarily require the introduction of the emergent fermionic composite states. Finally we note that in Fig. 2.18 we only show results from the three-body truncation $\Gamma_{3,k}$ since in the two-body truncation $\Gamma_{2,k}$, the vertex $\lambda_k = 0$ vanishes by definition throughout the RG flow. Moreover, since no polaron-to-molecule transition is present in this simpler truncation, $\tilde{m}_t$ always remains finite.

Atom-molecule scattering in the vacuum three-body limit Having discussed the atom-molecule scattering vertex in medium and having compared it to its value of $\tilde{\lambda} = \tilde{\lambda}^{(3B)} = -\epsilon_F/\epsilon_B$ in the three-body limit, let us briefly show how this asymptotic result comes about. To determine the value of the three-body vertex in the limit where two ψ-particles and a single ϕ-particle are present, we solve the flow equations under the initial conditions of the two-body problem discussed in Section 2.3.2.6, and additionally take into account the flow of λ_k. Since λ_k corresponds to the *on-mass-shell* scattering of a molecule and a quasi-free excess fermion, we supplement the two-body initial conditions by setting the fermionic chemical potential to a small, negative value $\mu_\psi = 0^-$ while we set $\mu_\phi = -\epsilon_B - 0^-$.

As in the two-body case, $G^{-1}_{\phi,k}$ and $G^{-1}_{\psi,k}$ do not flow and as a result neither does h_k. Consequentially, the flow of $m_{t,k}$ and $A_{t,k}$ is not influenced by the flow of λ_k such that according to Eqs. (2.48) and (2.49)

$$m_{t,k} = \frac{h^2}{8\pi} \log\left(1 + \frac{2k^2}{\epsilon_B}\right) \tag{2.53}$$

and similarly

$$A_{t,k} = 1 + \frac{h^2}{8\pi}\left(\frac{1}{\epsilon_B + 2k^2} - \frac{1}{\epsilon_B + 2\Lambda^2}\right) . \tag{2.54}$$

The flow equation of λ_k is then given by

$$\partial_k \lambda_k = \frac{k(h^2 + 2\lambda_k k^2 + \lambda_k \epsilon_B)^2}{\pi A_{t,k}(2k^2 + \epsilon_B)^2(3k^2 + 2m_{t,k}/A_{t,k} - 2\mu_\psi)} \tag{2.55}$$

leading to $\lambda_{k=0} = -h^2/\epsilon_B$ for large values of h. Combining this result with the definition of $\tilde{\lambda}$ in Eq. (2.50) yields Eq. (2.52).

2.3.3.3 The polaron energy within the gradient expansion scheme

Let us briefly discuss the weak non-monotonous behavior of the polaron energy as a function of ϵ_F/ϵ_B mentioned in Section 2.3.3.1. Generally, the polaron energy lies

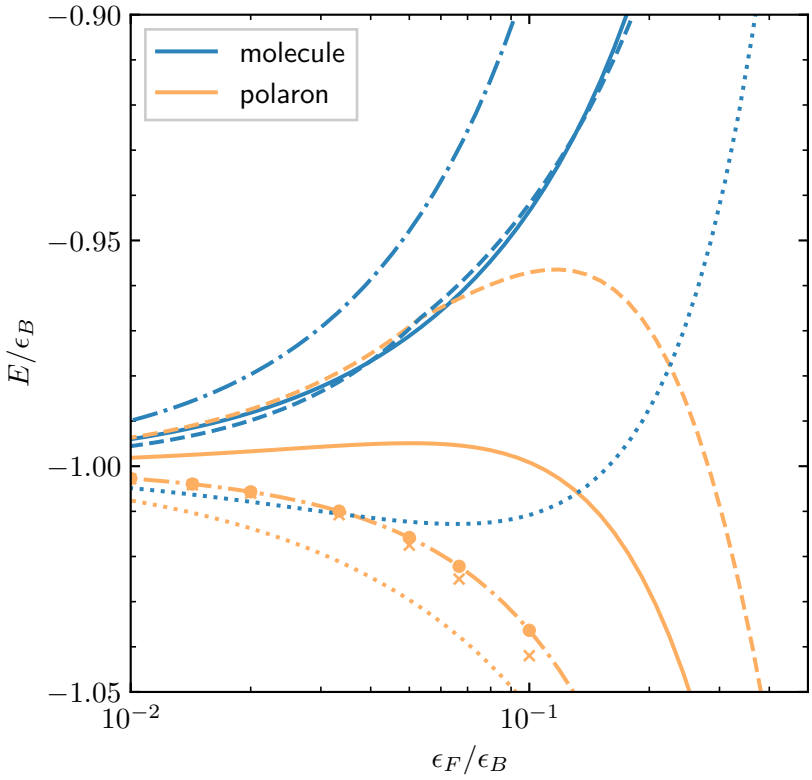

Figure 2.19. Energies of the polaron (orange lines) and the molecule (blue lines) as a function of dimensionless interaction strength using different fRG implementations. The solid lines show energies using $\Gamma_{2,k}$ while the dash-dotted lines show a two-step implementation of $\Gamma_{2,k}$ in which the molecule is renormalized in the first step and the ϕ-boson is renormalized in the second step. The dashed lines show the $\Gamma_{3,k}$ implementation and the dotted lines show a $\Gamma_{3,k}$ implementation in which the flow of h_k is neglected by setting $\partial_k h_k = 0$. The cross markers show the polaron energies resulting from a non-self-consistent T-matrix approximation [172], while the dot markers show the result of this calculation in a gradient expansion.

approximately within a range of $\pm\epsilon_F$ around the value of $-\epsilon_B$. For small values of ϵ_F/ϵ_B it is thus not surprising to see that $E \to -\epsilon_B$. Previous calculations [170–172, 174–176] indicate that for all values of ϵ_F/ϵ_B the value of the polaron energy should lie below $-\epsilon_B$, in disagreement with the results shown in Fig. 2.17. This discrepancy highlights one of the major shortcomings of fRG, namely the dependence on regulators and on the truncation scheme.

To analyze this finding in detail in Fig. 2.19 we show the polaron and the molecule energies using different truncation and regulator schemes. As one can see, the $\Gamma_{2,k}$ truncation (solid line) presented also in Fig. 2.17 results in polaron energies above $-\epsilon_B$. If, however, the same truncation is used and the regulators are changed such that the renormalization group flow consists of two steps, where in the first step only the molecule and in the second step only the minority particle is allowed to flow, this results (dash-dotted) in polaron energies strictly below $-\epsilon_B$. Within this

scheme, however, the resulting molecule energy lies higher than before. Effectively, by treating the molecule and polaron on different footing (i.e. by treating them in different steps of the fRG) we have improved the polaron energy at the cost of a higher-lying molecular energy. Interestingly, this two-step calculation is closely related to the results obtained within the variational approach in Ref. [170] and the ladder resummations performed in Ref. [172] (crosses). If the full frequency- and momentum-resolved T-matrix in these two approaches is replaced by a gradient expansion of the T-matrix, the resulting method is equivalent to the two-step fRG. The results for this modified variational/diagrammatic calculation are shown as dots and coincide with the two-step calculation as expected. A similar equivalence of the FMR scheme is discussed in Section 2.3.5.2.

Within the $\Gamma_{3,k}$ calculation presented in Fig. 2.19 (dashed) and also in Fig. 2.17 the polaron energy lies again above $-\epsilon_B$ for small ϵ_F/ϵ_B. If, however, the flow of h_k is turned off (dotted) the polaron energy lies once again strictly below $-\epsilon_B$. These observations illustrate the dependence of the absolute values of the energy on the regulators and truncation employed. For example, the flow of the Yukawa vertex h_k has a significant impact on the polaron energy, which is likely due to its point-like projection.

Although the relative deviations of these energies are only of the order of a few percent, we do not expect that the used fRG schemes are a reliable method of determining the *absolute* energy of the polaron and the molecule. Most of the variational approaches, however, do not consider the polaron and the molecule on an equal footing and therefore can produce ambiguous results when one considers transitions which depend on relative energy differences between the emergent quasiparticles. We thus believe that, by treating the polaron and the molecule on equal footing within a unified renormalization approach, the fRG scheme captures the qualitative physics correctly and can thus make qualitative predictions about a transition in the quantum many-body system.

2.3.4 Bose-Fermi mixture at finite boson density

We now turn to the mixture regime, where a finite density of bosons interacts with a bath of majority fermions. As discussed in Section 2.3.2.2, within our truncations we can identify two phases: a molecular phase, where all bosons are bound into molecules, and a mixed phase where molecules are hybridized with majority fermions and coexist with a condensate of polarons.

While we can describe the molecular phase directly, we can not fully access the regime in which a condensate of polarons exists since this would require to explicitly include the condensate and thus an effective potential for the bosonic field. However, we can still determine the critical system parameters at which the system becomes unstable towards condensation. Indeed, the associated phase boundary is determined by the vanishing of the scale-dependent boson gap $m_{\phi,k}/A_{\phi,k}$ at the end of the RG flow.

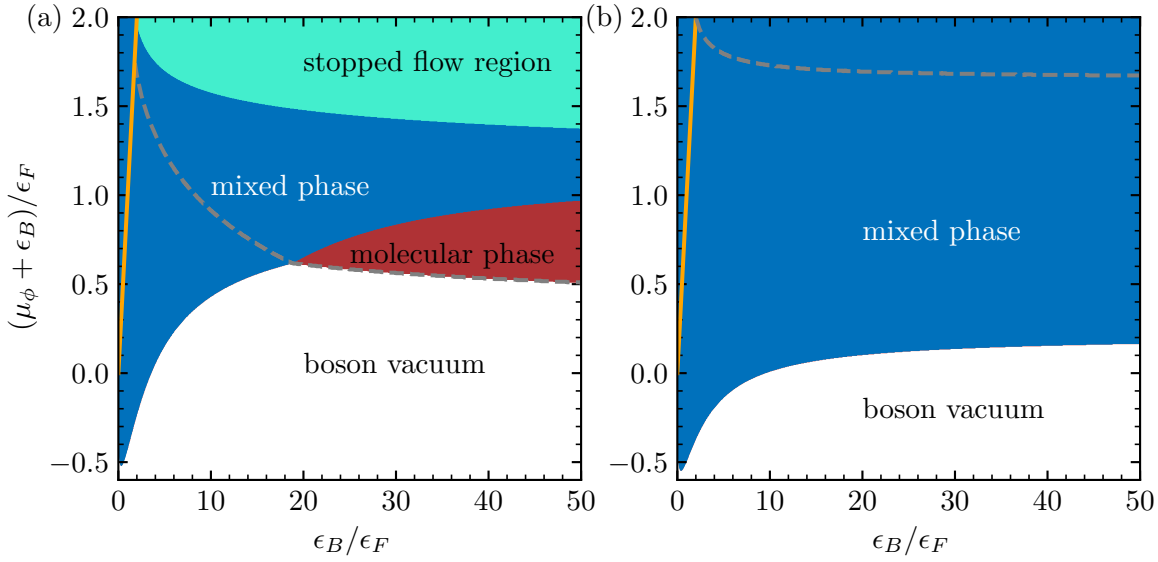

Figure 2.20. Phase diagram of the Bose-Fermi mixture for different ratios of μ_ϕ/ϵ_F and ϵ_B/ϵ_F using $\Gamma_{3,k}$ (a) and $\Gamma_{2,k}$ (b). The white regions indicate the vacuum phase, while the red and blue regions denote the *molecular* and the *mixed* phase. The mint-colored region above the mixed phase denotes the *stopped flow region* in which the flow was stopped at $k > 0$ because the molecular Fermi surface became larger than the majority's ($-2m_{t,k}/A_{t,k} > \epsilon_F$), indicating the breakdown of our approximation. The gray dashed line denotes the boundary above which the molecules form a Fermi surface at the end of the flow, i.e. $m_{t,k=k_{\text{end}}}/A_{t,k=k_{\text{end}}} < 0$. The orange line indicates the path along which $\mu_\phi = 0$. In both truncations the boundary between the vacuum and finite density phases approaches the origin for $\epsilon_B/\epsilon_F \to 0$.

For large values of the boson chemical potential μ_ϕ, the underlying assumption $n_B \ll n_F$ is no longer valid. When this condition breaks down, we thus terminate the fRG flow. While this does not define a phase, we dub this part of the phase diagram the *'stopped flow region'*, further discussed below.

2.3.4.1 Phase diagram as a function of chemical potential

In Fig. 2.20 we present the phase diagram of the Bose-Fermi mixture for both $\Gamma_{2,k}$ and $\Gamma_{3,k}$ [Eqs. (2.26) and (2.30)] at a fixed Fermi energy ϵ_F, as function of ϵ_B and μ_ϕ. In the three-body truncation $\Gamma_{3,k}$ [Fig. 2.20(a)] a molecular phase forms at finite boson density in the interaction regime where the molecule is the ground state of the quantum impurity limit discussed in Section 2.3.3.

In fact, the ground state energy of the quantum impurity limit determines the chemical potential $\mu_\phi = \mu_\phi^c(\epsilon_B, \epsilon_F)$ that separates the vacuum of bosons from the mixed phase or the phase of a finite density of molecules. Along this phase boundary the system undergoes a transition from a polaronic to a molecular ground state.

In the interaction regime $\epsilon_B/\epsilon_F > (\epsilon_B/\epsilon_F)^*$, increasing the boson chemical potential starting from values $\mu_\phi < \mu_\phi^c$ leads to a boson-vacuum-to-molecule transition as

μ_ϕ crosses the critical chemical potential. Directly on the critical line one enters the quantum impurity regime and a single molecule forms [3]. Increasing μ_ϕ beyond μ_ϕ^c one enters the molecular phase where a finite density of bosons, all bound into molecules, exists. In this phase $m_{t,k=0}/A_{t,k=0} < 0$, and the molecules acquire a Fermi surface. Tuning μ_ϕ further to larger values one reaches the phase boundary to the mixed phase. Here, a finite density of molecules coexists with gapless boson particles.

For $\epsilon_B/\epsilon_F < (\epsilon_B/\epsilon_F)^*$ there is no molecular phase and one transitions directly from the boson vacuum to the mixed phase. As the flow is terminated at a finite RG scale k_{end} once the boson becomes gapless $m_{\phi,k=k_{\text{end}}}/A_{\phi,k=k_{\text{end}}} = 0$, at the boundaries to the molecular phase and to the boson vacuum phase the boson turns gapless at the end of the flow at $k_{\text{end}} = 0$. Moving further into the phase from these boundaries the value of k_{end} at which the flow is terminated increases.

When the flow is stopped in the mixed phase, the molecules might have already formed a molecular Fermi level during the course of the RG flow. This is indicated by the dashed gray line in Fig. 2.20. Above this line the molecule has developed a Fermi surface when the flow ends or is terminated at $k = k_{\text{end}}$. Below the line the molecule has remained gapped. As expected, for $\epsilon_B/\epsilon_F > (\epsilon_B/\epsilon_F)^*$ this line parametrizes the boson-vacuum-to-molecule transition. For $\epsilon_B/\epsilon_F < (\epsilon_B/\epsilon_F)^*$ on the other hand, it bisects the mixed phase. These regions then correspond to phases of a single Fermi sea (boson vacuum), two Fermi seas (molecular phase), two Fermi seas with a bosonic condensate (mixed phase above the gray dashed line) and a bosonic condensate with only a single Fermi sea (mixed phase below the gray dashed line) as discussed in Refs. [96, 194].

Increasing the bosonic chemical potential μ_ϕ further within the mixed phase, the bosonic density increases until eventually the molecular Fermi wave vector becomes larger than the fermionic Fermi wave vector ($-2m_{t,k}/A_{t,k} > \epsilon_F$). Within this regime, the bosonic density has become comparable to the fermionic density. This means that it is no longer justified to neglect the renormalization of the fermionic Green's function and to disregard higher-order correlations along with sub-dominant interaction channels. As we expect that in this case our truncation no longer renders an appropriate description of the system, we terminate the flow at finite scale k_{end} once $-2m_{t,k}/A_{t,k} > \epsilon_F$. When this happens *during* the RG flow, a molecular Fermi sea has already formed while the bosons are still gapped $m_{\phi,k}/A_{\phi,k} > 0$. This *'stopped flow region'* (mint in Fig. 2.20) occurs after the bosonic chemical potential has been tuned well into the mixed phase. We therefore expect that in the stopped flow region, close to the boundary to the mixed phase, the system would still be in a mixed phase, if one were to continue the flow.

Within the two-body truncation [see Fig. 2.20(b)] it is unsurprising to see that no molecular phase forms at finite boson density, since already in the single-boson regime this *Ansatz* does not form a molecule in the ground state. Rather, one transitions from the boson vacuum phase directly to the mixed phase as the molecule only becomes

[3] Strictly speaking along the critical line any *finite* particle number can be realized as long as the boson density n_B vanishes in the thermodynamic limit. In a field theory approach the exact particle number considered is then determined by the highest-order vertex function taken into account.

gapless at k_{end} well within the mixed phase (gray dashed line). Within this truncation the stopped flow regime is not realized for the considered range of μ_ϕ and it only sets on at around $(\mu_\phi + \epsilon_B) \approx 2.4\epsilon_F$.

2.3.4.2 Phase diagram as a function of density

In the previous subsubsection results were given as a function of chemical potential. Experimentally it is, however, often simpler to determine the density of particles instead of their chemical potential. Thus, to make direct connection to experiments, it is useful to also consider the phase diagram as a function of particle densities. Since in the effective action formalism employed in this chapter, the chemical potentials are the parameters of the theory, the canonically conjugate densities have to be computed explicitly.

In principle, the fermion and boson densities can be determined directly from the two-point Green's functions. Within the derivative expansion and two-channel model an alternative approach is, however, more convenient. Here one makes use of the fact that the densities are connected to the derivative of the effective potential U evaluated at the equilibrium field configuration σ_{eq} by the standard relation

$$n_{F/B} = -\frac{\partial U(\sigma_{\text{eq}})}{\partial \mu_{\psi/\phi}} \,. \tag{2.56}$$

Here n_B and n_F, respectively, denote the total density of bosons and fermions in the system, including those bound into molecules. The effective potential $U(\sigma_{\text{eq}})$, in turn, is obtained from the derivative-free part of the infrared effective action evaluated at the field expectation values $U(\sigma_{\text{eq}}) = \Gamma_{k=0}[\sigma_{\text{eq}}]/(V/T)$ where for the considered phases $\sigma_{\text{eq}} = (\psi_{\text{eq}}, \phi_{\text{eq}}, t_{\text{eq}}) = 0$.

In the absence of approximations, determining the densities from the effective potential or from the Green's functions are equivalent methods, as follows from the *Luttinger* theorem [96, 195]. Within our fRG scheme we, however, expect it to be computed more accurately using the flow of U than using the flow of G_σ as this approach relies on lower-order vertices.

In the fRG, the effective action is promoted to a flowing effective action that depends on the RG scale k. Accordingly, it is convenient to define corresponding scale-dependent densities $n_{F/B,k}$ and to determine the densities of the systems from their value at the end of the RG flow. The resulting density values are then associated with the corresponding phases. Since there is no polaron-to-molecule transition for $\Gamma_{2,k}$, in the following we only discuss results obtained in the three-body truncation.

The flow equation of the effective potential is obtained by evaluating the Wetterich equation (1.78) at vanishing fields,

$$\partial_k U_k(\sigma_{\text{eq}}) = \sum_{\sigma=\psi,\phi,t} \xi_\sigma \int_P G^c_{\sigma,k}(\mathbf{p},\omega)\partial_k R_{\sigma,k}(\mathbf{p},\omega) \tag{2.57}$$

where $\xi_\phi = 1$ for bosons and $\xi_\sigma = -1$ for fermions (ψ and t). Due to the pole structure of the integrand, Eq. (2.57) can be simplified further: Expanding Eq. (2.57) and using

the explicit form of the sharp regulators in Eqs. (2.36) to (2.39) one obtains that $\partial_k U_k(\sigma_{\mathrm{eq}})$ has the following structure

$$\partial_k U_k(\sigma_{\mathrm{eq}}) \propto \sum_{\sigma=\psi,\phi,t} \left(\xi_\sigma \int_P \Theta_{\sigma,k}(\mathbf{p},\omega)\partial_k \left[\frac{1}{\Theta_{\sigma,k}(\mathbf{p},\omega)} - 1 \right] + \xi_\sigma \int_P [1-\Theta_{\sigma,k}(\mathbf{p},\omega)] G_{\sigma,k}(\mathbf{p},\omega)\partial_k G^{-1}_{\sigma,k}(\mathbf{p},\omega) \right) . \tag{2.58}$$

The integrand in the first term in Eq. (2.58) does not have a pole in the frequency domain as the $\Theta_{\sigma,k}$-functions are frequency-independent. Stemming from the construction of the quantum field theory and the convergence factor of $e^{i\omega 0^+}$, this integral thus evaluates to zero. The second term, in contrast, possesses a pole within $G_{\sigma,k}$ and therefore does not vanish. Note that because the integrand only falls off fast enough due to the convergence factor, these ω contour integrals need to be closed within the upper half of the complex plane. Consequently, the second term in Eq. (2.58) always vanishes for $\sigma = \phi$: In order to yield a finite value it would require the polaron to develop a finite density which we do not allow for within our phase identification scheme.

The flow equation of the effective potential in Eq. (2.57) can thus be simplified to

$$\begin{aligned} \partial_k U_k(\sigma_{\mathrm{eq}}) = &- \int_P [1-\Theta_{\psi,k}(\mathbf{p})]\, G_{\psi,k}(\mathbf{p},\omega)\partial_k G^{-1}_{\psi,k}(\mathbf{p},\omega) \\ &+ \int_P [1-\Theta_{\phi,k}(\mathbf{p})]\, G_{\phi,k}(\mathbf{p},\omega)\partial_k G^{-1}_{\phi,k}(\mathbf{p},\omega) \\ &- \int_P [1-\Theta_{t,k}(\mathbf{p})]\, G_{t,k}(\mathbf{p},\omega)\partial_k G^{-1}_{t,k}(\mathbf{p},\omega) \ , \end{aligned} \tag{2.59}$$

where we have left in the vanishing contribution due to the ϕ propagators for the sake of completeness. Here, the step functions $\Theta_{\sigma,k}(\mathbf{p})$ originate from the sharp regulators in the flow equations [see Eqs. (2.36), (2.38) and (2.39)]. For the bosonic and molecular field they are defined as $\Theta_{t,k}(\mathbf{p}) = \Theta_{\phi,k}(\mathbf{p}) = \Theta(\mathbf{p}^2 - k^2)$, while for the fermionic field $\Theta_{\psi,k}(\mathbf{p})$ is redefined in the following in Eq. (2.60) to cover the fermion density more accurately.

As the scheme described in Section 2.3.2 does not feature a renormalization of the majority propagator it is evident from Eq. (2.59) that, within that approximation, the fermions do not contribute to the flow of the effective potential U_k. Consequently, from the integration of Eq. (2.59) the density of fermions would not be calculated accurately since the depletion of majority carriers, resulting from fermions being bound into molecules, is not taken into account.

In order to take this effect into account, we derive —*separate* from the flow of the Green's functions of the bosons, molecules and the interaction vertices— a flow equation for the propagator of the majority species, that does not feed back into any flow other than that of the effective potential. Since the majority fermions have a finite density already at the start of the RG flow, we regulate the fermions around their flowing Fermi level $\epsilon_{F,k} = \epsilon_F - m_{\psi,k}/A_{\psi,k}$ [187]. Accordingly, the step function in the first line in Eq. (2.59) is given by

$$\Theta_{\psi,k}(\mathbf{p}) = \Theta(|\mathbf{p}^2 - \epsilon_F + m_{\psi,k}/A_{\psi,k}| - k^2) \ . \tag{2.60}$$

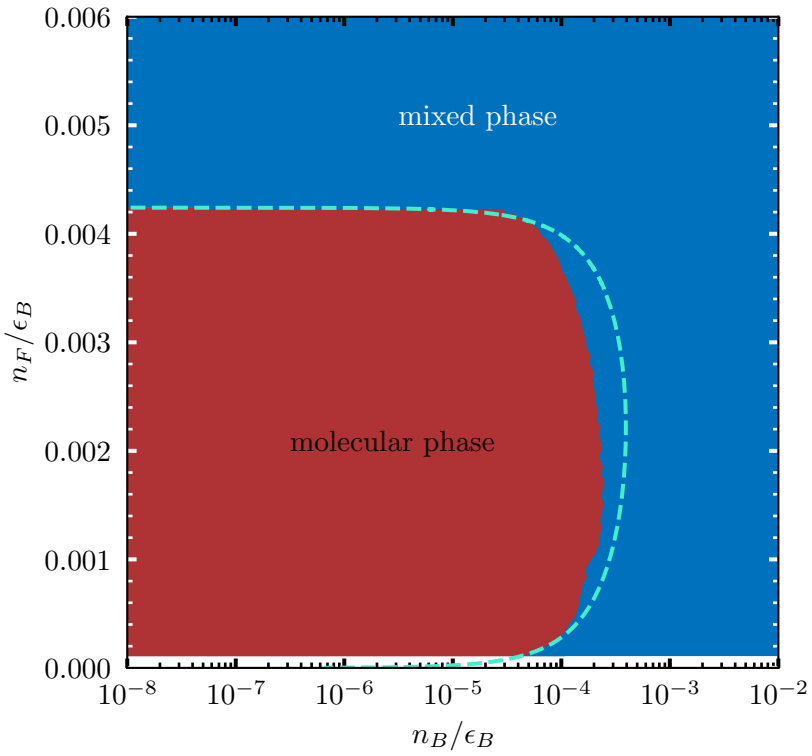

Figure 2.21. Phase diagram of the Bose-Fermi mixture for different boson and fermion densities n_F and n_B at a fixed interaction strength set by ϵ_B. The red region indicates the molecular phase while the blue region indicates the mixed phase. The mint-colored dashed line denotes the mean-field phase boundary extrapolated from the Fermi polaron problem.

To derive the flow equations of $A_{\psi,k}$ and $m_{\psi,k}$, we evaluate the RG flow of the associated vertex function at external frequency and momentum $(\mathbf{p}^2, \omega) = (\epsilon_F, 0)$, i.e., we perform the gradient expansion around the bare Fermi surface of the majority species as detailed in Section 2.3.2.5. This flow is then used to determine the effective potential U, and, in turn, the boson and fermion densities through Eq. (2.56). In order to reproduce the majority carrier density $\epsilon_F/4\pi$ in the UV with regard to Eq. (2.56), the initial condition for the density flow is given by the mean-field result $U_{k=\Lambda}(\sigma_{\text{eq}}) = -\epsilon_F^2/8\pi$.

In Fig. 2.21, we show the resulting phase diagram of the system as a function of the boson and fermion density. It can be regarded as the counterpart of Fig. 2.20(a), expressed in different variables. Specifically, to obtain Fig. 2.21, for the combinations of boson chemical potential μ_ϕ and interaction strength ϵ_B/ϵ_F that lie in the molecular phase we computed the corresponding values of n_B/ϵ_B and n_F/ϵ_B. For combinations that lie inside the mixed phase or the stopped flow region we can not compute the boson and fermion density as the flow is terminated at finite k_{end}. In Fig. 2.21 we

thus identify density combinations outside the molecular phase as being part of the mixed phase [4].

In Fig. 2.21, the single-boson limit discussed in Section 2.3.3 corresponds to the y-axis at $n_B/\epsilon_B = 0$, and the polaron-to-molecule phase transition occurs at $n_F/\epsilon_B = (\epsilon_F/\epsilon_B)^*/4\pi = 0.00424$. As the boson density is increased, the mixed phase becomes favorable, i.e., the *maximal* density of fermions for which all bosons are bound into molecules decreases. We find that there is also a *minimal* fermion density required to enter the molecular phase. Below that critical value one again enters the mixed regime.

2.3.4.3 Mean-field model

Remarkably, a simple mean-field-inspired argument can provide an approximate phase diagram of the model: In the single-boson limit, the polaron is a gapped excitation in the molecular regime. It has a gap $\Delta E = E_{\text{pol}} - E_{\text{mol}}$ which is a function of ϵ_F/ϵ_B, or equivalently n_F/ϵ_B (equal to $\epsilon_F/4\pi\epsilon_B$ along the y-axis in Fig. 2.21). This gap was determined numerically in Section 2.3.3 where we found,

$$\begin{aligned} &\Delta E((\epsilon_F/\epsilon_B)^*) = 0, \\ &\Delta E((\epsilon_F/\epsilon_B) \to 0) \approx 0.41\epsilon_F, \end{aligned} \tag{2.61}$$

reflecting that the energy gap vanishes at the polaron-to-molecule transition and attains a value proportional to ϵ_F in the strong-binding, low-density limit.

In our mean-field model of the molecular phase, the interactions are taken into account by considering the effective Hamiltonian

$$H^{MF} = \sum_{\mathbf{k}} \varepsilon_{\mathbf{k}} \psi^\dagger_{\mathbf{k}} \psi_{\mathbf{k}} + \frac{\varepsilon_{\mathbf{k}}}{2} t^\dagger_{\mathbf{k}} t_{\mathbf{k}} + (\varepsilon_{\mathbf{k}} + \Delta E(\epsilon_F/\epsilon_B)) \phi^\dagger_{\mathbf{k}} \phi_{\mathbf{k}} \tag{2.62}$$

where $\varepsilon_{\mathbf{k}} = \mathbf{k}^2/2m$ and the additional factor of $1/2$ in front of $t^\dagger_{\mathbf{k}} t_{\mathbf{k}}$ stems from the molecular mass of $2m$. Even though H^{MF} is quadratic in the fields, this effective model goes beyond naive mean-field as ΔE incorporates the non-trivial solution of the single-impurity polaron problem obtained through our fRG scheme in Section 2.3.3. The polaronic, mixed phase appears when it is energetically unfavorable to bind into molecules, i.e. when the Fermi energy $\epsilon_{F,t}$ of the molecules is larger than the gap ΔE. When this condition is reached the polarons start to form a condensate, as described previously.

For a molecular Fermi energy below the gap ΔE, the ground state of the mean-field model (2.62) is given by separate Fermi seas of densities $n_\psi = \epsilon_F/4\pi$ and $n_t = \epsilon_{F,t}/2\pi$ for the fermionic and molecular sectors, respectively. Hence, in the molecular phase, the *total* bosonic and fermionic densities are given by $n_B = n_\phi + n_t = n_t$ and $n_F = n_\psi + n_t = n_t + \epsilon_F/4\pi$. The mean-field transition line below which the molecular

[4] Fig. 2.21 only shows density ratios of the mixed phase in vicinity of the molecular phase. Since in Fig. 2.20(a) the stopped flow region does not border the molecular phase directly, we thus do not expect the stopped flow region to appear close to the molecular phase in Fig. 2.21.

state is favored (parametrized by $\epsilon_{F,t} = \Delta E$) is thus parametrized by

$$\frac{n_B}{\epsilon_B} = \frac{\Delta E(\epsilon_F/\epsilon_B)}{2\pi\epsilon_B} , \tag{2.63}$$

$$\frac{n_F}{\epsilon_B} = \frac{\epsilon_F}{4\pi\epsilon_B} + \frac{\Delta E(\epsilon_F/\epsilon_B)}{2\pi\epsilon_B} . \tag{2.64}$$

This mean-field phase boundary is shown as a dashed line in Fig. 2.21. While the mean-field picture is over-simplified and does not correctly capture the quantitative renormalization effects beyond the vacuum-to-molecule transition, it correctly captures the qualitative nature of the structure of the phase diagram. A similar behavior was observed in Section 2.2, where the many-body phase showed physical properties similar to a mean-field model of the single-impurity Fermi polaron. The phase boundary, by construction, reaches the y-axis at the polaron-to-molecule transition and approaches the origin at an angle of about $n_F/n_B \approx 2.22$ which directly follows from the behavior of the polaron gap $\Delta E((\epsilon_F/\epsilon_B) \to 0) \approx 0.41\epsilon_F$.

2.3.5 Quasiparticle properties of polarons and molecules in the quantum impurity limit from a frequency- and momentum-resolved scheme (FMR)

The calculations presented in Sections 2.3.3 and 2.3.4 only yield information about ground state properties of the system. In order to extract spectral information such as dispersion relations, particle lifetimes, effective masses or higher-lying excited states, however, the spectral functions need to be computed.

The spectral functions are obtained from the Green's functions $G_{\psi,\phi,t}$ by analytic continuation of the Matsubara frequencies $i\omega \to \Omega + i0^+$ which yields the retarded Green's functions $G^R_{\psi,\phi,t}(\mathbf{p}, \Omega)$. From this, the momentum- and frequency-resolved spectral functions are obtained as

$$\mathcal{A}_{\psi,\phi,t}(\mathbf{p}, \Omega) = \mathrm{Im}\,\frac{1}{\pi} G^R_{\psi,\phi,t}(\mathbf{p}, \Omega) . \tag{2.65}$$

Two difficulties arise when determining the spectral function within the fRG. First, an analytic continuation has to be performed, either at the level of the flow equations [196–198], see also Chapter 5, or the final output of the RG flow in the infrared [137]. Second, in order to capture non-trivial spectral functions one needs the full momentum- and frequency-dependence of the propagator, which the gradient expansion employed in Sections 2.3.3 and 2.3.4 does not provide. A solution to the latter difficulty can be found, e.g., by the direct implementation of fully frequency- and momentum-resolved Green's functions [137] or in the BMW scheme [74, 199], which also yields a full momentum- and imaginary frequency-dependence of the propagators. Both these approaches, however, do not resolve the analytic continuation issue. For this reason, we implement here a method developed in nuclear physics [198, 200–202] which was recently applied to the polaron problem in three dimensions [184]. In the following we shall refer to this method as the frequency- and momentum-resolved scheme (FMR).

In FMR, the flow equations [Eq. (1.78) and Eqs. (2.42) to (2.46)] are analytically continued to real frequencies. In order to achieve that, rather than projecting the flow equation onto the gradient expansion parameters, we retain the full momentum- and frequency-dependence of the single-particle Green's functions on the lhs. of the flow equations, while we keep the gradient expansion for the two-body [Eq. (2.26)] and three-body truncation [Eq. (2.30)] on the rhs. of the equations. This enables us to perform the loop integration over imaginary frequencies analytically. In turn, this allows us to perform the analytic continuation to real frequency to obtain direct access to the retarded Green's functions. From that we evaluate the single-particle spectral function using Eq. (2.65). We remark that, when applying a non-self-consistent implementation of FMR —in which only bare quantities appear on the rhs. of the flow equations— to the spectral function of the molecule, the differential equation system yields the same results as a corresponding T-matrix resummation [172] (see Section 2.3.5.2).

2.3.5.1 Frequency- and momentum-resolved flow equations

In order to compute the frequency- and momentum-resolved spectral functions within the FMR scheme, for a given value of ϵ_F, μ_ϕ and ϵ_B in a first step the flow of the expansion parameters is computed as detailed in Section 2.3.2.5. In a second step the solutions of the flow equations for the different gradient expansion parameters are plugged into the rhs. of the flow equations given in Eqs. (2.42) to (2.46). This time, however, the flow equations are considered for arbitrary external momentum and frequency. Next, the Matsubara integration is performed as usual and the complex frequency ω of $P = (\mathbf{p}, \omega)$ is continued to the real frequency axis $i\omega \to \Omega + i0^+$.

Let us demonstrate this process in detail for the flow of $G^R_{\phi,k}$. According to Eq. (2.42), for a Matsubara frequency ω and a momentum $\mathbf{p}$ this flow is given by

$$\begin{aligned}\partial_k G^{-1}_{\phi,k}(\mathbf{p},\omega) &= h_k^2 \tilde{\partial}_k \int \frac{d\nu}{2\pi}\frac{d\mathbf{q}}{(2\pi)^2} G^c_{t,k}(\mathbf{p}+\mathbf{q},\omega+\nu) G^c_{\psi,k}(\mathbf{q},\nu) \\ &= \frac{h_k^2\tilde{\partial}_k}{(2\pi)^3}\int d\nu d\mathbf{q} \frac{\Theta(|\mathbf{p}+\mathbf{q}|-k)}{A_{t,k}[-i\omega - i\nu + \frac{(\mathbf{p}+\mathbf{q})^2}{2}] + m_{t,k}} \frac{\Theta(|\mathbf{q}^2-\epsilon_F|-k^2)}{(-i\nu+\mathbf{q}^2-\epsilon_F)}\end{aligned} \tag{2.66}$$

such that after performing a Matsubara integration over ν one obtains

$$= -\frac{h_k^2\tilde{\partial}_k}{(2\pi)^2}\int d\mathbf{q} \frac{\Theta(|\mathbf{p}+\mathbf{q}|-k)\Theta(\epsilon_F-\mathbf{q}^2-k^2)}{A_{t,k}[-i\omega + \frac{(\mathbf{p}+\mathbf{q})^2}{2} - \mathbf{q}^2 + \epsilon_F] + m_{t,k}}. \tag{2.67}$$

Since for $\omega > 0$ we have that $G^{-1}_{\phi,k}(\mathbf{p},\omega) = G^{R,-1}_{\phi,k}(\mathbf{p}, i\omega)$, using the identity theorem from complex analysis we can now perform the analytical continuation of the flow equation $i\omega \to \Omega + i0^+$ to obtain

$$\partial_k \left(G^R_{\phi,k}\right)^{-1}(\mathbf{p},\Omega) = -\frac{h_k^2\tilde{\partial}_k}{(2\pi)^2}\int d\mathbf{q} \frac{\Theta(|\mathbf{p}+\mathbf{q}|-k)\Theta(\epsilon_F-\mathbf{q}^2-k^2)}{A_{t,k}[-\Omega - i0^+\frac{(\mathbf{p}+\mathbf{q})^2}{2} - \mathbf{q}^2 + \epsilon_F] + m_{t,k}}, \tag{2.68}$$

where we have suppressed the $i0^+$ in the argument of the retarded Green's function as in this section we will only evaluate retarded Green's functions infinitesimally above the real axis. Performing similar steps for the flow equations of $G^R_{t,k}$ the retarded Green's functions and carrying out the scale derivative $\tilde{\partial}_k$ one obtains the following flow equations

$$\partial_k \left(G^R_{\phi,k}\right)^{-1}(\mathbf{p},\Omega) = \frac{h_k^2 k}{A_{t,k}} \int \frac{d\theta}{(2\pi)^2} \left[\frac{\Theta\left(\epsilon_F - \mathbf{p}^2 - 2|\mathbf{p}|k\cos(\theta) - 2k^2\right)}{-\frac{k^2}{2} - \mathbf{p}^2 + \epsilon_F - 2|\mathbf{p}|k\cos(\theta) - \Omega + \frac{m_{t,k}}{A_{t,k}} - i0^+} \right.$$
$$\left. + \frac{\Theta\left(\mathbf{p}^2 + \epsilon_F + 2|\mathbf{p}|\sqrt{\epsilon_F - k^2}\cos(\theta) - 2k^2\right)\Theta\left(\epsilon_F - k^2\right)}{\frac{k^2}{2} + \frac{\mathbf{p}^2}{2} + \frac{\epsilon_F}{2} + |\mathbf{p}|\sqrt{\epsilon_F - k^2}\cos(\theta) - \Omega + \frac{m_{t,k}}{A_{t,k}} - i0^+} \right] \tag{2.69}$$

$$\partial_k \left(G^R_{t,k}\right)^{-1}(\mathbf{p},\Omega) = \frac{h_k^2 k}{A_{\phi,k}} \int \frac{d\theta}{(2\pi)^2} \left[\frac{\Theta(\mathbf{p}^2 + 2|\mathbf{p}|k\cos(\theta) - \epsilon_F)}{2k^2 + \mathbf{p}^2 - \epsilon_F - \Omega + 2|\mathbf{p}|k\cos(\theta) + \frac{m_{\phi,k}}{A_{\phi,k}} - i0^+} \right.$$
$$\left. + \frac{\Theta(\mathbf{p}^2 + \epsilon_F + 2|\mathbf{p}|\sqrt{\epsilon_F + k^2}\cos(\theta))}{2k^2 + \mathbf{p}^2 + \epsilon_F + 2|\mathbf{p}|\sqrt{\epsilon_F + k^2}\cos(\theta) - \Omega + \frac{m_{\phi,k}}{A_{\phi,k}} - i0^+} \right]$$
$$- \frac{k}{2\pi}\lambda_k \Theta(\epsilon_F - k^2). \tag{2.70}$$

2.3.5.2 Equivalence to a non-self-consistent T-matrix resummation

Let us show the close correspondence between the FMR scheme and diagrammatic ladder approximations, shown in Section 1.7. More specifically, let us show that a non-self-consistent implementation of the FMR method exactly corresponds to the result obtained for the molecule in a non-self-consistent T-matrix resummation as presented in Ref. [172].

Using only bare quantities on the rhs. of the flow equation (i.e. $\lambda_k = 0, h_k = h, A_{\phi,k} = 1, m_{\phi,k} = -\mu_\phi$) and performing the frequency integration in the quantum impurity limit, the flow of the retarded inverse molecule propagator reads

$$\partial_k \left(G^R_{t,k}\right)^{-1}(\mathbf{p},\Omega) = -h^2 \partial_k \int \frac{d\mathbf{q}}{(2\pi)^2} \frac{\Theta((\mathbf{p}-\mathbf{q})^2 - k^2)\Theta(\mathbf{q}^2 - \epsilon_F - k^2)}{\mathbf{q}^2 - \epsilon_F + (\mathbf{p}-\mathbf{q})^2 - \mu_\phi - \Omega - i0^+} \,. \tag{2.71}$$

Where we used that since we only use bare quantities on the rhs., we have $\tilde{\partial}_k = \partial_k$. Thus we can perform the k-integration analytically to obtain

$$\left(G^R_{t,k=0}\right)^{-1}(\mathbf{p},\Omega) = \left(G^R_{t,k=\Lambda}\right)^{-1}(\mathbf{p},\Omega)$$
$$- h^2 \int_{\mathbf{q}^2 > \epsilon_F} \frac{d\mathbf{q}}{(2\pi)^2} \frac{1}{\mathbf{q}^2 - \epsilon_F + (\mathbf{p}-\mathbf{q})^2 - \mu_\phi - \Omega - i0^+}$$
$$+ h^2 \int \frac{d\mathbf{q}}{(2\pi)^2} \frac{\Theta((\mathbf{p}-\mathbf{q})^2 - \Lambda^2)\Theta(\mathbf{q}^2 - \epsilon_F - \Lambda^2)}{\mathbf{q}^2 - \epsilon_F + (\mathbf{p}-\mathbf{q})^2 - \mu_\phi - \Omega - i0^+} \tag{2.72}$$

and using that for $h \to \infty$ we have (see Section 1.6)

$$G^{-1}_{t,k=\Lambda}(\mathbf{p},\omega) = h^2 \int_{\mathbf{q}^2 < \Lambda^2} \frac{d\mathbf{q}}{(2\pi)^2} \frac{1}{\epsilon_B + 2\mathbf{q}^2} \tag{2.73}$$

we obtain

$$\begin{aligned}\left(G^R_{t,k=0}\right)^{-1}(\mathbf{p},\Omega) = &- h^2\int_{\mathbf{q}^2>\epsilon_F}\frac{d\mathbf{q}}{(2\pi)^2}\frac{1}{\mathbf{q}^2-\epsilon_F+(\mathbf{p}-\mathbf{q})^2-\mu_\phi-\Omega-i0^+}\\ &+ h^2\int\frac{d\mathbf{q}}{(2\pi)^2}\left(\frac{\Theta((\mathbf{p}-\mathbf{q})^2-\Lambda^2)\Theta(\mathbf{q}^2-\epsilon_F-\Lambda^2)}{\mathbf{q}^2-\epsilon_F+(\mathbf{p}-\mathbf{q})^2-\mu_\phi-\Omega-i0^+}-\frac{\Theta(q-\Lambda)}{\epsilon_B+2\mathbf{q}^2}\right)\\ &+ h^2\int\frac{d\mathbf{q}}{(2\pi)^2}\frac{1}{\epsilon_B+2\mathbf{q}^2}\ .\end{aligned} \tag{2.74}$$

Finally, taking the limit $\Lambda\to\infty$ this can be evaluated to yield

$$\begin{aligned}\left(G^R_{t,k=0}\right)^{-1}(\mathbf{p},\Omega)\overset{(\Lambda\to\infty)}{=} &- h^2\left(\frac{i\pi+\log\left(\frac{\epsilon_B}{\Omega+\epsilon_F+\mu_\phi-\mathbf{p}^2/2+i0^+}\right)}{8\pi}\right.\\ &\left.-\int_{\mathbf{q}^2<\epsilon_F}\frac{d\mathbf{q}}{(2\pi)^2}\frac{1}{\mathbf{q}^2-\epsilon_F+(\mathbf{p}-\mathbf{q})^2-\mu_\phi-\Omega-i0^+}\right)\ ,\end{aligned} \tag{2.75}$$

reproducing the molecular results presented in Ref. [172]. Furthermore, similar analysis shows that performing a modified non-self-consistent two-step fRG of the FMR scheme also reproduces the polaron results presented in Ref. [172]. In such a two-step approach the molecular propagator is renormalized in the first step as described in Eq. (2.71), and in the second step the minority propagator is renormalized as prescribed by Eq. (2.42). In this second step, on the rhs. the coupling constants along with the majority propagator appear in their bare form and the molecular propagator with its full frequency- and momentum-dependence obtained in the first RG step is used instead of a gradient expansion. The polaron energy resulting from this calculation is shown as crosses in Fig. 2.19. It is worth noting, however, that as a starting point for the second step one may also perform a gradient expansion of the molecular propagator of the form

$$\left(G^{R,2^{\text{nd}}}_t\right)^{-1}(\mathbf{p},\Omega)=\left(G^R_{t,k=0}\right)^{-1}(0,0)-\left(-\Omega-i0^++\frac{\mathbf{p}^2}{2}\right)\left[\partial_\Omega\left(G^R_{t,k=0}\right)^{-1}(0,\Omega)\right]_{\Omega=0} \tag{2.76}$$

and still obtain similar results (dash-dotted lines and dot markers in Fig. 2.19). This then directly corresponds to a version of the FMR scheme used to obtain spectral functions in which the renormalization of the molecule and the minority is divided into two consecutive steps while retaining the gradient expansion on the rhs. of the flow equations.

2.3.5.3 Results

Polaron spectral function The polaron spectral function obtained using FMR is shown for different interaction strengths in Fig. 2.22. Subfigures (a), (c) and (d) are obtained in the three-body truncation $\Gamma_{3,k}$. Subfigure (b) shows the result from the two-body truncation $\Gamma_{2,k}$ in order to highlight the effect of the inclusion of irreducible three-body correlations.

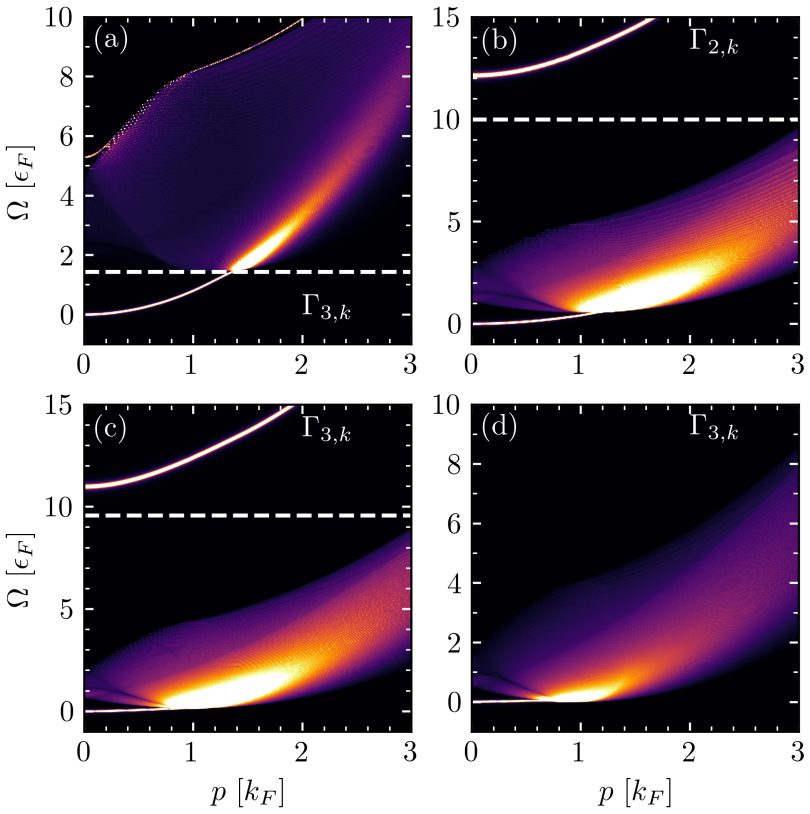

Figure 2.22. Polaron spectral function $\mathcal{A}_\phi$ for different dimensionless interaction strengths (ϵ_B/ϵ_F): (a) 1, (b) 10, (c) 10, (d) 20. In (a), (c) and (d) $\Gamma_{3,k}$ is used while in (b) $\Gamma_{2,k}$ is used to highlight the effect of the renormalization of the three-body sector. Dashed horizontal lines denote the Bose-Fermion scattering threshold at $\Omega = -\mu_\phi$. In (a) the range of the color spectrum is $[0, 0.5]$, while in (b), (c), (d) it is $[0, 0.05]$.

The polaron spectral functions show the same qualitative behavior as the corresponding spectra in 3D [137, 184]. Two quasiparticle peaks —the attractive and the repulsive polaron— can be discerned, and a molecule-hole continuum in between these dominant excitations is visible. The attractive polaron is the ground state in Fig. 2.22 (a), (b), (c), and thus is a gapless excitation. In contrast, in Fig. 2.22(d), the ground-state is a molecule, and thus a small gap at $p = 0$ can be seen. Generally, at finite but small momenta the attractive polaron is a well-defined quasiparticle with an interaction-dependent effective mass which, along with the effective masses of the repulsive polaron and the molecule, is shown in Table 2.3. For larger momenta, the attractive polaron peak eventually merges with the molecule-hole continuum, such that it is no longer a well-defined quasiparticle.

The repulsive polaron appears at energies above the scattering threshold (indicated by the dashed horizontal lines in Fig. 2.22) as a narrow peak, indicating a long quasiparticle life-time for the interaction strengths shown. Consistent with Ref. [172] we find that as ϵ_B/ϵ_F decreases, the repulsive polaron gradually disappears. Moreover, while at small interaction strength (Fig. 2.22(a)) the repulsive polaron eventually

	att. Pol.		rep. Pol.		Mol.	
(ϵ_B/ϵ_F)	$\Gamma_{3,k}$	$\Gamma_{2,k}$	$\Gamma_{3,k}$	$\Gamma_{2,k}$	$\Gamma_{3,k}$	$\Gamma_{2,k}$
1	0.62	0.6	0.05	0.056	$-.11$	$-.09$
10	2.29	1.2	0.3	0.42	≥ 6	$-.69$
20	≈ 5	1.42	0.32	0.46	1.84	-1.04

Table 2.3. Effective masses of the attractive and repulsive polaron as well as the molecule obtained from quadratic fits to the dispersion relation at $p = 0$, both in the three-body and the two-body truncation.

merges with the molecule-hole continuum at finite momentum, at larger interaction strength the repulsive polaron peak remains distinct from the molecule-hole continuum at any momentum and thus keeps a long life-time at high momenta.

As evident from the comparison of Fig. 2.22(b) and (c), the inclusion of the irreducible three-body correlations moves the molecule-hole continuum to lower energies. This has the effect that the dispersion relation of the attractive polaron becomes flatter, increasing the polaron effective mass compared to the two-body truncation (see Table 2.3). Furthermore, its quasiparticle peak joins the continuum at lower momenta. In Table 2.4 the energy of the repulsive polaron is shown relative to the ground state energy. For the repulsive polaron the inclusion of three-body correlations has the effect of slightly altering its effective mass and of lowering its energy relative to the scattering threshold. For a fermionic impurity this indicates a reduced tendency towards itinerant Stoner ferromagnetism [58].

Molecular spectral function In Fig. 2.23, the molecular spectral function is shown for different interaction strengths ϵ_B/ϵ_F. Here the subfigures (a), (c) and (e) in the left column are obtained in the three-body truncation while (b), (d) and (f) in the right column result from the two-body truncation. It can be seen that a general feature of this spectral function is spectral weight that appears above a parabola centered around $p = k_F$ and that is defined by the frequency $\Omega_p = (p - k_F)^2 + m_{\phi,k=0}/A_{\phi,k=0}$ as will be derived towards the end of this subsection. The quasiparticle peak of the molecule follows a distorted dispersion relation which, in the strong-binding limit, tends to a free-molecule dispersion relation. Dependent on the interaction strength, at low momenta the molecular quasiparticle peak lies outside of the particle-particle continuum and joins the continuum at finite momenta just to leave it again at higher momenta. More specifically, at low ϵ_B/ϵ_F, the quasiparticle peak joins the continuum at a low momentum, which increases with interaction strength ϵ_B/ϵ_F. Likewise, the momentum at which the peak leaves the continuum again increases with ϵ_B/ϵ_F as well.

Similar to a non-self-consistent T-matrix resummation, in our approach the molecular quasiparticle peak has a vanishing width when it is not embedded in the continuum. This can be seen analytically by inspecting the flow equation of the two-point function G_t^R which we will analyze later on in this section. Apart from the

(ϵ_B/ϵ_F)	rep Pol. $\Gamma_{2,k}$	rep. Pol. $\Gamma_{3,k}$
1	$E_{\mathrm{pol}} + 5.67\epsilon_F$	$E_{\mathrm{pol}} + 5.29\epsilon_F$
10	$E_{\mathrm{pol}} + 12.15\epsilon_F$	$E_{\mathrm{pol}} + 10.99\epsilon_F$
20	$E_{\mathrm{pol}} + 21.92\epsilon_F$	$E_{\mathrm{mol}} + 20.52\epsilon_F$

Table 2.4. Energy of the repulsive polaron at different interaction strengths obtained in the two-body and three-body truncation. The energies are given with respect to the respective ground state energies, E_{pol} and E_{mol}.

structure originating from the parabola-shaped particle-particle continuum and the quasiparticle peak, further structure exists within the parabola that originates from contributions in the RG flow where the Feynman diagrams are evaluated close to their poles (see the discussion in the next sub-subsection).

The minimal energy of the parabola Ω_p is equal to the renormalized energy gap of the polaron, indicating a close relationship between the polaron at $p = 0$ and the molecule at $p = k_F$, supporting the argument that both of these states overlap with the *actual* groundstate of the system and possibly with each other [167]. This finding can also be understood conceptually in a mean-field picture where a bosonic minority particle at $p = 0$ along with a majority fermions at the Fermi surface can be interpreted as either a polaron at $p = 0$ or a molecule at $p = k_F$ (previously noted by Cui [203]). Note that, because the particle-particle continuum in the molecular spectrum is shifted due to the renormalization of the boson gap, this effect can not be captured in a non-self-consistent approximation such as employed in Ref. [172]. In such an approximation spectral peaks distinct from the continuum are present, that in our implementation are a part of the continuum.

Within the spectral functions obtained using $\Gamma_{2,k}$, the quasiparticle peak at $p = 0$ —located at approximately $m_{t,k=0}/A_{t,k=0}$— is always at a finite energy whereas using $\Gamma_{3,k}$ it is moved closer to $\Omega = 0$ and eventually attains $\Omega = 0$ past the polaron-to-molecule transition. At the same time, the minimum of the parabola, given by $m_{\phi,k=0}/A_{\phi,k=0}$, detaches from $\Omega = 0$ as the polaron is no longer the ground state. Hence using $\Gamma_{3,k}$ the effective mass (see Table 2.3) of the molecule, which is negative at small ϵ_B/ϵ_F, diverges with increasing ϵ_B/ϵ_F and eventually becomes positive at an interaction strength before the polaron-to-molecule transition. Beyond the transition the molecule is gapless at $p = 0$ and its effective mass is positive. Using $\Gamma_{2,k}$, increasing ϵ_B/ϵ_F makes the molecule dispersion flatter leading to an increasingly negative effective mass.

Analytical structure of the FMR flow equations In the following, let us analyze the analytical structure of the flow of the retarded inverse Green's function of the molecule and how it is reflected in the spectral functions shown in Fig. 2.23. A similar analysis can be performed on the retarded inverse Green's function of the polaron as well.

Within the FMR scheme of analytic continuation, the retarded self-energy can only pick up a non-vanishing imaginary part in the limit of $i0^+ \to 0$ if during the flow

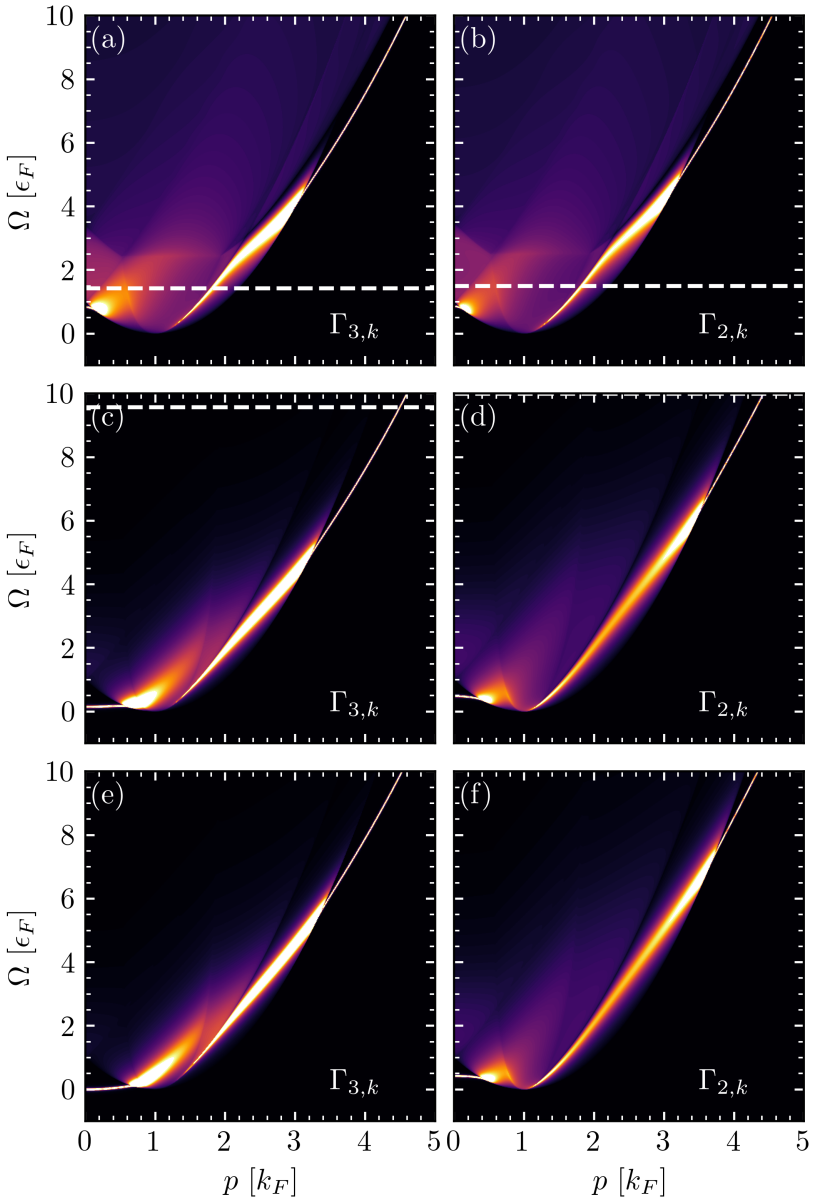

Figure 2.23. Molecular spectral function $\mathcal{A}_t$ for different dimensionless interaction strengths ϵ_B/ϵ_F: (a), (b), 1, (c), (d) 10, (e), (f) 20. In (a), (c) and (e) $\Gamma_{3,k}$ is used while in (b), (d) and (f) $\Gamma_{2,k}$ is used to highlight the effect of the renormalization of the three-body sector. Dashed horizontal lines denote the Bose-Fermion scattering threshold given by $\Omega = -\mu_\phi$. The range of the color spectrum is (a,b) $[0, 5 \times 10^{-6}]$, (c,d) $[0, 5 \times 10^{-5}]$ (e,f) $[0, 10^{-4}]$ for $h = 2 \times 10^3 k_F$.

one integrates over a pole caused by $i\omega \to \Omega$. In that case we have encountered a pole in the flow that is only avoided by the use of a retarded frequency and the self-energy picks up an imaginary part that is non-vanishing for all $i0^+$.

Contributions to the spectral function defined in Eq. (2.65) can have two different origins. Either the Green's function picks up an imaginary part in the course of the flow as described above, or the inverse Green's function tends to $i0^+$ resulting in a

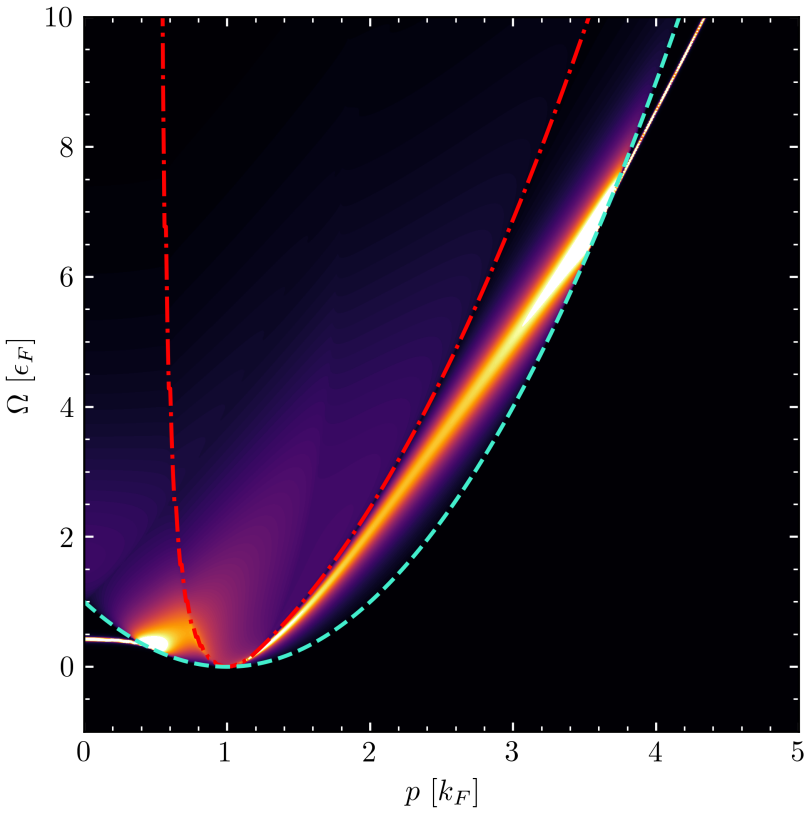

Figure 2.24. Molecular spectral function at $\epsilon_B/\epsilon_F = 20$ within $\Gamma_{2,k}$. The minimal frequencies $\Omega_{\mathrm{min},1} = \min\left[\Omega^{<}_{\mathrm{min},1}, \Omega^{>}_{\mathrm{min},1}\right]$ and $\Omega_{\mathrm{min},2}$ are shown in red (dash-dotted) and mint-color (dashed), respectively.

sharp excitation feature in the spectral function. In the former case the corresponding states are part of a particle-particle continuum of states with a finite lifetime, whereas in the latter case the corresponding excitations have an infinite lifetime.

Inspecting the first term of Eq. (2.70), one can see that it causes the self-energy to develop an imaginary part if during the flow

$$\Omega = 2k^2 + \mathbf{p}^2 - \epsilon_F + 2|\mathbf{p}|k\cos(\theta) + \frac{m_{\phi,k}}{A_{\phi,k}} \tag{2.77}$$

while $\mathbf{p}^2 + 2|\mathbf{p}|k\cos(\theta) - \epsilon_F > 0$. For $\mathbf{p}^2 < \epsilon_F$ the minimal frequency for which this can occur is given by

$$\Omega^{<}_{\mathrm{min},1} = \left[\frac{m_{\phi,k}}{A_{\phi,k}} + 2k^2\right]_{k=\frac{\epsilon_F-\mathbf{p}^2}{2|\mathbf{p}|}} , \tag{2.78}$$

where we made use of the fact that $m_{\phi,k}/A_{\phi,k}$ decreases monotonically during the flow. As a result the smallest value of k needs to be found for which $\mathbf{p}^2+2|\mathbf{p}|k\cos(\theta)-\epsilon_F > 0$ can barely be fulfilled. In turn, for $\mathbf{p}^2 > \epsilon_F$ this frequency is given by

$$\Omega^{>}_{\mathrm{min},1} = \min_{k,0\leq k\leq\frac{\mathbf{p}^2-\epsilon_F}{2|\mathbf{p}|}} \mathbf{p}^2 - 2|\mathbf{p}|k - \epsilon_F + 2k^2 + \frac{m_{\phi,k}}{A_{\phi,k}} . \tag{2.79}$$

Analogously, the minimal frequency for which the second term of Eq. (2.70) leads to an imaginary part is given by

$$\Omega_{\mathrm{min},2} = \min_{\substack{k,\ k>0,\\ k\leq \frac{|\epsilon_F-\mathbf{p}^2|}{2|\mathbf{p}|}}} k^2 + \left(|\mathbf{p}| - \sqrt{\epsilon_F + k^2}\right)^2 + \frac{m_{\phi,k}}{A_{\phi,k}} \ . \tag{2.80}$$

Given that this we find that this is solved by

$$\Omega_{\mathrm{min},2} = \left(|\mathbf{p}| - \sqrt{\epsilon_F}\right)^2 + \left[\frac{m_{\phi,k}}{A_{\phi,k}}\right]_{k=0} \tag{2.81}$$

for the interaction strengths studied here.

In Fig. 2.24, the spectral function from Fig. 2.23(f) is shown along with the minimal frequencies $\Omega_{\mathrm{min},1}$ and $\Omega_{\mathrm{min},2}$. As it can be seen, these frequencies determine the onset of the particle-particle continua. Furthermore, as the molecule peak at low and high momenta lies outside the boundaries of the continua, the corresponding excitations possess an infinite lifetime within this renormalization scheme.

2.3.6 Conclusion on strongly coupled two-dimensional Bose-Fermi mixtures

In this section we investigated the phase diagram of strongly-coupled Bose-Fermi mixtures in two dimensions. In order to make progress in the exploration of this complex phase diagram it is important to establish limits that can be understood controllably. To this end we focused on the regime of fermion-dominated population-imbalance which, in the extreme imbalance limit, connects to the Fermi polaron problem where a single bosonic impurity interacts with a Fermi sea. The opposite limit of a fermionic impurity coupled to a Bose-Einstein condensate corresponds to the Bose polaron problem which features qualitatively different physics. Already this asymmetry reflects the impact the interplay of different particle statistics has on the phase diagram away from the extreme population imbalanced limits.

In order to approach the problem we employed a functional renormalization group approach that allows to systematically incorporate high-order correlation functions. This enables us to reproduce the polaron-to-molecule transition in the single-boson limit which is a necessary condition for any theoretical approach that aims to describe this strong-coupling phase diagram. In contrast to the simpler three-dimensional case [54, 56, 137], we showed that three-body correlations have to be included to describe the polaron-to-molecule transition in two dimensions and we obtain excellent agreement with ab-initio approaches [175] that can be applied in the quantum impurity limit.

Using the fRG we extended the analysis to finite boson densities. There, depending on the boson and fermion densities (or equivalently their chemical potentials), we observed two phases: a fermionic liquid with two Fermi seas in which all bosons are bound into molecules, themselves immersed in a majority Fermi sea, and a hybridized liquid in which the condensation of bosons leads to a mixing of the fermionic and molecular sectors [96].

This hybridization and the associated mixing are not a result of the Hubbard-Stratonovich field used in our two-channel model, but they occur equally in atomic single-channel models whenever scattering vertices between fermions and bosons develop a pole in presence of a boson condensate. In this regard, the phase diagram away from the molecular phase at $n_B \ll n_F$ shares a remarkable similarity to the Bose polaron problem that describes the opposite limit of few fermions immersed in a Bose condensate, where the same hybridization mechanism leads to a *crossover* between the polaron and molecule instead of a transition [103, 108].

Naively, one may suspect that in a mixture of bosons and fermions as many particles as possible are bound into fermionic bound states in order to maximize attractive potential energy. This, however, does not take into account the properties of the system in two ways. First, this argument neglects the fermionic nature of the bound states which leads to the formation of a molecular Fermi energy, representing a kinetic energy cost. As a result, when the bosonic density is increased, the molecular Fermi energy eventually exceeds the energy of the lowest-lying polaron state and the system enters the mixed phase.

Second, the argument misses the fact that already in the limit of a vanishingly small boson density the formation of a bound state competes with the formation of a polaron state in which a single boson interacts collectively with a large number of surrounding fermionic bath particles [62]. For a fixed interaction strength, the polaron state can thus profit more efficiently from an increased density of bath particles. Vice versa, as the bath density is lowered polaron dressing looses efficiency so that eventually the composite bound state becomes the new ground state (in absence of Coulomb interactions).

While the fRG approach employed in this section provides nontrivial insights into the phase diagram of the Fermi-Bose mixture, the approximations used are insufficient to explore the phase diagram in its whole richness. First hints to a plethora of exciting phenomena can already be inferred from numerous quasiparticle features of the single-particle spectral functions uncovered using the FMR scheme in Section 2.3.5, ranging from non-trivial effective mass renormalization and the non-monotonous dispersion of molecules, to incoherent parts in the spectral function reflecting quasiparticle instability.

Indeed, for a more accurate description of such features it would be necessary to go beyond the gradient expansion we impose on our *Ansatz* and instead allowing for an arbitrary momentum and frequency dependence of vertex functions. While such a treatment has been used in the three-dimensional case [137], it remains challenging to implement numerically. Preliminary results (obtained from a calculation analogous to Chapter 5 in two dimensions), however, suggest that including the full momentum- and frequency-dependence indeed cures the spurious non-monotonous behavior of the polaron energy discussed in Section 2.3.3. Far from being only of quantitative importance, such a fully momentum- and frequency-resolved approach could give new qualitative insight into the phase diagram, e.g. by allowing for the description of transitions to non-trivial molecular Fermi surface topology [204] akin to Fulde-Ferrell-Larkin-Ovchinnikov phases in BCS superconductors [205, 206].

We did not include Bose-Einstein condensation in our formalism. Its explicit inclusion would allow for the study of subregions of the mixed phase in which a bosonic condensate is accompanied by molecular or fermionic Fermi seas. Additionally, the presence of a condensate will require the incorporation of a repulsive Bose-Bose interaction to ensure the mechanical stability of the condensate. Since the bosons are strongly-coupled to the fermions a strong renormalization of the boson-boson interaction has to be expected which may enhance or suppress the stability of Bose-Einstein condensation. While fermionic self-energy corrections are expected to play a subdominant role in the limit of strong population imbalance $n_F \gg n_B$, for a study of the phase diagram away from this limit these also become an essential ingredient and may lead to striking effects such as boson-mediated p-wave pairing at sufficient interaction strength [92].

The question as to which vertices (i.e. correlation functions) to include in more refined approximations of our fRG scheme is dependent on the type of phases one may expect to govern the Bose-Fermi mixture phase diagram away from the strongly-imbalanced limit —see the introductory Fig. 2.1. Quite generally, and similar to variational techniques, in field theoretical approaches the range of phases one can discern is limited by the variety of —potentially competing— channels taken into account in the renormalization procedure. In this regard, the strongly-coupled Bose-Fermi mixtures present a vast testbed to develop comprehensive theoretical approaches to competing order where a manifold of scenarios and phases may unfold, including: phase separation between the fermionic species in case of repulsive effective interactions, competing bipolaron and trion formation, boson-mediated s- or p-wave pairing of fermions, fermion-induced phonon softening that may result in supersolidity, higher-order pairing mechanisms such as boson-mediated Cooper binding of trions and phases of Efimov-type states that may condense depending on their statistics.

Moreover, as discussed in Appendix A, the formation of bound states containing several bosons may be considered. However, in ultracold quantum gases these higher-body bound states are usually subject to rapid decay to deeply bound states. The competition between such dissipative multi-particle losses and the formation of many-body phases is an intriguing perspective for future studies, posing a significant theoretical challenge that requires extension beyond equilibrium theory.

Another compelling question is what the impact of Coulomb interactions between the fermionic degrees of freedom may be. These long-range interactions will ultimately impose limits on the universal connection between strongly-coupled Bose-Fermi mixtures in atomically thin semiconductors and ultracold atoms (see Table 1.1). Coulomb interaction can be expected to play a key role in particular at low doping where screening becomes increasingly ineffective. Taking Coulomb interactions into account may indeed suppress the formation of well-defined electronic and molecular Fermi surfaces and instead lead to qualitatively different physics even in the limit of extreme population imbalance ϵ_B/ϵ_F, where understanding the interplay of Coulomb interaction, favoring Wigner crystallization, and boson-mediated Fermi-Fermi interactions, remains an open challenge.

Considering the myriad of open questions, the full exploration of the phase diagram of two-dimensional Bose-Fermi mixtures remains a formidable task. Due to the strong-coupling nature of the problem, uncovering the possible in- and out-of-equilibrium phases and phenomena will ultimately require a concerted effort between theory and experiment. Starting from limiting cases, such as considered in this chapter, that can be controllably understood and combining *ab initio* approaches with experimental observations will be key to tackle this outstanding challenge and can lead to new insight into effective descriptions of strongly-coupled many-body quantum systems.

Chapter 3

Impurity-induced pairing in two-dimensional Fermi gases

This chapter is based on the following publication:

[3] R. Li*, **J. von Milczewski***, A. Imamoglu, R. Oldziejewski, R. Schmidt, *Impurity-induced pairing in two-dimensional Fermi gases*,

Physical Review B 107, 155135 (2023).

In this chapter we study induced pairing between two identical fermions mediated by an attractively interacting quantum impurity in two-dimensional systems. Based on a Stochastic Variational Method (SVM), in the first part of this chapter we investigate the influence of confinement and finite interaction range effects on the mass ratio beyond which the ground state of the quantum three-body problem undergoes a transition from a composite bosonic trimer to an unbound dimer-fermion state. We find that confinement as well as a finite interaction range can greatly enhance trimer stability, bringing it within reach of experimental implementations such as found in ultracold atom systems. In the context of solid-state physics, our solution of the confined three-body problem shows that exciton-mediated interactions can become so dominant that they can even overcome detrimental Coulomb repulsion between electrons in atomically-thin semiconductors. This work is thus of relevance as it paves the way towards a universal understanding of boson-induced pairing across various fermionic systems at finite density, and opens perspectives towards realizing novel forms of electron pairing beyond the conventional paradigm of Cooper pair formation. As such it offers insights that we will also draw upon in Chapter 4 dealing with boson-induced superconductivity in two-dimensional semiconductor materials as this system shows properties of a many-body system despite being a few-body system in every sense of the word.

Finally in Section 3.5, we will investigate the effect of confinement and interaction strength, parametrized by the vacuum dimer energy, to identify signatures of the polaron-to-molecule transition introduced in Section 1.7.

The findings presented in Sections 3.1 to 3.4 are based on the work published in Ref. [3]. The findings presented in Section 3.5 are based on unpublished work.

3.1 Introduction

Frequently, the relevant physics of a many-body system is determined by the properties of its few-particle correlators, and thus a deep understanding of a many-body problem often comes only after carefully examining its few-body counterpart. An excellent example is given by the discovery of Cooper pair formation as the key ingredient leading to superconductivity [83, 84, 207]. No matter the type of a superconductor, be it s-wave, p-wave, d-wave, or other like charge-$4e$ superconductors [208–217], the phenomenon requires electrons to be bound into bosonic compounds. While, for conventional superconductors, the binding originates from phonon-mediated attraction, a variety of bosons —partially stemming from collective excitations of the electronic system itself— have been considered as the mediating particle [218–221].

More generally, quantum impurity-mediated pairing of fermions in the mass imbalanced $1+N$ fermion problem has been scrutinized extensively in recent years [177, 222–232]. The vast majority of theoretical efforts have focused on non-interacting fermions and point-like impurity-fermion attraction that can be studied experimentally with ultracold gases [128, 233, 234]. Interestingly, in the unconfined case, the system supports cluster-bound states whenever the mass m_I of the quantum impurity is sufficiently light compared to the mass m_F of the fermions . The critical mass ratio $\alpha = m_F/m_I$ required for such bound states to appear depends on the dimensionality of the system: in two dimensions (2D), the role of interactions is enhanced, and hence the mass ratio can be smaller compared to the three dimensional (3D) case [186, 235].

A recent twist to the quantum impurity problem in 2D emerged with the advent of atomically-thin van der Waals materials, particularly semiconducting transition metal dichalcogenides (TMDs) [22, 33]. In TMDs, excitons (bosons) can be either employed as an experimental probe of the many-body physics exhibited by electrons (fermions), ranging from Mott physics [236], excitonic insulators [39] and the fractional Quantum Hall effect [237] to the recent observation of Wigner crystallisation [238, 239], or they can be viewed as novel constituents of Bose-Fermi mixtures [1, 33, 62], potentially supporting superconductivity [95, 101, 102]. Importantly, in this case, strong Coulomb repulsion is present between the fermionic electrons, and the impurity-fermion interaction itself is characterized by a substantial range [61]. So far, little is known about the existence and character of bosonic cluster-bound states in such a scenario.

Recent advances in controlling 2D external confinement in ultracold setups [48, 240] and TMDs [241] open an exciting possibility of exploring the physics of the quantum impurity problem in a fermionic background in a controlled bottom-up approach [242–244]. Quite intriguingly, from the perspective of many-body physics, an alternative interpretation of the confinement potential is that of imitating a finite fermion density found in many-body paradigms such as the Fermi polaron problem

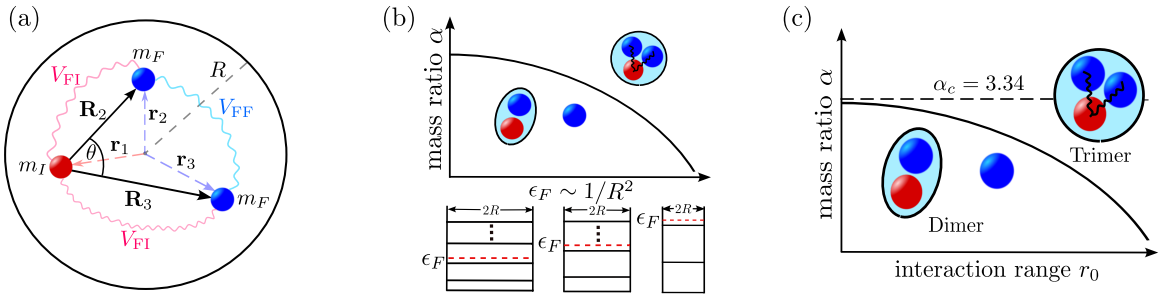

Figure 3.1. Impurity-induced fermion pairing. (a) Illustration of the three-body system solved in this work. A mobile impurity particle ('I', red) of mass m_I interacts with two fermions ('F', blue) of mass m_F with all particles confined in a two-dimensional spherical box of radius R. Their positions, measured from the center of the box potential, are denoted by $\mathbf{r}_1$, $\mathbf{r}_2$ and $\mathbf{r}_3$. The coordinates $\mathbf{R}_2$, $\mathbf{R}_3$ and θ, in turn, denote the positions of the fermions and their angle relative to the impurity, respectively. (b) Qualitative influence of the system size R on the critical mass ratio $\alpha = m_F/m_I$ required for induced fermion pairing. By tuning the system size R, the density and Fermi energy ϵ_F of the fermions are tuned. This allows to infer how an increase of the Fermi level in a many-body system may enable impurity-induced bound state formation. (c) Qualitative effect of the range r_0 of the impurity-fermion interaction on the critical mass ratio $\alpha_c = (m_F/m_I)_c$ of the dimer-trimer transition. The critical value obtained in free space ($R \to \infty$) for contact interactions ($r_0 \to 0$) is shown as a dashed line. Both, increasing interaction range or the Fermi energy, favors trimer formation (which can even withstand detrimental Coulomb repulsion between the fermions, denoted as V_{FF} in (a)).

[9, 128–130]. Specifically, the change of the confinement ($\sim R$, see Fig. 3.1) can be regarded as a primitive means of tuning the bath density ($n_F \sim 1/R^2 \sim k_F^2$), realizing a few-body analog of the full many-body problem [245].

In this chapter, we refine the understanding of 2D systems comprised of one impurity and two identical fermions (quantum statistically, the smallest Fermi sea possible) by studying the effects of a finite-range impurity-fermion potential, confinement, and strong inter-fermion repulsion on the ground state properties using a Stochastic Variational Method (SVM).

Our first key result is that we show that the critical mass ratio of the dimer-to-trimer transition strongly departs from previous findings obtained for the simpler case of ideal fermions and zero-range impurity-fermion attraction (see Fig. 3.1(b,c) for a schematic illustration). Remarkably, for TMDs, where the transition occurs between a fermionic trion and a bosonic p-wave bound state of two electrons glued together by an exciton, we find that trimer formation is robust against Coulomb repulsion. Moreover, our numerical calculations show that the stability (in the sense of an increase of the dissociation energy required to unbind the trimer into a dimer state) of emerging bosonic p-wave bound states is enhanced by confinement. This

suggests that direct exciton-mediated p-wave superconductivity may be well in reach in solid-state systems.

Next, we study signatures of the polaron-to-molecule transition in the few-body regime, by tuning the dimer energy from the non-interacting regime to a regime where the dimer is the ground state. We find a qualitative analog of the polaron-to-molecule transition which upon tuning the fermion density shows the same behavior as the transition in the many-body problem. Furthermore, we show that the states we identify as the polaron and the molaron exihibit similar quasiparticle properties to their many-body analogs, introduced in Section 1.7.

3.2 Model

We consider an interacting system of two fermions and a quantum impurity confined in a two-dimensional spherical box; for an illustration, see Fig. 3.1(a). This could represent two electrons interacting with an exciton in a quantum dot within a TMD, as well as two degenerate ultracold fermionic atoms interacting with an atom of a different quantum number within an oblate optical trap. Using an effective mass approximation, the Hamiltonian for this system reads

$$\begin{aligned}\hat{H} = &-\frac{\hbar^2}{2m_I}\nabla_1^2 - \frac{\hbar^2}{2m_F}\nabla_2^2 - \frac{\hbar^2}{2m_F}\nabla_3^2 + \sum_{i=1}^{3} V_{\text{conf}}(\mathbf{r}_i) \\ &+ V_{\text{FI}}(\mathbf{r}_1 - \mathbf{r}_2) + V_{\text{FI}}(\mathbf{r}_1 - \mathbf{r}_3) + V_{\text{FF}}(\mathbf{r}_2 - \mathbf{r}_3).\end{aligned} \tag{3.1}$$

Here $\mathbf{r}_1$, $\mathbf{r}_2$ and $\mathbf{r}_3$ denote the positions of the impurity and the two fermions, respectively, while m_I and m_F are their masses. The fourth term in the Hamiltonian represents the external confinement potential, which is modeled by an infinite potential well. In practice, this is achieved by setting

$$V_{\text{conf}}(\mathbf{r}) = E_{\text{ref}}\left(\frac{\mathbf{r}}{R}\right)^p \tag{3.2}$$

where R is the box size, E_{ref} is a reference energy scale and p is a large integer so that an infinite potential well is approximated. In our calculation, we set $p = 30$ and use the vacuum dimer energy as the reference energy $E_{\text{ref}} = E_{2B}^{\infty}$.

To account for finite range effects, the fermion-impurity interaction is modeled via a square well potential

$$V_{\text{FI}}(\mathbf{r}) = \begin{cases} -V_0, & |\mathbf{r}| \leq r_0 \\ 0, & |\mathbf{r}| > r_0 \end{cases}, \tag{3.3}$$

of depth V_0 and range r_0. Using this model potential, we mimic the finite range effects of the short-range interactions both in two-dimensional materials [22, 61] as well as ultracold atoms [20].

A possible Coulomb interaction between the two fermions,

$$V_{\text{FF}}(\mathbf{r}) = \frac{e^2}{4\pi\epsilon_0\epsilon}\frac{1}{|\mathbf{r}|}, \tag{3.4}$$

is included by the last term in Eq. (3.1). Here, e is the electron charge and ϵ the dielectric constant of a given material. Note that in cold atoms this direct interaction is absent ($V_{\mathrm{FF}} = 0$). For TMD Eq. (3.4) is a good approximation at large distance scales. At short range, the interaction between charge carriers is more accurately modeled using the Rytova-Keldysh potential [246, 247]. However, to capture the essential physics of the interplay of Coulomb repulsion, confinement, and electron-exciton attraction, we restrict ourselves to the use of the pure Coulomb potential in Eq. (3.4). On the one hand, this allows for efficient numerics, and, on the other hand, this does not complicate the analysis by introducing additional physical tuning parameters, such as the screening length. In the following, we set $\hbar = 1$, unless stated otherwise.

3.3 Method

Apart from the task of solving the quantum mechanical problem of three interacting particles, this system brings with itself the challenge of the additional confinement potential. This confinement is, however, crucial in order to imitate the effect of a finite fermion density n_F in many-body systems, which scales as $n_F \sim 1/R^2 \sim k_F^2$. Here k_F denotes the Fermi wavevector of the fermions. The confinement breaks translational symmetry and thus is not susceptible to momentum space approaches using conventional variational wavefunctions or quantum field theory and diagrammatic methods.

To solve for the ground state and its energy, we employ the SVM [248]. To this end, the Hamiltonian H is diagonalized with respect to a set of wavefunctions $\{\Phi_n\}_{n=1}^{N}$ which is successively extended by drawing from a manifold of trial functions. In every extension step $N \to N+1$, the choice of the new wavefunction Φ_{N+1} is optimized in a stochastic random walk, minimizing the lowest-lying eigenstates of the Hamiltonian H with respect to the vector space spanned by the set $\{\Phi_n\}_{n=1}^{N+1}$. During the optimization, we first draw a set of independent samples from the manifold of trial functions and then perform a random descend walk around the best proposal state. Having performed an extension step, the Hamiltonian H is diagonalized with respect to the vector space spanned by the $\{\Phi_n\}_{n=1}^{N+1}$. The resulting i-lowest eigenstate Ψ_i is then given by a superposition of these basis states, i.e.

$$\Psi_i = \sum_{n=1}^{N+1} c_n^i \Phi_n, \tag{3.5}$$

where $i = 1, ..., N+1$ and the eigenstates $\{\Psi_i\}_{i=1}^{N+1}$ are mutually orthogonal.

In many applications of SVM, trial functions are generated from explicitly correlated Gaussians (ECG). These are parametrized as

$$\Phi(\mathbf{r}_1, \mathbf{r}_2, \mathbf{r}_3) = \frac{1}{r_B^3} \mathcal{P} \exp\left(-\frac{1}{2} \left(\mathbf{r}_1^T \mathbf{r}_2^T \mathbf{r}_3^T \right) \mathcal{A} \begin{pmatrix} \mathbf{r}_1 \\ \mathbf{r}_2 \\ \mathbf{r}_3 \end{pmatrix} \right) \tag{3.6}$$

where $\mathcal{A}$ denotes a positive definite, symmetric 6×6 matrix and $\mathcal{P}$ is an antisymmetrization operator. The length scale r_B, introduced in Section 3.4, characterizes

the size of the dimer bound state. Throughout our work in this chapter the matrix $\mathcal{A}$ in Eq. (3.6) is given by

$$\mathcal{A} = \begin{pmatrix} A_{11}\mathcal{R}(0) & A_{12}\mathcal{R}(\phi_1) & A_{13}\mathcal{R}(\phi_2) \\ A_{12}\mathcal{R}(-\phi_1) & A_{22}\mathcal{R}(0) & A_{23}\mathcal{R}(\phi_3) \\ A_{13}\mathcal{R}(-\phi_2) & A_{23}\mathcal{R}(-\phi_3) & A_{33}\mathcal{R}(0) \end{pmatrix}, \tag{3.7}$$

where A is a symmetric matrix, and $\mathcal{R}(\phi)$ is a 2 rotation matrix by the angle ϕ with $\mathcal{R}(0)$ given by the identity matrix $\mathcal{R}(\phi) = \mathcal{I}_2$. In the first parts of this chapter when investigating the dimer-trimer transition a significantly simplified wavefunction Ansatz is used where the matrix $\mathcal{A}$ of Eq. (3.6) is given by

$$\mathcal{A} = A \otimes \mathcal{I}_2, \tag{3.8}$$

where A is a positive definite, symmetric 3×3 matrix, and $\mathcal{I}_2$ the 2×2 identity matrix. With this simplification the wavefunction simplifies to [248, 249]

$$\Phi(\mathbf{r}_1, \mathbf{r}_2, \mathbf{r}_3) = \frac{1}{r_B^3}\mathcal{P}\exp\left(-\frac{1}{2}\sum_{i,j=1}^{3} A_{ij}\mathbf{r}_i \cdot \mathbf{r}_j\right). \tag{3.9}$$

Here, A denotes a positive definite, symmetric 3×3 matrix. While this simplification works well when studying dimer and trimer particles, in Section 3.5 we discuss shortcomings of this wavefunction in describing the polaron state which necessitate the use of the more general wavefunction Eq. (3.6).

The advantage of using these trial functions is threefold. First, they allow one to find the analytical solution to the matrix elements of the Hamiltonian [249, 250]. Second, by using them, high accuracy in the energy can be achieved. Finally, the ECG contain the relevant physical states (dimers, trimers, and scattering states in our system) and, as such, they have been used to calculate exciton, trion and even biexciton energies in solid state systems with high precision [251–254].

3.3.1 Algorithm and Sampling

Let us provide further information on the optimization process undertaken in every step of the SVM [248]. The sampling method and algorithm described here were used for the results obtained to describe the dimer-to-trimer transition in Section 3.4. For some of the calculations, the algorithm and the sampling were modified to achieve faster convergence. The modifications will be mentioned in the respective places and these modifications will be with respect to the base algorithm and sampling described in this subsection.

For the results regarding the dimer-to-trimer transition, we performed 10 independent calculations for every data point. In each of these calculations, 100 basis states are computed. In the following, we refer to each one of these calculations as a run, and the combination of 10 runs makes up a single data point.

To compile a set of 100 basis states $\{\Phi_n\}_{n=1}^{100}$ in a single run, we successively increase the set of basis states by drawing from the manifold of trial wavefunctions described

in Eq. (3.9), which have $\phi_1 = \phi_2 = \phi_3 = 0$ when comparing with the form shown in Eqs. (3.6) and (3.7).

In a step $N \to N+1$, we draw proposal states $\{\Phi_\alpha\}$ independently. From these proposals, we choose the state Φ_β which produces the lowest-lying eigenstate of the Hamiltonian H with respect to the vector space V_α^N spanned by the previously chosen states $\{\Phi_n\}_{n=1}^N$ and the proposal state Φ_α[1]

$$V_\alpha^N = \text{span}\left(\{\Phi_n\}_{n=1}^N \cup \Phi_\alpha\right) \tag{3.10}$$

where

$$\sigma((H|_{V_\alpha^N})) = \{\lambda_{\alpha,1}^N, ..., \lambda_{\alpha,N+1}^N\} \tag{3.11}$$

denotes the spectrum of the Hamiltonian H, restricted to the vector space V_α^N. The minimization is carried out as

$$\beta = \min_\alpha \left[\min_i(\{\lambda_{\alpha,i}^N\}_i)\right], \tag{3.12}$$

where the minimization over i chooses the lowest eigenvalue of $H|_{V_\alpha^N}$, while the minimization over α optimizes the proposal state.

Next, we perform a random descent walk in the vicinity of Φ_β, for which every step is accepted so long as it lowers the lowest eigenvalue. This process is terminated after a fixed number of proposals which is specified below and can be varied depending on the speed of numerical convergence to stable results.

A straightforward method to draw independently from the ECG manifold is to draw proposal states Φ_α as

$$m_\alpha = \frac{1}{R}\begin{pmatrix} x_{11} & x_{12} & x_{13} \\ x_{21} & x_{22} & x_{23} \\ x_{31} & x_{32} & x_{33} \end{pmatrix} \tag{3.13}$$

with

$$A_\alpha = m_\alpha^T m_\alpha. \tag{3.14}$$

Here, the x_{ij} are drawn from a uniform distribution in the interval $x_{ij} \in [-1, 1]$. The corresponding (unrenormalized) basis state is then given as $\Phi_\alpha(\mathbf{r}_1, \mathbf{r}_2, \mathbf{r}_3) r_B^3 = \mathcal{P}\exp\left\{\left(-\frac{1}{2}\sum_{i,j=1}^3 A_{\alpha,ij}\mathbf{r}_i \cdot \mathbf{r}_j\right)\right\}$. In the second part of the optimization, in which we perform the random descent walk, the proposal is updated as

$$m'_\beta = m_\beta + \delta x \begin{pmatrix} x_{11} & x_{12} & x_{13} \\ x_{21} & x_{22} & x_{23} \\ x_{31} & x_{32} & x_{33} \end{pmatrix} \tag{3.15}$$

with

$$A'_\beta = (m'_\beta)^T m'_\beta. \tag{3.16}$$

[1] for a detailed description of SVM and different optimization strategies see Ref. [248].

In practice, a value of $\delta x = 0.1/r_B$ has shown to yield good results for the parameters considered in this work (for a detailed analysis of convergence see Section 3.4.4 and Appendix D).

As the manifold of trial functions is fairly large, a large number of random proposals is necessary in every step of the algorithm to ensure convergence. This choice of sampling quickly yields reliable results for dimer states. For trimer states, convergence is much slower, and especially close to the dimer-to-trimer transition, it can occur that no trimer state is obtained. To address this challenge, we leverage the physical intuition that a trimer state should feature all particles confined within a length scale of the interaction range. Exploiting this fact also allows us to reduce the number of required steps, as well as improve stability of the algorithm.

In order to implement this idea in the algorithm, it is important to note that the matrices A_α^{-1} carry the meaning of a covariance matrix

$$\langle \mathbf{x}_i \mathbf{x}_j^T \rangle \sim (A_\alpha^{-1})_{ij} \mathcal{R}(\theta_{\alpha,ij}). \tag{3.17}$$

For the trimer, this suggests a covariance matrix of close to constant value (proportional to the mean distance squared of the particles from the center of the trap), with fluctuations around this value of the order of the interaction range. We thus introduce a further sampling method described as

$$\begin{aligned} B &= 5Rx_0 + 2r_0 \begin{pmatrix} x_{11} & x_{12} & x_{13} \\ x_{21} & x_{22} & x_{23} \\ x_{31} & x_{32} & x_{33} \end{pmatrix}, \\ A_\alpha^{-1} &= \frac{B + B^T}{2}, \end{aligned} \tag{3.18}$$

where $x_0 \in [0,1] r_B$, $x_{i,j} \in [-1,1] r_B$. Using $\delta x' = 0.1 r_B$ the corresponding random walk method is determined by

$$\begin{aligned} B' &= B + \delta x' \begin{pmatrix} x_{11} & x_{12} & x_{13} \\ x_{21} & x_{22} & x_{23} \\ x_{31} & x_{32} & x_{33} \end{pmatrix}, \\ (A'_\alpha)^{-1} &= \frac{B' + (B')^T}{2}. \end{aligned} \tag{3.19}$$

In Eq. (3.18), the value of $5R$ (representing a sampling range of the mean distance squared of the particle from the center of the trap) was chosen to ensure reasonable convergence. The value of $2r_0$, in turn, representing the interparticle distances was selected based on the fact that the localization of particles with respect to each other should be on the order of the interaction range. In the first part of the algorithm, where states are independently drawn, we then alternate between the two sampling methods, Eqs. (3.13) and (3.18), while in the second part (where the random walk is performed) we alternate between the methods defined by Eqs. (3.15) and (3.19).

While the sampling method described by Eq. (3.18) may seem very biased at first glance, this presumption does not capture the full picture for several reasons. First,

states of the form of Eq. (3.18) are usually also found using the sampling method described in Eq. (3.13). There, however, many more sampling steps are necessary for this to occur, implying less efficiency. Second, states found using Eq. (3.18) are often accepted in the regime where the trimer is the ground state, but indeed also where the dimer is the ground state. Furthermore, we use a large number of sampling steps, namely about 15000 independent samples and 15000 local descents, each repeated twenty times for every run. Thus the exact form of the sampling coefficients used in Eqs. (3.13) and (3.19) does not play a dominant role as long as the space of eligible wavefunctions is sufficiently small (*i.e.* the confinement is not too big) and the space of appropriate wavefunction is large enough (*i.e.* the interaction range is not too small). However, as can be seen in Fig. 3.2, for some parameter regimes, the data begins to develop a scatter which could be addressed by increasing the number of sampling steps further, or by restricting the sampling method described in Eq. (3.19) to a smaller parameter space.

After we have finally performed 10 different runs, each yielding 100 basis states, we then combine the results of these different runs to obtain a basis set of 1000 basis states $\{\Phi_n\}_{n=1}^{1000}$. In the very end, the Hamiltonian is diagonalized with respect to these 1000 states and the physical quantities are extracted from the resulting ground state.

3.3.2 The Hamiltonian in the ECG basis

Having discussed the Hamiltonian, the trial wavefunctions and the sampling method, all that is left to do calculations are the matrix elements of the Hamiltonian. In the following we give a detailed account of the representation of the Hamiltonian in Eq. (3.1) within the manifold spanned by the ECG. For simplicity, we give expressions for the simplified wavefunction Ansatz in Eq. (3.9), for the more general Ansatz in Eq. (3.6), these expressions can be obtained in the same way.

Given two basis functions $|A\rangle$ and $|B\rangle$, corresponding to

$$\langle \mathbf{x}|A\rangle r_B^3 = \exp\left\{\left(-\frac{1}{2}\sum_{i,j=1}^{3} A_{ij}\mathbf{r}_i\cdot\mathbf{r}_j\right)\right\}$$

and

$$\langle \mathbf{x}|B\rangle r_B^3 = \exp\left\{\left(-\frac{1}{2}\sum_{i,j=1}^{3} B_{ij}\mathbf{r}_i\cdot\mathbf{r}_j\right)\right\}$$

with $\mathbf{x}^{\mathrm{T}} = (\mathbf{r}_1^{\mathrm{T}}, \mathbf{r}_2^{\mathrm{T}}, \mathbf{r}_3^{\mathrm{T}})$, the matrix elements of the kinetic parts $-\frac{\hbar^2}{2m_i}\nabla_i^2 = \frac{\mathbf{p}_i^2}{2m_i}$ are given by [250]

$$\begin{aligned}\langle A|\mathbf{p}_i^2|B\rangle r_B^6 &= \int d\mathbf{x}(\nabla_i\langle\mathbf{x}|A\rangle)\cdot(\nabla_i\langle\mathbf{x}|B\rangle)\\ &= \sum_{k,l=1}^{3} A_{ik}B_{il}\int d\mathbf{x}\ \mathbf{r}_k\cdot\mathbf{r}_l\langle\mathbf{x}|A+B\rangle\\ &= \frac{16\pi^3}{\det\{(A+B)\}}\sum_{k,l=1}^{3} A_{ik}B_{il}(A+B)^{-1}_{kl}\\ &= \frac{16\pi^3}{\det\{(A+B)\}}[A(A+B)^{-1}B]_{ii}. \end{aligned} \tag{3.20}$$

The remaining parts of the Hamiltonian consist of one-and two-body potentials of the form $V(\mathbf{r}_i)$ and $V(\mathbf{r}_i - \mathbf{r}_j)$. Given a suitable vector $w^{\mathrm{T}} = (w_1, w_2, w_3)$, both types of potential can thus be written in the form $V(\tilde{w}^{\mathrm{T}}\mathbf{x})$ where $\tilde{w}^{\mathrm{T}} = w^{\mathrm{T}} \otimes \mathbb{I}_{2\times 2}$ such that $\tilde{w}^{\mathrm{T}}\mathbf{x} = w_1\mathbf{r}_1 + w_2\mathbf{r}_2 + w_3\mathbf{r}_3$. Then, the matrix element of this general form of the potential reads [250, 255]

$$\begin{aligned}\langle A|V(\tilde{w}^{\mathrm{T}}\mathbf{x})|B\rangle &= \int d\mathbf{x}\ V(\tilde{w}^{\mathrm{T}}\mathbf{x})\langle\mathbf{x}|A+B\rangle = \int d\mathbf{x}d\mathbf{r}V(\mathbf{r})\delta(\mathbf{r}-\tilde{w}^{\mathrm{T}}\mathbf{x})\langle\mathbf{x}|A+B\rangle\\ &= \frac{1}{4\pi^2}\int d\mathbf{x}d\mathbf{r}V(\mathbf{r})\int d\mathbf{k}\exp\left(i\mathbf{k}\cdot\left[\mathbf{r}-\tilde{w}^{\mathrm{T}}\mathbf{x}\right]\right)\langle\mathbf{x}|A+B\rangle\\ &= \frac{4\pi^2}{\det(A+B)}\frac{r_B^{-6}}{w^{\mathrm{T}}(A+B)^{-1}w}\int d\mathbf{r}V(\mathbf{r})\exp\left(-\frac{1}{2w^{\mathrm{T}}(A+B)^{-1}w}\mathbf{r}^2\right), \end{aligned} \tag{3.21}$$

where we have inserted a Dirac δ-distribution for which we then used a representation in terms of exponentials.

From this expression, the matrix elements of $V_{\mathrm{conf}}(\mathbf{r}_i) = E_{2B}^{\infty}(|\mathbf{r}_i|/R)^n$, $V_{\mathrm{FI}}(\mathbf{r}_i - \mathbf{r}_j)$, and $V_{\mathrm{FF}}(\mathbf{r}_i - \mathbf{r}_j)$ can be obtained for appropriate choices of w. For $V_{\mathrm{conf}}(\mathbf{r}_i)$, $w_j = \delta_{ij}$, while for $V_{\mathrm{FI}}(\mathbf{r}_i - \mathbf{r}_j)$ and $V_{\mathrm{FF}}(\mathbf{r}_i - \mathbf{r}_j)$, $w_k = \delta_{ik} - \delta_{jk}$. The matrix element of $V_{\mathrm{conf}}(\mathbf{r}_i)$ is then given by

$$\begin{aligned}\langle A|V_{\mathrm{conf}}(\mathbf{r}_i)|B\rangle &= E_{2B}^{\infty}\frac{4\pi^2}{\det(A+B)}\frac{r_B^{-6}}{(A+B)^{-1}_{ii}}\int d\mathbf{r}\frac{|\mathbf{r}|^n}{R^n}\exp\left(-\frac{\mathbf{r}^2}{2(A+B)^{-1}_{ii}}\right)\\ &= \frac{E_{2B}^{\infty}}{R^n r_B^6}\frac{8\pi^3}{\det(A+B)}\left[2(A+B)^{-1}_{ii}\right]^{\frac{n}{2}}\Gamma\left(\frac{n+2}{2}\right), \end{aligned} \tag{3.22}$$

where $\Gamma(x)$ is the Gamma function. In practice we use $n = 30$.

The matrix element of the fermion-impurity interaction reads

$$\begin{aligned}\langle A|V_{\mathrm{FI}}(\mathbf{r}_i - \mathbf{r}_j)|B\rangle &= -\frac{8\pi^2 V_0 b_{ij}}{r_B^6\det(A+B)}\int d\mathbf{r}\Theta(r_0 - |\mathbf{r}|)e^{-b_{ij}\mathbf{r}^2}\\ &= -\frac{8\pi^3}{r_B^6\det(A+B)}V_0\left(1 - e^{-b_{ij}r_0^2}\right), \end{aligned} \tag{3.23}$$

where

$$b_{ij} = \frac{1}{2w^{\mathrm{T}}(A+B)^{-1}w} = \frac{1}{2\left[(A+B)^{-1}_{ii} + (A+B)^{-1}_{jj} - 2(A+B)^{-1}_{ij}\right]}. \tag{3.24}$$

Finally, the matrix element of $V_{\mathrm{FF}}(\mathbf{r}) = E_{2B}^{\infty} r_B q^2/|\mathbf{r}|$ is given by

$$\begin{aligned}\langle A|V_{\mathrm{FF}}(\mathbf{r}_2-\mathbf{r}_3)|B\rangle r_B^6 &= E_{2B}^{\infty} r_B q^2 \frac{8\pi^2 b_{23}}{\det(A+B)} \int d\mathbf{r}\ \frac{e^{-b_{23}\mathbf{r}^2}}{|\mathbf{r}|} \\ &= E_{2B}^{\infty} r_B q^2 \frac{8\pi^3}{\det(A+B)} \sqrt{\pi b_{23}}. \end{aligned} \tag{3.25}$$

3.3.3 Angular Momentum in the ECG basis

For reasons that will become clear in Section 3.4.2, let us also define a total angular momentum of the (2+1) system relative to the impurity by

$$\mathbf{L}_{\mathrm{tot}} = \mathbf{L}_2 + \mathbf{L}_3 = \mathbf{R}_2 \times \mathbf{P}_2 + \mathbf{R}_3 \times \mathbf{P}_3, \tag{3.26}$$

where $\mathbf{R}_2$, $\mathbf{R}_3$, $\mathbf{P}_2$, $\mathbf{P}_3$ are the positions and momenta of the two fermions relative to the impurity. Because our variational wavefunctions are real functions, it follows that $\langle \mathbf{L}_{\mathrm{tot}} \rangle = 0$ [248]. As a result, even when describing states with $\langle \mathbf{L}_{\mathrm{tot}} \rangle \neq 0$, superpositions of different expectation values will be formed resulting in $\langle \mathbf{L}_{\mathrm{tot}} \rangle = 0$.

In order to capture the transition from the dimer state (which will have $\langle \mathbf{L}_{\mathrm{tot}} \rangle = 0$) to the trimer state (which will have $\langle \mathbf{L}_{\mathrm{tot}} \rangle = \pm 1$), we focus on the expectation value of $\mathbf{L}_{\mathrm{tot}}^2$, which may be nonzero. To that end, let us first define the coordinate transformation

$$\begin{aligned}\mathbf{R}_1 &= \frac{m_I \mathbf{r}_1 + m_F \mathbf{r}_2 + m_F \mathbf{r}_3}{(m_I + 2m_F)} \\ \mathbf{R}_2 &= \mathbf{r}_2 - \mathbf{r}_1, \\ \mathbf{R}_3 &= \mathbf{r}_3 - \mathbf{r}_1. \end{aligned} \tag{3.27}$$

Given an ECG wavefunction $|A\rangle$ with $\langle \mathbf{x}|A\rangle r_B^3 = \exp\left\{\left(-\frac{1}{2}\sum_{i,j=1}^{3} A_{ij}\mathbf{r}_i \cdot \mathbf{r}_j\right)\right\}$ and $\mathbf{x}^{\mathrm{T}} = (\mathbf{r}_1^{\mathrm{T}}, \mathbf{r}_2^{\mathrm{T}}, \mathbf{r}_3^{\mathrm{T}})$, this can be represented in the relative coordinates as $\langle \tilde{\mathbf{x}}|A\rangle r_B^3 = \exp\left\{\left(-\frac{1}{2}\sum_{i,j=1}^{3} \tilde{A}_{ij}\mathbf{R}_i \cdot \mathbf{R}_j\right)\right\}$ where $\tilde{\mathbf{x}}^{\mathrm{T}} = (\mathbf{R}_1^{\mathrm{T}}, \mathbf{R}_2^{\mathrm{T}}, \mathbf{R}_3^{\mathrm{T}})$, and $\tilde{A}$ is defined as

$$\tilde{A} = O^{\mathrm{T}} A O \tag{3.28}$$

with

$$O = \begin{pmatrix} \frac{m_I}{m_I+2m_F} & \frac{m_F}{m_I+2m_F} & \frac{m_F}{m_I+2m_F} \\ -1 & 1 & 0 \\ -1 & 0 & 1 \end{pmatrix}^{-1}. \tag{3.29}$$

The matrix element of $\mathbf{L}_{\mathrm{tot}}^2$ is then given as (for more detail see Ref. [248])

$$\begin{aligned}\langle A|\mathbf{L}_{\mathrm{tot}}^2|B\rangle r_B^6 =& 8\pi^3 \left[\frac{\mathrm{Tr}\left(f(\tilde{A})\left[\left(\tilde{A}+\tilde{B}\right)^{-1} \otimes \mathbb{I}_{2\times 2}\right]\right) \mathrm{Tr}\left(f(\tilde{B})\left[\left(\tilde{A}+\tilde{B}\right)^{-1} \otimes \mathbb{I}_{2\times 2}\right]\right)}{4\det\left(\tilde{A}+\tilde{B}\right)} \right. \\ &\left. + \frac{\mathrm{Tr}\left(f(\tilde{A})\left[\left(\tilde{A}+\tilde{B}\right)^{-1} \otimes \mathbb{I}_{2\times 2}\right] f(\tilde{B})\left[\left(\tilde{A}+\tilde{B}\right)^{-1} \otimes \mathbb{I}_{2\times 2}\right]\right)}{2\det\left(\tilde{A}+\tilde{B}\right)} \right]. \end{aligned} \tag{3.30}$$

Here, we have defined the function $f(\tilde{A})$ in the following way. Given a symmetric 3×3 matrix

$$\tilde{A} = \begin{pmatrix} \tilde{A}_{11} & \tilde{A}_{12} & \tilde{A}_{13} \\ \tilde{A}_{12} & \tilde{A}_{22} & \tilde{A}_{23} \\ \tilde{A}_{13} & \tilde{A}_{23} & \tilde{A}_{33} \end{pmatrix}, \tag{3.31}$$

we define $R = \begin{pmatrix} 0 & 1 \\ -1 & 0 \end{pmatrix}$, such that $f(\tilde{A})$ reads

$$f(\tilde{A}) = \begin{pmatrix} 0 & -\tilde{A}_{12} & -\tilde{A}_{13} \\ \tilde{A}_{12} & 0 & 0 \\ \tilde{A}_{13} & 0 & 0 \end{pmatrix} \otimes R \,. \tag{3.32}$$

3.4 Ground state transition between a dimer and a trimer state

Let us finally calculate the ground state near the dimer-to-trimer transition using the SVM. As the 2D system features binding via the fermion-impurity potential V_{FI} for any potential depth[2], states composed of a dimer and a fermion in a scattering state are expected to play a vital role [53]. Moreover, for sufficiently light impurities, the formation of a trimer is expected. In this state, two fermions and the impurity bind together by the mediating force of the impurity [225]. This is similar to the three-dimensional case where a p-wave trimer and eventually Efimov states appear for sufficiently light impurities [222, 227, 229].

In the limit of a vanishing interaction range $r_0 \to 0$ and infinite system size $R \to \infty$, a ground state transition from a dimer to a trimer state is predicted to occur when the mass ratio $\alpha = m_F/m_I$ is tuned across the critical value $\alpha_c \approx 3.34$ [177, 186, 235]. Having this limiting case as a benchmark, we investigate the effect of interaction range r_0 and confinement (determined by the system size R) on the critical value α_c. It is important to note that the transition will occur as a crossover because of the finite size of the system. Specifically, we study how the ground state characteristics and energy change as we tune α, r_0, and R and, as a result, how the critical mass ratio varies with r_0 and R.

In the following, we will refer to the two-body bound state appearing in an untrapped ($R \to \infty$) two-body problem consisting of the impurity and a fermion as the 'vacuum dimer'. Its binding energy will be denoted as the 'vacuum dimer energy' E_{2B}^{∞}. The terms 'dimer' and 'trimer', in turn, will refer to states in the three-body problem. Specifically, the dimer refers to a state comprised of a fermion in a scattering state along with a two-body bound state of an impurity and a fermion, while the trimer denotes a three-body bound state consisting of an impurity bound to both fermions.

To study the dimer-to-trimer transition, we vary α, r_0 and R while keeping the non-trapped ($R \to \infty$) vacuum dimer energy E_{2B}^{∞} constant. We define a corresponding

[2] As long as the size of the impurity-fermion bound state is smaller than the confinement length scale.

binding length $r_B = 1/\sqrt{2m_F E_{2B}^{\infty}}$, and, unless explicitly stated otherwise, we will work in units where the fermion mass is set to $m_F = 1/2$. Note, that we have defined r_B by the fermion mass and not the reduced mass. This convention ensures a fixed value of r_B as α is changed. One has to keep in mind, however, that now r_B is proportional to the physical binding length of the dimer state. The two-body Hamiltonian of one fermion and one impurity interacting via V_{FI} can be solved exactly [256], as we will show in the following in Section 3.4.1. This allows to obtain the required potential depth V_0 for given values of α, r_0, and E_{2B}^{∞}.

3.4.1 Two-body problem without confinement

Let us consider an impurity (with mass m_I) interacting with a single fermion (with mass m_F) via $V_{\mathrm{FI}}(\mathbf{r}) = -V_0\Theta(r_0 - |\mathbf{r}|)$ where $\Theta(x)$ is the Heaviside function. The Schrödinger equation in the relative coordinate frame then reads

$$-\frac{\nabla^2}{2\mu}\psi(\mathbf{r}) + V_{\mathrm{FI}}(\mathbf{r})\psi(\mathbf{r}) = -E_{2B}^{\infty}\psi(\mathbf{r}) \tag{3.33}$$

where $\mu = m_F m_I/(m_F + m_I)$ is the reduced mass of an impurity and a fermion. The wavefunction $\psi(\mathbf{r})$ can be decomposed into a radial part and an angular part, i.e. $\psi(\mathbf{r}) = u(r)e^{im\theta}$ with m the angular momentum of the state. For the ground state, we have $m = 0$. Thus the equation for the radial wavefunction is given by

$$r^2u'' + ru' + 2\mu[-E_{2B}^{\infty} + V_0\Theta(r_0 - r)]r^2u = 0, \tag{3.34}$$

which takes the form of a Bessel differential equation in the regions $r < r_0$ and $r > r_0$. As a result, the solution of this equation can be found in text books [256], as the Bessel differential equation is simply solved on the two domains $r < r_0$ and $r > r_0$ and a matching conditions in between the two domains is enforced. The ground state energy E_{2B}^{∞} is found by the solution of the implicit equation

$$\frac{J_0\left(\sqrt{2\mu(-E_{2B}^{\infty} + V_0)}r_0\right)}{\sqrt{2\mu(-E_{2B}^{\infty} + V_0)}K_0\left(\sqrt{2\mu E_{2B}^{\infty}}r_0\right)} = \frac{J_1\left(\sqrt{2\mu(-E_{2B}^{\infty} + V_0)}r_0\right)}{\sqrt{2\mu E_{2B}^{\infty}}K_1\left(\sqrt{2\mu E_{2B}^{\infty}}r_0\right)} \tag{3.35}$$

with J_0, J_1 Bessel functions of the first kind, and K_0, K_1 modified Bessel functions of the second kind. In Appendix C, the two-body problem including confinement is solved using the SVM.

3.4.2 Non-interacting fermions

We now begin our numerical study by first considering the system without Coulomb interactions ($V_{\mathrm{FF}} = 0$). After establishing the dimer-to-trimer transition for this case, in Section 3.4.3 we will switch on Coulomb interactions ($V_{\mathrm{FF}} > 0$), and systematically explore their effect.

Fig. 3.2 shows the energy of the SVM ground state as function of the mass ratio α, for different values of r_0 and R. Here, r_0 and R are varied in terms of the dimensionless

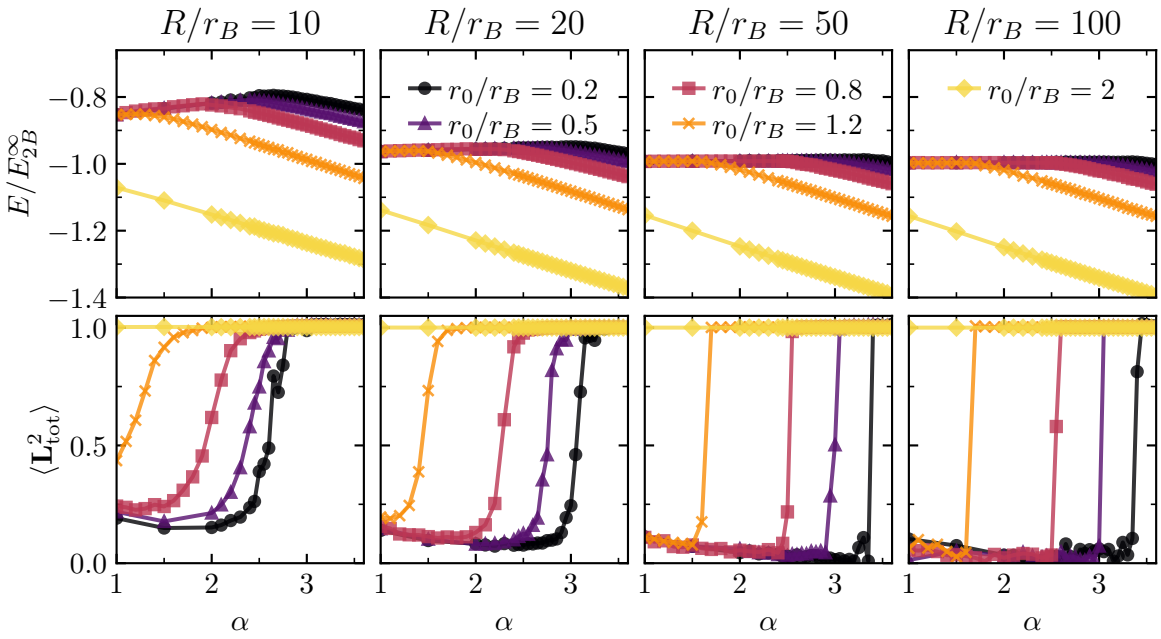

Figure 3.2. Energies E/E_{2B}^{∞} (top panels) and angular momentum expectation values $\langle \mathbf{L}_{\mathrm{tot}}^2 \rangle$ (bottom panels) of the ground state as a function of mass imbalance α for various dimensionless interaction ranges r_0/r_B and system sizes R/r_B. The energies are located around E_{2B}^{∞} with upward shifts mainly due to the confinement contributions to the kinetic energy of the particles. The crossover from the dimer to the p-wave trimer bound state is visible in the angular momentum (lower panels) which crosses over from being close to 0 to approximately 1. This crossover is similarly reflected in a drop of the ground state energy which develops an almost linear dependence on α beyond the crossover from the dimer to the trimer ground state. For increasing values of r_0/r_B (R/r_B), this crossover region is shifted to lower (higher) mass ratios α. For $R/r_B \to \infty$, the crossover becomes a sharp transition which, for $r_0/r_B \to 0$, occurs at $\alpha_c \approx 3.34$ [177, 186, 235].

quantities r_0/r_B and R/r_B. The ground state energies are all located in the vicinity of $-E_{2B}^{\infty}$. For fixed r_0/r_B and R/r_B, the ground state energies first increase slightly with the mass ratio and then show a drop at a critical mass ratio. Beyond the critical mass ratio, the ground state energy decreases steadily, exhibiting an almost linear dependence on the mass ratio, $E \propto -\alpha$ [177, 186, 235]. One can see that r_0 and R have a strong influence on the energies and the critical mass ratio at which the qualitative change in the ground state energy occurs. For a fixed system size R/r_B, upon increasing r_0/r_B, both the ground state energies and the critical mass ratio decrease. On the other hand, for a fixed interaction range r_0/r_B, an increase in system size R leads to a decrease of the energy that is accompanied by an increase of the critical mass ratio.

Let us now turn to a detailed discussion of the qualitative change observed in the ground state energy. This change signifies a transition of the ground state, where, for values of α smaller than a critical value, the system is in the 'dimer' state, i.e. it is composed of a bound dimer along with an unbound fermion. In contrast, beyond

the critical value of α, the ground state energy falls below the dimer-fermion scattering threshold energy, indicating the emergence of the trimer state, similar to the unconfined system [177, 186, 235].

While the energy is a good indicator of a qualitative change, a reliable identification of the nature of the ground state requires a deeper analysis of the corresponding wavefunction. In the following, we will show that the angular momentum and the density distribution provide two measures to clearly distinguish the dimer and trimer state.

First, let us focus on the analysis of angular momentum. To this end, we introduce the relative coordinates $\mathbf{R}_2 = \mathbf{r}_2 - \mathbf{r}_1$ and $\mathbf{R}_3 = \mathbf{r}_3 - \mathbf{r}_1$, where $\mathbf{R}_2$ and $\mathbf{R}_3$ denote the positions of the fermions relative to the impurity. The total angular momentum relative to the impurity particle is then given by $\mathbf{L}_{\text{tot}} = \mathbf{L}_2 + \mathbf{L}_3$, where $\mathbf{L}_2 = \mathbf{R}_2 \times \mathbf{P}_2$ and $\mathbf{L}_3 = \mathbf{R}_3 \times \mathbf{P}_3$. Here, $\mathbf{P}_2$ and $\mathbf{P}_3$ are the momentum operators corresponding to $\mathbf{R}_2$ and $\mathbf{R}_3$, respectively. This is the same angular momentum operator as the one introduced briefly in Section 3.3.3. In this relative coordinate frame, fermionic statistics imposes the trimer to have odd, finite angular momentum $\langle \mathbf{L}_{\text{tot}} \rangle = \pm 1$, while the dimer state has $\langle \mathbf{L}_{\text{tot}} \rangle = 0$ [177, 186, 225, 235, 257].

As a result of the ECG functions used, the basis functions are real and hence any measured value of $\langle \mathbf{L}_{\text{tot}} \rangle$ has to vanish. As a consequence of this constraint, the wavefunction of the trimer state obtained from the SVM is an equal superposition of degenerate ground states with $\langle \mathbf{L}_{\text{tot}} \rangle = 1$ and $\langle \mathbf{L}_{\text{tot}} \rangle = -1$; resulting in the expectation value $\langle \mathbf{L}_{\text{tot}} \rangle = 0$. Thus, in order to obtain a characterization of the ground state, we consider the expectation value $\langle \mathbf{L}_{\text{tot}}^2 \rangle$. This allows us to distinguish the dimer and trimer state in a reliable way.

We show the ground state value of $\langle \mathbf{L}_{\text{tot}}^2 \rangle$ in the lower column of Fig. 3.2. As one can see, $\langle \mathbf{L}_{\text{tot}}^2 \rangle$ sharply increases from values close to 0 to approximately 1 as the mass ratio is tuned beyond a critical value. The region in which this qualitative change occurs coincides with the critical mass ratio at which the drop in energy is observed (upper panels of Fig. 3.2). The close link between the behavior of the ground state energy and angular momentum is robust across all values of r_0/r_B and R/r_B. While for smaller system sizes, the transition region is larger, with increasing system size, the transition region becomes more narrow. This indicates that, as expected, the crossover found for a finite system turns into a sharp transition for an infinite system size.

From the behavior of energy and angular momentum, a simple physical picture of the crossover from a dimer to a trimer arises. At smaller mass ratios α, the ground state is given by a dimer along with a fermion in a delocalized scattering state. Thus, for large system sizes, the energy approaches the two-body energy $-E_{2B}^{\infty}$. However, for smaller system sizes the confinement induces exchange-, correlation- and confinement-energies between the two fermions increasing the energy above $-E_{2B}^{\infty}$. This increase in energy is larger for smaller system sizes and features an additional weak dependence on the mass ratio that can be understood already from the non-interacting system where the confinement energy is given by $E_{\text{conf}} = z_{01}^2/2m_I R^2 + z_{11}^2/m_F R^2 = (z_{01}^2\alpha/2 + z_{11}^2)/m_F R^2$ with z_{01} and z_{11} the first

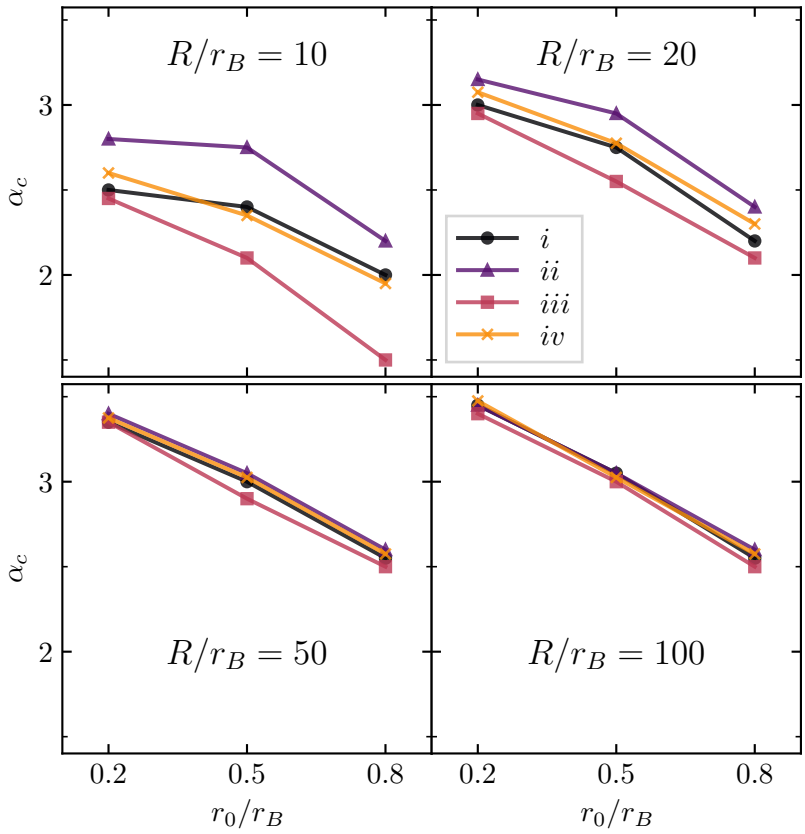

Figure 3.3. Critical mass ratio for the dimer-to-trimer transition as function of the interaction range r_0/r_B for $R/r_B = 10, 20, 50, 100$. The mass ratios are determined using four different criteria: i. appearance of ground state energy decrease (black dots); ii. $\langle \mathbf{L}^2_{\text{tot}} \rangle \approx 1$ (purple triangles); iii. $\langle \mathbf{L}^2_{\text{tot}} \rangle \approx 0$ (red squares); iv. $\langle \mathbf{L}^2_{\text{tot}} \rangle \approx 0.5$ (yellow crosses). The different criteria lead to different values of α_c, with the $\langle \mathbf{L}^2_{\text{tot}} \rangle \approx 0$ criterion consistently giving the lowest mass ratio, while the $\langle \mathbf{L}^2_{\text{tot}} \rangle \approx 1$ criterion yields the highest. With increasing R/r_B, the crossover region becomes more narrow, and the results from the different methods converge.

zeros of the Bessel functions J_0 and J_1, respectively. Beyond the critical mass ratio, the ground state is described by a trimer state, and its energy starts to decrease close to linearly with the mass ratio, as also found in the continuum case [177, 186, 235].

We now turn to a more detailed analysis of how the system size R and interaction range r_0 affect the critical mass ratio α_c (see Fig. 3.3). Decreasing the system size has a stronger effect on the dimer state than on the trimer state. This is caused by the fact that the unbound fermion in its delocalized scattering state feels the confinement more strongly than a fermion bound tightly to the impurity. As a result, the trimer state is subject to a confinement energy contribution less than the dimer state. Consequently, decreasing system size moves the transition to smaller mass ratios.

Increasing the interaction range r_0 affects the trimer state stronger than it affects the dimer state. For $R \gg r_0$, the average distance between the fermions in a trimer state is related to the short distance scales r_B and r_0 while, in the dimer state (which includes the unbound fermion), it is related to R. Thus, increasing r_0, lowers the

Pauli-repulsion within the trimer state, making the trimer favorable which decreases the critical mass ratio. This intuitive picture is reflected in the numerical results presented in Fig. 3.3. In this Figure, we additionally analyze the increasing sharpness of the transition as the system size is increased by showing the critical mass ratio as obtained from different criteria imposed on the energy and the angular momentum. As one can see, for $R/r_B = 100$, all criteria give nearly identical results, and only the dependence on the scale r_0 remains.

As can be seen from the lower panel in Fig. 3.2, the impact of the interaction range and system size on the dimer and trimer state is also reflected in the angular momentum. Due to the confinement, the free fermion in the dimer state is forced to take on a finite angular momentum state, resulting in a nonzero value of $\langle \mathbf{L}_{\mathrm{tot}}^2 \rangle$. As the system size is increased, the free fermion is less affected and $\langle \mathbf{L}_{\mathrm{tot}}^2 \rangle$ approaches zero. The trimer, on the other hand, is hardly affected by the finite system size as long as $R \gg r_0$, and thus $\langle \mathbf{L}_{\mathrm{tot}}^2 \rangle$ is very close to 1.

Our finding of a strong dependence of α_c on r_0 and R shows that the critical mass ratio of 3.34, obtained in the limit $r_0 \to 0$ and $R \to \infty$ [177, 186, 235], potentially features only a small window of universality. In this regard we note that the critical mass ratios in Fig. 3.3 for $R/r_B = 100$, $r_0/r_B = 0.2$ tend to lie slightly higher than the asymptotic value of 3.34. This is due to the stochastic nature of our method which is particularly challenged when the energetic difference between dimer and trimer particles becomes very small, which precisely occurs close to the transition. As a result, especially for larger system size and shorter interaction range, a suitable trimer wavefunction can only be found for a high number of proposed wavefunctions. In Section 3.4.4, the deviation from the asymptotic value of $\alpha_c = 3.34$ is studied in detail, and additionally, a convergence analysis, including an estimate for the basis set extrapolation error, is undertaken.

The spatial localization of the fermions around the impurity —or the lack thereof— provides a further means to confirm the presence of two- and three-body bound states. To that end, we study the spatial structure of the ground state wavefunction. It is expected that in the trimer state the two fermions are both close to the impurity, while in the dimer state, one fermion should be close to the impurity while the other resides in a delocalized scattering state. To study this behavior, we consider the correlation functions (which can be regarded as reduced density distributions)

$$u_1(R_2, R_3) = \int |\Psi(\mathbf{r}_1, \mathbf{r}_1 + \mathbf{R}_2, \mathbf{r}_1 + \mathbf{R}_3)|^2 d^2\mathbf{r}_1 d\theta_2 d\theta_3, \tag{3.36}$$

$$u_2(R_2) = R_2 \int dR_3 R_3 u_1(R_2, R_3). \tag{3.37}$$

Here, Ψ denotes the three-body wavefunction, and the angles θ_2, θ_3 are defined via $\mathbf{R}_2 = R_2(\cos\theta_2, \sin\theta_2)$ and $\mathbf{R}_3 = R_3(\cos\theta_3, \sin\theta_3)$. From this definition, one can see that the reduced density distribution u_1 measures the probability of simultaneously finding one electron at a distance R_2 while the other is situated at distance R_3 from the impurity. The distribution is obtained by integrating out the coordinates of the impurity followed by a further average over the angular orientation of the fermions with respect to the impurity. Performing an additional integral over the distance of

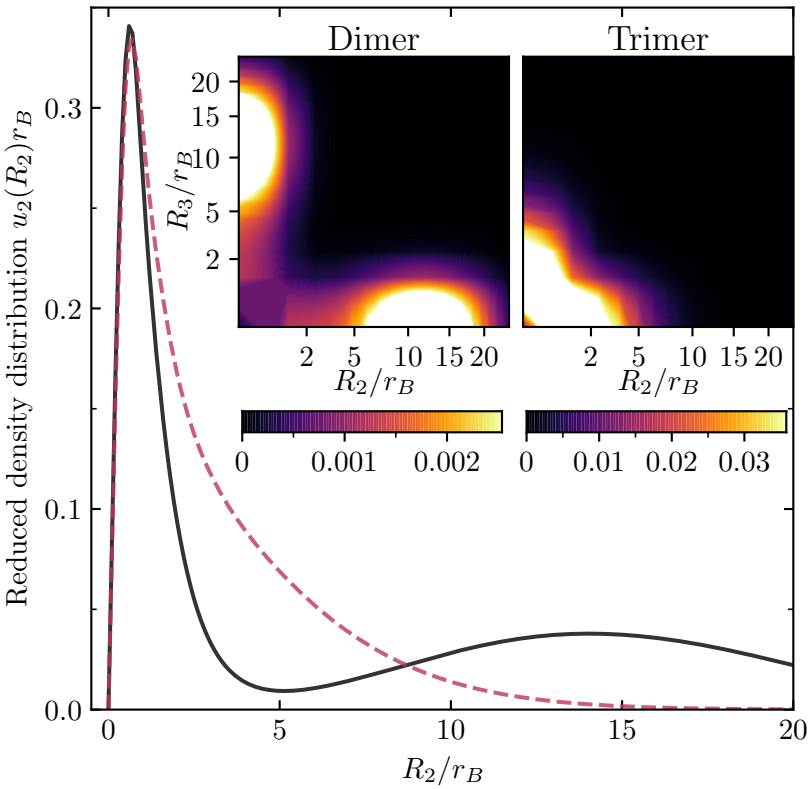

Figure 3.4. Reduced density distributions of a dimer ($\alpha = 2$) and trimer ($\alpha = 3$) state. The main plot shows $u_2(R_2)r_B$ for the dimer (black, solid) and the trimer (red, dashed) state for $R/r_B = 20$ and $r_0/r_B = 0.8$. The exponential decay of the trimer distribution is clearly visible while the dimer state contains a fermion that is delocalized at the length scale of the system size. The insets show $u_1(R_2, R_3)r_B^4$ for the dimer (left) and the trimer state (right). For the trimer state, $u_1(R_2, R_3)r_B^4$ attains its largest values when R_2 and R_3 are both small, which shows that both fermions are close to the impurity, while for the dimer state $u_1(R_2, R_3)r_B^4$ attains its maximum on the x- and y-axis.

one of the fermions from the impurity, one obtains a measure for the probability (u_2) of finding one fermion at a distance R_2 from the impurity.

In Fig. 3.4, density distributions are shown for exemplary trimer and dimer states. For the trimer state, the density distribution u_2 indeed exhibits an exponential decay, in line with the expectation that both fermions are closely-bound to the impurity. In contrast, for the dimer state, u_2 does not decay exponentially but features a tail that corresponds to one of the fermions being situated in a scattering state. Note that for the confinement length of $R/r_B = 20$ chosen in this figure, the distance between particles can be up to twice as large. Thus the density distribution does not vanish beyond $R_2/r_B = 20$ but rather beyond the maximal interparticle distance (not shown in the graph).

Density plots of the correlation function u_1 are shown in the inset of Fig. 3.4. They give further insight into the anatomy of the dimer and trimer states with respect to their radial distribution. For the dimer state, the density distribution

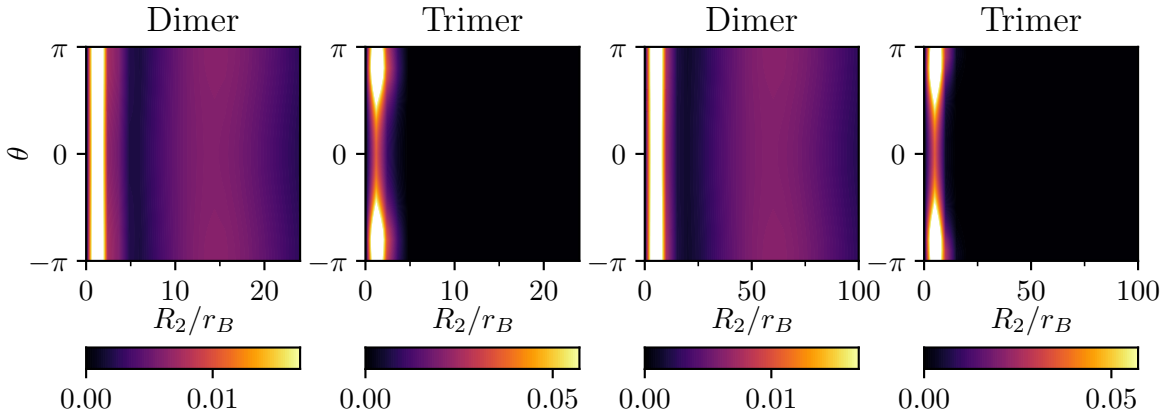

Figure 3.5. Reduced density distribution $u_3(R_2, \theta)r_B$ for systems with and without Coulomb interaction (see Section 3.4.3). Upper panel: Results for a dimer ($\alpha = 2$, left) and a trimer state ($\alpha = 3$, right) for $r_0/r_B = 0.8$, $R/r_B = 20$, and $q = 0$. Lower panel: Results for a dimer ($\alpha = 2$, left) and a trimer state ($\alpha = 3.5$, right) for $r_0/r_B = 0.8$, $R/r_B = 100$ and $q = 0.3$. For the trimer state, $u_3(R_2, \theta)r_B$ has an angular dependence such that it achieves its minimal value around $\theta = 0$ and its maximal value around $\theta = \pi$. This shows that the fermions in the trimer state have a preference for an anti-parallel configuration that is mainly caused by Pauli exclusion.

u_1 almost vanishes along the diagonal and achieves its maximum at approximately $(R_2/r_B, R_3/r_B) \approx (0, 12)$. This exemplifies how in the dimer state one fermion is closely bound to the impurity while the other fermion is delocalized. For the trimer state, u_1 attains its largest values when R_2 and R_3 are both small. Moreover, u_1 vanishes rapidly for larger R_2 and R_3, which shows that both fermions are tightly bound to the impurity. However, the analysis of u_1 also reveals that, within the trimer state, there is always one fermion that is bound tightly to the impurity, while the second fermion will be in a bound 'orbit' at a slightly larger distance.

To further study the anatomy of the dimer and trimer states with respect to their angular distribution, let us define the reduced density distribution $u_3(R_2, \theta)$ as

$$u_3(R_2, \theta) = R_2 \int d^2\mathbf{r}_1 d^2\mathbf{R}_3 |\Psi(\mathbf{r}_1, \mathbf{r}_1 + \mathbf{R}_2, \mathbf{r}_1 + \mathbf{R}_3)|^2. \tag{3.38}$$

Here, the vectors $\mathbf{R}_2$ and $\mathbf{R}_3$ are parametrized as $\mathbf{R}_2 = R_2(\cos(\theta_3 + \theta), \sin(\theta_3 + \theta))$, $\mathbf{R}_3 = R_3(\cos\theta_3, \sin\theta_3)$. Fig. 3.5 shows the density distribution $u_3(R_2, \theta)$ for dimer and a trimer states. For the trimer states, when R_2 is close to 0, the density distribution u_3 almost vanishes around $\theta = 0$ and achieves its maximum at approximately $\theta = \pi$ which shows that the fermions tend to locate at opposite sides of the impurity mainly due to Pauli exclusion. On the other hand, u_3 shows no visible angular dependence for the dimer state as the distance between the two fermions is relatively large and thus Pauli exclusion does not play an important role.

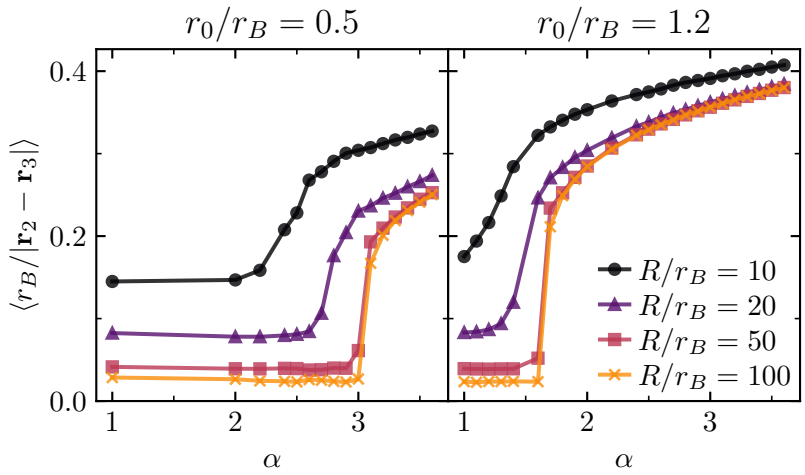

Figure 3.6. Expectation value of $r_B/|\mathbf{r_2} - \mathbf{r_3}|$ of the ground state wavefunctions obtained in Section 3.4.2, for $r_0/r_B = 0.5$ (left) and 1.2 (right), shown for a range of system sizes R/r_B. The crossover from the dimer to trimer state is visible in the steep increase of the expectation value. Increasing the box size R and decreasing the interaction range r_0 moves the crossover to higher α, consistent with our previous results. Moreover, the expectation value increases as the box size becomes smaller, because the confinement of the fermions in a smaller area results in a larger Coulomb energy.

3.4.3 Coulomb interaction

We now consider the impact a repulsive interaction potential between the two fermions ($V_{\mathrm{FF}} > 0$) has on the dimer-to-trimer transition. In particular, we focus on Coulomb interactions present in 2D semiconductors (see Eq. (3.4)). In the trimer state, both electrons bind to the exciton bringing themselves closer together. Intuitively, this can give rise to a considerable increase in the total energy of the cluster, weakening its binding. Consequently, given a fixed mass ratio, if the repulsive Coulomb energy becomes larger than the energy gap between the trimer and dimer states, the ground state is expected to unbind into a state comprised of a dimer and a free electron.

To roughly estimate the impact of the Coulomb energy on the total energy, we first calculate the expectation value of the Coulomb interaction $\sim \langle r_B/|\mathbf{r_2} - \mathbf{r_3}|\rangle$ with respect to the ground state of the system without Fermi-Fermi interaction. We stress again (see Section 3.2) that, in the following, we shall use the Coulomb potential instead of a more accurate approximation of 2D interactions between charges given by the Keldysh potential. In any case, since the Coulomb interaction is more extreme than the Keldysh potential at short range, we expect our choice to be more restrictive than the Keldysh interaction (at short distance the Coulomb interaction diverges as $1/r$, while the Keldysh potential diverges as $\log(r/r_{sc})$; with r_{sc} the screening length).

The expectation value of $r_B/|\mathbf{r_2} - \mathbf{r_3}|$ is shown in Fig. 3.6. We find a transition in the expectation value for increasing mass ratio. For dimer states, two electrons are relatively distant, rendering the value of $\langle r_B/|\mathbf{r_2} - \mathbf{r_3}|\rangle$ small. In contrast, for trimer states, this value is considerable and increases as the mass ratio rises. The

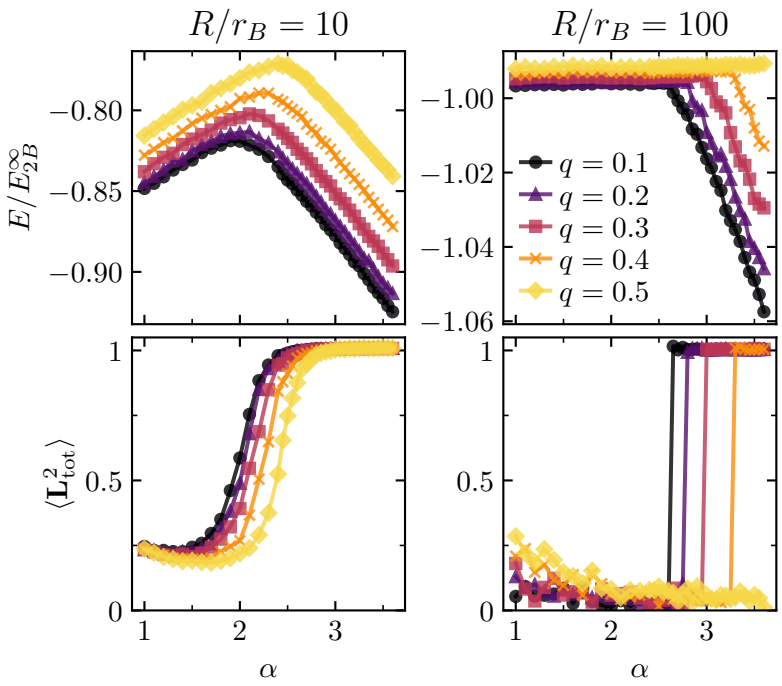

Figure 3.7. Energies and expectation values of $\mathbf{L}_{\mathrm{tot}}^2$ of the ground state of the system in presence of Coulomb repulsion (parametrized by the effective charge q) for system sizes $R/r_B = 10$ (left), and 100 (right). The interaction range of the fermion-impurity potential is chosen as $r_0/r_B = 0.8$. As in Fig. 3.2, the steep decrease in energy beyond a critical mass ratio reflects the crossover from a dimer to a trimer state. The position, at which this transition occurs, moves to higher α upon increasing the box size R and the effective charge q.

moderate increase of the Coulomb energy in the trimer state as function of the mass ratio, suggests already in this simple estimate that the existence of the dimer-to-trimer transition will persist even in presence of Coulomb repulsion.

Motivated by the above, we now solve numerically for the ground states of the system including the Coulomb interaction (Eq. (3.4)) by applying the SVM for different values of a dimensionless effective charge q, defined by the square root of the ratio of Coulomb repulsion to dimer binding energy

$$q = \sqrt{\frac{V_{\mathrm{FF}}(r_B)}{E_{2B}^{\infty}}} = \sqrt{\frac{2m_{\mathrm{F}} r_B}{4\pi\epsilon_0 \epsilon \hbar^2}} e, \tag{3.39}$$

where we have restored the factor of $\hbar$ for clarity.

From the SVM, we calculate the energy and the expectation value of $\mathbf{L}_{\mathrm{tot}}^2$ for an interaction range $r_0/r_B = 0.8$ and box sizes $R/r_B = 10$ and $R/r_B = 100$. The result is shown in Fig. 3.7. Depending on the effective charge q, the energies start to decrease significantly beyond a critical mass ratio. At the same time, the corresponding values of $\mathbf{L}_{\mathrm{tot}}^2$ rapidly increase, signaling a dimer-to-trimer crossover.

The larger the effective charge q, the larger the critical value α_c becomes. Conversely, the larger the density n_F ($\sim 1/R^2 \sim k_F^2$), the smaller the critical value of α_c.

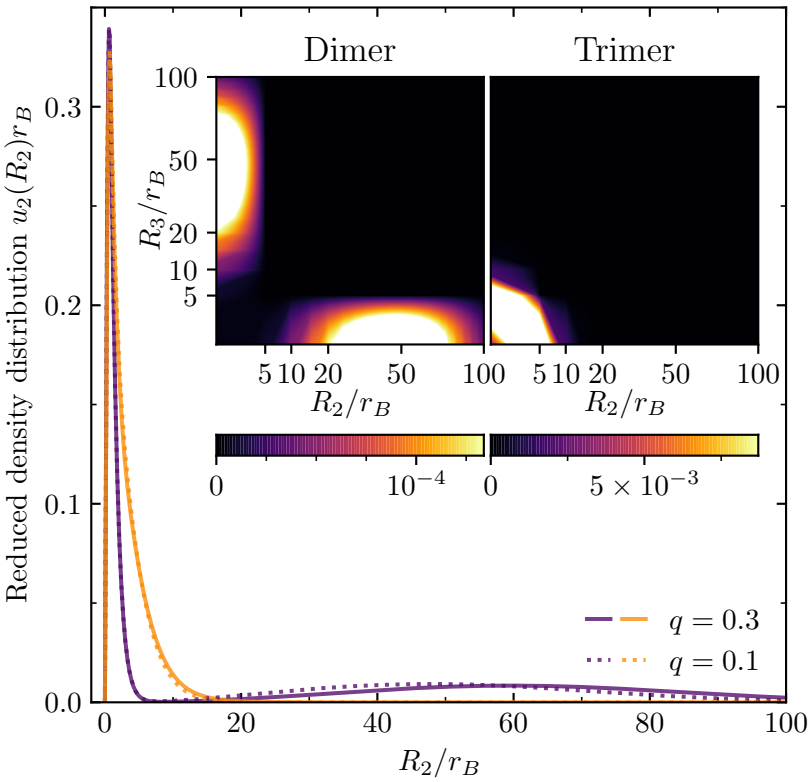

Figure 3.8. Reduced density distributions of a dimer ($\alpha = 2$) and trimer ($\alpha = 3.5$) state in presence of Coulomb repulsion. The plot shows $u_2(R_2)r_B$ for a dimer (purple, solid) and a trimer (orange, solid) state for $R/r_B = 100$, $r_0/r_B = 0.8$ and $q = 0.3$. For comparison the result is also shown for a smaller value of effective charge $q = 0.1$ in orange. The insets show $u_1(R_2, R_3)r_B^4$ for the trimer ($\alpha = 3.5$, right) and the dimer state ($\alpha = 2$, right) with $R/r_B = 100$, $r_0/r_B = 0.8$ and $q = 0.3$. As in Fig. 3.4, the qualitative distribution of fermions within the dimer and the trimer state is visible.

Notably, the dimer-to-trimer transition remains robust upon the strong, long-range Coulomb repulsion. Thus, while Coulomb repulsion weakens trimer formation (increasing the critical value), it does not inhibit it. Indeed, for all effective charges we considered[3], we have observed the eventual transition into a trimer state. Importantly, one can also always offset the detrimental effects of Coulomb repulsion on forming a trimer, either by tighter confinement (i.e. larger effective electron density), or a larger interaction range.

We show the reduced density distribution for the system in presence of Coulomb repulsion in Fig. 3.8. The effective charges and mass ratios were chosen to realize both dimer and trimer states as in Fig. 3.4. As can be seen, both states feature a localized part, while the dimer again exhibits the additional contribution of a delocalized scattering state. The density plots of u_1, shown in the inset of Fig. 3.8, exhibit the same qualitative behavior as those in Fig. 3.4. Fig. 3.8 also shows that, increasing the effec-

[3]the $q = 0.5$, $R/r_B = 100$ data set shown in Fig. 3.7 does not show a trimer state, however, this is merely due to the chosen plot range. A trimer state appears eventually upon increasing the mass ratio.

tive charge q, the density distribution of the trimer decays over a larger length scale. This clearly shows that the Fermi-Fermi repulsion tends to favor a larger separation between fermions, while still supporting the formation of a trimer state. Similarly, within the dimer state, Coulomb repulsion has the effect of pushing the scattering tail away from the impurity-fermion bound state.

For typical parameters and energy scales in TMDs, i.e. $\epsilon \approx 4.4$, $m_{\mathrm{F}} \approx 0.5\, m_{\mathrm{e}}$, where m_{e} indicates the bare electron mass, and $|E_{2B}^{\infty}| \approx 30$ meV (trion binding energy) [61], one arrives at $q \approx 2.6$. This value is consistent with the absence of experimental observations of higher-order bound states as the ground state. While at first sight this might suggest the absence of the p-wave trimer state for typical TMD realizations, this estimate is obtained assuming an electronic system at vanishing density. In this regard, it is important to note that, as we also find, confinement naturally decreases the role of Coulomb interaction. In turn, regarding the increase in confinement as an increase in the effective electron density, our results suggest that at sufficiently high fermion densities, p-wave bosonic trimers could indeed be stabilized as the actual ground state in the system already for the typical experimental parameters. Moreover, our results show that the critical mass ratio α_c could be changed by experimentally tuning the effective charge q. This could, for instance, be realized by appropriate dielectric engineering of the materials [258] that encapsulate the TMD layer [4].

3.4.4 Deviation from the asymptotic result $\alpha_c \approx 3.34$

As it can be seen in Fig. 3.2, for $R/r_B = 100$ and $r_0/r_B = 0.2$ the $\langle \mathbf{L}_{\mathrm{tot}}^2 \rangle$ value begins to increase at around $\alpha = 3.35$ and has arrived at approximately 1 at the data point corresponding to $\alpha = 3.45$. Thus, the data indicates that the transition occurs for $3.35 < \alpha_c < 3.45$, which lies higher than the asymptotic value of $\alpha_c \approx 3.34$. This is in opposition to our finding that, generally, confinement and a finite interaction range should in fact cause a reduction of the value of α_c.

To study this deviation, for each mass ratio we perform single runs of up to 1000 basis states, rather than performing ten runs of up to 100 basis states. These runs are executed in two different ways which are motivated by noting the important point that for $R/r_B = 100$, $r_0/r_B = 0.2$ the transition region is very narrow (for further information, see also the detailed discussion in Appendix D). Hence, few basis states share overlaps with both the dimer and the trimer state. As a consequence, the ground and the excited state each have to be optimized for with a significant number of basis states, as few basis states optimize the energy of both the trimer and the dimer, and it is thus easy to miss the true ground state.

This is visible in Fig. 3.9, where the purple dots show the result of a single run in which the expansion of the basis set towards 1000 states keeps optimizing with respect to the current ground state (and convergence is thus slow when the dimer and trimer state are almost degenerate in energy). In contrast, convergence can be dramatically

[4] Such a modification of the dielectric environment will also affect the trion binding energy resulting in a redefinition of E_{2B}^{∞}.

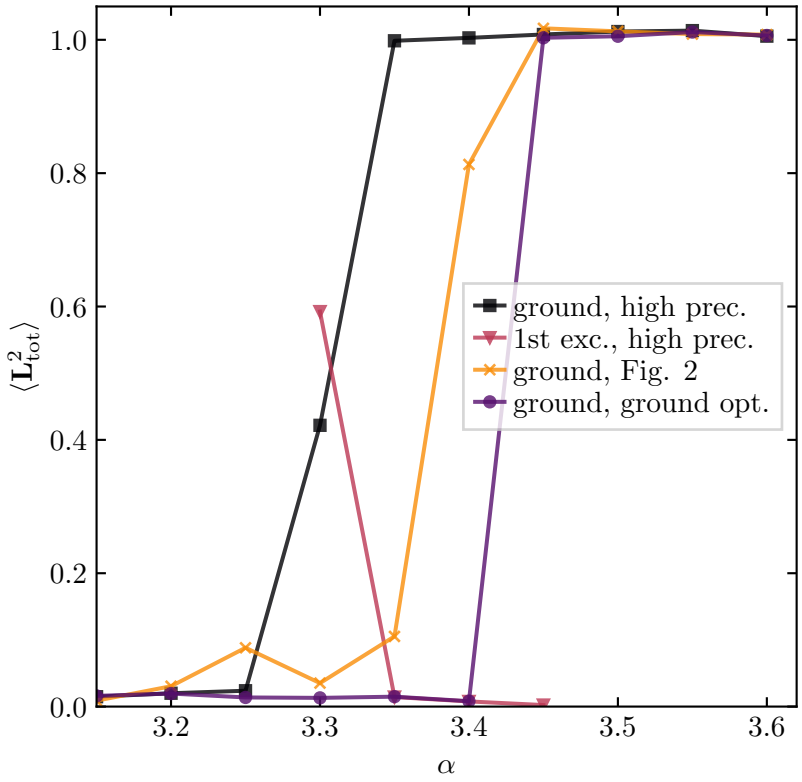

Figure 3.9. Angular momentum values as function of the mass imbalance α, for $R/r_B = 100$ and $r_0/r_B = 0.2$. The data of the ground state from Fig. 3.2 is shown (yellow, crosses) along with ground state data obtained from single runs with $N = 1000$ basis states. This data was obtained using two different optimization strategies: either by optimizing with respect to the ground state (purple dots), or by optimizing for the first excited state in the second half of the run (black squares). For the latter, the corresponding expectation value of the first excited state properties is shown as red triangles.

sped up by allowing for more drastic updates; specifically, by adapting the acceptance criteria for basis states such that for the first 500 basis states acceptance depends on improving the ground state, and, for the next 500 basis states, it depends on improving the first excited state. Away from the transition this is not an efficient method to obtain a good ground state estimate. However, close to the transition this approach offers dramatically improved efficiency in describing the ground state. The result is shown as black squares in Fig. 3.9. For both optimization criteria one can see that, compared to the data shown in Fig. 3.2 (reproduced also in Fig. 3.9), the scatter in $\langle \mathbf{L}^2_{\mathrm{tot}} \rangle$ is absent, and the transition region has become sharper. While for the pure ground state optimization, the transition still occurs for $3.4 < \alpha_c < 3.45$, for the first excited state optimization criterion in the second half of the run, it now sets on shortly before $\alpha = 3.3$ and $\langle \mathbf{L}^2_{\mathrm{tot}} \rangle \approx 1$ is reached shortly before $\alpha = 3.35$, consistent with the free space result.

In order to offer further insight into the two different optimization criteria, in Fig. 3.10, energy and angular momentum data of the ground and first excited state

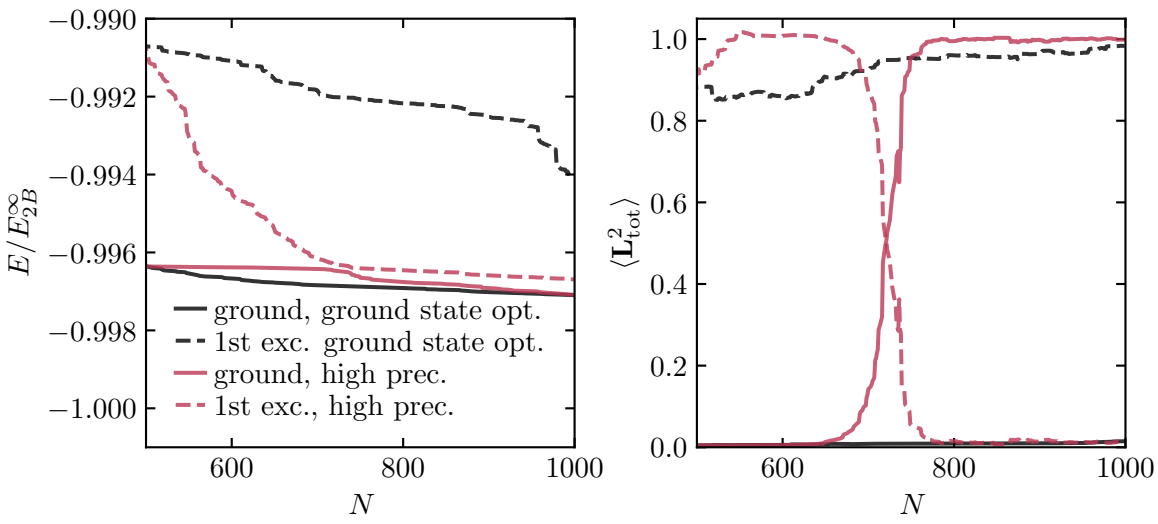

Figure 3.10. Energy (top) and angular momentum (bottom) values of the ground and first excited state as a function of basis states N for SVM calculations at $\alpha = 3.35$, $R/r_B = 100$ and $r_0/r_B = 0.2$ using a single run of up to 1000 basis states. The results were obtained in two different ways: optimizing the ground state for all 1000 states (black) and optimizing the ground state for 500 states and then optimizing the first excited state for another 500 states (red), showing ground (solid) and first excited state properties (dashed).

are shown for parameters $\alpha = 3.35$, $R/r_B = 100$, $r_0/r_B = 0.2$ close to the free-space dimer-to-trimer transition. The data, shown as a function of the number of basis states, is obtained in the two different ways described above. That is, optimizing the ground state for all 1000 basis states ('ground state opt.'), and optimizing the ground state for the first 500 basis states followed by the optimization of the first excited state for the next 500 basis states ('high prec.'). By construction, the latter algorithm is more efficient in allowing admixtures of the excited state manifold to the optimized basis set.

As one can see from Fig. 3.10, in the first approach that optimizes for the ground state only, the energy of the ground state saturates already early on, and the first excited state sees very little improvement. Optimizing the first excited state as well, however, the energies cross over, triggering a transition from dimer to trimer behavior as can be seen in the corresponding angular momentum plot in Fig. 3.10. Here, it can also be seen that optimizing the ground state only, its angular momentum remains close to 0, while the first excited state does not immediately attain a value close to 1; which is natural, since it is not optimized for. Optimizing for the first excited state in the second half of the algorithm, one can see that its expectation value attains a value close to 1 already after being optimized for only about 100 basis states. At around 700 basis states, the first excited state has been optimized enough to trigger the crossover between ground and first excited state.

3.5 Polaron-to-molecule transition within a few-body system

We are interested in seeing a precursor of the many-body polaron-to-molecule transition in a few-body system. In a many-body system, the ratio of the two-body bound state energy to the Fermi energy can be tuned to trigger a polaron-to-molecule transition, as long as the impurity is heavy enough. With confinement as a few-body analog of finite density, a similar tuning can be performed in the few-body limit.

For sufficiently heavy impurities, without any confinement, the ground state of a system with one impurity and many fermions consists of the impurity forming a dimer/molecule with one of the fermions. Neglecting the influence of the range of the potential well, the binding length of this molecule is given approximately by r_B (or at least by a quantity that scales like r_B) which is related to the binding energy of the dimer. At the same time, our physical understanding of a polaron state is that of being adiabatically connected to the ground state of a non-interacting system.

For given r_0, V_0 and a given mass ratio α, one can compute the corresponding two-body vacuum binding energy E_{2B}^{∞} as described in Section 3.4.1. Furthermore, as seen in previous sections one can choose a range of these parameters in which a dimer/molecule is formed. Tuning the depth of the potential well $V_0^{'}$ continuously from V_0 to 0, we can then tune the system from a molecular ground state into a non-interacting ground state (given of course that we had a molecular state to begin with). Equivalently, every value of $V_0^{'}$ corresponds to an unconfined two-body energy $E_{2B}^{\infty'}$, which in turn can be used to define a length scale $r_B^{'} = 1/\sqrt{2m_F E_{2B}^{\infty'}}$. As $V_0^{'}$ is tuned from V_0 to 0, the effective confinement length $r_B^{'}$ increases from r_B to ∞. At some point, however, $r_B^{'}$ becomes of the order of R and thus it should no longer be physically possible to form molecules.

3.5.1 Triggering a polaron-to-molecule transition by tuning the potential depth

In the following, we show results for the system described in Section 3.2 which we interpret as a precursor of a polaron-to-molecule transition. As will become clear in Section 3.5.4, the generalized form of the ECG introduced in Eq. (3.6) is necessary to reproduce the non-interacting ground state and as a result the simplification that was possible in describing the dimer to trimer transition (i.e. setting $\phi_1 = \phi_2 = \phi_3 = 0$ to use Eq. (3.9)) in previous sections is no longer appropriate when describing the polaron.

From Fig. 3.2, it is clear that at $\alpha = 1.5$, $r_0/r_B = 0.8$, $R/r_B = 10$ and also for $\alpha = 1.5$, $r_0/r_B = 0.8$, $R/r_B = 20$ the system holds a molecular ground state. Thus, these parameters serve as ideal starting parameters to then tune V_0' (and by that $E_{2B}^{\infty'}$ and $r_B^{'}$).

As the depth of the potential well V_0' is tuned continuously between the molecular ground state at V_0 and the non-interacting ground state at V_0', it is natural to expect

that the properties of the ground state change: While for small V_0' we expect the ground state to have good overlap with the non-interacting ground state, a molecular state should hold small overlap with the non-interacting ground state as it stems from a strong interaction. Naturally, for a finite box size a molecular state will hold a finite overlap even with a non-interacting ground state, however when increasing the box size this overlap should decrease.

Furthermore, we have seen in Fig. 3.2 that the molecular states hold $\langle \mathbf{L}^2_{\mathrm{tot}} \rangle \approx 0$, while in Section 3.5.3 we will show that the non-interacting ground state for $R = 10 r_B$ has $\langle \mathbf{L}^2_{\mathrm{tot}} \rangle \approx 1.035$.

It is thus natural to expect that the nature of the ground state changes smoothly between these different qualitative features as the potential depth $V_0^{'}$ is tuned between V_0 and 0. Furthermore, the changes in the ground state should also be visible upon inspection of the reduced density distributions such as the $u_1(R_1, R_2)$ function defined in Eq. (3.36): While we expect the molecular state to have one fermion tightly confined to the impurity (on the order of the binding length $r_B^{'}$) and one fermion in a scattering state (confined to the impurity on the order of the box size R), the polaron is expected to have both fermions rather tightly confined to the impurity. Not necessarily as tight as the molecule, but certainly the second fermion should not be in a scattering state whose mean distance from the impurity scales with R.

From the analogy to the many-body case where the polaron-to-molecule transition occurs at a fixed ratio of the binding energy to the Fermi energy ϵ_B/ϵ_F (see Sections 1.7 and 2.3 for details), we expect the polaron-to-molecule transition to occur at lower values of $E_{2B}^{\infty'}/E_{2B}^{\infty}$ for $R = 20 r_B$ than for $R = 10 r_B$, because in the former case the corresponding 'Fermi energy' is lower.

In the left panel of Fig. 3.11, the energies of the ground as well as the first excited state are shown for $R = 10 r_B$ as well as $R = 20 r_B$ as a function of $E_{2B}^{\infty'}/E_{2B}^{\infty}$ for $r_0 = 0.8 r_B$ and a mass imbalance of $\alpha = 1.5$. For convenience, these energies are shifted by the varying two-body vacuum bound state energy $E_{2B}^{\infty'}$. Furthermore, in the right panel of Fig. 3.11 the corresponding energy gap ΔE between the ground and the first excited state is shown. As one can see, in both cases the first excited state energy approaches the ground state energy and then moves away from it again. For $R = 10 r_B$ this happens around $E_{2B}^{\infty'}/E_{2B}^{\infty} = 0.2$, while for $R = 20$ this happens around $E_{2B}^{\infty'}/E_{2B}^{\infty} = 0.03$. This gives a first indication towards the occurrence of a transition or crossover behavior between the ground and the first excited state. In the following, we will characterize this behavior which results in a qualitative change in the nature of the ground and first excited space using different observables.

To begin the characterization, in the upper and lower left panels of Fig. 3.12 we show the expectation value of the squared angular momentum around the impurity $\langle \mathbf{L}^2_{\mathrm{tot}} \rangle$ (introduced in Section 3.4) for the ground and the first excited state at both $R = 10 r_B$ and $R = 20 r_B$. As one can see, for both values of R, the squared angular momentum of the ground state starts at a value slightly above 0.8, before rising to a value around 1.1 quickly (more on this later). It remains at that value before crossing over quickly to a lower value around 0.3 near $E_{2B}^{'\infty}/E_{2B}^{\infty} = 0.2$ for $R = 10 r_B$ and below 0.2 near $E_{2B}^{\infty'}/E_{2B}^{\infty} = 0.03$ for $R = 20 r_B$, respectively. Similarly, the squared angular

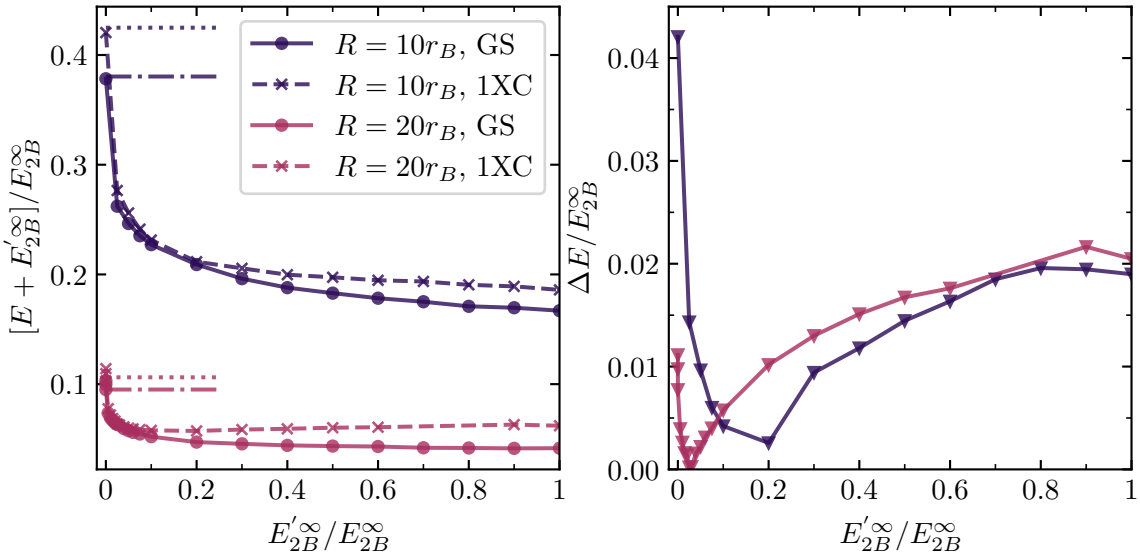

Figure 3.11. Ground and first excited state energies as a function of two-body binding energy. The left panel shows the ground (solid) and first excited state (dashed) energies at $r_0 = 0.8$ for $R = 10r_B$ (purple) and $R = 20r_B$ (red) as a function of the varying two-body binding energy $E^{\infty'}_{2B}$. For convenience, the energies are shifted by $E^{\infty'}_{2B}$. The right panel shows the energy gape between the ground and the first excited state. The energy gap closes at $E^{\infty'}_{2B}/E^{\infty}_{2B} \approx 0.2$ for $R = 10r_B$ and at $E^{\infty'}_{2B}/E^{\infty}_{2B} \approx 0.03$ for $R = 20r_B$. The dash-dotted and dotted lines in the left panel show the exact particle-in-a-box ground and first excited state energies at $E^{\infty'}_{2B}$ as computed in Section 3.5.3.

momentum of the first excited state performs the opposite maneuver, it starts at a low value and eventually swaps places with the ground state angular momentum. These crossovers coincide with the closing of the energy gap seen in Fig. 3.11. To identify the corresponding states, it is useful to recall that in Section 3.4 we have previously identified the ground state at $E'_B/E_B = 1$ as a molecule/dimer state and the low angular momentum expectation value $\langle \mathbf{L}^2_{\text{tot}} \rangle$ confirms this further. Similarly, we will show analytically in Section 3.5.3 that the angular momentum expectation value $\langle \mathbf{L}^2_{\text{tot}} \rangle$ of the non-interacting ground state can be computed to give $\langle \mathbf{L}^2_{\text{tot}} \rangle \approx 1.035$. This closely connects the corresponding state shown in Fig. 3.12 to the non-interacting ground state and therefore to the polaron state which consider as being adiabatically connected to the non-interacting ground state. In Section 3.5.3 we will comment on this further.

To further this connection, in the upper and lower right panels of Fig. 3.12 we show the overlap $|\langle \Psi | \Psi_0 \rangle|$ of the ground (solid lines) or first excited (dashed lines) state $|\Psi\rangle$ at a given value of $E^{\infty'}_{2B}/E^{\infty}_{2B}$ with the non-interacting ground state $|\Psi_0\rangle$ at $E^{\infty'}_{2B}/E^{\infty}_{2B} = 0$. As one can see, a crossover behavior between the ground and the first excited state takes place which coincides with the behavior seen in energy and angular momentum. Furthermore, the state we identified as a polaron based on its angular momentum retains significant overlap with the non-interacting ground state and is

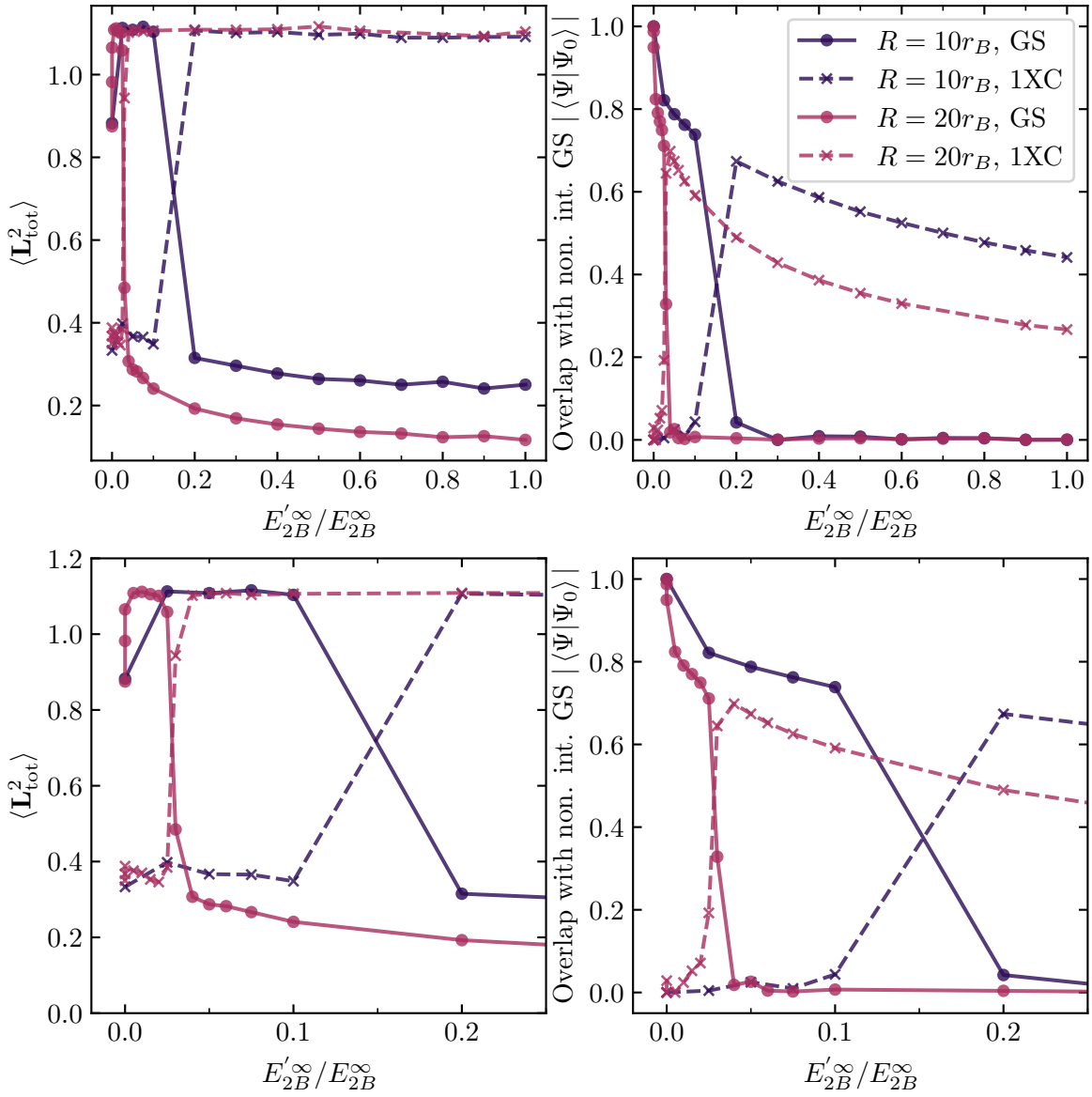

Figure 3.12. Angular momentum and overlaps with the non-interacting ground state of the ground and first excited state as a function of two-body binding energy. The left panels show the angular momentum expectation value $\langle \mathbf{L}^2_{\mathrm{tot}} \rangle$ of the ground (solid) and first excited state (dashed) at $r_0 = 0.8r_B$ for $R = 10r_B$ (purple) and $R = 20r_B$ (red) as a function of the varying two-body binding energy E'^{∞}_{2B}. The right panels show the overlap $|\langle \Psi | \Psi_0 \rangle|$ of the ground (solid lines) or first excited (dashed lines) state $|\Psi\rangle$ at a given value of $E'^{\infty}_{2B}/E^{\infty}_{2B}$ with the non-interacting ground state $|\Psi_0\rangle$ at $E'^{\infty}_{2B}/E^{\infty}_{2B} = 0$. The lower panels show enlargements of the crossover regions seen in the upper panels. In the angular momentum a crossover behavior between the polaron state at $\langle \mathbf{L}^2_{\mathrm{tot}} \rangle \approx 1.12$ and the dimer state at low values of $\langle \mathbf{L}^2_{\mathrm{tot}} \rangle$ is visible which coincides with the behavior observed also in Fig. 3.11. A similar behavior is seen in the overlap with the non-interacting ground state which is rather significant for the polaron state and almost vanishing for the dimer state.

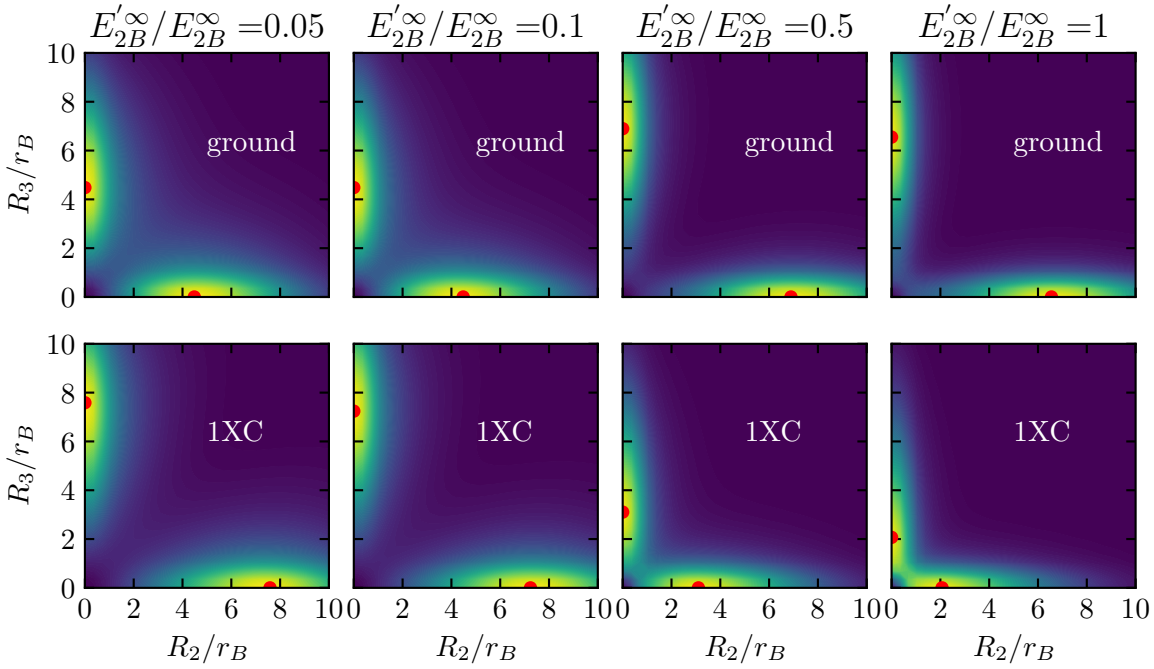

Figure 3.13. Reduced density distribution function u_1 of the ground (top) and the first excited state (bottom) for $E^{\infty'}_{2B}/E^{\infty}_{2B} = 0.05$, 0.1, 0.5 and 1 (from left to right) at $r_0 = 0.8r_B$, $R = 10r_B$. The red dots indicate the positions where the distribution function attains its maximal value. Molecule states feature a fermion located near the impurity and a fermion in a scattering state centered $\approx 7r_B$ away from the impurity (in a box with radius $R = 10r_B$). Unlike the molecule state, the polaron features a tighter confinement of the second fermion to the impurity which becomes tighter as $E^{\infty'}_{2B}$ increases.

thus adiabatically connected to it. The molecule/dimer state on the other hand holds close to vanishing overlap with the non-interacting ground state which comes as no surprise as it stems from strong interactions unlike the non-interacting ground state.

3.5.2 Spatial wavefunction analysis of the polaron and the molecule

To understand better the spatial structure of the polaron and molecule states observed in the previous subsection, let us analyze their reduced density distribution function u_1 which was introduced in Eq. (3.36). In Fig. 3.13 the u_1 function of the ground and the first excited state is shown for different two-body binding energies. While the contour plots corresponding to the polaron and the molecule look similar, they hold a qualitative difference in the position of the second, less confined fermion with respect to the position of the impurity: Molecule states feature a fermion located near the impurity and a further fermion in a scattering state centered $\approx 7r_B$ away from the impurity, which is on the order of the box radius $R = 10r_B$. The polaron on the other hand confines the second fermion much tighter to the impurity and as the two-body binding energy $E^{\infty'}_{2B}$ increases this confinement becomes tighter.

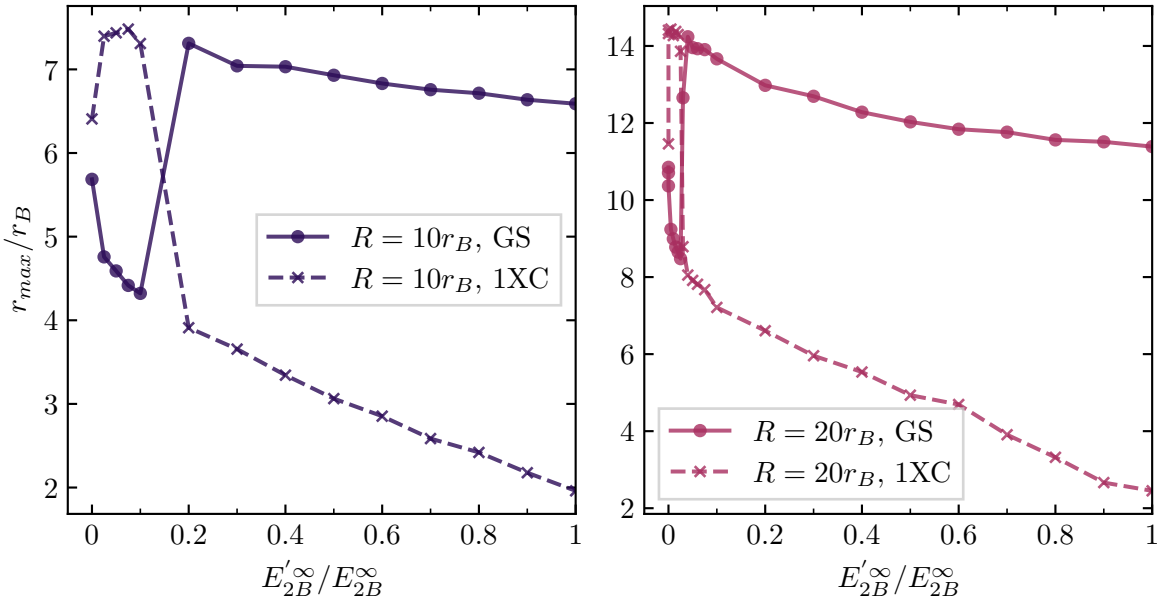

Figure 3.14. Position of the maximum r_{max} of the reduced density distribution function u_1 along the $R_2 = 0$ axis for the data shown in Fig. 3.11. This maximum is shown for the ground state as well as the first excited state wavefunction both for $R = 10r_B$ (left) and for $R = 20r_B$ (right). The transition/crossover behavior is clearly visible for both box sizes and the two states show qualitatively different behavior: the molecule is strongly sensitive to the box size R, while the polaron is strongly sensitive to the varying two-body bound state energy $E^{\infty'}_{2B}$.

To illuminate this behavior, using the reduced density distribution function u_1 of the SVM runs with $R = 10r_B$ and $R = 20r_B$ (shown in Fig. 3.11), we can determine the maximum r_{max} of the u_1 function for $R_2 = 0$

$$r_{max} = \max_{R_3} u_1(R_2 = 0, R_3) \tag{3.40}$$

as a function of $E^{\infty'}_{2B}$. Note that we may also lift the requirement of $R_2 = 0$ and define

$$(r^2_{max}, r^3_{max}) = \max_{R_2,R_3} u_1(R_2, R_3), \tag{3.41}$$

and we would find that except for very close to $E^{\infty'}_{2B} = 0$, either $r^2_{max} = 0$ or $r^3_{max} = 0$. Thus to keep better comparability, we use the r_{max} measure defined in Eq. (3.40). In Fig. 3.14 this measure is shown and as one can see there, for $R = 10r_B$, the position of the second fermion within the molecule state is nearly insensitive to the two-body binding energy $E^{\infty'}_{2B}$. For the polaron, the position decreases much stronger as $E^{\infty'}_{2B}$ increases. Comparing with the curves obtained for $R = 20r_B$ this picture solidifies: the position of the molecule maximum has almost doubled in comparison to $R = 10r_B$, while the polaron shows a behavior similar to that of $R = 10r_B$. The behavior observed in Fig. 3.14 thus matches the physical intuition that the position of the second fermion in the molecule state is strongly sensitive to the box size R, while the position of the second fermion in the polaron state is strongly sensitive to the varying two-body bound state energy $E^{\infty'}_{2B}$.

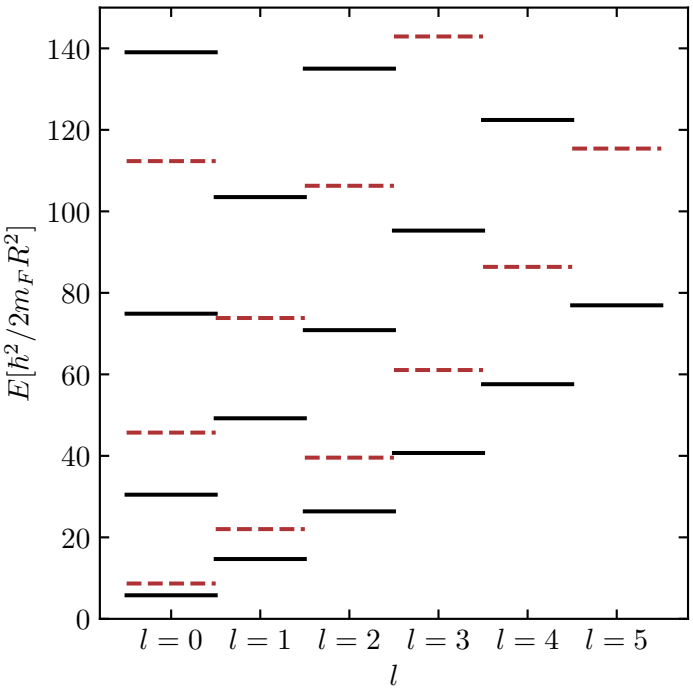

Figure 3.15. Level diagram of the non-interacting Hamiltonian Eq. (3.42) for $\alpha = 1.5$. Different (integer) angular momentum values l are shown and the energies are given in units of $\hbar^2/2m_F R^2$. Black, solid lines denote the spectrum of the fermions while red, dashed lines denote the spectrum of the impurity. The different lines for a single value of l represent the different values of n where the energy increases wit n. Note that every energy with $|l| > 0$ is twofold degenerate in $\pm l$.

3.5.3 Angular momentum expectation values $\langle \mathbf{L}^2_{\mathbf{tot}} \rangle$, $\langle \mathbf{L}^2_I \rangle$ and $\langle \mathbf{L}^2_F \rangle$ of the non-interacting ground state

The angular momentum expectation value $\langle \mathbf{L}^2_{\mathrm{tot}} \rangle$ of the non-interacting ground state can be computed exactly and serves as a further physical limit to which the state found in Figs. 3.11 and 3.12 can be compared. In the following we give a brief sketch of how this angular momentum value can be computed as it is not a standard computation.

For vanishing impurity-fermion and fermion-fermion interactions, the Hamiltonian reduces to a simply form

$$H = -\frac{\hbar^2}{2m_I}\nabla_1^2 - \frac{\hbar^2}{2m_F}\nabla_2^2 - \frac{\hbar^2}{2m_F}\nabla_3^2 \tag{3.42}$$

which due to a lack of interactions can be solved using a three-body wavefunction Ψ which consists of single particle wavefunctions ψ. The confinement range R imposes that any solution to this Hamiltonian fulfills $\psi(|\mathbf{r}| > R) = 0$. The single particle wavefunction solutions to the corresponding Schrödinger equation are given in radial coordinates by

$$\begin{aligned} \psi_{ln}(r,\theta) &= \frac{e^{il\theta}}{\sqrt{A_{ln}}} J_l\left(\frac{z_{ln} r}{R}\right), \\ A_{ln} &= \pi R^2 J_{|l|+1}(z_{ln})^2 \end{aligned} \tag{3.43}$$

where z_{ln} is the n-th zero of the l-th order Bessel function J_l and the single particle energies are given by

$$E_{ln} = \frac{\hbar^2}{2mR^2} z_{ln}^2. \tag{3.44}$$

As a result of the level diagram (see Fig. 3.15) and the requirement that the three-body wavefunction have vanishing total angular momentum, for $\alpha = 1.5$ the resulting three-body wavefunction is given by

$$\Psi(\mathbf{r}_1, \mathbf{r}_2, \mathbf{r}_3) = \sqrt{\frac{2}{A_{01} A_{11}^2}} \sin(\theta_2 - \theta_3) J_0\left(\frac{z_{01} r_1}{R}\right) J_1\left(\frac{z_{11} r_2}{R}\right) J_1\left(\frac{z_{11} r_3}{R}\right), \tag{3.45}$$

that is, the impurity is in $l = 0$ and the fermions are in $l = 1$ and $l = -1$, all for $n = 1$. Here r_i, θ_i parametrize the $\mathbf{r}_i$ in circular coordinates.

As defined in Eq. (3.27) the relative coordinates $\mathbf{R}_2$ and $\mathbf{R}_3$ along with the center-of-mass coordinate $\mathbf{R}_1$ are defined as

$$\begin{pmatrix} \mathbf{R}_1 \\ \mathbf{R}_2 \\ \mathbf{R}_3 \end{pmatrix} = \begin{pmatrix} \frac{m_I}{m_I+2m_F} & \frac{m_F}{m_I+2m_F} & \frac{m_F}{m_I+2m_F} \\ -1 & 1 & 0 \\ -1 & 0 & 1 \end{pmatrix} \begin{pmatrix} \mathbf{r}_1 \\ \mathbf{r}_2 \\ \mathbf{r}_3 \end{pmatrix} \tag{3.46}$$

and the corresponding momenta $\mathbf{P}_1, \mathbf{P}_2 \mathbf{P}_2$ are defined as

$$\begin{pmatrix} \mathbf{P}_1 \\ \mathbf{P}_2 \\ \mathbf{P}_3 \end{pmatrix} = \left(\begin{pmatrix} \frac{m_I}{m_I+2m_F} & \frac{m_F}{m_I+2m_F} & \frac{m_F}{m_I+2m_F} \\ -1 & 1 & 0 \\ -1 & 0 & 1 \end{pmatrix}^{-1} \right)^T \begin{pmatrix} \mathbf{p}_1 \\ \mathbf{p}_2 \\ \mathbf{p}_3 \end{pmatrix}. \tag{3.47}$$

Using that

$$\begin{aligned} \mathbf{r}_i \times \mathbf{p}_i &= -i \begin{pmatrix} x_i \\ y_i \end{pmatrix} \times \begin{pmatrix} \partial_{x_i} \\ \partial_{y_i} \end{pmatrix} \\ &= -i \left[r_i \sin(\theta_j - \theta_i) \partial_{r_j} + \frac{r_i}{r_j} \cos(\theta_j - \theta_i) \partial_{\theta_j} \right] \end{aligned} \tag{3.48}$$

one can then compute the action of $\mathbf{L}_{\text{tot}}$ on Ψ as

$$\begin{aligned} \hat{\mathbf{L}}_{\text{tot}} \Psi(\mathbf{r}_1, \mathbf{r}_2, \mathbf{r}_3) &= (\mathbf{R}_2 \times \mathbf{P}_2 + \mathbf{R}_3 \times \mathbf{P}_3) \Psi(\mathbf{r}_1, \mathbf{r}_2, \mathbf{r}_3) \\ &= \left[\frac{m_F}{m_I + 2m_F} ((2\mathbf{r}_1 - \mathbf{r}_2 - \mathbf{r}_3) \times \mathbf{p}_1 + (\mathbf{r}_2 - \mathbf{r}_3) \times (\mathbf{p}_2 - \mathbf{p}_3)) \right. \\ &\left. + \frac{m_I}{m_I + 2m_F} ((-\mathbf{r}_1 + \mathbf{r}_2) \times \mathbf{p}_2 + (-\mathbf{r}_1 + \mathbf{r}_3) \times \mathbf{p}_3) \right] \Psi(\mathbf{r}_1, \mathbf{r}_2, \mathbf{r}_3) \end{aligned} \tag{3.49}$$

and finally the angular momentum expectation value can be computed as

$$\langle \mathbf{L}_{\text{tot}}^2 \rangle = \left(\prod_{i=1}^{3} \int_0^R dr_i \int_0^{2\pi} d\theta_i r_i \right) \left| \hat{\mathbf{L}}_{\text{tot}} \Psi(\mathbf{r}_1, \mathbf{r}_2, \mathbf{r}_3) \right|^2. \tag{3.50}$$

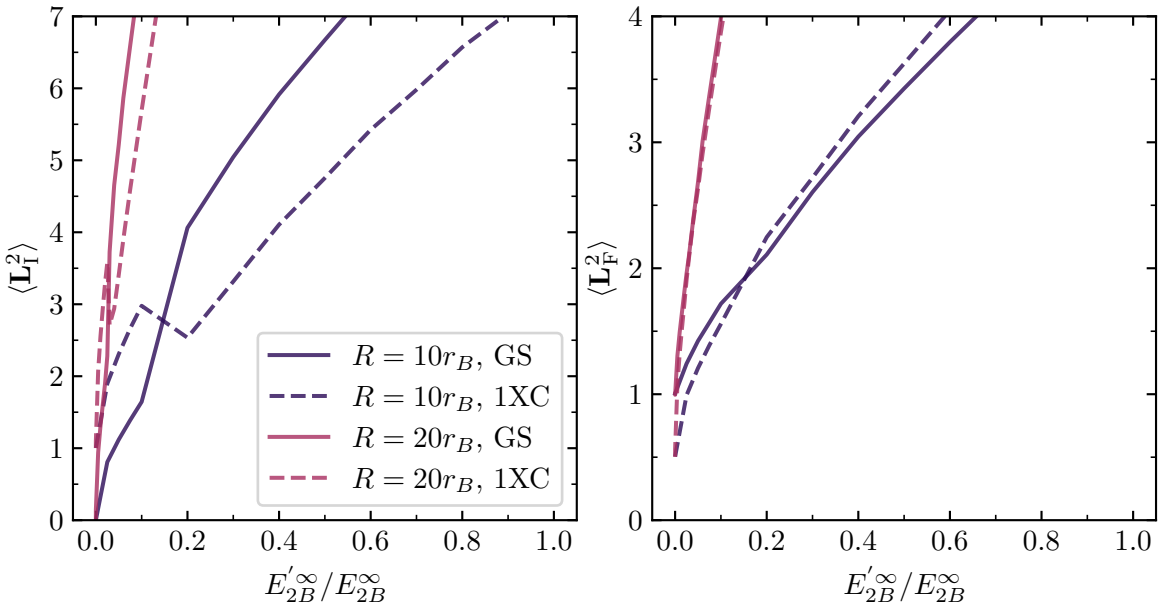

Figure 3.16. Angular momentum expectation values $\langle \mathbf{L}_I^2 \rangle = \langle (\mathbf{r}_1 \times \mathbf{p}_1)^2 \rangle$ and $\langle \mathbf{L}_F^2 \rangle = \langle (\mathbf{r}_2 \times \mathbf{p}_2)^2 \rangle$ of the ground (solid) and the first excited (dashed) state wavefunctions shown in Figs. 3.11 and 3.12 as a function of $E_{2B}^{\prime\infty}/E_{2B}^{\infty}$. For both $R = 10r_B$ (purple) and $R = 20r_B$ (red), the expectation values of the ground and first excited states in Eqs. (3.45) and (3.52) are found.

For the non-interacting ground state wavefunction in Eq. (3.45) and $\alpha = 1.5$, this integral can be evaluated numerically and yields

$$\langle \mathbf{L}_{\text{tot}}^2 \rangle \approx 1.0345. \tag{3.51}$$

This value differs from the values found using the SVM in Fig. 3.11: There, the angular momentum expectation value is approximately $\langle \mathbf{L}_{\text{tot}}^2 \rangle \approx 0.87$ at $E_{2B}^{\prime\infty} = 0$ and quickly rises to $\langle \mathbf{L}_{\text{tot}}^2 \rangle \approx 1.12$. Interestingly, this behavior is attained for both $R = 10r_B$ and $R = 20r_B$. The nature of this deviation is not entirely clear: As marked by the dash-dotted lines in Fig. 3.11, in the case of $R = 10r_B$ the ground and first excited state energies found by the SVM lie slightly lower than the energy of the non-interacting ground state computed using Eqs. (3.44) and (3.45). At the same time, the energies computed for $R = 20r_B$ lie sightly higher.

In Fig. 3.16 for the ground and the first excited states shown in Figs. 3.11 and 3.12, the angular momentum expectation values of the impurity $\langle \mathbf{L}_I^2 \rangle = \langle (\mathbf{r}_1 \times \mathbf{p}_1)^2 \rangle$ and the fermions $\langle \mathbf{L}_F^2 \rangle = \langle (\mathbf{r}_2 \times \mathbf{p}_2)^2 \rangle$ are shown as $E_{2B}^{\prime\infty}$ is varied. For $E_{2B}^{\prime\infty} \to 0$ for both $R = 10r_B$ and $R = 20r_B$ the ground state has $\langle \mathbf{L}_I^2 \rangle = 0$ and $\langle \mathbf{L}_F^2 \rangle = 1$ as expected from the analytical wavefunction in Eq. (3.45). Meanwhile, the first excited state has $\langle \mathbf{L}_I^2 \rangle = 1$ and $\langle \mathbf{L}_F^2 \rangle = 0.5$ as can be inferred from the first excited state wavefunction (impurity in $l = 1$, fermions in $l = 0, -1$)

$$\Psi(\mathbf{r}_1, \mathbf{r}_2, \mathbf{r}_3) = \psi_{11}(r_1, \theta_1) \left[\psi_{-11}(r_2, \theta_2) \psi_{01}(r_3, \theta_3) - \psi_{-11}(r_3, \theta_3) \psi_{01}(r_2, \theta_2) \right]. \tag{3.52}$$

The reason for the deviation in $\langle \mathbf{L}^2_{\mathrm{tot}} \rangle$ is thus unclear: while the SVM seems to find the correct ground state with the correct distribution of angular momentum onto the impurity and the fermions, the SVM energy lies slightly below the analytical result, which should be a strict lower bound; especially for a method that can only approximate the ground state. A possible explanation for these deviations may lie in the nature of the confinement: While the analytical result is obtained for a hard wall, the SVM uses a confinement that merely approximates a hard wall as can be seen in Eq. (3.2).

3.5.4 Could the polaron be the trimer? Comparison of the simplified Ansatz in Eq. (3.9) in the polaron-to-molecule transition

Having explored both the polaron-to-molecule/dimer transition and the dimer-to-trimer transition, it is natural to ask whether in this $1+2$ problem the polaron and the trimer state are the same. After all, they share a similar angular momentum expectation value $\langle \mathbf{L}^2_{\mathrm{tot}} \rangle$ and at least conceptually one may be tempted to interpret them similarly: While the interpretation is that the dimer state has bound a fermion closely to the impurity and has a further fermion in a scattering state, the difference between polaron and trimer is not as clear. Leaving aside the qualitative nature of the confinement of fermions to the impurity, the trimer has two fermions confined close to the impurity, while the polaron attracts all fermions to the impurity, which in a $1+2$ system is two fermions. Naturally, this argument would then connect the polaron to a tetramer state in a $1+3$ system.

To investigate this possible similarity, we recall that when describing the dimer-to-trimer transition in Section 3.4, we were able to use a simplified wavefunction for which $\phi_1 = \phi_2 = \phi_3 = 0$ in Eq. (3.6). The dimer and trimer state were described sufficiently well within this Ansatz. On the other hand, for the polaron-to-molecule/dimer transition, this simplification was not used and instead the more general Ansatz with $\phi_1 \neq$, $\phi_2 \neq 0$, $\phi_3 \neq 0$ was used. In Fig. 3.17 the simplified Ansatz with $\phi_1 = \phi_2 = \phi_3 = 0$ is compared with results obtained using the more general Ansatz. As is can be seen, for small values of $E^{\infty'}_{2B}/E^{\infty}_{2B}$ the energy of the ground state of the simplified Ansatz follows the first excited state energy of the more general Ansatz, while at larger values of $E^{\infty'}_{2B}/E^{\infty}_{2B}$ the energy of the ground state of the simplified Ansatz follows the ground state energy of the more general Ansatz. This change in behavior coincides with the polaron-to-molecule transition observed in Figs. 3.11 and 3.12 and indicates that the simplified wavefunctions Ansatz is not capable of capturing the polaron state, while it is capable of capturing the dimer state. This is also evident from the corresponding angular momentum expectation values shown in Fig. 3.17, where it can be seen that the angular momentum expectation values of the ground state in the simplified wavefunction Ansatz reproduces the behavior of the dimer state. Finally, in Fig. 3.18 the angular momentum expectation values $\langle \mathbf{L}^2_{\mathrm{I}} \rangle$ and $\langle \mathbf{L}^2_{\mathrm{F}} \rangle$ are shown and at $E^{\infty'}_{2B}$ a ground state with $\langle \mathbf{L}^2_{\mathrm{I}} \rangle = 1$ and $\langle \mathbf{L}^2_{\mathrm{F}} \rangle = 0.5$ is obtained which corresponds to the first excited state in the general Ansatz shown in Fig. 3.16. As the non-interacting ground state in Eq. (3.45) is of the form $\sim \sin(\theta_{\mathbf{r}_2} - \theta_{\mathbf{r}_3}) J_0(|\mathbf{r}_1|) J_1(|\mathbf{r}_2|) J_1(|\mathbf{r}_3|)$ this

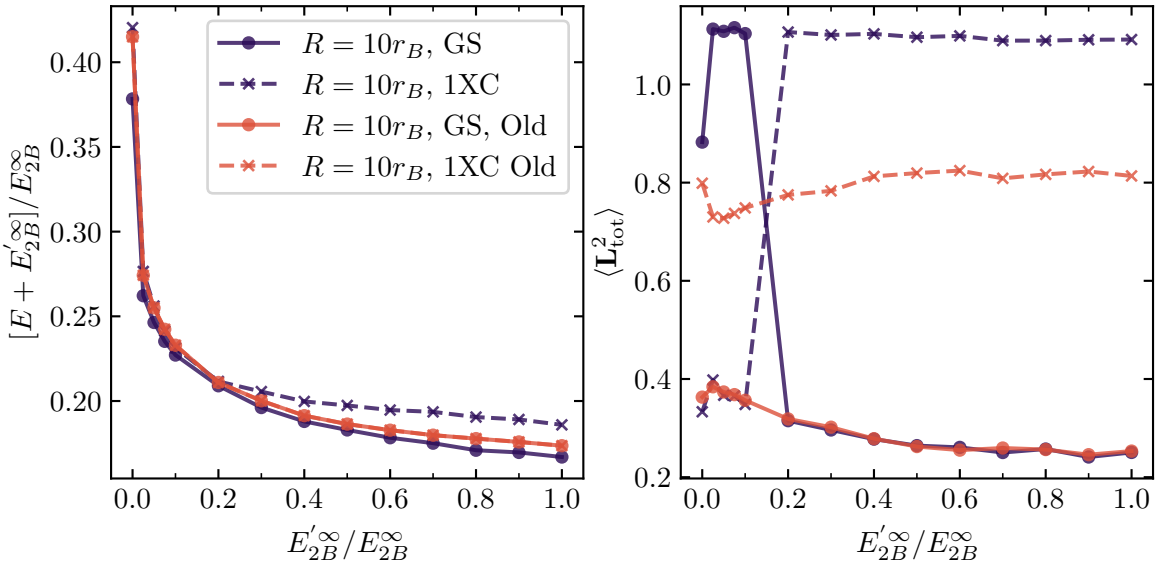

Figure 3.17. Comparison of the simplified Ansatz Eq. (3.9) to the more general Ansatz Eq. (3.6). The energy (left) and angular momentum expectation value $\langle \mathbf{L}^2_{\mathrm{tot}} \rangle$ (right) of the ground (solid) and first excited state (dashed) are shown at $r_0 = 0.8$, $R = 10r_B$ as a function of the varying two-body binding energy E'^{∞}_{2B}. The simplified Ansatz Eq. (3.9) with $\phi_1 = \phi_2 = \phi_3 = 0$ (orange) and the more general Ansatz Eq. (3.6) with $\phi_1 \neq$, $\phi_2 \neq 0$, $\phi_3 \neq 0$ are used for comparison. The simplified Ansatz can reproduce the dimer state, while it cannot reproduce the polaron state.

can easily be explained: Of course, this form cannot be obtained exactly using the ECG wavefunctions, but to have at least an explicit dependence on the sine of the angle between $\mathbf{r_2}$ and $\mathbf{r}_3$ one would have to set $\theta_3 = \pi/2$ in Eq. (3.6), at variance with $\theta_1 = \theta_2 = \theta_3 = 0$.

Furthermore, the overlap with the non-interacting ground state shows now transition or crossover behavior using this Ansatz as can be seen in Fig. 3.18.

As a result, we can conclude that while the trimer and the polaron state may seem similar at a first glance, they are in fact not the same and are adiabatically connected to different states, the polaron to the non-interacting ground state and the trimer to a strongly-interacting three-body bound state.

3.6 Discussion

In this chapter we started by studying the influence of confinement and finite interaction ranges on the formation of ground state trimers in confined three-body systems where two identical fermions interact with a mobile quantum impurity. We showed that the position of the dimer-to-trimer transition, previously characterized in Refs. [177, 186, 235], varies significantly under these effects. Our results show how these effects can, in principle, be leveraged to realize p-wave trimers in atomically-thin semiconductors and ultracold quantum gases.

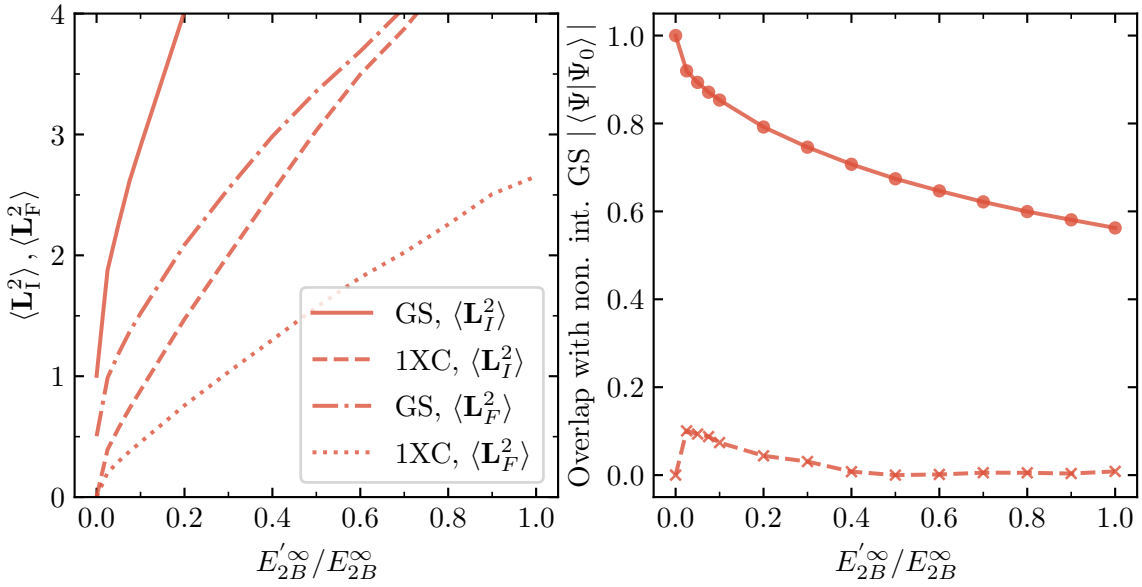

Figure 3.18. Angular momentum expectation values $\langle \mathbf{L}_I^2 \rangle$, $\langle \mathbf{L}_F^2 \rangle$ (left) and overlap with the non-interacting ground state (right) of the ground (solid) and the first excited (dashed) state as a function of $E'^{\infty}_{2B}/E^{\infty}_{2B}$ for the results shown in Fig. 3.17. The non-interacting ground state obtained using this simplified Ansatz admits the angular momentum expectation values as the first excited state shown in Fig. 3.16.

While in two-dimensional cold atom systems already a great variety of mass ratios is available, trimer formation could be further enhanced using a longitudinal trapping confinement. In TMDs, the available mass ratios are more restricted (unless, e.g., flat Moiré bands are considered). However, our results show that a finite exciton-electron interaction range as well as confinement can enhance and stabilize trimer formation. Furthermore, we have argued that, given a suitable TMD, trimers can, in principle, survive Coulomb repulsion as long as the effective charge, given by material parameters such as the dielectric constant, remains below a critical value.

In regards to interpreting confinement as a means to imitate a finite bath density, the remarkable robustness of the dimer-to-trimer transition suggests that bosonic p-wave trimers might already appear as the ground state of realistic TMD heterostructures [22]. Our work thus highlights that experiments may already be close to the point of exploring exciton-induced p-wave electron pairing, opening up the avenue to novel mechanisms of exciton-mediated p-wave superconductivity in van-der Waals materials.

We then moved on to study physics akin to the Fermi polaron to see whether traces of this many-body behavior may already be found in the few-body limit. We showed that there is a crossover between a state, adiabatically connected to the non-interacting ground state, to a dimer state, which we interpret as a few-body analog of the polaron-to-molecule transition. This crossover becomes sharper as the confinement length increases which we also saw for the dimer-to-trimer transition, suggesting that this crossover connects to the polaron-to-molecule transition. Interestingly, the point

at which this occurs shows the same qualitative behavior as the transition point in the true many-body regime.

Moving forward from our work, there are several exciting paths to pursue. For one, it has been shown that for systems with a greater number of bath particles also higher-order bound states may play an important role [235], which could lie lower in energy than the trimer state. The influence of confinement and finite range on these states is unexplored, and might drastically change the position of ground state transitions as well as the occurrence of these transitions in the first place. Similarly, to confirm the connection of the polaron-to-molecule transition studied in this chapter, one might look to study the same system in $1 + 3$ and $1 + 4$, to see if the same trend towards the many-body regime appears, possibly even approaching the many-body observables asymptotically.

Going beyond $1 + N$-type systems, the phase diagram of Bose-Fermi mixtures [2] at a given density imbalance of the constituent species might be studied in few-body systems with comparable density ratios. In this regard, the occurrence, nature, and dynamics of interesting phenomena such as phase separation in the many-body regime could be illuminated by corresponding observations in a few-body system. For instance, in a system of type $2 + 3$, one might compare the formation of a four- or five-particle bound state to the coexistence of a dimer with a trimer.

Cold atomic systems offer a wealth of tunable parameters such as mass ratio, bound-state energy and confinement [48]. Moreover, ultracold polar molecules and magnetic atoms with strong dipolar interactions can now be realized experimentally [132, 259, 260]. Exploiting the long-range character of their interactions, the effects of Coulomb repulsion between identical fermions in solid-state structures can now be mimicked in cold atom systems, highlighting these as an exciting platform to gain new insights into the physics of the exciton-electron mixtures in layered van der Waals materials.

Chapter 4

Superconductivity induced by strong electron-exciton coupling in doped atomically thin semiconductor heterostructures

This chapter is based on the following publication:

[4] **J. von Milczewski**, X. Chen, A. Imamoglu, R. Schmidt,
Superconductivity induced by strong electron-exciton coupling in doped atomically thin semiconductor heterostructures,

arXiv:2310.10726 (2023).

In this chapter we study a mechanism to induce superconductivity in atomically thin semiconductors where excitons mediate an effective attraction between electrons. Our model includes interaction effects beyond the paradigm of phonon-mediated superconductivity and connects to the well-established limits of Bose and Fermi polarons. By accounting for the strong-coupling physics of trions, we find that the effective electron-exciton interaction develops a strong frequency and momentum dependence accompanied by the system undergoing an emerging BCS-BEC crossover from weakly bound s-wave Cooper pairs to a superfluid of bipolarons. Even at strong-coupling the bipolarons remain relatively light, resulting in critical temperatures of up to 10% of the Fermi temperature. This renders heterostructures of two-dimensional materials a promising candidate to realize superconductivity at high critical temperatures set by electron doping and trion binding energies.

4.1 Introduction

In the past decade van der Waals materials have been shown to host a plethora of quantum phases of matter ranging from Mott and Wigner crystals [236, 238, 239,

261], the anomalous quantum Hall effect [237, 262–264], chiral edge states [265] and Chern insulators [266] to interaction-driven insulators [267]. Following the observation of unconventional superconductivity in NbSe2 monolayers [268], the discovery of superconductivity in magic-angle graphene [269, 270] and twisted bilayers of atomically thin semiconductors [36] have advanced van der Waals materials as a platform to realize novel forms of superconductivity.

The existence of strongly bound excitons in transition metal dichalcogenides (TMD) [22] has inspired studies exploring new routes to superconductivity. Recently, repulsive pairing mechanisms in twisted Moiré materials came into focus [271–277]. In this setting flat bands limit Fermi energies and thus the critical transition temperature. In absence of flat bands, theoretical works have explored exciton-mediated interactions between electrons analogous to the phonon-exchange in conventional BCS theory [92, 95, 101, 102, 278]. However, TMDs feature an exciton-electron coupling that is strong enough to feature exciton-electron bound states, trions, that remain stable up to room temperature [22], which cannot be captured by previously employed Fröhlich-type models [92, 95, 101, 102, 278]. Including this non-perturbative pairing physics in theoretical models has remained a central challenge, and the question how trion formation impacts superconductivity has been left unanswered.

In this chapter, we present a theory of boson-induced superconductivity which incorporates the strong-coupling physics of the Bose-Fermi mixtures [1, 2, 34, 99, 100, 124] comprised of excitons and electrons. We do not rely on flat bands and our theory applies to heterostructures of van der Waals materials where electrons interact with excitons in separated layers. We account for trion formation by considering beyond-linear electron-exciton coupling terms that extend the Fröhlich paradigm of electron-phonon exchange [104, 105]. As a result we find that the effective exciton-electron vertex becomes strongly retarded and non-local leading to strong dressing of electrons by the excitonic background. As the doping level in the TMD is tuned, the mutual dressing of electrons and excitons leads to an emergent crossover from a weak-coupling BCS superconductor into a superfluid state of bipolarons, akin to the BCS-BEC crossover observed in cold atoms [244, 279–294]. Remarkably, we find the bipolarons to remain relatively light, facilitating the transition temperature to reach values of up to 10 % of the Fermi temperature. The physics of a BCS-BEC crossover emerging from mediated interactions complements the direct interaction mechanism in cold atoms and opens perspectives to reach high transition temperatures in van der Waals materials.

In the following, in Section 4.2 we motivate and introduce the model we work with. Next, in Section 4.3 we introduce our diagrammatic approach to computing the critical pairing temperature while taking into account strong-coupling physics between electrons and excitons. In Section 4.4 we provide detailed analytical expressions and provide information on the practical computation of the diagrams introduced in Section 4.3. Finally, in Section 4.5 we show the resulting critical pairing temperatures and extend on the conditions under which these may be interpreted as critical temperatures of superconductivity. In Section 4.6 we draw conclusions from our results. Furthermore, in Section 4.7 we provide an RG analysis of the used Hamiltonian

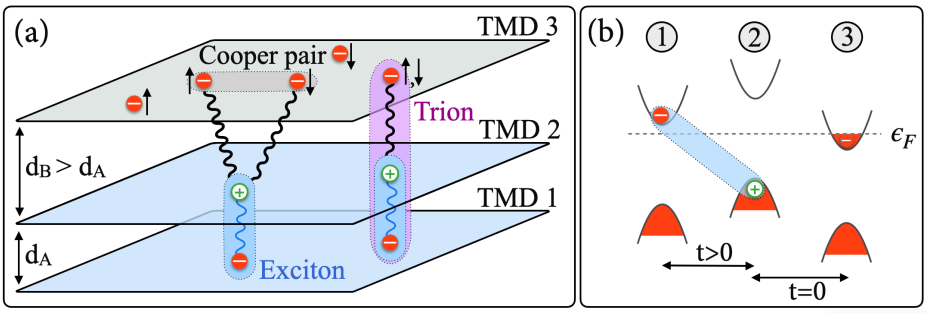

Figure 4.1. (a) Illustration of the TMD heterostructure. Charge carriers in the tunnel-coupled ($t > 0$) layers 1 and 2 form interlayer excitons which can bind with electrons in the spatially separated, tunnel-decoupled ($t = 0$) top layer into deeply-bound trions. (b) Using gates the band alignment of the layers can be modified to allow doping of the third layer, while the interlayer (12) exciton remains stable. ϵ_F marks the Fermi level.

and show that strong-coupling is a relevant interaction mechanism which cannot be disregarded safely.

4.2 Model

We start from a two-dimensional Fermi gas of electrons ($\hat{c}_{\uparrow\mathbf{p}}$, $\hat{c}_{\downarrow\mathbf{p}}$) in absence of a magnetic field. The electrons interact with long-lived interlayer excitons in a spatially separated heterobilayer which could be realized in a MX_2-WX_2-MX'_2 heterostructure (X, X' label chalcogen atoms) shown in Fig. 4.1(a). Electron tunneling between the top layers is fully suppressed by a large layer separation $d_B > d_A$ enabling s-wave pairing between electrons in the top layer. Gating can be employed to allow for doping of layer 3 in presence of a long-lived interlayer-(12) exciton. Since interlayer-(12) exciton energies for vanishing separation of the lower TMD layers 1 and 2 would be in the range 100 to 150 meV [39], Fermi energies of around 30 meV in the TMD layer 3 would be possible. Importantly, due to the dipolar character of the system, the interlayer-(123) trion can have a substantial binding energy $\epsilon_T \sim 30$ meV comparable with the Fermi energy which brings the system into the strong coupling regime. We also emphasize that the generation of interlayer excitons need not require optical excitation [37, 38]. The interaction between electrons and the interlayer excitons, described by operators $\hat{X}^\dagger_{\mathbf{p}}$, can be modelled by an attractive contact interaction of strength g which can be directly related to the trion energy ϵ_T [53, 295]. In experiments the value of ϵ_T could for instance be tuned by changing the thickness of the hBN layer separating TMD layers 2 and 3, or using dielectric engineering [22, 63, 258]. The corresponding

Hamiltonian is given by

$$\begin{aligned}\hat{H} = &\sum_{\sigma=\uparrow,\downarrow}\sum_{\mathbf{k}} \epsilon^c_{\mathbf{k}} \hat{c}^\dagger_{\sigma\mathbf{k}}\hat{c}_{\sigma\mathbf{k}} + \sum_{\mathbf{k}} \epsilon^X_{\mathbf{k}} \hat{X}^\dagger_{\mathbf{k}}\hat{X}_{\mathbf{k}} \\ &+ \frac{g\sqrt{n_0}}{\sqrt{A}} \sum_{\sigma=\uparrow,\downarrow}\sum_{\mathbf{kq}} \hat{c}^\dagger_{\sigma\mathbf{k}+\mathbf{q}}\hat{c}_{\sigma\mathbf{k}}(\hat{X}^\dagger_{\mathbf{q}} + \hat{X}_{-\mathbf{q}}) \\ &+ \frac{g}{A} \sum_{\sigma=\uparrow,\downarrow}\sum_{\mathbf{kk'q}} \hat{c}^\dagger_{\sigma\mathbf{k}+\mathbf{q}}\hat{c}_{\sigma\mathbf{k}}\hat{X}^\dagger_{\mathbf{k'}-\mathbf{q}}\hat{X}_{\mathbf{k'}},\end{aligned} \tag{4.1}$$

with A the system area. Assuming an effective mass approximation, the electron and exciton dispersion relations are

$$\epsilon^c_{\mathbf{k}} = \frac{\mathbf{k}^2}{2m_F} \tag{4.2}$$

$$\epsilon^X_{\mathbf{k}} = \frac{\mathbf{k}^2}{2m_B}. \tag{4.3}$$

Although we investigate superconductivity in TMD, the Hamiltonian in Eq. (4.1) may also be realized in ultracold atomic systems where the mass ratio between bosons and fermions can vary substantially. Considering the universal relevance of the model, we work at an equal mass ratio of excitons and electrons $m_B = m_F$. As the Fermi gas is spin-balanced, both components $\sigma = \uparrow, \downarrow$ are described by the Fermi wavevector $k_F = \sqrt{4\pi n_F}$ with density n_F. The Fermi level ϵ_F and temperature T_F are given by $\epsilon_F = T_F = k_F^2/2m$. We set $\hbar = k_B = 1$.

We employ a mean-field description of the Bose gas that is sufficient to demonstrate the mechanism of exciton-induced superconductivity enhanced by the presence of trions. This mean-field picture, in which the exciton gas is described by a condensate of density n_0, is justified by the algebraic decay of the boson correlator in the BKT phase [296–300] which occurs on scales larger than the range of induced interactions. In Eq. (4.1) we have expanded in fluctuations around the condensate, i.e.

$$\hat{X}_{\mathbf{k}} \to \delta_{\mathbf{k},0}\sqrt{n_0 A} + \hat{X}_{\mathbf{k}}. \tag{4.4}$$

Considering the much smaller separation between layers 1 and 2 compared to recent experiments [37], we can consider the regime of a weakly interacting exciton gas with healing length ξ much larger than the interelectron distance. Moreover, considering that the exciton-electron interaction dominantly probes the particle-like branch of the exciton Bogoliubov dispersion we treat the excitons as an ideal Bose gas.

The first interaction term in Eq. (4.1) describes a Fröhlich-type electron-phonon interaction $\lambda \sim g\sqrt{n_0}$. In perturbative approaches to exciton-induced superconductivity [95, 101, 102, 278], induced interactions between electrons originated solely from this term and scale with λ^2; i.e. independent of the sign of λ. However, the microscopic origin of this phonon-like interaction is the attractive potential parametrized by the last term $\sim g$ in Eq. (4.1). This term is responsible for the formation of trions, and its relevance has been demonstrated by observations in cold atoms and TMD that show strong deviations from the Fröhlich model [34, 106–108]. Using a renormalization group (RG) analysis presented at the very end of this chapter in Section 4.7, we

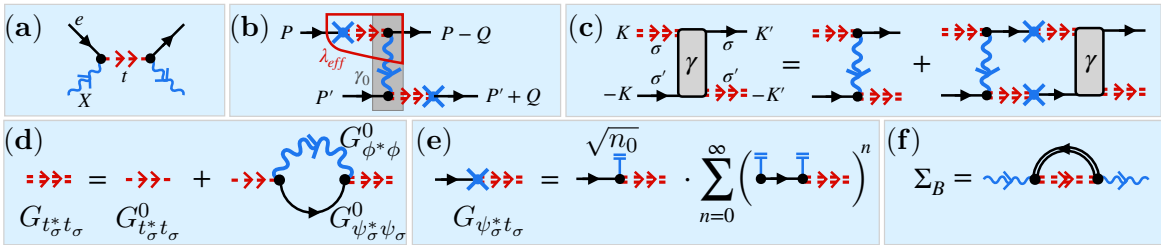

Figure 4.2. Feynman diagrams for (a) bare exciton-electron scattering vertex, (b) induced electron-electron vertex, (c) renormalized electron-trion scattering vertex, (d) full trion propagator, and (e) off-diagonal electron-trion propagator. The exciton self-energy (f) is used within the Hugenholtz-Pines condition and contains the renormalized electron propagator (black, double line). Bare electron (black, single line) and excitons (blue) interact via the exchange of the trion field (bare: dashed red, renormalized: double red line). The Bethe-Salpether equation in (c) contains the renormalized, hybridized electron-trion propagator $G_{\psi^*_\sigma t_\sigma}$ shown in (e), representing the geometric sum of condensate insertions. Analytical expressions are introduced in Sections 4.3 and 4.4.

show this term to be RG-relevant and crucial in the strong-coupling regime. Unlike previous works we consider this term fully and study its non-perturbative effect on exciton-induced electron pairing.

Note, that in principle the Hamiltonian in Eq. (4.1) involves terms $\sim g n_0 \hat{c}^\dagger \hat{c}$ due to the presence of the condensate. However, g is regulated using an upper momentum cutoff Λ [170] and thus these terms vanish as Λ is increased and are hence left out in Eq. (4.1) and in the following.

4.3 Method

In this section, we introduce our diagrammatic method with a focus on its qualitative nature. The technical details along with the analytical expressions and numerical computation methods of the different introduced quantities will be covered in detail in Section 4.4.

To study electron pairing we employ finite-temperature quantum field theory [49, 50]. Using a diagrammatic approach, it is practical to study the system in a two-channel model that is equivalent to Eq. (4.1). To arrive at this model one employs a Hubbard-Stratonovich transformation where a trion field t manifests the strong-coupling physics and formally mediates the electron-exciton interaction (Fig. 4.2(a)). The corresponding action is given by

$$S = \int_Q \left[\phi^*_Q P_\phi(Q) \phi_Q + \begin{pmatrix} \psi^*_{\sigma,Q} \\ t^*_{\sigma,Q} \end{pmatrix}^T \begin{pmatrix} P_\psi(Q) & h\sqrt{n_0} \\ h\sqrt{n_0} & P^0_t(Q) \end{pmatrix} \begin{pmatrix} \psi_{\sigma,Q} \\ t_{\sigma,Q} \end{pmatrix} \right] + h \int_{P,Q} \left[\psi^*_{\sigma,Q-P} \phi^*_P t_{\sigma,Q} + \text{h.c.} \right], \tag{4.5}$$

where the relation $g = -h^2/P_t^0$ establishes the equivalence of the models (4.1) and (4.5) in the contact interaction limit $h \to \infty$. The fields $\rho \in \{\psi_{\sigma,Q}, t_{\sigma,Q}, \phi_Q\}$ correspond to electrons, trions, and fluctuations of the exciton gas around its mean value $\sqrt{n_0}$. Capital letters $Q = (\mathbf{q}, \omega_n)$ refer to momenta $\mathbf{q}$ and Matsubara frequencies ω_n,

$$P_\phi(\mathbf{q}, \omega) = -i\omega + \epsilon^X_{\mathbf{q}} - \mu_B \tag{4.6}$$

$$P_\psi(\mathbf{q}, \omega) = -i\omega + \epsilon^c_{\mathbf{q}} - \mu_F, \tag{4.7}$$

and $\int_Q$ contains Matsubara and spin summations. Electron and exciton chemical potentials are denoted by μ_F, μ_B.

The presence of the exciton condensate hybridizes electrons and trions into a joint excitation (see the term $\sim\sqrt{n_0} t^*_\sigma \psi_\sigma$ in Eq. (4.5)). This hybridization is key for inducing the electron-electron interaction shown in Fig. 4.2(b). Due to the hybridization, this vertex is internally governed by a trion-electron scattering vertex at tree level $h^2\gamma^0(Q) t^*_\sigma \psi^*_{\sigma'} \psi_\sigma t_{\sigma'}$ (gray box in Fig. 4.2(b)), where $\gamma^0(Q) = 1/P_\phi(Q)$ represents the exchange of an exciton. We study exciton-induced Cooper pair formation in terms of the renormalization of this trion-electron vertex, accounting for the infinite ladder of exciton exchanges (Fig. 4.2(c)). In this ladder resummation, the strong-coupling physics between excitons and electrons is accounted for by the self-energy $\Sigma^t_\sigma(\mathbf{p}, \omega)$ of the trion field (Fig. 4.2(d), Section 4.4.1). As a result of the $(\mathbf{p}, \omega)$-dependence of Σ_t, the effective electron-exciton vertex (red box in Fig. 4.2(b)), becomes retarded and non-local, adding a new ingredient to the mechanism of exciton-induced superconductivity.

We approach the pairing problem within a non-self-consistent T-matrix (NSCT) approach [1, 54–56, 59, 137, 170, 172] (for details see Sections 4.4.1 to 4.4.4), which describes both the non-perturbative scattering physics of electrons and excitons, and the self-energy corrections for the excitons and electrons via the diagrams shown in Fig. 4.2(e,f). In this way we recover the associated Fermi [1, 170–176] and Bose polaron formation [103, 301] observed in ultracold atoms [2, 9, 106–108, 128–130, 233] and TMDs [33, 34, 302–305]. Recently it has been shown that this approach applies equally to nearly population balanced, strongly-coupled Bose-Fermi mixtures [1, 2, 99, 100]. Hence, our approach is based on a model (4.1) that has been firmly tested in experiments on a quantitative level.

We incorporate self-energy effects by using the renormalized (matrix-valued) Green's function G,

$$\left(G^{-1}\right)_{\rho\rho'} = \left(G_0^{-1}\right)_{\rho\rho'} - \frac{\partial^2}{\partial\rho\partial\rho'} \sum_\sigma t^*_\sigma \Sigma^t_\sigma t_\sigma \Big|_{\psi_\sigma, \phi, t_\sigma = 0}, \tag{4.8}$$

rather than the bare Green's function G_0 defined by

$$\left(G_0^{-1}\right)_{\rho\rho'} = \frac{\partial^2}{\partial\rho\partial\rho'} S \Big|_{(\psi_\sigma, \phi, t_\sigma) = 0}. \tag{4.9}$$

In Eq. (4.8) we have suppressed $(\mathbf{p}, \omega)$-arguments; for analytic expressions see Section 4.4.2. The pole of the trion Green's function $G_{t^*_\sigma t_\sigma}$ in the two-body limit determines the trion energy ϵ_T [295].

The electron pairing problem is solved in terms of the effective Bethe-Salpether equation for the renormalized electron-trion vertex function (Fig. 4.2(c)),

$$\gamma(K-K',K,K')_{\sigma,\sigma'} = \gamma_0(K-K') + h^2 \int_P \left[\gamma_0(K-P) \times G_{\psi^*_\sigma t_\sigma}(P) G_{t^*_{\sigma'}\psi_{\sigma'}}(-P) \gamma(P-K',P,K')_{\sigma,\sigma'}\right]. \tag{4.10}$$

A singularity in γ indicates a pairing instability. As Pauli exclusion suppresses bound state formation between equal spin fermions, we consider s-wave pairing of electrons of opposite spin, $\sigma \neq \sigma'$ [1]; see Section 4.4.5. In Eq. (4.10) we focus on a subset of diagrams where the γ-vertex couples to itself and which contains the off-diagonal Green's function $G_{\psi^*_\sigma t_\sigma}$ (Fig. 4.2(e)). This approximation leaves out exchange diagrams leading to bosonic three-body bound state formation already in the few-body limit [227]. Hence we expect that including such diagrams would enhance Cooper pair formation even further.

The Green's functions for electrons and excitons in Eq. (4.8) contain the chemical potentials μ_F and μ_B. For given n_0, n_F, T and ϵ_T, the chemical potentials are determined self-consistently to fulfill two conditions:

(i) The number equation, $n_F = \frac{T}{(2\pi)^2} \int d\mathbf{p} \sum_n G_{\psi^*_\sigma \psi_\sigma}(\mathbf{p}, \omega_n)$, to set the density of fermions.

(ii) The Hugenholtz-Pines relation, $0 = \mu_B + \Sigma_B(\mathbf{0}, 0)$, to ensure that excitations from the condensate are gapless (the condensate is kept as a background field in our model), where $\Sigma_B(\mathbf{p}, \omega)$ is the boson self-energy of the bosons (see Fig. 4.2(f)), which will be introduced in Section 4.4.3.

These two conditions naturally incorporate the physics of both Bose and Fermi polarons: For a vanishing fermion density $n_F = 0$, (i) determines the energy of Bose polarons [103] in agreement with experiments [34, 106–108]. In the opposite limit of a vanishing boson density $n_0 = 0$, (ii) yields the Fermi polaron energy in excellent agreement with experiments [9, 33, 54–56, 59, 128–130, 170–172, 302–305].

4.4 Analytical expressions and practical computation

In this section, we present explicit expressions for the method introduced in the previous section. Furthermore, as the introduced diagrammatics contain finite temperature Matsubara sums, we provide details on their practical computation as a straightforward computation may not result in converging numerics.

The results of the calculations described here and in the previous section will be shown in Section 4.5 and readers not interested in the technical details of the previously presented method may safely skip this section.

[1] We assume equal interaction strength of ↑-, ↓-electrons with the excitons as the layer separation strongly suppresses exchange effects.

As the diagrammatics introduced in Fig. 4.2 have a certain hierarchy to them, in the following we will discuss the different objects appearing in the diagrammatics. Starting from the smallest building block, the trion self-energy, we will work our way up from there.

4.4.1 Trion self-energy

The trion self-energy Σ_t^σ shown in Fig. 4.2(d) is given by

$$\begin{aligned}\Sigma_t^\sigma(\mathbf{p},\omega) &= h^2 \lim_{T\to 0} \int_{\mathbf{q},n} G^0_{\psi_\sigma^* \psi_\sigma}(\mathbf{p}-\mathbf{q},\omega-\nu_n) G^0_{\phi^*\phi}\ (\mathbf{q},\nu_n) \\ &= \frac{h^2}{(2\pi)^3} \int d\mathbf{q} d\nu \frac{1}{P_\psi(\mathbf{p}-\mathbf{q},\omega-\nu) P_\phi(\mathbf{q},\nu)}. \end{aligned} \tag{4.11}$$

Here we have approximated the diagram by its zero temperature $T = 0$ expression which allows us to obtain an analytical result that can be readily employed in the following numerical computation. Based on favorable comparisons of $T = 0$ theory and experimental observations at finite temperature in the Fermi polaron limit, we expect finite temperature corrections to yield only small quantitative changes to the results. The microscopic short-range interaction has to be regularized and renormalized (see Section 1.6) which gives the condition [1, 170, 171]

$$P_t^0(\mathbf{q},\omega) = \frac{h^2}{(2\pi)^2} \int_{|\mathbf{q}|<\Lambda} d\mathbf{q} \frac{1}{\epsilon_T + 2\mathbf{q}^2}, \tag{4.12}$$

where Λ is the upper momentum cutoff [170], so that

$$P_t(\mathbf{q},\omega) = P_t^0(\mathbf{q},\omega) - \Sigma_t^\sigma(\mathbf{p},\omega). \tag{4.13}$$

This function is related to the non-self-consistent T-matrix used commonly in single-channel approaches [1] via

$$T(\mathbf{p},\omega) = -\frac{h^2}{P_t(\mathbf{q},\omega)}, \tag{4.14}$$

which can easily be seen when the trion field is integrated out. For $\mu_F > 0$ it is given in Eq. (3) of Ref [172]. For $\mu_F < 0$ and $\omega > 0$ it is given by [1]

$$P_t(\mathbf{p},\omega) = -h^2 \frac{i\pi + \log\left(\frac{\epsilon_T}{\mu_F+\mu_B-\mathbf{p}^2/2+i\omega}\right)}{8\pi}, \ (\mu_F < 0, \omega > 0) \tag{4.15}$$

and one can use $P_t(\mathbf{p},\omega) = P_t(\mathbf{p},-\omega)^*$ to obtain values with $\omega < 0$.

4.4.2 Renormalized Green's functions

Having introduced the trion self-energy to capture the strong coupling physics and the trion formation between electrons and excitons, the propagators used in the remaining

diagrams are computed using Eq. (4.8). They are thus obtained as

$$G_{\psi_\sigma^*\psi_\sigma}(\mathbf{p},\omega) = \left(\frac{P_t}{P_tP_\psi - h^2n_0}\right)(\mathbf{p},\omega) \tag{4.16}$$

$$G_{t_\sigma^* t_\sigma}(\mathbf{p},\omega) = \left(\frac{P_\psi}{P_tP_\psi - h^2n_0}\right)(\mathbf{p},\omega) \tag{4.17}$$

$$G_{t_\sigma^*\psi_\sigma}(\mathbf{p},\omega) = \left(\frac{-h\sqrt{n_0}}{P_tP_\psi - h^2n_0}\right)(\mathbf{p},\omega) \tag{4.18}$$

$$G_{\psi_\sigma^* t_\sigma}(\mathbf{p},\omega) = \left(\frac{-h\sqrt{n_0}}{P_tP_\psi - h^2n_0}\right)(\mathbf{p},\omega) \tag{4.19}$$

$$G_{\phi^*\phi}\ (\mathbf{p},\omega) = \left(\frac{1}{P_\phi}\right)(\mathbf{p},\omega), \tag{4.20}$$

where changing the order of fermionic (bosonic) indices results in an additional factor of $-1(1)$. The remaining matrix elements of the matrix valued Green's function G, which cannot be generated from changing the order of indices in Eqs. (4.16) to (4.20), vanish.

4.4.3 Exciton self-energy

As discussed in Section 4.3, the bosonic chemical potential is fixed by the Hugenholtz-Pines relation used in the condition (ii). The exciton self-energy entering this condition is represented by the diagram in Fig. 4.2(f). It is given by

$$\Sigma_B(\mathbf{q},\nu_m) = \frac{h^2T}{(2\pi)^2}\int d\mathbf{p}\sum_{n,\sigma} G_{t_\sigma^* t_\sigma}(\mathbf{p}+\mathbf{q},\omega_n+\nu_m)G_{\psi_\sigma\psi_\sigma^*}(\mathbf{p},\omega_n). \tag{4.21}$$

Instead of numerically evaluating the Matsubara sum directly (leading to poor convergence), we rather compute an equivalent contour integral for which a contour is laid around the Matsubara frequencies and then deformed to the real axis to arrive at

$$\Sigma_B(0,0) = \sum_\sigma \frac{1}{4\pi^3}\int d\mathbf{p}\int_{-\infty}^{\infty} d\Omega n_F(\Omega)\,\mathrm{Im}\left(\frac{P_t(\mathbf{p},-iz)P_\psi(\mathbf{p},-iz)}{\left[P_t(\mathbf{p},-iz)P_\psi(\mathbf{p},-iz) - h^2n_0\right]^2}\right)\Bigg|_{z=\Omega+i0^+} \tag{4.22}$$

where $n_F(\Omega) = 1/(1+e^{\Omega/T})$ is the Fermi-distribution function. This allows for efficient numerical evaluation.

In obtaining Eq. (4.22) from Eq. (4.21), a modification analogous to Section 4.2 of Ref. [52] was conducted, where by introducing suitable poles using a Fermi/Bose distribution function a Matsubara summation was mapped onto an equivalent contour integration around the imaginary frequency axis. Using that the integrand may have poles and branch cuts along the real axis, but is otherwise analytic, this contour can then be inflated where the arcs to infinity vanish and only the counter-propagating paths along the real axis remain which result in Eq. (4.22).

4.4.4 Fermion number equation

Similar to the exciton self-energy Σ_B in Eq. (4.21), the Matsubara summation for the number equation, entering the condition (i) of Section 4.3, converges only slowly. Hence we again deform the integration contour to wrap around the real freqency axis. In this way, the fermion density can be computed as follows:

$$\begin{aligned} n_F =& -\frac{1}{(2\pi)^2}\int d\mathbf{p}\frac{1}{\beta}\sum_n \frac{P_t(\mathbf{p},\omega_n)}{P_t(\mathbf{p},\omega_n)P_\psi(\mathbf{p},\omega_n)-h^2n_0} \\ =& \frac{1}{(2\pi)^2}\int d\mathbf{p}\frac{1}{\pi}\int_{-\infty}^{\infty} d\Omega n_F(\Omega)\,\mathrm{Im}\left(\frac{P_t(\mathbf{p},-iz)}{P_t(\mathbf{p},-iz)P_\psi(\mathbf{p},-iz)-h^2n_0}\right)\Bigg|_{z=\Omega+i0^+} \end{aligned} \tag{4.23}$$

4.4.5 Computation of electron-trion scattering vertex

As mentioned in Section 4.3, we perform an s-wave projection of the electron-trion scattering vertex in which we consider scattering at the Fermi-wavevector k_F of the balanced two component Fermi gas of electrons

$$\tilde{\gamma}_{\sigma,\sigma'} = \frac{1}{2\pi}\int d\theta_{\mathbf{k},\mathbf{k}'}\frac{1}{2}\Big[\gamma(K_+-K'_+,K_+,K'_+)_{\sigma,\sigma'}+\gamma(K_--K'_-,K_-,K'_-)_{\sigma,\sigma'}\Big]. \tag{4.24}$$

Here $K_\pm = (\mathbf{k},\pm\pi T), K'_\pm = (\mathbf{k}',\pm\pi T)$, $|\mathbf{k}| = |\mathbf{k}'| = k_F$, $\theta_{\mathbf{k},\mathbf{k}'}$ denotes the angle between $\mathbf{k}$ and $\mathbf{k}'$ and $\tilde{\gamma}_{\sigma,\sigma'}$ is used within Eq. (4.10).

Using Eqs. (4.10) and (4.24) the expression for the s-wave projection of the electron-electron scattering vertex is then given by

$$\begin{aligned} \tilde{\gamma}_{\sigma,\sigma'} = \tilde{\gamma}^0_{\sigma,\sigma'} + \tilde{\gamma}_{\sigma,\sigma'}\int_{\mathbf{p}}\frac{T}{2}\sum_{\omega_n}\left(\frac{1}{P_\phi(\mathbf{p}-\mathbf{k},\omega_n+\pi T)}+\frac{1}{P_\phi(\mathbf{p}-\mathbf{k},\omega_n-\pi T)}\right) \\ \times \frac{h^2n_0}{[P_t(\mathbf{p},\omega_n)P_\psi(\mathbf{p},\omega_n)-h^2n_0]\,[P_t(-\mathbf{p},-\omega_n)P_\psi(-\mathbf{p},-\omega_n)-h^2n_0]}, \end{aligned} \tag{4.25}$$

where $|\mathbf{k}| = k_F$. The pairing instability is computed by rearranging Eq. (4.25) to $\tilde{\gamma}_{\sigma,\sigma'} = \tilde{\gamma}^0_{\sigma,\sigma'}/(1-F)$ and solving for $F = 1$ where

$$F = \frac{\tilde{\gamma}_{\sigma,\sigma'}-\tilde{\gamma}^0_{\sigma,\sigma'}}{\tilde{\gamma}_{\sigma,\sigma'}}. \tag{4.26}$$

F represents the integral and sum part in Eq. (4.25). As this integral decays faster in frequency than the number equation and the exciton self-energy, the Matsubara summation in Eq. (4.25) can be directly computed numerically, without the need to deform the integration contour.

4.4.6 Solving for the chemical potentials and determining the critical pairing temperature

To estimate the critical pairing temperature for given values of ϵ_T/ϵ_F and n_0/n_F, the critical pairing condition (see Section 4.4.5) needs to be solved for, while fulfilling

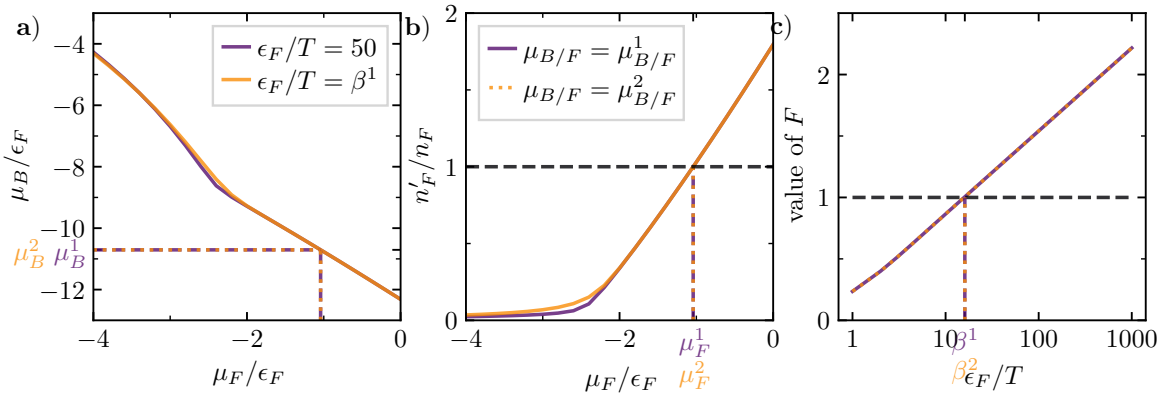

Figure 4.3. Exemplary optimization procedure to simultaneously solve for the Hugenholtz-Pines relation and the number equation at $\epsilon_T = 5\epsilon_F$, $n_0/n_F = 1$. (a) The boson chemical potential $\mu_B(\mu_F, n_0, \epsilon_T, T)$ to fulfill the Hugenholtz-Pines relation is shown as a function of the fermion chemical potential. At an initial temperature of $T_0 = \epsilon_F/50$ (purple) the critical boson chemical potential is computed as a function of the fermion chemical potential and the resulting pairs of $(\mu_F, \mu_B(\mu_F, n_0, \epsilon_T, T_0))$ are used to compute the corresponding fermion density $n'_F(\mu_F, \mu_B(\mu_F, n_0, \epsilon_T, T_0))$, shown in (b). The point at which $n'_F(\mu^1_F, \mu_B(\mu^1_F, n_0, \epsilon_T, T_0)) = n_F$ is used to determine μ^1_F. From this, the corresponding boson chemical potential μ^1_B is computed as $\mu^1_B = \mu_B(\mu^1_F, n_0, \epsilon_T, T_0)$. In (c) the value of F obtained using μ^1_F and μ^1_B is shown for varying temperatures and it is used to determine a critical inverse temperature $\beta^1 = 1/T_1$ by locating where $F = 1$. This temperature is used in a second iteration (yellow) from which μ^2_F and μ^2_B are found which are used in (c) to find a critical inverse temperature $\beta^2 = 1/T_2$. This cycle is repeated until the chemical potentials and critical temperatures are found to be converged.

the number equation (i) and the Hugenholtz-Pines relation (ii). This is done in a self-consistent optimization procedure which we describe in the following.

First, for given values of $n_0/\epsilon_F, \epsilon_T/\epsilon_F$ and an initial temperature of $T_0 = \epsilon_F/50$ the critical boson chemical potential to fulfill the Hugenholtz-Pines relation (i) is computed as $\mu_B(\mu_F, n_0, \epsilon_T, T_0)$ for a varying fermion chemical potential μ_F. Next, these chemical potentials are used within the number equation (4.23) to compute the Fermi density $n'_F(\mu_F, \mu_B(\mu_F, n_0, \epsilon_T, T_0))$. From this, the fermion chemical potential μ^1_F fulfilling $n_F = n'_F(\mu^1_F, \mu_B(\mu^1_F, n_0, \epsilon_T, T_0))$ is found and the corresponding boson chemical potential is determined as $\mu^1_B = \mu_B(\mu^1_F, n_0, \epsilon_T, T_0)$.

Using μ^1_F and μ^1_B, the critical temperature T_1, where $F = 1$, is then found using Eq. (4.25). This critical temperature T_1 is then used as an input to find μ^2_F and μ^2_B which are in turn used to find a critical temperature T_2. This cycle is repeated until the chemical potentials and the temperature have converged to a fixed point which simultaneously satisfies the number equation, the Hugenholtz-Pines relation and the critical pairing condition. For given values of $n_0/\epsilon_F, \epsilon_T/\epsilon_F$ the temperature found gives the critical pairing temperature T^*_c. This procedure is shown in Fig. 4.3 for the first two iterations of this cycle.

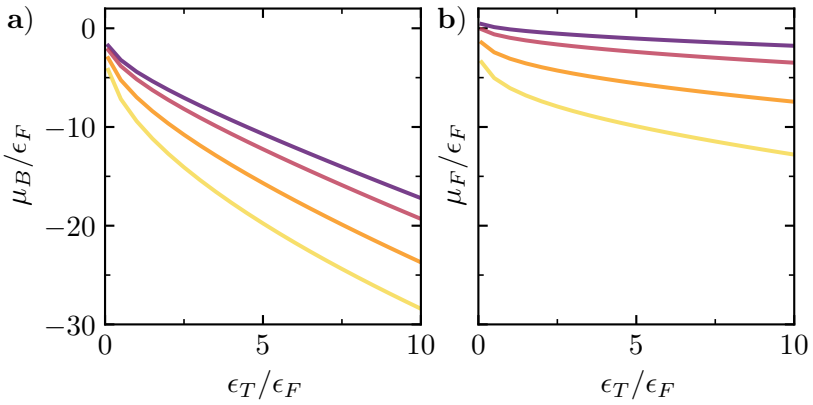

Figure 4.4. The boson (a) and fermion (b) chemical potentials μ_B and μ_F at the critical temperature T_c^* are shown as a function of ϵ_T/ϵ_F for the condensate densities $n_0/n_F = 1$ (purple), 2 (red), 5 (orange), and 10 (yellow). These potentials are simultaneous solutions of the number equation (i) and the Hugenholtz-Pines relation (ii), and to satisfy these, the chemical potentials increase in magnitude with increasing binding energy.

The resulting chemical potentials for the results shown in Fig. 4.5 of Section 4.5 are given in Fig. 4.4.

4.5 Results: critical pairing temperature

The critical temperature T_c^* for the instability towards s-wave pairing is determined by lowering the temperature until γ develops a singularity as described in Section 4.4.6. The results for T_c^* are shown in Fig. 4.5 in dependence of the dimensionless trion energy ϵ_T/ϵ_F for different exciton densities n_0/ϵ_F.

As ϵ_T/ϵ_F is increased, T_c^*/T_F increases monotonously. Similarly, T_c^* increases with n_0, reflecting the role of excitons as the mediators of interactions. Increasing interactions and condensate density leads to dressing of bosons and fermions by many-body fluctuations. This results in a strong increase of the boson and fermion chemical potentials (see Fig. 4.4) as imposed by the conditions (i) and (ii). Since these chemical potentials enter the propagators in our diagrammatics, they suppress pairing fluctuations. Despite this suppression, we find that T_c^* keeps on increasing without apparent bound.

In the weak-coupling limit, where T_c^* is small, an effective BCS theory applies. In the BCS regime, it has been established that T_c^* is close to the actual BKT transition temperature T_c towards superfluidity [300, 306, 307]. This equivalence typically applies when the size of Cooper pairs l_C is extended over many interfermion distances $d{\sim}k_F^{-1}$. However, as l_C becomes comparable to the interfermion distance, T_c^* rather starts to indicate only the formation of pairs but does not imply their transition into a superfluid state, i.e. $T_c < T_c^*$.

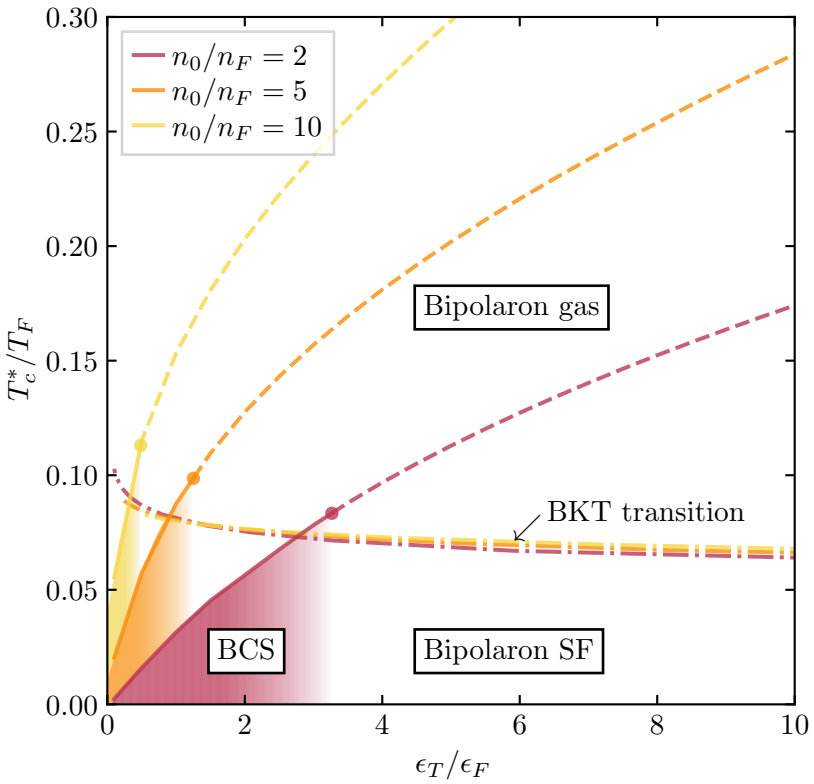

Figure 4.5. Critical pairing temperatures T_c^*/T_F as a function of trion energy ϵ_T/ϵ_F for various condensate densities. In the BCS limit where T_c^* is close to the BKT temperature T_c (see Fig. 4.6) the data is shown as solid lines, while at strong coupling bipolarons are formed and the dashed lines represent their dissociation temperature. The solid dots represent the critical interaction strength $[\epsilon_T/\epsilon_F]^c$ where the bipolaron energy becomes comparable to the Fermi energy (see also Fig. 4.6 and Section 4.5.1). The dash-dotted lines give $T_c = T_{BKT}$ where the bipolaron gas turns superfluid (see Section 4.5.2).

4.5.1 Determining the boundary of the BCS regime from the bipolaron binding energy

At strong coupling we expect the superfluid transition temperature T_c to be more accurately captured by a BKT theory of a Bose gas of bipolarons and a different criterion to determine T_c is thus required. At zero temperature the vertex described in Eq. (4.10) and the s-wave projected pairing vertex $\tilde{\gamma}_{\sigma,\sigma'}$ defined in Eq. (4.24) admit a bound state between two electrons even in the polaron limit where $n_F = 0$, $n_0 > 0$ [127], representing a bipolaron. By determining where the bipolaron energy E_{BP} becomes comparable to the Fermi energy ϵ_F, we obtain an estimate for where the Cooper pair size becomes comparable to the interparticle distance, $l_C \approx d$, which yields an estimate for the point where the system crosses over from a BCS-type to a BKT/BEC-type behavior.

To this end, we calculate E_{BP} by solving Eq. (4.10) in the polaron limit. The critical values of $[\epsilon_T/\epsilon_F]^c$ corresponding to this criterion are shown in Fig. 4.5 as dots

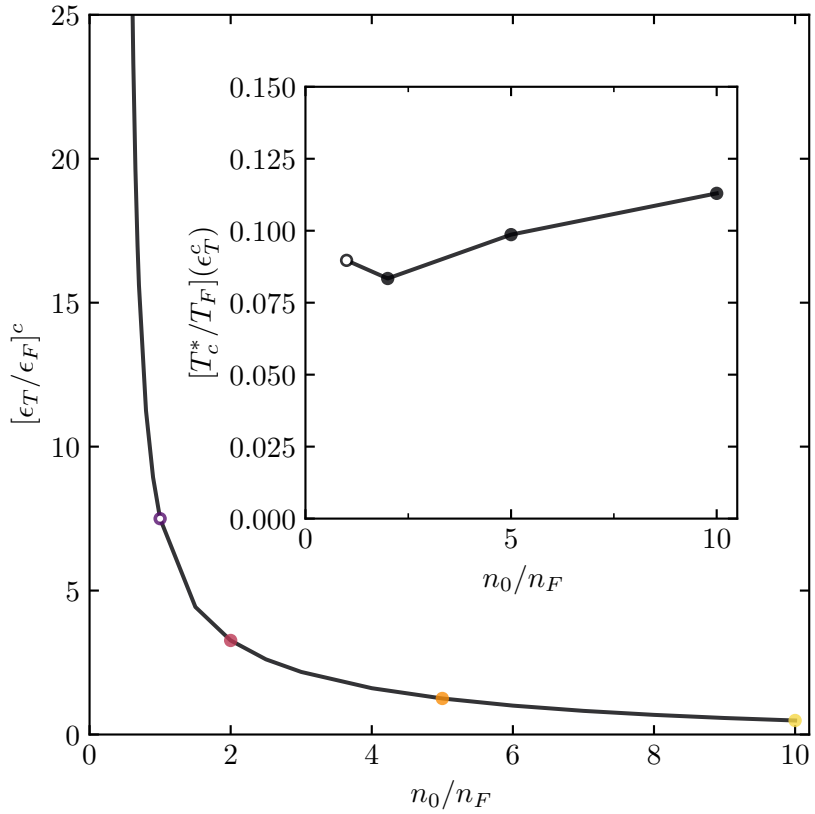

Figure 4.6. Critical interaction strength ϵ_T/ϵ_F (as a function of condensate density n_0/n_F) beyond which the bipolaron binding energy exceeds the Fermi energy. Colored points mark densities n_0/n_F shown in Fig. 4.5. Inset: Critical temperature at the critical interaction strengths. For illustration we also show a data point for $n_0/n_F = 1$ (open circle) where trion formation might deplete the condensate to a degree beyond our description [1, 2, 100, 171, 173].

and the full dependence on n_0/n_F is shown in Fig. 4.6. For interaction strengths beyond $[\epsilon_T/\epsilon_F]^c$ a description in terms of pairs that immediately condense as they form is clearly invalid. In this regime, T_c^* should instead be regarded as the molecular dissociation temperature of bipolarons. Bipolarons at T_c^* form a thermal bipolaron gas that has to be cooled further to facilitate the transition into a superfluid state.

To compute the Bipolaron energy, we note that finding a singularity in $\tilde{\gamma}$ implies the formation of a bound state between two Bose polarons, which we refer to as the bipolaron [127]. At $T = 0$ in the polaron limit ($n_F = 0$) the exciton self-energy vanishes identically and as a result we set $\mu_B = 0$. Thus for given values of ϵ_T, n_0 there exists a critical chemical potential $\mu_{F,n_F=0}(n_0, \epsilon_T)$ for which

$$n_F = 0 \text{ for } \mu_F < \mu_{F,n_F=0}(n_0, \epsilon_T),$$
$$n_F > 0 \text{ for } \mu_F > \mu_{F,n_F=0}(n_0, \epsilon_T).$$

This chemical potential in fact determines the Bose polaron energy which, for three dimensional systems, has been shown to agree remarkable well with experimental observations [106].

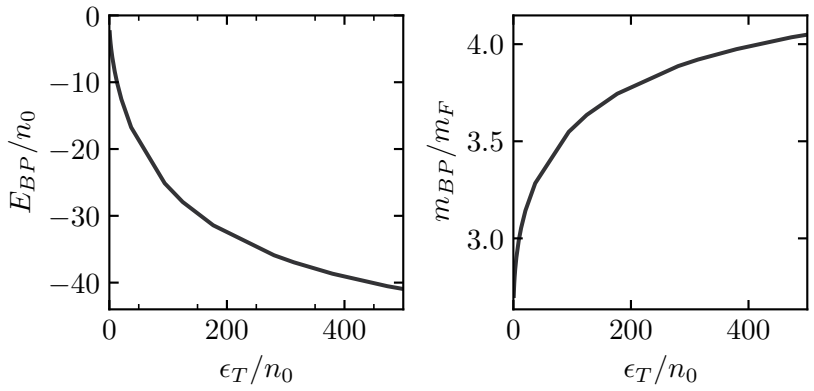

Figure 4.7. Bipolaron binding energy E_{BP} (left) and bipolaron effective mass m_{BP} (right) as a function of the trion energy ϵ_T. The energies are given in units of condensate density n_0 while the mass is given in units of the fermion mass m_F. With increasing ϵ_T the bipolaron becomes deeper bound and acquires a moderate effective mass.

The binding energy of the bipolaron is determined from the divergence of $\tilde{\gamma}_{BP}$,

$$\tilde{\gamma}_{BP} = \tilde{\gamma}^0_{BP} + \tilde{\gamma}_{BP} \int \frac{d\mathbf{p}d\omega}{(2\pi)^3} \frac{h^2 n_0}{P_\phi(\mathbf{p},\omega)} \times \frac{1}{P_t(\mathbf{p},\omega)P_\psi(\mathbf{p},\omega) - h^2 n_0} \frac{1}{P_t(-\mathbf{p},-\omega)P_\psi(-\mathbf{p},-\omega) - h^2 n_0}, \tag{4.27}$$

which is obtained from Eq. (4.25) in the limit $k_F \to 0$, $T \to 0$. The divergence of $\tilde{\gamma}_{BP}$ occurs at a fermion chemical potential $\mu_{F,BP}(n_0,\epsilon_T) < \mu_{F,n_F=0}(n_0,\epsilon_T)$. Thus the bipolaron binding energy is given as

$$E_{BP} = 2\left[\mu_{F,BP}(n_0,\epsilon_T) - \mu_{F,n_F=0}(n_0,\epsilon_T)\right]. \tag{4.28}$$

The resulting bipolaron binding energies are shown in Fig. 4.7. Hence, requiring the binding energy per particle of the bipolaron to be smaller than the Fermi energy each fermion experiences, we require

$$\mu_{F,n_F=0}(n_0,\epsilon_T) - \epsilon_F < \mu_{F,BP}(n_0,\epsilon_T) < \mu_{F,n_F=0}(n_0,\epsilon_T) \tag{4.29}$$

for the BCS theory to be applicable. The resulting critical dimensionless interaction strengths ϵ_T/ϵ_F for given values of n_0/n_F are shown in Fig. 4.6 and the end points of the BCS regime are indicated in Fig. 4.5.

4.5.2 Approximation of the BKT transition temperature

For large ϵ_T/n_0, bipolarons are sufficiently deeply bound that, at finite fermion density $n_F > 0$, the system can be described by an effective theory of weakly interacting, rigid bosons using BKT theory [300, 308–310]. To estimate the critical temperature for the BKT transition into the superfluid state, we employ the Nelson criterion [300, 308–310],

$$T_{BKT} = \frac{2\pi n_F}{m_{BP}} \frac{1}{\log\left(\frac{\eta}{4\pi}\log\left(\frac{1}{n_F d_*^2}\right)\right)}. \tag{4.30}$$

Here the density of bipolarons is given by n_F (all fermions can be assumed to be paired into bipolarons), and $\eta \approx 380$ [300]. The bipolaron-bipolaron scattering length is given by d_* , and m_{BP} is the effective bipolaron mass. The bipolaron scattering length is approximated by the binding length of the bipolaron [300], which in turn is parametrized by the bipolaron binding energy as

$$d_* = \sqrt{-\frac{1}{2E_{BP}}\left(\frac{1}{m_F} + \frac{1}{m_F + m_B}\right)}. \tag{4.31}$$

The bipolaron effective mass is computed by evaluating Eq. (4.27) at a finite incoming momentum $\mathbf{q}$ which is distributed along the two fermionic propagator legs as $\mathbf{p} + \mathbf{q}/2$ and $\mathbf{q}/2 - \mathbf{p}$. From this, the bipolaron dispersion relation is computed as a function of $|\mathbf{q}|$ and the effective bipolaron mass m_{BP} is obtained from a quadratic fit to this dispersion relation. The resulting bipolaron effective mass is shown in Fig. 4.7.

We note that the bipolarons remain relatively light which, similar to recent studies of bipolarons in the Peierls model [311, 312], facilitates rather large values of T_c. The BKT transition temperatures obtained from Eq. (4.30) are shown in Fig. 4.5 as dashed-dotted lines. We see that the predictions from the BCS limit and the bipolaron theory intersect in the expected region indicated by the dots in Fig. 4.5.

4.5.3 BCS-BEC crossover

Connecting these two results for T_c from weak to strong coupling makes evident that the systems is governed by an *emerging* BCS-BEC crossover from superfluid Cooper pairs to a quasi-condensate of bipolarons.

Remarkably, despite originating from mediated interactions, the maximal T_c/T_F in our model reaches values on the order of 10%, not far below the values obtained in the conventional model of the BCS-BEC crossover [183, 223, 295, 300, 306, 313–318] which describes fermions that interact via direct, short-range potentials. We estimate this maximum value of T_c/T_F by considering the temperature at the endpoints calculated in Fig. 4.5. The results are shown in the inset of Fig. 4.6 and demonstrate insensitivity with respect to the density of the exciton gas. In particular at exciton densities $n_0/n_F \gg 1$ the critical temperature remains robust. At such densities, neither thermal nor interaction-driven depletion of the condensate —not taken into account in our work— plays a significant role, attesting to the robustness of the mechanism of trion-enhanced, exciton mediated superconductivity.

4.6 Conclusion

Incorporating the strong-coupling physics of exciton-electron mixtures, we have shown that exciton-mediated pairing of electrons in doped, atomically thin semiconductor heterostructures offers a promising route towards realizing superconductivity at high temperatures T_c/T_F. Our work applies in the experimentally realizable regime where exciton densities are larger than the electron density. A unified description of the

strong-coupling regime where all scales, ϵ_F, n_0, ϵ_T are of the same order is an interesting venue for future studies. In this regime, a fully self-consistent treatment of quasiparticles is required and interaction driven condensate depletion may have a significant effect.

In this chapter we did not discuss the impact of the underlying repulsive Coulomb interaction. While this can be justified by screening at sufficient electron densities (as evidenced by the agreement of the model (4.1) with experimental observations [33]), it remains an open problem to formally study the interplay of Coulomb screening and pairing fluctuations. Ultimately this competition may result in p-wave pairing becoming the leading instability in certain density regimes [3] while, in turn, higher-order correlation functions [227] may favor the s-wave pairing studied in this work.

4.7 RG analysis of the extended Fröhlich model in the few-body limit

For the interested reader, in this section we conduct a renormalization group (RG) analysis in the few-body limit of the running coupling constants within the Hamiltonian, introduced in Eq. (4.1) of Section 4.2. To begin, we consider the action

$$\begin{aligned} S = &\int_Q \phi_Q^* P_\phi(Q)\phi_Q + \psi_Q^* P_\psi(Q)\psi_Q \\ &+\lambda \int_{Q,P} \psi_Q^*\psi_P \left(\phi_{P-Q}^* + \phi_{Q-P}\right) \\ &+g \int_{Q,P,P'} \psi_P^*\psi_{Q-P}\phi_{P'}^*\phi_{Q-P'}. \end{aligned} \tag{4.32}$$

The λ term originates from the term proportional to the condensate density n_0, $\lambda{\sim}\sqrt{n_0}g$. We will use a functional RG approach in the following [82]. For an analysis excluding terms in λ, see Ref. [50]. The truncation of the relevant flowing effective action corresponding to Eq. (4.32) is given by

$$\begin{aligned} \Gamma_k = &\int_Q \phi_Q^* P_\phi(Q)\phi_Q + \psi_Q^* P_\psi(Q)\psi_Q \\ &+\lambda_k \int_{Q,P} \psi_Q^*\psi_P \left(\phi_{P-Q}^* + \phi_{Q-P}\right) \\ &+g_k \int_{Q,P,P'} \psi_P^*\psi_{Q-P}\phi_{P'}^*\phi_{Q-P'}. \end{aligned} \tag{4.33}$$

Here k is the RG scale, above which all fluctuations have been integrated out. It runs from the UV cutoff scale $k = \Lambda$ to the infrared at $k = 0$. As before, ψ denotes the electron (fermion) field, while ϕ denotes the exciton (boson) field. We fix the initial conditions such that $\lambda_{k=\Lambda} = \lambda$ and $g_{k=\Lambda} = g$. In the following, we treat these running couplings as independent to establish a complete picture of the RG flow of the model. We disregard that the flowing coupling constants may acquire a frequency and momentum dependence during the RG flow and instead use a projection

$$\lambda_k = \frac{\delta^3}{\delta\phi_0^*\delta\psi_0\delta\psi_0^*}\Gamma_k\bigg|_{\psi=\phi=0} \tag{4.34}$$

$$g_k = \frac{\delta^4}{\delta\phi_0\delta\phi_0^*\delta\psi_0\delta\psi_0^*}\Gamma_k\bigg|_{\psi=\phi=0}, \tag{4.35}$$

where the subindices on the fields indicate a projection onto zero frequency and momentum. Using the Wetterich equation [82] we compute the flow of the effective action Γ_k

$$\partial_k\Gamma_k = \frac{1}{2}\,\mathrm{STr}\left[\left(\Gamma_k^{(2)} + R_k\right)^{-1}\partial_k R_k\right], \tag{4.36}$$

from which we can determine the flow of the coupling constants λ_k and g_k.

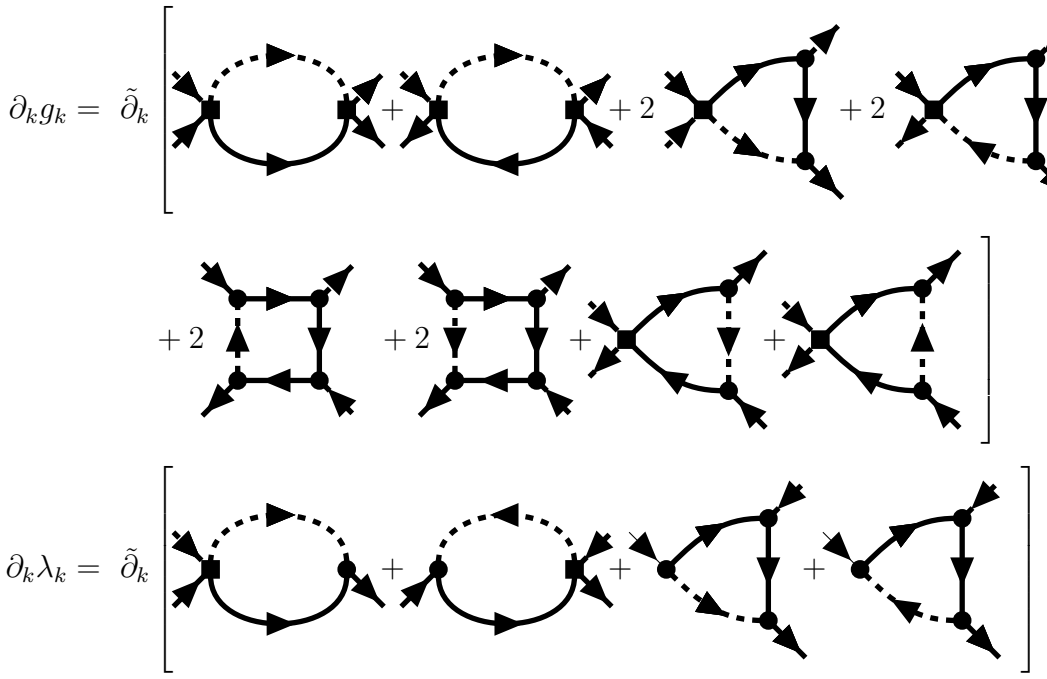

Figure 4.8. Diagrammatic representation of the flow equations of the coupling constants g_k and λ_k. In the flows of $\partial_k g_k$ (Eq. (4.37)) and $\partial_k \lambda_k$ (Eq. (4.38)) dashed lines denote exciton propagators and solid lines denote electron propagators. Dots denote the electron-exciton three point vertex $\sim\lambda_k$, while squares denote the electron-exciton four point vertex $\sim g_k$.

The corresponding diagrams are shown in Fig. 4.8. Choosing a sharp momentum regulator as done in Refs. [1, 137], the RG flows are given by

$$\partial_k g_k = \tilde{\partial}_k \int_P \left(-\frac{g_k^2}{P_\psi(P)} + \frac{3\lambda_k^2 g_k}{P_\psi(P)^2} - \frac{2\lambda_k^4}{P_\psi(P)^3} \right) \left(\frac{1}{P_\phi(P)} + \frac{1}{P_\phi(-P)} \right) \Theta(|\mathbf{p}| - k) \tag{4.37}$$

$$\partial_k \lambda_k = \tilde{\partial}_k \int_P \left(-\frac{g_k \lambda_k}{P_\psi(P)} + \frac{\lambda_k^3}{P_\psi(P)^2} \right) \left(\frac{1}{P_\phi(P)} + \frac{1}{P_\phi(-P)} \right) \Theta(|\mathbf{p}| - k). \tag{4.38}$$

4.7.1 Flow of coupling constants in two dimensions

To evaluate the flow equations in the few-body limit, we set the chemical potentials to $\mu_B = \mu_F = 0$ following similar RG analysis, e.g., of the BEC-BCS crossover [50]. After performing the momentum and frequency integrals, defining a dimensionless RG scale

$$t = \log\left(\frac{k}{\Lambda}\right) \tag{4.39}$$

and the dimensionless coupling constant

$$\tilde{\lambda}_k = \frac{\lambda_k}{k}, \tag{4.40}$$

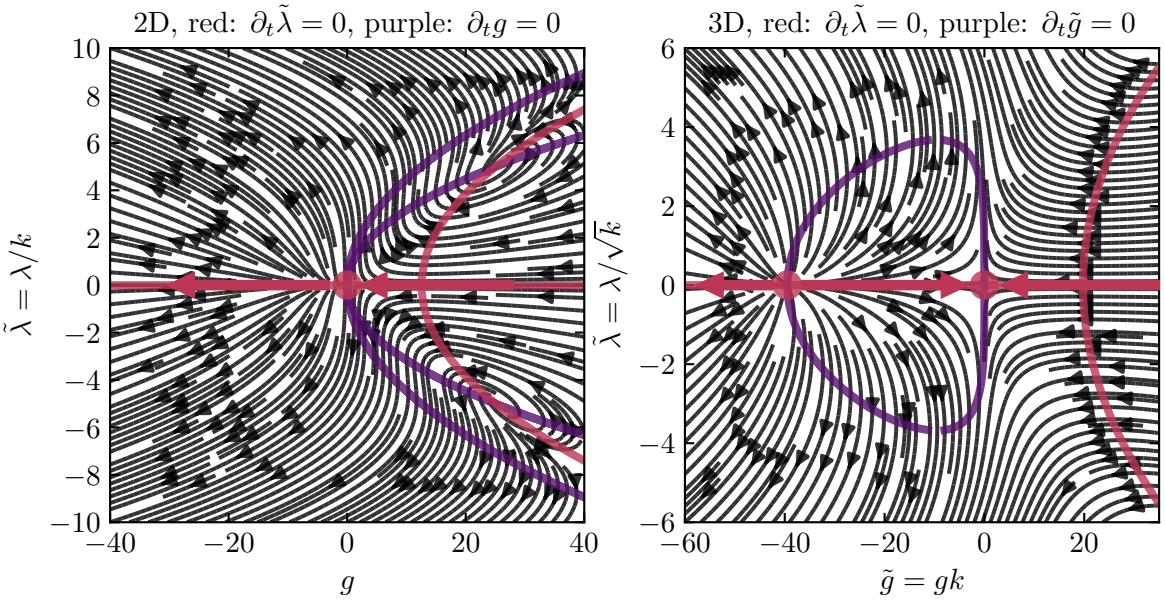

Figure 4.9. Flow chart for the dimensionless coupling constants $\tilde{\lambda}$ and $\tilde{g}$ in (a) two dimensions and (b) three dimensions, obtained from a functional renormalization group analysis of the model Eq. (4.33). Using the dimensionless RG scale $t=\log(k/\Lambda)$, for given values of g_k and $\tilde{\lambda}_k=\lambda_k/k$ ($\tilde{g}_k=g_k k$ and $\tilde{\lambda}_k=\lambda_k/\sqrt{k}$ in 3D) the direction of the RG flow, given by the beta functions $\partial_t\tilde{\lambda}_t$ and $\partial_t g_t$ ($\partial_t\tilde{\lambda}_t, \partial_t\tilde{g}_t$ in 3D) is shown. In the left panel the purple curves denote points with $\tilde{\lambda}_t^2=g_t$ and $\tilde{\lambda}_t^2=2g_t$ where $\partial_t g_t=0$ while the red curves denote points with $g_t=(8\pi+\tilde{\lambda}_t^2)/2$ and $\tilde{\lambda}_t=0$ where $\partial_t g=0$. Similarly, in the right panel the purple curve denotes points with $\partial_t\tilde{g}_t=0$ and the red curves represent points with $\partial_t\tilde{\lambda}_t=0$. RG fixed points occur when the red and purple lines cross. The thick arrows indicate the flow of g and $\tilde{g}$ when $\tilde{\lambda}=0$.

the flow equations in dimensionless form read

$$\partial_t g_t=\frac{1}{2\pi}\left(\frac{g_t^2}{2}-\frac{3}{4}\tilde{\lambda}_t^2 g_t+\frac{\tilde{\lambda}_t^4}{4}\right) \tag{4.41}$$

$$\partial_t\tilde{\lambda}_t=\frac{1}{2\pi}\left(\frac{\tilde{\lambda}_t g_t}{2}-\frac{\tilde{\lambda}_t^3}{4}\right)-\tilde{\lambda}_t. \tag{4.42}$$

The corresponding flow chart is shown in Fig. 4.9, where flows begin in the UV at $t=0$ and end in the IR at $t=-\infty$. For a given point in the flow diagram the arrows point in the direction of the flow. As one can see for $\tilde{\lambda}_{k=\Lambda}=0$ and $g_{k=\Lambda}>0$ the coupling constant g flows towards the Gaussian, i.e. weak-coupling, fixed point, $\lim_{k\to 0} g_k=0$. On the other hand, for $\tilde{\lambda}_{k=\Lambda}=0$ and $g_{k=\Lambda}<0$ the coupling flows to $\lim_{k\to 0} g_k=-\infty$, indicating bound state formation; this RG behavior reflects that a bound state exists for any attractive interaction in 2D [53]. For $\tilde{\lambda}_{k=\Lambda}=\pm\sqrt{8\pi}$, $g_{k=\Lambda}=\pm 8\pi$ we find two additional repulsive fixed points, while for all other initial values with $|\tilde{\lambda}_{k=\Lambda}|>0$ the flows are always driven towards $\lim_{k\to 0} g_k=-\infty$, meaning that bound state formation is inevitable and g_k always represents a relevant correlation function that cannot be ignored.

4.7.2 Flow of coupling constants in three dimensions

For completeness we also perform the RG analysis in three dimensions. After again using $t = \log(k/\Lambda)$ we can define the dimensionless coupling constants

$$\tilde{g}_k = g_k k, \tag{4.43}$$

$$\tilde{\lambda}_k = \frac{\lambda_k}{\sqrt{k}} \tag{4.44}$$

and obtain the flow equations

$$\partial_t \tilde{g}_t = \frac{1}{2\pi^2}\left(\frac{\tilde{g}_t^2}{2} - \frac{3}{4}\tilde{\lambda}_t^2 \tilde{g}_t + \frac{\tilde{\lambda}_t^4}{4}\right) + \tilde{g}_t \tag{4.45}$$

$$\partial_t \tilde{\lambda}_t = \frac{1}{2\pi^2}\left(\frac{\tilde{\lambda}_t \tilde{g}_t}{2} - \frac{\tilde{\lambda}_t^3}{4}\right) - \frac{\tilde{\lambda}_t}{2}. \tag{4.46}$$

The resulting flow chart is shown in Fig. 4.9(b). For $\tilde{\lambda}_{k=\Lambda} = 0$ it shows three different qualitative regions [50]

$$\lim_{k\to 0} \tilde{g}_k = \begin{cases} 0^+, & \text{for } \tilde{g}_{k=\Lambda} > 0 \\ 0^-, & \text{for } -4\pi^2 < \tilde{g}_{k=\Lambda} < 0 \\ -\infty, & \text{for } \tilde{g}_{k=\Lambda} < -4\pi^2. \end{cases} \tag{4.47}$$

which yield different results with respect to the relevance of $\tilde{g}_k$. For $\tilde{\lambda}_{k=\Lambda} \neq 0$, on the other hand, both dimensionless coupling constants are always relevant:

$$\lim_{k\to 0} \tilde{g}_k = -\infty \tag{4.48}$$

$$\lim_{k\to 0} \tilde{\lambda}_k = \mathrm{sign}(\tilde{\lambda}_{k=\Lambda})\infty \tag{4.49}$$

again demonstrating that there exists no scenario where bound state formation becomes irrelevant. Note, the fixed point at $\tilde{g} = -1$, $\tilde{\lambda} = 0$ is the well-known fixed point representing the regime of unitary interactions in the BEC-BCS crossover in three dimensions.

4.7.3 Discussion

The flows of coupling constants in Fig. 4.9 show a qualitatively similar picture in both two and three dimensions. Without the electron-exciton three-point vertex $\sim\lambda_k$ the relevance of the four-point vertex g_k is dependent on the initial value of the four point vertex g. In both cases, for repulsive initial values $g > 0$ the four point vertex is irrelevant and vanishes as a result of the renormalization process $\lim_{k\to 0} g_k = 0$. For attractive initial values $g < 0$ in two dimensions the coupling is relevant and flows to strong-coupling physics featuring an exciton-electron bound state. In three dimensions, it is not sufficient that the coupling is attractive, but rather it needs to be sufficiently attractive $g < -4\pi^2/\Lambda$. If these conditions are fulfilled, the few-body system flows to strong coupling and thus the bound state physics needs to be taken into account.

Considering the electron-exciton three-point vertex $\sim\lambda_k$, the qualitative nature of the relevance of the coupling changes. In two and three dimensions, apart from the two repulsive fixed points in 2D, a finite value of λ always leads to the system flowing to strong coupling, highlighting the relevance of the four-body vertex. This behavior is akin to the *in medium* behavior of the two-body bound state in three dimensions: as the three-point vertex may be regarded as stemming from the immersion of a two-body problem within a bosonic medium $\lambda\sim\sqrt{n_0}g$, represented by the condensate. While in the vacuum two-body limit in three dimensions the bound state exists only for positive scattering lengths, when introducing a bosonic or fermionic medium, however, the two-body bound state exists for all scattering lengths.

This analysis thus indicates that the four-point vertex is relevant and therefore needs to be taken into consideration, including the associated strong-coupling physics.

Chapter 5

Momentum-dependent quasiparticle properties of the Fermi polaron from the functional renormalization group

This chapter is based on the following publication:

[5] **J. von Milczewski**, R. Schmidt,
Momentum-dependent quasiparticle properties of the Fermi polaron from the functional renormalization group,

arXiv:2312.05318 (2023).

In this chapter, we study theoretically the lifetimes of attractive and repulsive Fermi polarons, as well as the molecule at finite momentum in three dimensions. To this end, we developed a new technique that allows for the computation of Green's functions in the whole complex frequency plane using exact analytical continuation within the functional renormalization group. The improved numerical stability and reduced computational cost of this method yield access to previously inaccessible momentum-dependent quasiparticle properties of low-lying excited states. While conventional approaches like the non-selfconsistent T-matrix approximation method cannot determine these lifetimes, we are able to find the momentum-dependent lifetime at different interaction strengths of both the attractive and repulsive polaron as well as the molecule. At weak coupling our results confirm predictions made from effective Fermi liquid theory regarding the decay of the attractive polaron, and we demonstrate that Fermi liquid-like behavior extends far into the strong-coupling regime where attractive polaron and molecule exhibit a p^4 momentum scaling in their decay widths. Our results offer an intriguing insight into the momentum-dependent quasiparticle properties of the Fermi polaron problem, which can be measured using techniques such as Raman transfer and Ramsey interferometry.

5.1 Introduction

In recent years, the polaron problem which we introduced in Section 1.7, has attracted significant theoretical and experimental attention, due to its fundamental nature, its significance in understanding strongly coupled systems such as ultracold atoms and two-dimensional semiconductor heterostructures, and its widespread occurrence in a range of different experimental and natural systems, such as dilute mixtures of protons within neutron stars [319, 320] or electrons moving through a crystal lattice of atoms [104, 321].

In two-dimensional semiconductor heterostructures, the Fermi and Bose polaron problems capture the physical properties of the interaction of electrons and excitons, along with the formation of trion states [33, 34, 302–305]. As such, these systems have been used to implement these limiting cases of extreme population imbalance. An understanding of these limits is an important step towards understanding the strong-coupling physics in such systems, which may render useful in exploring whether they might be used for practical applications such as inducing superconductivity [4, 95, 101, 102, 278, 322] (see Chapter 4).

In ultracold atom systems, the understanding of polaron problems has helped characterize the phase diagram of both Fermi-Fermi and Bose-Fermi mixtures at strong coupling [1, 2, 8, 9, 99, 100, 124, 130] (see Chapter 2). Experimental observations of the Fermi [9, 128–130] and the Bose polaron problem [106–108] have been flanked by theoretical insights obtained from different methods such as variational [54–57, 169–171, 174, 203, 323], diagrammatic [58, 59, 166, 167, 172], Monte Carlo [141–143, 173, 175, 176] and functional renormalization group (fRG) approaches [1, 50, 103, 137, 168, 184, 301]. These methods have been used to characterize properties such as the polaron-to-molecule transition/crossover and the competition with the formation of higher-order bound states. Furthermore, quasiparticle properties such as the energy, effective mass, and quasiparticle width have been extracted from these methods with great success.

The decay widths, or equivalently the quasiparticle lifetimes of the different collective excitations within the Fermi polaron problem, however, have largely remained elusive to a theoretical description. As the decay width may be determined from the self-energy of a quasiparticle, its self-energy needs to contain the correct low-energy states to decay into. As a result, at $T = 0$ common non-self-consistent T-matrix approaches which contain bare propagators can yield qualitatively correct decay widths for the repulsive polaron [58, 324, 325] but not for the attractive polaron or the molecule state as these renormalized particles lie lower in energy than the bare particles contained in their self-energies. Of course, at $T > 0$ these particles may decay via thermal excitations [326–328]. Thus, at strong coupling, a description of the decay channels of polaron and molecule states needs to feature a form of self-consistency, requiring the use of renormalized Green's functions within the computation of the quasiparticle self-energies and decay widths.

Such self-consistency is challenging to achieve within conventional methods using a wavefunction Ansatz or a non-selfconsistent T-matrix approach [54–56, 59, 170,

172]. As a result, decay widths have been analyzed using Fermi liquid theory and Fermi's golden rule [329], in which the renormalization process is taken into account by using simplified Green's functions with modified quasiparticle weight, energy gap, and effective mass. This works well when the lower-lying particles are well described using Fermi liquid theory [130] and may yield scaling laws for the decay rates in different decay channels [58, 167, 330–333], however it is expected to break down at strong coupling [334] and thus the applicability of Fermi liquid theory can only really be tested by comparison to a fully self-consistent calculation.

Within fRG treatments [137] this self-consistency is naturally included and thus the decay width may be computed without the need to rely on the validity of Fermi liquid theory. However, as the decay width of the zero-momentum ground state vanishes identically, at a fixed interaction parameter momentum-dependent decay widths of low-lying excited states can vary across several orders of magnitude within a small momentum range. Especially at smaller decay widths, this puts high requirements of numerical stability and precision on the used methods. Previous treatments using fRG [137] lacked precisely this stability due to the need of a costly Matsubara integration and an analytic continuation of the resulting Green's function to real frequencies using numerical methods.

In this chapter, we present a novel, improved fRG treatment of the method used in Ref. [137]. By incorporating all information about the analytical structure of the Fermi polaron problem, we are able to carry out the Matsubara integration over imaginary frequencies *exactly*. By a subsequent mapping of the fRG onto a horizontal line above the real frequency axis we perform an *exact* analytical continuation of the problem onto the whole complex frequency plane. While this treatment is formally equivalent to the treatment used in Ref. [137], it provides greatly enhanced numerical stability and precision at a significantly lower computational cost. These improvements are not only used to study previously inaccessible quasiparticle properties such as momentum-dependent decay widths of low-lying excited states but also allow to revisit previous results in the literature that implied a 9/2-power law scaling of the decay of the excited polaron and molecule as function of the energy gap towards the respective ground state [167].

This chapter is structured as follows: In Section 5.2 the model along with the fRG are introduced. In Section 5.3 the exact frequency integration and the exact analytical continuation onto an equivalent fRG operating on a horizontal line above the real frequency axis are performed. Next, in Section 5.4 the numerical solution of the resulting coupled flow equations is described along with the initial conditions of the flow and the parametrization of the renormalized Green's functions. In Section 5.5 the quasiparticle properties of the two polaron states and the molecule are analyzed using this method, complemented by an analysis in terms of Fermi liquid theory. Finally, in Section 5.6 we discuss possible experimental probes of quasiparticle properties such as the momentum-dependent decay width and we consider theoretical extensions of our work to finite impurity concentrations.

5.2 Model

We study the three-dimensional Fermi polaron problem consisting of a mixture in which a bosonic or fermionic impurity ϕ is immersed in a fermionic bath ψ (see also Sections 1.7 and 2.3). This is a well-studied system whose microscopic action is given by

$$\begin{aligned} S = &\int_x \psi_x^* \left(\partial_\tau - \frac{\boldsymbol{\nabla}^2}{2m_\psi} - \mu_\psi \right) \psi_x \\ &+ \int_x \phi_x^* \left(\partial_\tau - \frac{\boldsymbol{\nabla}^2}{2m_\phi} - \mu_\phi \right) \phi_x \\ &+ g \int_x \psi_x^* \phi_x^* \phi_x \psi_x \end{aligned} \tag{5.1}$$

where $x = (\mathbf{r}, \tau)$ denotes the coordinate $\mathbf{r}$ and imaginary time $\tau \in [0, 1/T]$ and $\int_x = \int_0^{1/T} d\tau \int d^d\mathbf{r}$ with $d = 3$ the dimension. In the following, we consider zero temperature, $T = 0$, and assume that impurity and bath particles have a bare dispersion described by the same mass $m = m_\psi = m_\phi$. We work in units $\hbar = k_\mathrm{B} = 1$, and set $2m = 1$ unless indicated otherwise. The field ψ is of fermionic Grassmann nature, while the statistic of ϕ is irrelevant due to the single-impurity limit taken in this work. The fields ϕ and ψ interact by means of an attractive contact potential of strength $g < 0$, regularized in the ultraviolet (UV) by a momentum cutoff Λ.

In the vacuum and single-impurity limit this system can host a bound state between a bath and an impurity particle, both in 2D and 3D. Thus, in order to facilitate the description of this composite particle in a convenient way we consider an equivalent two-channel model [49, 50] in which the interspecies interaction is mediated by a molecule field t describing the composite particle of mass $2m$ [43, 44, 47, 48]

$$\begin{aligned} S = &\int_{\mathbf{p},\omega} \Bigg\{ \sum_{\sigma=\psi,\phi} \sigma^*(\omega,\mathbf{p}) \left(-i\omega + \mathbf{p}^2 - \mu_\sigma \right) \sigma(\omega,\mathbf{p}) \\ &+ t^*(\omega,\mathbf{p}) G_{t,\Lambda}^{-1}(\omega,\mathbf{p}) t(\omega,\mathbf{p}) \Bigg\} \\ &+ h \int_x \left\{ \psi_x^* \phi_x^* t_x + t_x^* \phi_x \psi_x \right\} \ . \end{aligned} \tag{5.2}$$

Here the momentum $\mathbf{p}$ and the Matsubara frequency ω are the Fourier variables of $\mathbf{r}$ and τ and $\int_{\mathbf{p},\omega} \equiv (2\pi)^{-d-1} \int d^d\mathbf{p} d\omega$. In this two-channel model a bath and an impurity particle can be converted into a molecule with a Yukawa coupling h and $G_{t,\Lambda}$ denotes the bare molecule propagator. We operate in the limit where $h \to \infty$ such that t becomes a purely auxiliary Hubbard-Stratonovich field with no dynamics, i.e. it can be integrated out to yield back the original action Eq. (5.1) for $h^2 G_{t,\Lambda} = -g$ [49, 50].

To obtain access to the physical properties of this system, inscribed in the full Green's and vertex functions we deploy a functional renormalization group approach similar to the constructions used in Section 2.3 and Refs. [137, 184]. For a detailed explanation of the Fermi polaron problem we refer to Section 1.7 and Refs. [1, 50, 54, 56, 57, 59, 137, 141–143, 166–176, 323], for a detailed discussion of the fRG in

general we refer to Refs. [64–67, 79]. In the following we provide a brief summary of the involved steps, see Section 2.3 and Refs. [137, 184] for more detail.

5.2.1 fRG equations

The fRG accounts for the renormalization of Green's functions due to quantum fluctuations by providing coupled differential equations linking the quantum effective action Γ (the generating functional of all one-particle irreducible vertices) to the bare action S using a flowing effective action Γ_k. This is achieved using the Wetterich equation [82]

$$\partial_k \Gamma_k = \frac{1}{2} \mathrm{STr} \left[\left(\Gamma_k^{(2)} + R_k \right)^{-1} \partial_k R_k \right] , \tag{5.3}$$

where $\Gamma_k^{(2)}$ represents the matrix of second functional derivatives of Γ_k in the fields and R_k is a matrix containing so-called regulator functions which control the integration of quantum fluctuations. The supertrace STr denotes a summation over all momenta and frequencies, as well as the different fields, including a minus sign for fermions.

Provided that the regulator functions within R_k fulfill certain conditions [65, 66], in the *ultraviolet* (UV) at $k = \Lambda$ the flowing effective action will be equivalent to the bare action $\Gamma_{k=\Lambda} = S + const.$ while in the *infrared* at $k = 0$ the quantum effective action is obtained as $\Gamma_{k=0} = \Gamma$. Having obtained this functional, all physical information can be extracted from it.

While the treatment of the problem so-far using Eq. (5.3) is exact; it is also impossible to solve as the effective quantum action contains infinitely-many vertices yielding an infinite-dimensional set of coupled differential equations. It is thus customary to introduce an *Ansatz* containing finitely-many terms representing the physically most relevant processes in a so-called vertex expansion. Following the treatment in Refs. [1, 137, 184] we thus choose the following effective action truncation

$$\begin{aligned} \Gamma_k = \int_{\mathbf{p},\omega} \Bigg\{ & \sum_{\sigma=\psi,\phi} \sigma(\omega,\mathbf{p})^* G_{\sigma,k}^{-1}(\omega,\mathbf{p}) \sigma(\omega,\mathbf{p}) \\ & + t^*(\omega,\mathbf{p}) G_{t,k}^{-1}(\omega,\mathbf{p}) t(\omega,\mathbf{p}) \Bigg\} \\ & + h \int_x (\psi_x^* \phi_x^* t_x + t_x^* \phi_x \psi_x) \ . \end{aligned} \tag{5.4}$$

From this truncation one can obtain flow equations for its different constituents using appropriate functional derivatives of Eq. (5.3). Their diagrammatic representation is shown in Fig. 5.1 and in terms of the flowing Green's functions they read [137]

$$\partial_k G_{\phi,k}^{-1}(\omega,\mathbf{p}) = h^2 \tilde{\partial}_k \int_{\mathbf{q},\nu} G_{t,k}^c(\omega+\nu,\mathbf{p}+\mathbf{q}) G_{\psi,k}^c(\mathbf{q},\nu), \tag{5.5}$$

$$\partial_k G_{\psi,k}^{-1}(\omega,\mathbf{p}) = -h^2 \tilde{\partial}_k \int_{\mathbf{q},\nu} G_{t,k}^c(\omega+\nu,\mathbf{p}+\mathbf{q}) G_{\phi,k}^c(\mathbf{q},\nu), \tag{5.6}$$

$$\partial_k G_{t,k}^{-1}(\omega,\mathbf{p}) = -h^2 \tilde{\partial}_k \int_{\mathbf{q},\nu} G_{\phi,k}^c(\omega-\nu,\mathbf{p}-\mathbf{q}) G_{\psi,k}^c(\mathbf{q},\nu). \tag{5.7}$$

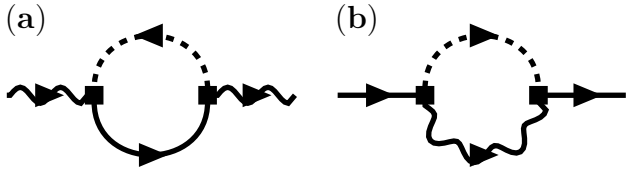

Figure 5.1. Diagrammatic representation of the fRG flow equations in Eqs. (5.5) and (5.7). The flows of the impurity Green's function $\partial_k G^{-1}_{\phi,k}$ **(a)** as well as the molecular Green's function $\partial_k G^{-1}_{t,k}$ **(b)** are shown, where wiggly and dashed lines denote impurity and bath propagators, while solid lines denote molecular propgators. The coupling vertex $\sim h_k \psi^* \phi^* t$ is denoted by square dots.

Here, the G^c denote the regulated Green's functions given by

$$(G^c_{\sigma,k})^{-1} = (G_{\sigma,k})^{-1} + R_{\sigma,k}, \tag{5.8}$$

where $R_{\sigma,k}$ is a regulator function contained within R_k, which will be defined in the following. In these expressions $\tilde{\partial}_k$ denotes a derivative with respect to the k-dependence of the regulator only, i.e. $\tilde{\partial}_k = (\partial_k R_k)\partial_{R_k}$. As we will see in the following, $\partial_k G^{-1}_{\psi,k} = 0$, and thus the bath Fermi energy ϵ_F is equivalent to its chemical potential $\mu_\psi = \epsilon_F$.

In the single-impurity limit, we expect the low-energy excitations of the impurity and the composite molecule particle to lie at low momenta while those of the bath lie around its Fermi surface where $p^2 = \epsilon_F$. It is desirable for these fluctuations to be integrated out towards the end of the flow near $k = 0$. To this end, we use sharp momentum regulators [79, 185] which yield regulated flowing propagators of the form

$$G^c_{\psi,k}(\omega, \mathbf{p}) = G_{\psi,k}(\omega, \mathbf{p})\Theta(|\mathbf{p}^2 - \epsilon_F| - k^2) \ , \tag{5.9}$$
$$G^c_{\phi,k}(\omega, \mathbf{p}) = G_{\phi,k}(\omega, \mathbf{p})\Theta(|\mathbf{p}| - k) \ , \tag{5.10}$$
$$G^c_{t,k}(\omega, \mathbf{p}) = G_{t,k}(\omega, \mathbf{p})\Theta(|\mathbf{p}| - k) \ . \tag{5.11}$$

While this choice of regulator functions allows for simple comparison to different approximations, it holds a further advantage that is not immediately obvious. In the following, we will see how its trivial dependence on frequency and its simple structure allow for an *exact* evaluation of the Matsubara integration in Eqs. (5.5) to (5.7) and an *exact* analytical continuation of the obtained Green's function to a horizontal line in the complex frequency plane (see Fig. 5.2).

5.3 Exact Matsubara integration

So far, our treatment of the Fermi polaron problem in 3D is exactly equivalent to the treatment developed in Ref. [137]. A treatment in 2D can be achieved as a natural extension of that work using also Section 2.3. In Ref. [137] the flowing inverse Green's functions $G^{-1}_{\sigma,k}$ are parametrized by laying out a grid in Matsubara frequencies and

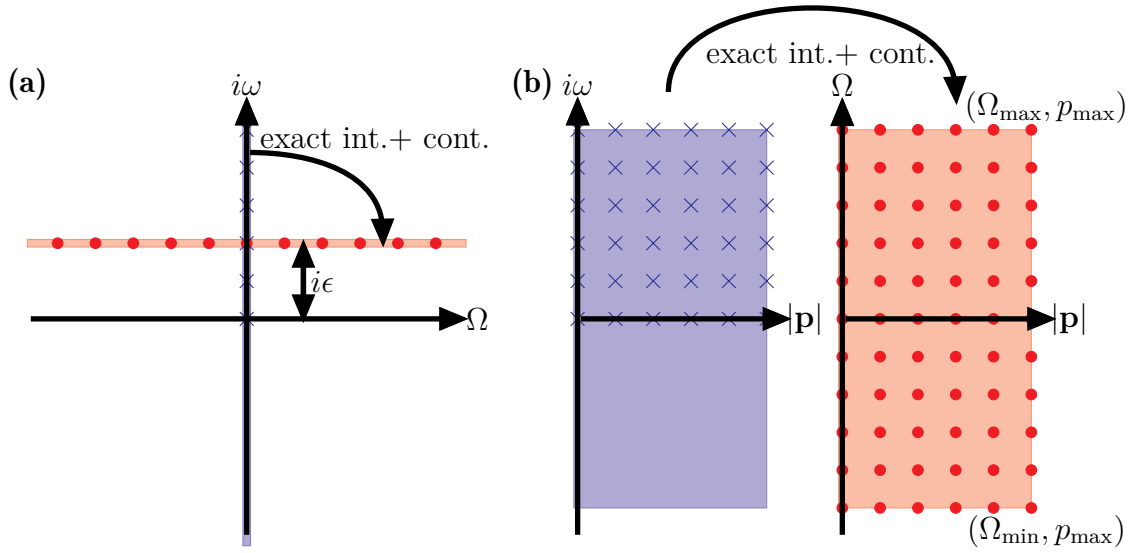

Figure 5.2. Schematic diagram of the complex plane and the interpolation space. The complex frequency plane is shown in **(a)**, with the Matsubara frequencies along the vertical axis (blue shaded) and the real frequencies along the horizontal. The theory originally operates on the Matsubara frequencies and the inverse Green's functions $G^{-1}_{\sigma,k}(\omega, \mathbf{p})$ are parametrized by laying out a grid $(i\omega_i, p_j)$ in frequency and momentum space (blue crosses in **(b)**) and interpolating between the grid points (blue shaded region in **(b)**), using also the symmetry $G^{-1}_{\sigma,k}(-\omega, \mathbf{p}) = G^{-1}_{\sigma,k}(\omega, \mathbf{p})^*$. After exact Matsubara integration and exact continuation, the RG is defined on a horizontal line $\mathbb{R}+i\epsilon$ (red shaded region in **(a)**) and the retarded inverse Green's functions $G^{R,-1}_{\sigma,k}(\Omega + i\epsilon, \mathbf{p})$ are parametrized by laying out a grid $(\Omega_i + i\epsilon, p_j)$ (red dots in **(b)**) and interpolating between the grid points (red shaded region in **(b)**). For $\Omega < \Omega_{\min}$ or $p > p_{\max}$ the retarded Green's functions are approximated by asymptotic functions $G^{R,-1}_{>,\sigma,k}$ in the flow equations (see Eqs. (5.21) and (5.22)), while $\Omega > \Omega_{\max}$ is never accessed due to the structure of the flow equations (5.19) and (5.20). By comparison in Ref. [137], the RG equations are solved on a grid of Matsubara frequencies (blue in **(b)**) and only afterwards are the results continued to real frequencies using numerical analytic continuation.

momenta (ω_i, p_j) (see Fig. 5.2). The full frequency- and momentum-dependence of $G^{-1}_{\sigma,k}$ is then obtained interpolating over the function values at these points $C^{i,j}_{\sigma,k} \equiv G^{-1}_{\sigma,k}(\omega_i, p_j)$. In Ref. [137] the flow of these coefficients is computed as a coupled differential equation and at the end of the flow the full Green's function in terms of Matsubara frequencies is obtained as an interpolation over these coefficients. To obtain the retarded Green's function just above the real axis, in Ref. [137] this function is then continued analytically using a Padé approximation (see Fig. 5.2).

During the course of the evaluation of the flow equations, however, in Ref. [137] a costly integration over the Matsubara frequencies is performed numerically. Due to the slow convergence rate of this integration, its evaluation yields only moderate

precision for reasonable computation times. For ground-state properties, this yields reasonable results. However, for the study of excited state properties the points of interest in the complex frequency plane lie further away from the points at which the fRG was performed. Thus, the numerical error incurred from the Matsubara integration is propagated during the numerical analytical continuation, rendering the obtained results for excited states highly unstable. This may lead to misleading results such as a p^2 dispersion with positive effective mass of the attractive polaron in a region where it is known to have a negative effective mass [55, 335] (see also Fig. 5.8).

Leveraging the analytical structure of the flowing propagators in the single-impurity system we will now demonstrate how these two problems can be circumvented in a simply maneuver by performing the Matsubara integration *exactly* which yields an *exact* analytical continuation of the propagator functions to the whole complex frequency plane.

5.3.1 Analytical structure of zero-density propagators and the residue theorem

To begin, we recall general analytical properties of the Green's functions at hand [51, 52]. In the complex frequency plane, the Matsubara frequencies $\omega \in \mathbb{R}$ lie along the imaginary axis $z = i\omega$ and the flowing Matsubara Green's functions $G_{\sigma,k}$ are evaluated along this axis. Along this axis in the upper half of the complex frequency plane (UCP), they correspond to the retarded Green's functions $G_{\sigma,k}(\omega > 0, \mathbf{p}) = G^R_{\sigma,k}(i\omega, \mathbf{p})$ and since the retarded Green's function $G^R_{\sigma,k}(z, \mathbf{p})$ is analytic for $\mathrm{Im}(z) > 0$, the Matsubara Green's function can be continued to the retarded Green's function here. The analogous statement holds for the advanced Green's function $G^A_{\sigma,k}(z, \mathbf{p})$ for $\mathrm{Im}(z) < 0$. Along the real axis, the retarded and the advanced Green's functions fulfill the relations $\mathrm{Re}\, G^R_{\sigma,k}(\Omega + i0^+, \mathbf{p}) = \mathrm{Re}\, G^A_{\sigma,k}(\Omega - i0^+, \mathbf{p})$ and $\mathrm{Im}\, G^R_{\sigma,k}(\Omega + i0^+, \mathbf{p}) = -\mathrm{Im}\, G^A_{\sigma,k}(\Omega - i0^+, \mathbf{p})$ for $\Omega \in \mathbb{R}$. Furthermore, from the retarded Green's function one can obtain the flowing spectral function

$$\begin{aligned} \mathcal{A}_{\sigma,k}(\Omega, \mathbf{p}) &= G^R_{\sigma,k}(\Omega + i0^+, \mathbf{p}) - G^A_{\sigma,k}(\Omega - i0^+, \mathbf{p}) \\ &= 2\,\mathrm{Im}\left[G^R_{\sigma,k}(\Omega + i0^+, \mathbf{p})\right] \end{aligned} \tag{5.12}$$

from which the occupation of states with momentum $\mathbf{p}$ can be obtained as

$$n_{\sigma,k}(\mathbf{p}) = \int_\Omega n_{B/F}(\Omega)\mathcal{A}_{\sigma,k}(\Omega, \mathbf{p}), \tag{5.13}$$

where depending on the statistics of the σ-field $n_{B/F}(\Omega) = 1/(\exp(\Omega/T) \mp 1)$ denotes a Bose- or Fermi-distribution function and $n_{B/F}\mathcal{A}_{\sigma,k} \geq 0$.

Since we work in the single-impurity limit, the occupation of impurity and molecule states must vanish at all times: $n_{\sigma,k}(\mathbf{p}) = 0$ for $\sigma = \phi, t$ and for all $k, \mathbf{p}$. Thus, from Eq. (5.13) it is easy to see that at $T = 0$ for $\Omega < 0$, irrespective of the statistic of the impurity, it holds that

$$\mathcal{A}_{\phi/t,k}(\Omega < 0, \mathbf{p}) = 0. \tag{5.14}$$

This has striking consequences: while the functional form of the impurity and molecule Green's function is generally unknown (it is exactly these functions that we are solving for), the bath Green's function is known exactly as it does not flow. Suppressing the momentum-dependencies for now and using the analytic properties for $\omega > 0$, Eq. (5.6) can be rewritten as

$$\begin{aligned}\int_\nu G^c_{t,k}(\omega+\nu)G^c_{\phi,k}(\nu) = &\int_0^\infty \frac{d\nu}{2\pi} G^{c,R}_{t,k}(i\omega+i\nu)G^{c,R}_{\phi,k}(i\nu)\\ &+\int_{-\omega}^0 \frac{d\nu}{2\pi} G^{c,R}_{t,k}(i\omega+i\nu)G^{c,A}_{\phi,k}(i\nu)\\ &+\int_{-\infty}^{-\omega} \frac{d\nu}{2\pi} G^{c,A}_{t,k}(i\omega+i\nu)G^{c,A}_{\phi,k}(i\nu).\end{aligned} \tag{5.15}$$

After (i) performing contour integration along the paths shown in Fig. 5.3a), (ii) using that the integrands are analytic in the interior of these paths, and (iii) respecting that the integrand vanishes along the arcs to infinity, this is equivalent to

$$\begin{aligned}= -\int_0^{-\infty} \frac{d\Omega}{2\pi} \Big[&G^{c,R}_{t,k}(i\omega+\Omega)\mathcal{A}^c_{\phi,k}(\Omega)\\ &+\mathcal{A}^c_{t,k}(\Omega)G^{c,A}_{\phi,k}(-i\omega+\Omega)\Big] = 0.\end{aligned} \tag{5.16}$$

Here $G^{c,R}_{\sigma,k}$ and $\mathcal{A}^c_{\sigma,k}$ are defined analogous to the regulated flowing propagators in Eqs. (5.9) to (5.11). As a result $\partial_k G^{-1}_{\psi,k} = 0$ and $G^{-1}_{\psi,k}(\omega,\mathbf{p}) = -i\omega + \mathbf{p}^2 - \epsilon_F$ such that $G^{R,-1}_{\psi,k}(z,\mathbf{p}) = G^{A,-1}_{\psi,k}(z,\mathbf{p}) = -z + \mathbf{p}^2 - \epsilon_F$, which can be used to significantly simplify the remaining flow equations.

In Eqs. (5.5) and (5.7), the appearing bath propagators have poles at $\nu = -iz = -i(\mathbf{q}^2 - \epsilon_F)$ and $\nu = -iz = i(\mathbf{q}^2 - \epsilon_F)$, respectively, which each lie in the left half of the complex plane for $\mathbf{q}^2 - \epsilon_F < 0$ and $\mathbf{q}^2 - \epsilon_F > 0$, respectively. Replacing the integrand in Eqs. (5.5) and (5.7) with the corresponding advanced and retarded propagators and carrying out a contour integration along the contours shown in Fig. 5.3b) and Fig. 5.3c), while taking into account the pole of the bath propagator and the vanishing of the spectral functions described above for $\omega > 0$, one thus obtains

$$\begin{aligned}&\partial_k G^{-1}_{\phi,k}(\omega,\mathbf{p})\\ &\quad= -h^2\tilde{\partial}_k \int_{\mathbf{q}} \frac{\Theta(|\mathbf{p}+\mathbf{q}|-k)\Theta(\epsilon_F-\mathbf{q}^2-k^2)}{G^{-1,R}_{t,k}(i\omega+\mathbf{q}^2-\epsilon_F,\mathbf{p}+\mathbf{q})},\end{aligned} \tag{5.17}$$

$$\begin{aligned}&\partial_k G^{-1}_{t,k}(\omega,\mathbf{p})\\ &\quad= -h^2\tilde{\partial}_k \int_{\mathbf{q}} \frac{\Theta(|\mathbf{p}+\mathbf{q}|-k)\Theta(\mathbf{q}^2-\epsilon_F-k^2)}{G^{R,-1}_{\phi,k}(i\omega-\mathbf{q}^2+\epsilon_F,\mathbf{p}+\mathbf{q})}.\end{aligned} \tag{5.18}$$

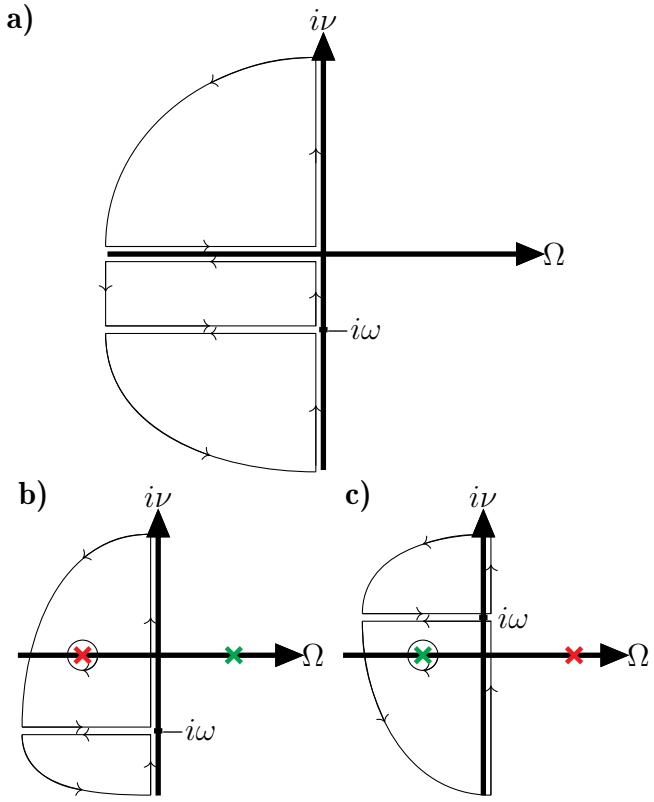

Figure 5.3. Schematic drawing of the contours in the complex plane used to obtain Eqs. (5.16), (5.19) and (5.20). **(a)** The Matsubara summation on the lhs. of Eq. (5.15) is broken up into the three pieces shown along the y-axis, where the Matsubara Green's functions can be replaced with the corresponding retarded/advanced Green's functions. Using the analyticity of the integrands, the integral along the whole contour vanishes and the integral along the arcs to infinity vanishes due to the decay of the Green's functions. As result, the vertical components of this contour integration (Eq. (5.15)) can be inferred from the horizontal components shown in Eq. (5.16), which vanish due to the single-impurity limit (see Eq. (5.14)). In **(b)** and **(c)** the contours used to obtain Eqs. (5.19) and (5.20), respectively, are shown. For $\mathbf{q} - \epsilon_F < 0$ (red crosses) and $\mathbf{q} - \epsilon_F > 0$ (green crosses) the position of the pole in the bath propagator is shown and it contributes to the integral if it lies within the contour.

Finally, the flow of the imaginary-time Green's function can be continued to an arbitrary horizontal line in the upper complex plane $i\omega \to \Omega + i\epsilon$ to arrive at

$$\begin{aligned}
&\partial_k G^{R,-1}_{\phi,k}(\Omega + i\epsilon, \mathbf{p}) \\
&\qquad = -h^2 \tilde{\partial}_k \int_{\mathbf{q}} \frac{\Theta(|\mathbf{p}+\mathbf{q}| - k)\Theta(\epsilon_F - \mathbf{q}^2 - k^2)}{G^{-1,R}_{t,k}(\Omega + i\epsilon + \mathbf{q}^2 - \epsilon_F, \mathbf{p}+\mathbf{q})}, \qquad (5.19) \\
&\partial_k G^{R,-1}_{t,k}(\Omega + i\epsilon, \mathbf{p}) \\
&\qquad = -h^2 \tilde{\partial}_k \int_{\mathbf{q}} \frac{\Theta(|\mathbf{p}+\mathbf{q}| - k)\Theta(\mathbf{q}^2 - \epsilon_F - k^2)}{G^{R,-1}_{\phi,k}(\Omega + i\epsilon - \mathbf{q}^2 + \epsilon_F, \mathbf{p}+\mathbf{q})}, \qquad (5.20)
\end{aligned}$$

where $\epsilon > 0$ is a positive number that does not necessarily have to be close to 0. The $\tilde{\partial}_k$ acts only on the Heaviside functions and under suitable parametrization, the rhs. of Eqs. (5.19) and (5.20) contains only an integral over the angle between $\mathbf{p}$ and $\mathbf{q}$. The Matsubara integration has been eliminated completely and the coupled differential equation in Matsubara frequencies has been mapped to a coupled differential equation within a horizontal line in the complex frequency plane.

5.4 Solution of the coupled flow equations

After the elimination of the Matsubara integration along with the analytical continuation, we can now solve the coupled differential equation system in Eqs. (5.19) and (5.20). Importantly, upon choosing a horizontal line in the complex plane (see Fig. 5.2) these differential equations only couple the retarded impurity and molecule Green's functions within the given horizontal line, without coupling to other horizontal lines.

5.4.1 Parametrization of inverse retarded Green's functions

To parametrize the flowing inverse retarded Green's functions we lay out a grid consisting of momenta $\mathbf{p}_i$ and frequencies $\Omega_j + i\epsilon$ on which we store the function values of the Green's functions in form of the coefficients $D^{i,j}_{\sigma,k} \equiv G^{R,-1}_{\sigma,k}(\Omega_j + i\epsilon, p_i)$ for $\Omega \in \mathbb{R}$ and $\epsilon > 0$. The momenta and frequencies in this grid need to be chosen such that they

1. resolve well the regions of interest in the retarded Green's function, and
2. enable a good resolution in the regions that are integrated over in the evaluation of the flow equations (5.19) and (5.20), such the interpolating function approximates the actual Green's function well.

From Eqs. (5.19) and (5.20) it can easily be seen that for a point of interest $\Omega + i\epsilon$ only retarded Green's functions at points $\Omega' + i\epsilon$ with $\Omega' < \Omega$ are evaluated. Furthermore, all Green's functions have spherical symmetry in their momentum component such that $G^{R,-1}_{\sigma,k}(\Omega + i\epsilon, \mathbf{p}) = G^{R,-1}_{\sigma,k}(\Omega + i\epsilon, |\mathbf{p}|)$, enabling a parametrization by the modulus of the momentum component. Thus the grid is contained within $(p_i, \Omega_j + i\epsilon) \in [0, p_{\max}] \times [\Omega_{\min} + i\epsilon, \Omega_{\max} + i\epsilon]$ where $\Omega_{\max}$ is chosen according to interest in physical properties and $p_{\max}, \Omega_{\min}$ are chosen to enable integration during the evaluation of flow equations. The choice of the value of ϵ follows from a compromise: It needs to be chosen such that $\mathbb{R} + i\epsilon$ is close enough to the real axis to yield a good approximation for the spectral function Eq. (5.29). However, if the chosen value of ϵ is too small, the integration of the flow equations will be over strongly peaked functions which requires small step sizes as the differential equation is solved along the flow parameter k.

Within the grid, the $G^{R,-1}_{\sigma,k}$ are obtained from the coefficients $D^{i,j}_{\sigma,k}$ using a bivariate cubic spline interpolation, while for values outside the grid we use that asympotically

for $p \to \infty, \Omega \to -\infty$ the $G^{R,-1}_{\sigma,k}$ take on their bare form. Thus, ensuring continuity at the boundaries of the grid, for $|\mathbf{p}| > p_{\max}$ or $\Omega < \Omega_{\min}$ they are approximated by functions of the functional form of their vacuum solutions [137]

$$G^{R,-1}_{>,\phi,k}(z,\mathbf{p}) = -z + \mathbf{p}^2 - \mu_\phi + f^1_{\text{cont}}, \tag{5.21}$$

$$G^{R,-1}_{,>t,k}(z,\mathbf{p}) = \frac{h^2}{8\pi}\left(-\frac{1}{a} + \sqrt{-\frac{z}{2} + \frac{\mathbf{p}^2}{4} + f^2_{\text{cont}}}\right), \tag{5.22}$$

where $f^{1,2}_{\text{cont}}$ ensure continuity at the boundary.

5.4.2 Initial conditions of the flow

The initial conditions for the flow of the impurity at the cutoff scale $k = \Lambda$ are given by the bare impurity propagator

$$G^{R,-1}_{\phi,k=\Lambda}(\Omega + i\epsilon, \mathbf{p}) = -(\Omega + i\epsilon) + \mathbf{p}^2 - \mu_\phi. \tag{5.23}$$

The initial condition of the molecule propagator is chosen such that for a flow in the vacuum two-body limit, which is obtained by tuning the chemical potentials accordingly, it reproduces the vacuum molecule propagators at $k = 0$ (see Section 1.6 and Ref. [137])

$$G^{R,-1}_{t,k=\Lambda}(\Omega + i\epsilon, \mathbf{p}) = -\frac{h^2}{8\pi a} + \frac{h^2\Lambda}{4\pi^2} - h^2 \int_{\mathbf{q}} \left[\frac{\Theta(|\mathbf{p}+\mathbf{q}| - \Lambda)\Theta(|\mathbf{q}| - \Lambda)}{-\Omega - i\epsilon + \mathbf{q}^2 + (\mathbf{p}+\mathbf{q})^2} - \frac{\Theta(|\mathbf{q}| - \Lambda)}{2\mathbf{q}^2}\right]. \tag{5.24}$$

The initial condition of the bath fermions is given by

$$G^{R,-1}_{\psi,k=\Lambda}(\Omega + i\epsilon, \mathbf{p}) = -(\Omega + i\epsilon) + \mathbf{p}^2 - \epsilon_F. \tag{5.25}$$

From the flow equations in Eqs. (5.19) and (5.20) one can see that the impurity propagator does not flow for $k^2 > \epsilon_F$. Thus for $\epsilon_F < k^2 < \Lambda^2$, the impurity propagator remains in its bare form and Eqs. (5.19) and (5.20) can be integrated analytically from $k = \Lambda$ down to $k = \sqrt{\epsilon_F}$. Hence the actual numerical solution of the flow equations begins at $k = \sqrt{\epsilon_F}$ with the initial condition

$$G^{R,-1}_{\phi,k=\sqrt{\epsilon_F}}(\Omega + i\epsilon, \mathbf{p}) = G^{R,-1}_{\phi,k=\Lambda}(\Omega + i\epsilon, \mathbf{p}) \tag{5.26}$$

for the impurity and

$$G^{R,-1}_{t,k=\sqrt{\epsilon_F}}(\Omega + i\epsilon, \mathbf{p}) = G^{R,-1}_{t,k=\Lambda}(\Omega + i\epsilon, \mathbf{p}) - \int_{\sqrt{\epsilon_F}}^{\Lambda} dk' \left[\partial_k G^{R,-1}_{t,k=k'}\right](\Omega + i\epsilon, \mathbf{p})$$

for the molecule. As a result, the molecule's initial condition is given by

$$G^{R,-1}_{t,k=\sqrt{\epsilon_F}}(\Omega+i\epsilon,\mathbf{p}) = G^{R,-1}_{t,k=\Lambda}(\Omega+i\epsilon,\mathbf{p}) + h^2\int_{\mathbf{q}}\Bigg[\frac{\Theta(|\mathbf{p}+\mathbf{q}|-\Lambda)\Theta(\mathbf{q}^2-\epsilon_F-\Lambda^2)}{G^{R,-1}_{\phi,\Lambda}(\Omega+i\epsilon-\mathbf{q}^2+\epsilon_F,\mathbf{p}+\mathbf{q})} - \frac{\Theta(|\mathbf{p}+\mathbf{q}|^2-\epsilon_F)\Theta(\mathbf{q}^2-2\epsilon_F)}{G^{R,-1}_{\phi,\Lambda}(\Omega+i\epsilon-\mathbf{q}^2+\epsilon_F,\mathbf{p}+\mathbf{q})}\Bigg] \tag{5.27}$$

$$= -\frac{h^2}{8\pi a} + h^2\int_{\mathbf{q}}\Bigg[\frac{1}{2\mathbf{q}^2} - \frac{1}{G^{R,-1}_{\phi,\Lambda}(\Omega+i\epsilon-\mathbf{q}^2+\epsilon_F,\mathbf{p}+\mathbf{q})} - \frac{\Theta(|\mathbf{p}+\mathbf{q}|-\epsilon_F)\Theta(\mathbf{q}^2-2\epsilon_F)-1}{G^{R,-1}_{\phi,\Lambda}(\Omega+i\epsilon-\mathbf{q}^2+\epsilon_F,\mathbf{p}+\mathbf{q})}\Bigg], \tag{5.28}$$

where we have cancelled the third term in Eq. (5.24) against the second term in Eq. (5.27). Due to the start of the flow not at $k=\Lambda$, but rather at $k=\sqrt{\epsilon_F}$ in Eq. (5.27) we can safely take the limit $\Lambda\to\infty$ during the computation of the molecular initial condition such that the solution of the flow equations is entirely independent of the upper cutoff scale. The integrals in Eq. (5.28) can be solved analytically.

5.5 Results

From the numerical evaluation of the flow equations down to $k=0$, we obtain the renormalized retarded Green's functions of the molecule and the impurity along a horizontal line in the complex frequency plane $G^{R,-1}_{\phi/t}(\Omega+i\epsilon,\mathbf{p}) = G^{R,-1}_{\phi/t,k=0}(\Omega+i\epsilon,\mathbf{p})$. Performing the same calculation several times for different horizontal lines (characterized by the value of $\epsilon\in\mathbb{R},\epsilon>0$), one then obtains a discretized parametrization of these Green's functions in the whole upper half of the complex frequency plane [1].

Several quantities can be deduced from this data via analytical continuation of the retarded Green's function. The single particle spectral function of the molecule and the impurity can be obtained by analytical continuation to the real axis

$$\mathcal{A}_{\phi/t}(\Omega,\mathbf{p}) = \lim_{\epsilon\to 0}\operatorname{Im} G^R_{\phi/t}(\Omega+i\epsilon,\mathbf{p})\ . \tag{5.29}$$

Here, in practice, a small but finite value of ϵ is sufficient, such that the results of our flow solution can be used without further analytical continuation.

To obtain the exact energies and lifetimes of the quasiparticles visible as sharp peaks in the spectral function, one needs to find the poles of the retarded Green's function in the lower half of the complex plane (LCP) via analytic continuation of the retarded Green's function across the real axis. At such a pole the inverse retarded Green's functions vanish

$$G^{R,-1}_{\phi/t}(\Omega'_{\phi/t}(\mathbf{p})-i\Gamma_{\phi/t}(\mathbf{p}),\mathbf{p}) = 0, \Gamma_{\phi/t}>0 \tag{5.30}$$

[1] Similarly, performing the calculation for $\epsilon<0$ one obtains the advanced Green's function in the lower half of the complex plane.

and the momentum-dependent quasiparticle energy and decay width of the respective quasiparticle are given by $E_{\phi/t}(\mathbf{p}) = \Omega'_{\phi/t}(\mathbf{p}) + \mu_\phi$ and $\Gamma_{\phi/t}$, respectively. Finally, the inverse quasiparticle weight can be obtained as

$$Z^{-1}_{\phi/t} = -\frac{\partial}{\partial\Omega} G^{R,-1}_{\phi/t}\left(\Omega'_{\phi/t}(\mathbf{p}) - i\Gamma_{\phi/t}(\mathbf{p}), \mathbf{p}\right). \tag{5.31}$$

The analytic continuation to the LCP can be achieved using a Padé approximation in which data from the UCP is used as input. Alternatively, one can also employ an approximation to linear order making use of the Cauchy-Riemann equations to find the location of the quasiparticle poles, yielding very similar results.

5.5.1 Energies and lifetimes at zero momentum in 3D

To begin, we study the energies, quasiparticle weights and lifetimes of the attractive and the repulsive polaron as well as the molecule. In Fig. 5.4 we show the zero-momentum energies $E_{\phi/t}(\mathbf{p} = 0)$ as obtained in Ref. [137]. Below a critical interaction strength of $1/(k_F a)_c \approx 0.9$ [137] the ground state is given by the attractive polaron while at the critical interaction strength the polaron-to-molecule transition [54, 56, 137, 141–143] takes place, beyond which the ground state is given by a molecular state. The repulsive polaron exists as an excited state in the spectrum above the scattering threshold and its energy vanishes asymptotically for $1/k_F a \to \infty$. The quasiparticle weight Z of the attractive and the repulsive polaron is shown as well, and as expected [58, 137] with increasing $1/k_F a$, the quasiparticle weight of the attractive polaron decreases while the quasiparticle weight of the repulsive polaron increases.

Additionally, in Fig. 5.4 we show the decay widths of the zero-momentum attractive and repulsive polaron, $\Gamma^{\text{att.}}_\phi(\mathbf{p} = 0)$ and $\Gamma^{\text{rep.}}_\phi(\mathbf{p} = 0)$, as well as the molecule, $\Gamma_t(\mathbf{p} = 0)$. Furthermore, the decay widths of the repulsive polaron as obtained from a non-selfconsistent T-matrix approach are shown [58, 59, 166]. As expected, the respective ground state particles have a decay width consistent with zero. In the regime where the attractive polaron or the molecule are excited state particles, their decay widths increase as one moves away from the polaron-to-molecule transition. With increasing quasiparticle weight, the decay width of the repulsive polaron $\Gamma^{\text{rep.}}_\phi(\mathbf{p} = 0)$ decreases.

Compared to previous work using a similar model (but a different method of solving the flow equations), we obtain decay widths about an order of magnitude larger than those obtained in [137], highlighting the delicacy of obtaining these roots and the need for a numerically stable method with many grid points and a small step size. For higher-excited states the decay widths are larger and the poles are further inside the LCP. As a result the numerical fluctuations of our method are clearly visible, but remain on the order of a few percent in contrast to previous work.

We note that for most interaction strengths, the decay widths of the attractive polaron and the molecule are not accessible in simple non-selfconsistent approaches, but rather approaches with some degree of self-consistency (such as a treatment in Fermi liquid theory, in self-consistent T-matrix theory [328] or as in our work with fRG) are necessary to obtain access to these quantities. Compared to the decay widths

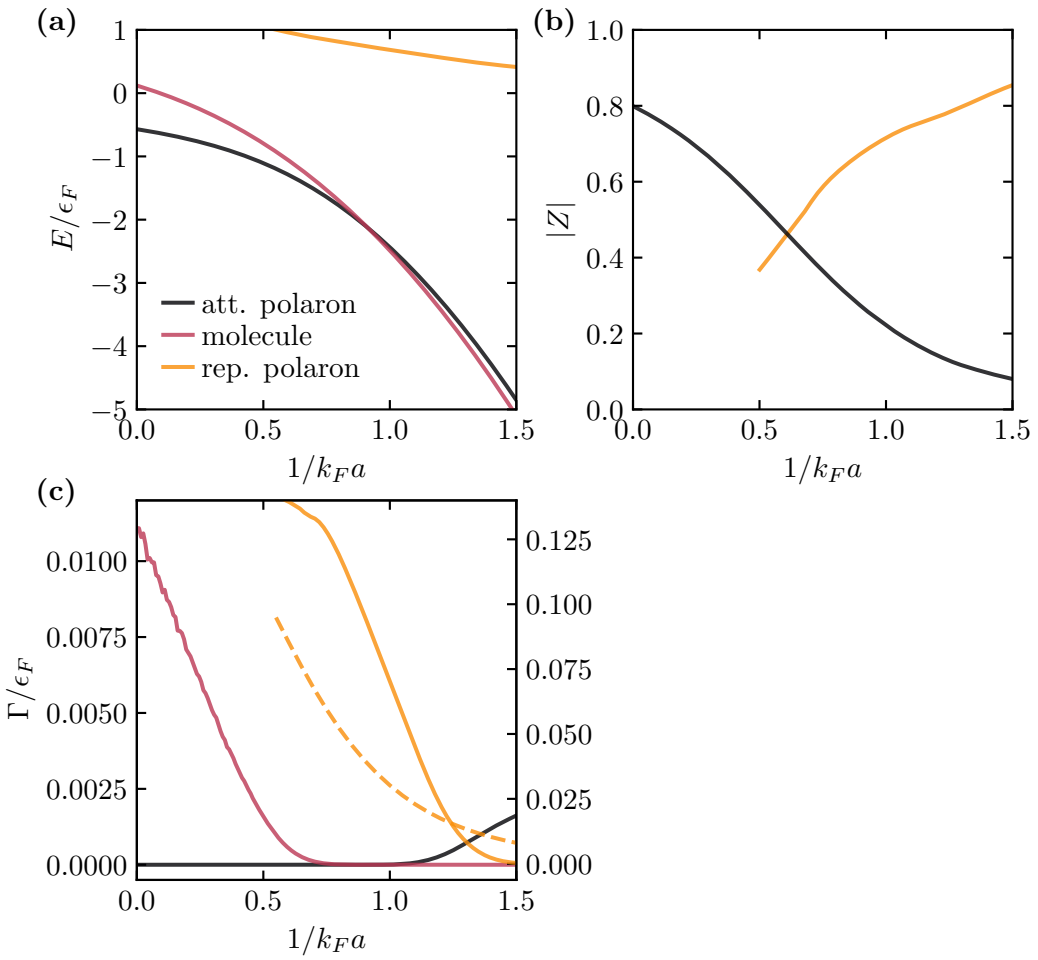

Figure 5.4. Energy, quasiparticle weight and decay width of the attractive and repulsive polaron and the molecule, as function of $1/k_Fa$. **(a)** Zero-momentum energies are shown for the attractive polaron $E_\phi^{\text{att.}}(\mathbf{p}=\mathbf{0})$ (black), the repulsive polaron $E_\phi^{\text{rep.}}(\mathbf{p}=\mathbf{0})$ (yellow) and the molecule $E_t(\mathbf{p}=\mathbf{0})$ (red) in units of the Fermi energy ϵ_F. A ground state transition at $1/(k_Fa)_c \approx 0.9$ between the molecule and the attractive polaron can be seen, while the repulsive polaron is an excited state above the scattering threshold. For increasing $1/k_Fa$ the modulus of the quasiparticle weight $|Z|$ **(b)** of the attractive polaron decreases and the spectral weight is shifted to the repulsive polaron, for which $|Z|$ increases. **(c)** Approaching the transition, the decay width Γ_t of the molecule, shown in units of the Fermi energy ϵ_F, decreases and eventually turns to zero (within numerical accuracy) as the transition is reached. The decay width **(c)** of the attractive polaron $\Gamma_\phi^{\text{att.}}$, is zero before the transition and begins to increase beyond it. The repulsive polaron has a decreasing decay width $\Gamma_\phi^{\text{rep.}}$ as its quasiparticle weight increases. While the decay widths of the attractive polaron $\Gamma_\phi^{\text{att.}}$ and the molecule Γ_t are shown for the scale on the left, the repulsive polaron decay width $\Gamma_\phi^{\text{rep.}}$ is shown with respect to the right scale. In addition to the results obtained from the fRG (solid), the decay width of the repulsive polaron is shown as obtained from a conventional non-selfconsistent T-matrix approach (dashed) [58, 59, 166].

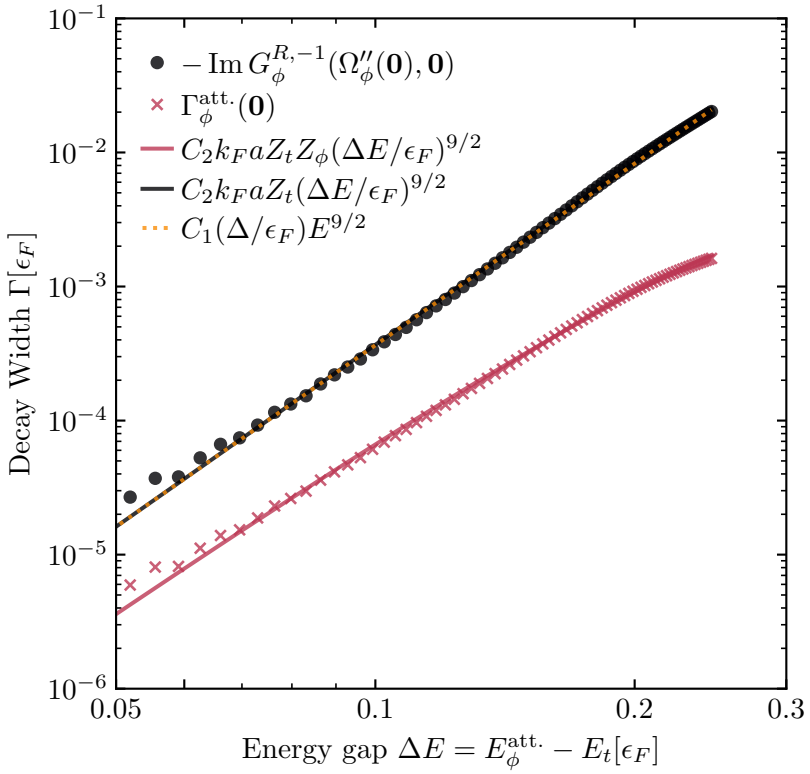

Figure 5.5. Decay width of the attractive polaron as a function of the energy gap $\Delta E = E_\phi^{\text{att.}} - E_t$, both in units of the Fermi energy ϵ_F. The decay width $\Gamma_\phi^{\text{att.}}(\mathbf{p} = \mathbf{0})$ of the attractive polaron as obtained from Eq. (5.30) is shown (red crosses) along with the imaginary part of the inverse polaron propagator $G_\phi^{R,-1}(\Omega''_\phi(\mathbf{0}), \mathbf{0})$ at the pole position as obtained from Eq. (5.33) (black dots). Note, that along the real axis, the imaginary parts of the self-energy and the inverse propagator coincide. A curve proportional to $\Delta E^{9/2}$ is shown in yellow dots and fits the imaginary part of the self-energy. Furthermore, a fit according to Eq. (5.32) is shown (solid black line). Multiplying the power law shown in Eq. (5.32) with the quasiparticle weight of the attractive polaron Z_ϕ, in analogy to Eq. (5.34), closely matches the decay width as obtained form Eq. (5.30) (solid red line).

of the repulsive polaron obtained from non-selfconsistent approaches, the fRG yields larger decay widths in the regime where the attractive polaron is the ground state, however the decay width of the fRG yields a more stable polaron as $1/k_F a$ is increased.

In Ref. [167] the decay width of the attractive polaron in the excited state was predicted to follow a $\Delta E^{9/2}$ scaling where $\Delta E = E_\phi(\mathbf{p} = 0) - E_t(\mathbf{p} = 0) > 0$ denotes the energy gap between the attractive polaron and the molecule. To be precise, it was predicted that the imaginary part of the retarded self-energy follows a scaling

$$\operatorname{Im} \Sigma_\phi^R \left(\Omega''_\phi(\mathbf{p} = 0), \mathbf{p} = 0\right) \propto Z''_t k_F a \left(\frac{\Delta E}{\epsilon_F}\right)^{\frac{9}{2}} \epsilon_F, \tag{5.32}$$

where in contrast to Eq. (5.30), Ω'' is defined as

$$\mathrm{Re}\, G^{R,-1}_{\phi/t}(\Omega''_{\phi/t}(\mathbf{p}), \mathbf{p}) = 0 \tag{5.33}$$

and $Z''_{\phi/t}$ is evaluated at $\Omega''_{\phi/t}(\mathbf{p} = \mathbf{0})$. In this scheme one can then approximate the decay width as

$$\Gamma''_{\phi/t} \approx \mathrm{Re}(Z''_{\phi/t})\, \mathrm{Im}\left[\Sigma^R_{\phi/t}\left(\Omega''_{\phi/t}(\mathbf{p} = \mathbf{0}), \mathbf{p} = \mathbf{0}\right)\right]. \tag{5.34}$$

Using Eq. (5.33), in Fig. 5.5 we show the imaginary part of the inverse polaron propagator $G^{R,-1}_{\phi}$ at $\Omega''_{\phi}(\mathbf{p} = \mathbf{0})$ and $\mathbf{p} = \mathbf{0}$ as a function of the energy gap for $1/k_F a > 1/k_F a_c$. Note that the self-energy and the inverse propagator are related by $G^{R,-1}_{\phi/t} = G^{R,-1}_{\phi/t,k=\Lambda} - \Sigma^R_{\phi/t}$. Furthermore we show the polaron quasiparticle decay width as obtained from Eq. (5.30). As it can be seen the imaginary parts as obtained using Eq. (5.33) fit well with a power law scaling of $\Delta E^{9/2}$, obtained by fitting a function of the form $C_1(\Delta E/\epsilon_F)^{9/2}$, where $C_1 \in \mathbb{R}$. Furthermore, they fit well with the scaling proposed in Ref. [167], obtained by fitting the function $C_2 Z_t k_F a\,(\Delta E/\epsilon_F)^{9/2}$, $C_2 \in \mathbb{R}$. Multiplying that same curve with the polaron quasiparticle weight Z_ϕ results in a curve that fits well with the quasiparticle decay widths computed according to Eq. (5.30). This relation between the imaginary part of the self-energy and the decay width remains accurate for all the results shown in this work. At small energy gaps the value of $\epsilon = 10^{-4}$ we used becomes larger than the decay widths and thus the decay widths become inaccurate and begin to fluctuate.

Conducting the same analysis for the molecule for $1/k_F a < 1/k_F a_c$, in Fig. 5.6 we show the imaginary part of the molecule self-energy along with the molecule decay widths. As before, at small energy gaps the decay widths and imaginary parts fluctuate, but for $\Delta E > 0.06\epsilon_F$ they are stable. As can be seen, the imaginary parts fit well a $C_3(\Delta E/\epsilon_F)^4$ scaling with $C_3 \in \mathbb{R}$ which is notably different from the $\Delta E^{9/2}$ scaling proposed in [167]. While the diagrammatics in Ref. [167] does not include decay processes to infinite order like our fRG, there is also a fundamental difference in the diagrammatics used. Due to the coupling of the impurity-majority interaction into a molecule channel, crossed diagrams are excluded in our approach at all orders. In Ref. [167], however, a low-order diagrammatic expansion is employed that includes crossed diagrams. Within that diagram, two T-matrices appear which contain no crossed diagrams within them (see Section 5.5.2). As a result, as one approaches the transition, in the diagrammatics in Ref. [167] the available phase space for decay processes vanishes as $\Delta E^{7/2}$, while the corresponding matrix element vanishes as ΔE. The vanishing of the matrix element in that approach, however, is entirely due to the use of a non-crossed T-matrix within a crossed diagrammatics. Performing a similar analysis as in Ref. [167], but excluding crossed diagrams we analytically obtain a scaling proportional to $\sim Z_\phi^3 Z_t^2 (m^*_\phi)^{7/2} (m^*_t)^2 \Delta E^{7/2}$ (see Section 5.5.2 for detail). This scaling is shown in Fig. 5.6 as well, but it fits the data points only for $0.05\epsilon_F < \Delta E < 0.2\epsilon_F$, as the effective mass of the molecule eventually diverges and turns negative (see Fig. 5.8), and thus the pure ΔE^4 scaling fits more accurately.

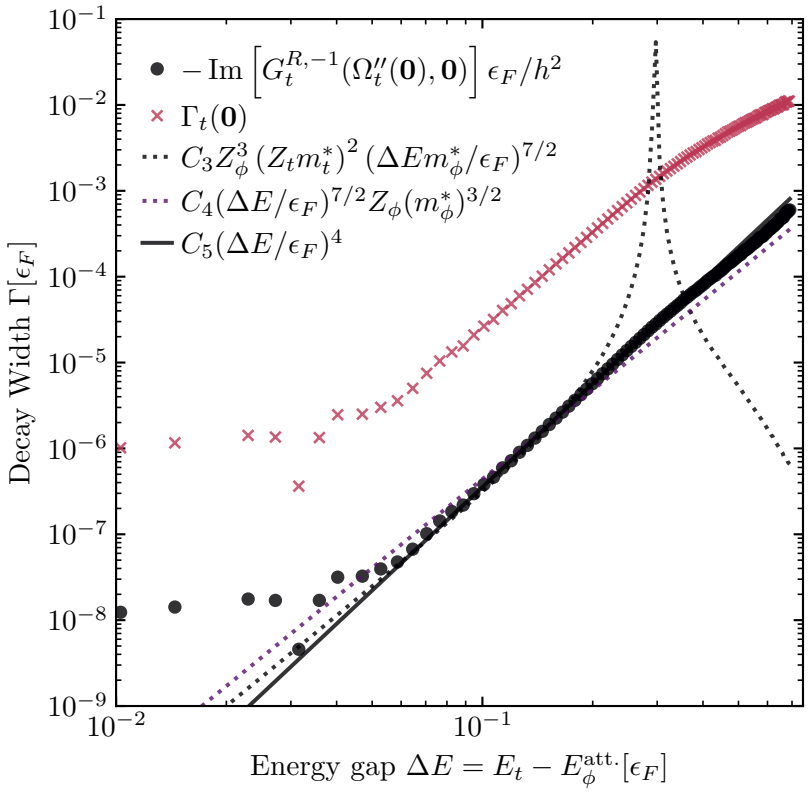

Figure 5.6. Decay width of the molecule as a function of the energy gap $\Delta E = E_t - E_\phi^{\text{att.}}$, both in units of the Fermi energy ϵ_F. Like in Fig. 5.5, the decay width $\Gamma_t(\mathbf{p} = \mathbf{0})$ of the molecule obtained from Eq. (5.30) is shown (red crosses) along with the imaginary part of $G_t^{R,-1}(\Omega_t''(\mathbf{0}), \mathbf{0})\epsilon_F/h^2$ at the pole position as obtained from Eq. (5.33) (black dots). A curve fit proportional to ΔE^4 is shown as a solid line and fits the imaginary part of the self-energy. Furthermore, a fit following a $\sim Z_\phi^3 Z_t^2 (m_\phi^*)^{7/2} (m_t^*)^2 \Delta E^{7/2}$ power law is shown (dotted black line) along with a simplified scaling $\sim Z_\phi (m_\phi^*)^{3/2} \Delta E^{7/2}$ (dotted purple line), for detail see Section 5.5.2.

5.5.2 Decay width of the excited state molecule from Fermi liquid theory

To highlight the dependence of the decay width on the diagrammatic method used, in the following we discuss how a similar approach as used in Ref. [167] may yield a different power law behavior of the molecule decay width. As mentioned in Section 5.5.1, the self-energy diagrammatics used in Ref. [167] employ a T-matrix (containing no crossed diagrams) within a crossed diagram (see Fig. 5.7(c)) to obtain a $\sim \Delta E^{9/2}$ dependence of the molecule decay width. We show that neglecting the crossed diagrams, as is done within conventional T-matrix approaches, and using a Fermi liquid theory approximation for these particles, one obtains a different power law dependence.

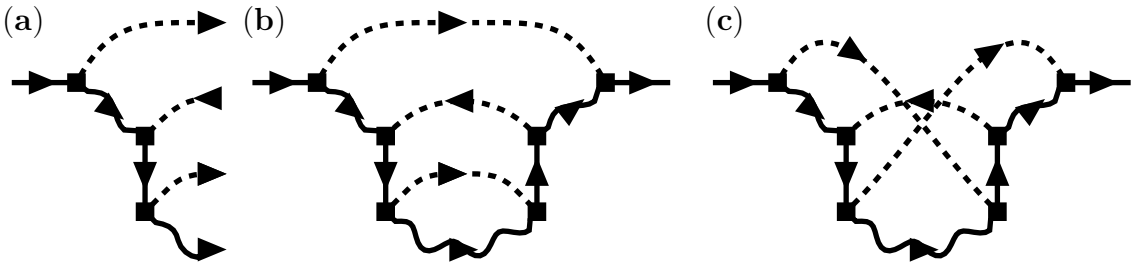

Figure 5.7. Diagrammatic representation of the decay of the excited state molecule. **(a)** Possible decay channel of an excited state molecule (solid line) into a ground state polaron (wavy line) and several bath particles and holes (dashed lines), which correspond to self-energy contributions **(b,c)** using the optical theorem. The decay channel in (a) allows for two distinct self-energy contributions, a crossed in **(c)** and a non-crossed in **(b)**. The square dots denote coupling vertices $\sim h$.

The non-crossed self-energy contribution Σ_t (see Fig. 5.7(b)) corresponding to the decay process shown in Fig. 5.7(a) is then proportional to

$$\Sigma_t(\omega,\mathbf{0}) \propto \int_{\mathbf{k},\mathbf{k}',\mathbf{q},\nu_1,\nu_2,\nu_3} \left(\frac{G_\phi^R(i[\omega-\nu_1],-\mathbf{k})^2 G_\phi^R(i[\omega-\nu_1-\nu_2+\nu_3],\mathbf{q}-\mathbf{k}-\mathbf{k}')}{(-i\nu_1+\mathbf{k}^2-\epsilon_F)\left(-i\nu_2+\mathbf{k}'^2-\epsilon_F\right)(-i\nu_3+\mathbf{q}^2-\epsilon_F)} \times T^R(i[\omega-\nu_1+\nu_3],\mathbf{q}-\mathbf{k})^2 \right). \tag{5.35}$$

To proceed, we use a pole expansion for the retarded molecule propagator T^R and the retarded impurity propagator G_ϕ^R

$$G_\phi^R(z,\mathbf{p}) \propto \frac{Z_\phi}{-z+\frac{\mathbf{p}^2}{2m_\phi^*}} \tag{5.36}$$

$$T^R(z,\mathbf{p}) \propto \frac{Z_t}{-z+\frac{\mathbf{p}^2}{2m_t^*}+\Delta E}, \tag{5.37}$$

where m_ϕ^* and m_t^* are the effective masses of the attractive polaron and the molecule and ΔE denotes the energy difference between the attractive polaron and the molecule. Carrying out the frequency integrations and evaluating the self-energy near the pole of the molecule, we then obtain

$$\operatorname{Im}\Sigma_t^R(\Delta E+i0^+,\mathbf{0}) \propto \int_{\mathbf{k},\mathbf{k}',\mathbf{q}} \frac{Z_\phi^3 Z_t^2 \delta\left(\mathbf{k}^2+\mathbf{k}'^2-\mathbf{q}^2-\epsilon_F+\frac{(\mathbf{q}-\mathbf{k}-\mathbf{k}')^2}{2m_\phi^*}-\Delta E\right)}{\left(\mathbf{k}^2-\mathbf{q}^2+\frac{(\mathbf{q}-\mathbf{k})^2}{2m_t^*}\right)^2\left(\mathbf{k}^2-\epsilon_F+\frac{\mathbf{k}^2}{2m_\phi^*}-\Delta E\right)^2}. \tag{5.38}$$

For $\Delta E \ll \epsilon_F$, the condition of the δ-function in Eq. (5.38) is fulfilled when $\mathbf{k}$, $\mathbf{k}'$ and $\mathbf{q}$ form an almost equilateral triangle at the Fermi surface with $|\mathbf{k}|, |\mathbf{k}'|, |\mathbf{q}| \approx k_F$. Thus the two terms in the denominator of Eq. (5.38) approach $[k_F^2/(2m_t^*)]^2$ and $[k_F^2/2m_\phi^*]^2$,

while in Ref. [167] it was shown that the phase space integral scales as $(m_\phi^*)^{3/2}\Delta E^{7/2}$. Hence, within this approximation we obtain that

$$\mathrm{Im}\,\Sigma_t^R(\Delta E + i0^+, \mathbf{0}) \propto Z_\phi^3 Z_t^2 \Delta E^{7/2} (m_\phi^*)^{7/2} (m_t^*)^2. \tag{5.39}$$

Alternatively, one may disregard the dynamics of the propagators in Eq. (5.35), as these propagators are not evaluated near their pole. Approximating these as constant instead, one obtains only the scaling due to the phase space integral given by $\sim Z_\phi (m_\phi^*)^{3/2}\Delta E^{7/2}$ which is also shown in Fig. 5.6.

5.5.3 Momentum-dependent energies and decay widths

Using the precision available within our numerical approach it is possible to obtain not only zero-momentum properties but also momentum-resolved energies (i.e. the full dispersion relation, including effective mass) as well as lifetimes and quasiparticle weight. In Fig. 5.8, we show the momentum-dependent attractive polaron and molecule dispersion relations with respect to the energy of the ground state. As can be seen, for $1/k_F a < 1/k_F a_c$, the polaron energies at $\mathbf{p} = 0$ coincide with the ground state energies. The dispersion relations follow a close to quadratic behavior with $|\mathbf{p}|$. Approaching and crossing the transition at $1/k_F a_c$ this quadratic dependence becomes weaker as the effective polaron mass increases and eventually diverges, as can be seen from the polaron dispersions at $1/k_F a = 1.25$ and $1/k_F a = 1.5$ [55]. Accordingly, the decay width of the attractive polaron has $\Gamma_\phi^{\mathrm{att.}}(\mathbf{p} = 0) \approx 0$ for $1/k_F a < 1/k_F a_c$ and for $1/k_F a > 1/k_F a_c$ it has $\Gamma_\phi^{\mathrm{att.}}(\mathbf{p} = 0) > 0$. In both regimes the decay width of the attractive polaron increases monotonously as $|\mathbf{p}|$ increases, see Fig. 5.8(c,d).

Similarly, the dispersion of the molecule is gapped for $1/k_F a < 1/k_F a_c$ and exhibits a negative effective mass at sufficient detuning from $1/k_F a_c$. Approaching the transition the effective mass diverges and turns towards a quadratic dispersion with positive effective mass before the transition is crossed. Beyond the transition, the dispersion is ungapped and the effective mass is always positive. As expected, the decay width of the zero-momentum molecule vanishes for $1/k_F a > 1/k_F a_c$, while it is finite for $1/k_F a < 1/k_F a_c$. As for the polaron, the decay width of the molecule increases as the momentum $|\mathbf{p}|$ increases.

The momentum-dependent decay widths observed in Fig. 5.8 are qualitatively different from the decay described in Figs. 5.4 to 5.6: There, the decay is from a zero-momentum excited state such as the attractive polaron to a lower-lying ground state manifold such as the molecule. In Fig. 5.8 on the other hand, the decay may take place within the ground-state manifold from higher to lower momenta [331]. For example, as can be seen from Fig. 5.8, at $1/k_F a = 0$ the attractive polaron with $|\mathbf{p}| = 0.5 k_F$ lies lower in energy than the molecule state and the respective particle-particle continuum. As a result, the attractive polaron with $|\mathbf{p}| = 0.5 k_F$ decays to attractive polaron states with $|\mathbf{p}'| < 0.5 k_F$, necessitating at least a minimal degree of self-consistency to capture this process.

As can be seen in Fig. 5.8, for $1/k_F a \ll 1/k_F a_c$ the polaron exhibits a near quadratic dispersion relation, while the molecule exhibits a near quadratic dispersion

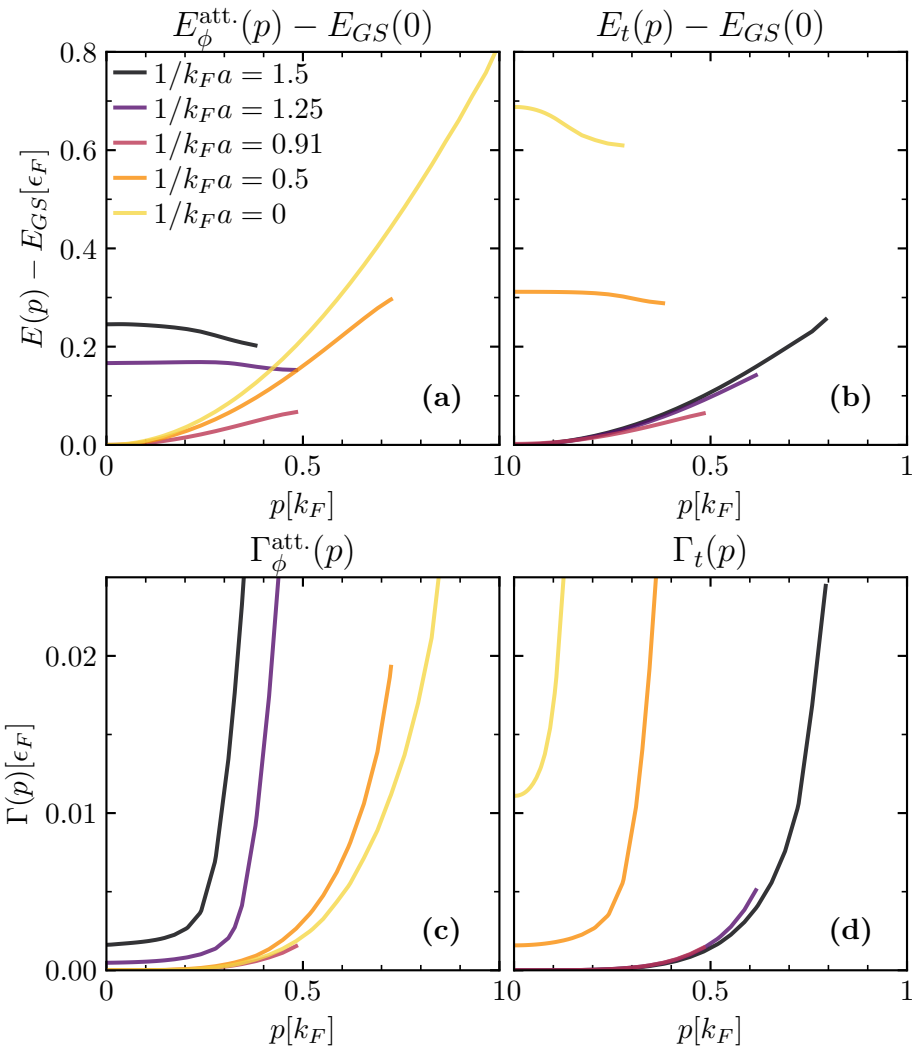

Figure 5.8. Momentum-dependent dispersion relations and decay widths of the attractive polaron and the molecule at different interaction parameters. The momentum-dependent energies of the attractive polaron $E_\phi^{\text{att.}}(p)$ **(a)** and the molecule $E_t(p)$ **(b)** are shown in units of ϵ_F as a function of momentum $p = |\mathbf{p}|$ for interaction strengths, $1/k_Fa = 1.5$ (black), 1.25 (purple), 0.91 (red), 0.5 (orange) and 0 (yellow). The zero-momentum ground-state energy, $E_\phi^{\text{att.}}(0)$ for $1/k_Fa < 0.91$ and $E_t(0)$ for $1/k_Fa > 0.91$ is subtracted for reference. The corresponding decay widths, $\Gamma_\phi^{\text{att.}}(p)$ and $\Gamma_t(p)$ are shown in **(c)** and **(d)**, respectively. As can be seen, away from the transition, the ground state develops a quadratic dispersion relation, while the excited state acquires a negative effective mass. In both cases, increasing the momentum leads to increasing decay widths.

relation for $1/k_Fa \gg 1/k_Fa_c$. This suggests that the decay width within the ground state manifold may follow a simple behavior with respect to its dependence on momentum. In the following, we investigate the momentum-dependent decay widths of the attractive polaron and the molecule, in regions where they are the ground state

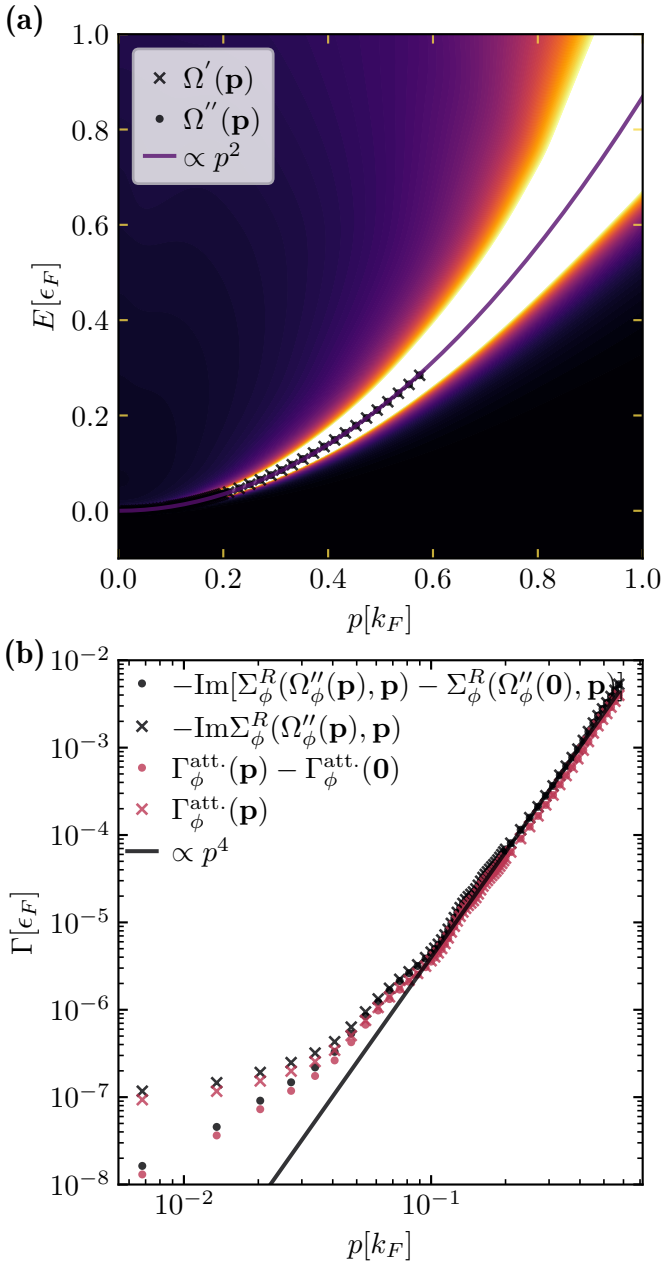

Figure 5.9. Impurity spectral function and momentum-dependent decay width of the attractive polaron at unitarity. The impurity spectral function $\mathcal{A}_\phi(\Omega, \mathbf{p})$ is shown in **(a)**, along with a quadratic fit to the dispersion relation, which coincides with both energies $\Omega'_\phi(\mathbf{p})$ and $\Omega''_\phi(\mathbf{p})$ obtained from different criteria, (5.30) and (5.33). In **(b)** the momentum-dependent decay width $\Gamma^{\mathrm{att.}}_\phi$ (red crosses) as well as the self-energy contribution $\mathrm{Im}\,\Sigma^R_\phi(\Omega''_\phi(\mathbf{p}), \mathbf{p})$ (black crosses), each also offset by their zero-momentum contribution (dots) are shown. For $p \gtrsim 0.1 k_F$ they all follow a $\sim p^4$ scaling (solid black line). A value of $\epsilon = 10^{-4}\epsilon_F$ was used.

and where their dispersion relations suggest that a treatment of the particle within Fermi liquid theory may be appropriate.

In Fig. 5.9(a) we show the momentum-resolved impurity spectral function $\mathcal{A}_\phi$ (see Eq. (5.29)) at unitarity. The attractive polaron is the dominant feature of the plot and its energy as obtained from Eqs. (5.30) and (5.33) shows a quadratic dependence $\sim p^2$ with respect to momentum with effective mass $m^*/m \approx 1.15$. Moreover, the attractive polaron shows a continuously increasing broadening for increasing momentum. This is directly reflected in the behavior of the momentum-dependent decay width of the attractive polaron shown in Fig. 5.9(b). In this figure we show both $\Gamma_\phi^{\text{att.}}(\mathbf{p})$ as evaluated from Eq. (5.30) as well as the imaginary part of the self-energy $\operatorname{Im}\Sigma_\phi(\Omega''_\phi(\mathbf{p}), \mathbf{p})$. Both evaluations yield consistent results indicating a $\propto p^4$ scaling for $p \gtrsim 0.1 k_F$.

The p^4 scaling can be obtained from an analysis within Fermi liquid theory (see Section 5.5.4) [330]. In this analysis the attractive polaron at small momenta is treated as a free particle with quasiparticle properties such as energy, effective mass, quasiparticle weight and decay width that are modified compared to the original bare particle. In this picture one thus makes full use of the quasiparticle picture of the attractive polaron that despite strong renormalization by strong-coupling at unitarity still behaves as essentially a free particle (building the basis of Fermi liquid theory).

In Fig. 5.9, it can be seen that for $p \lesssim 0.1 k_F$ the decay width and the self-energy depart from the $\propto p^4$ scaling. At this point, the decay width has become so small that it is comparable to the distance from the real axis ($\epsilon = 10^{-4}\epsilon_F$) and thus the numerical continuation of the obtained grid data from $z = \Omega + i\epsilon$ to $z = \Omega - i\Gamma$ incurs errors that are comparable to $i\epsilon$. At the same time, lowering the value of $i\epsilon$ further slows down the integration over the renormalization group scale k and the momentum $\mathbf{q}$ within Eqs. (5.19) and (5.20) as effectively a narrowly shaped Lorentzian curve needs to be integrated over numerically, which requires an increasing amount of computational effort as the Lorentzian becomes sharper. Thus, it can be seen that the decay width of the zero-momentum attractive polaron $\Gamma_\phi^{\text{att.}}(\mathbf{p} = 0)$ does not tend to zero (the expected behavior for a ground state) but rather approaches a small, but finite value. Subtracting the contribution of the decay width and the self-energy at zero momentum, we see that both are closer to the $\propto p^4$ scaling, but there is still residual error left.

In Fig. 5.10(a) we show the spectral function of the molecule $\mathcal{A}_t$ (see Eq. (5.29)) for $1/k_F a = 3$ as well as its dispersion relations. Again, both methods to determine the energy coincide and the dispersion is well characterized by a $\propto p^2$ scaling. In Fig. 5.10(b) in turn the momentum-dependent decay widths and self-energy evaluations of the molecule are shown. As for the polaron, the $\propto p^2$ dispersion suggests a $\propto p^4$ scaling in decay width and its self-energy contribution. In Fig. 5.10(b) such a scaling can be seen to develop for $p \gtrsim 0.12$. At smaller momenta the value of ϵ dominates the results. In this calculation $\epsilon = 10^{-5}\epsilon_F$ was used. Interestingly, the values obtained for $\Gamma_t(\mathbf{0})$ and also those obtained for the corresponding imaginary self-energy contribution are so small that subtracting them does not alter the shown results significantly. Instead, for $p \lesssim 0.12$ a $\propto p^2$ scaling is observed. A similar observation was noted in Ref. [330], where for a strongly population-imbalanced mixture of two Fermi gases, the decay width scaled quadratically with impurity momentum,

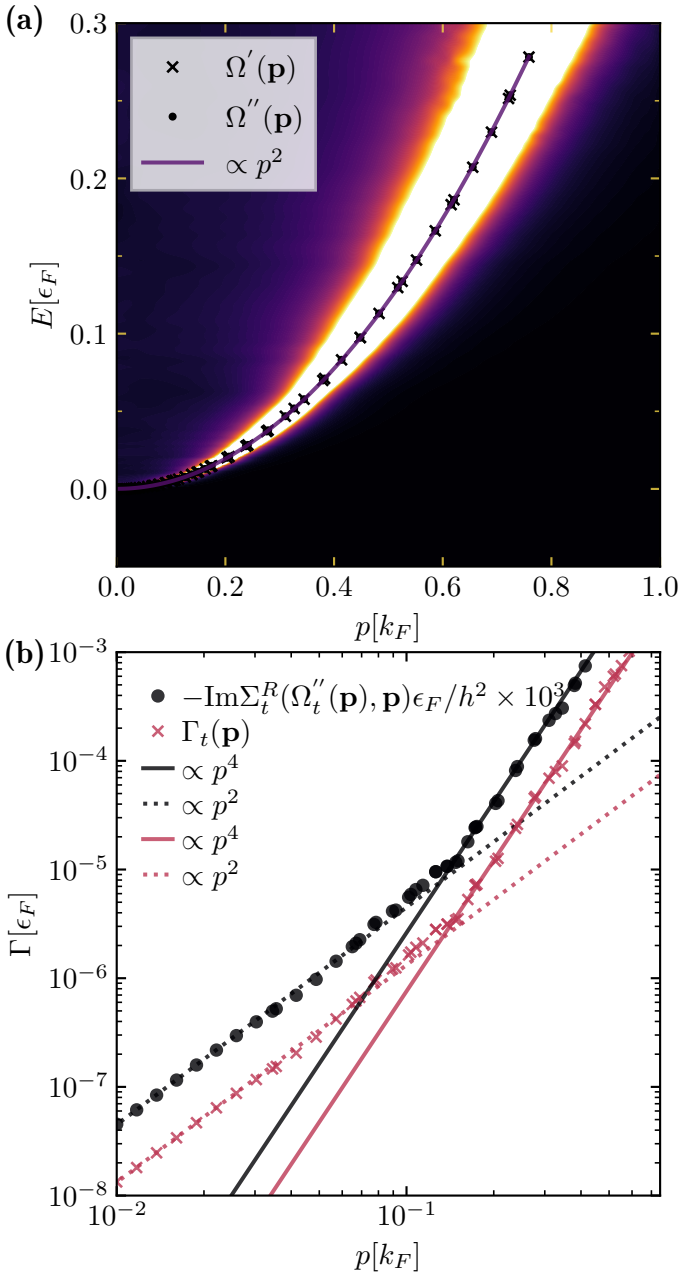

Figure 5.10. Molecule spectral function and momentum-dependent decay width of the molecule state at $1/k_F a = 3$. The molecule spectral function $\mathcal{A}_t(\Omega, \mathbf{p})$ is shown in **(a)**, along with a quadratic fit to the dispersion relation, which reproduces both energies $\Omega_t'(\mathbf{p})$ and $\Omega_t''(\mathbf{p})$ obtained from Eqs. (5.30) and (5.33). The momentum-dependent decay width $\Gamma_t(\mathbf{p})$ (red crosses) as well as the self-energy contribution $\mathrm{Im}\,\Sigma_t^R(\Omega_\phi''(\mathbf{p}), \mathbf{p})$ (black dots, rescaled by a factor of $10^3\epsilon_F/h^2$) are shown in **(b)** and follow a $\sim p^4$ scaling (black and red solid lines) for $p \gtrsim 0.1k_F$. Interestingly, for $p \lesssim 0.12$ a $\sim p^2$ scaling is observed (black and red dotted lines). A value of $\epsilon = 10^{-5}\epsilon_F$ was used.

when the impurity momentum was below the impurity Fermi wavevector, representing the well-known scaling of fermionic quasiparticles in Fermi liquid theory. Of course,

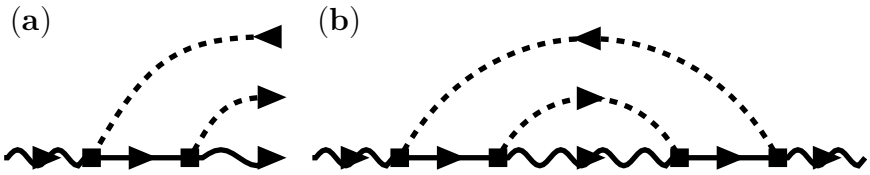

Figure 5.11. Diagrammatic representation of the decay of ground-state polarons at finite momentum into lower-lying polarons. **(a)** Possible decay channel of a polaron at finite momentum into a ground-state polaron at lower momentum and a particle and hole excitation, which corresponds to a self-energy contribution **(b)**. Unlike in Fig. 5.7, the decay channel in **(a)** allows only for a single self-energy contribution **(b)**.

the impurity Fermi level vanishes in our work (and therefore so does the impurity Fermi wavevector), however it is possible that the error incurred from a small, but non-vanishing ϵ and the ensuing analytical continuation from the horizontal line $\mathbb{R}+i\epsilon$ effectively results in a small, effective pseudo impurity Fermi wavevector, leading to an analogous quadratic scaling at very small momenta.

5.5.4 Decay of the ground state attractive polaron at finite momentum from Fermi liquid theory

At $1/k_F a \ll 1/k_F a_c$ the decay of the attractive polaron at small momentum is only into attractive polaron states of a smaller momentum because the lowest-lying molecule state lies higher in energy. The simplest decay process representing this route is shown in Fig. 5.11(a) and involves a particle-hole exchange with the bath particles. Using the optical theorem, this process can easily be turned into a corresponding self-energy contribution, which is shown in Fig. 5.11(b). As a result, the self-energy is proportional to

$$\Sigma_\phi(\omega, \mathbf{p}) \propto \int_{\mathbf{k},\mathbf{q},\nu_1,\nu_2} \frac{G^R_\phi(i[\omega+\nu_1-\nu_2], \mathbf{p}+\mathbf{q}-\mathbf{k}) T(\omega+\nu_1, \mathbf{q}+\mathbf{p})^2}{(-i\nu_1+\mathbf{q}^2-\epsilon_F)(-i\nu_2+\mathbf{k}^2-\epsilon_F)}, \tag{5.40}$$

where T denotes the T-matrix [59]. Carrying out the integration over ν_1 and ν_2 analytically by closing the contours in the right and in the left half of the complex plane, respectively, we obtain

$$\propto \int_{|\mathbf{k}|>k_F, |\mathbf{q}|<k_F} G^R_\phi(i[\omega+-i(\mathbf{q}^2-\mathbf{k}^2)], \mathbf{p}+\mathbf{q}-\mathbf{k}) T(\omega-i(\mathbf{q}^2-\epsilon_F), \mathbf{q}+\mathbf{p})^2. \tag{5.41}$$

Considering the attractive polaron as a free particle, whose interactions with the bath have been taken into account via a modification of the quasiparticle gap (to zero, as the $\mathbf{p}=0$ attractive polaron is the ground state), quasiparticle weight Z_ϕ and the effective mass m^*_ϕ, we approximate the polaron propagator $G^R_\phi(z, \mathbf{p})$ using Eq. (5.36).

Furthermore, as the decay of the attractive polaron is not into a molecule state, we approximate the scattering matrix $T \approx g$ via the bare coupling constant. Later

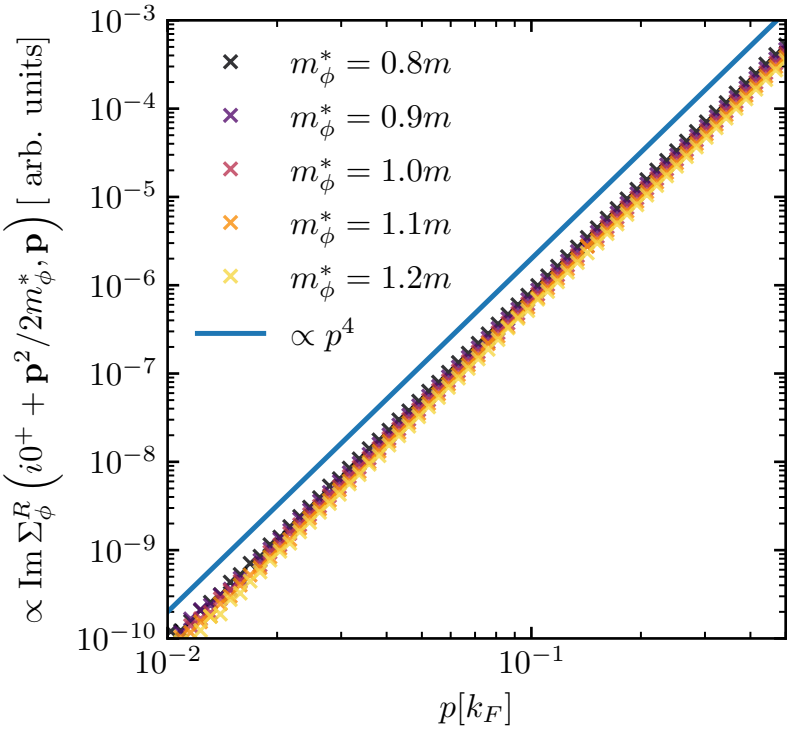

Figure 5.12. Imaginary part of the polaron self-energy contribution in Eq. (5.42) for different effective polaron masses. The self-energy contribution $\mathrm{Im}\,\Sigma^R_\phi\left(\frac{\mathbf{p}^2}{2m^*_\phi} + i0^+, \mathbf{p}\right)$ is shown in arbitrary units for different effective polaron masses ($m^*_\phi = 0.8m$(black), $0.9m$(purple), m(red), $1.1m$(orange), $1.2m$(yellow)) as a function of momentum p. The contributions follow a $\sim p^4$ scaling (blue line).

we will investigate how the inclusion of T changes the behavior of the decay width. Thus, evaluating the self-energy near the real axis at the location of the quasiparticle pole $\Omega = \mathbf{p}^2/2m^*_\phi$, we obtain that

$$\mathrm{Im}\,\Sigma^R_\phi\left(\frac{\mathbf{p}^2}{2m^*_\phi} + i0^+, \mathbf{p}\right) \propto \int_{\mathbf{k}>k_F, \mathbf{q}<k_F} \delta\left(-\frac{\mathbf{p}^2}{2m^*_\phi} + \frac{(\mathbf{p}+\mathbf{q}-\mathbf{k})^2}{2m^*_\phi} - \mathbf{q}^2 + \mathbf{k}^2\right), \quad (5.42)$$

where we have dropped the dependence on Z_ϕ.

The imaginary part of the self-energy Eq. (5.42), is shown in Fig. 5.12 for different values of the effective mass m^*_ϕ and it can be seen that the imaginary part of the self-energy at the quasiparticle pole follows a $\propto p^4$ scaling, as also seen for the full fRG model in Section 5.5.3.

Suppose now that the scattering T-matrix was not approximated by g, then along the real axis it is clear that for $i\omega \to \Omega + i0^+ = \mathbf{p}^2/2m^*_\phi + i0^+$ and $\mathbf{q}^2 < \epsilon_F$ we have that

$$\mathrm{Im}\,T^R\left(\frac{\mathbf{p}^2}{2m^*_\phi} + (\mathbf{q}^2 - \epsilon_F) + i0^+, \mathbf{q}+\mathbf{p}\right) = 0 \quad (5.43)$$

because the lowest-lying molecule state lies higher in energy (see also the discussion Section 5.3.1). One thus arrives at

$$\operatorname{Im}\Sigma_\phi^R\left(\frac{\mathbf{p}^2}{2m_\phi^*}+i0^+,\mathbf{p}\right)\propto\int_{\mathbf{k}>k_F,\mathbf{q}<k_F}\delta\left(-\frac{\mathbf{p}^2}{2m_\phi^*}+\frac{(\mathbf{p}+\mathbf{q}-\mathbf{k})^2}{2m_\phi^*}-\mathbf{q}^2+\mathbf{k}^2\right)\times T^R\left(\frac{\mathbf{p}^2}{2m_\phi^*}+(\mathbf{q}^2-\epsilon_F)+i0^+,\mathbf{q}+\mathbf{p}\right)^2. \tag{5.44}$$

Since the molecule is a higher-lying excited state by assumption, at small momentum $\mathbf{p}$ the T-matrix approaches a finite, constant value and thus the scaling of the imaginary part of the self-energy is solely determined by the phase space configuration scaling enforced by the δ-function.

5.6 Conclusion

In this chapter we have presented a modified fRG treatment of the Fermi polaron problem which not only avoids the necessity to carry out a numerical integration over imaginary Matsubara frequencies but also the need of continuing analytically to real frequencies. This is achieved by leveraging the analytical structure of the Fermi polaron problem to carry out the integration and continuation exactly. As a result, the fRG in imaginary frequencies is mapped onto an equivalent fRG on a horizontal line above the real axis, which can be shifted arbitrarily close to the real axis. The resulting fRG is significantly simpler to solve and allows to consider quasiparticle properties that either may not be accessible to previous treatments due to a lack in stability and precision or that fundamentally cannot be accessed in these treatments.

Using this modified fRG, the Fermi polaron problem was solved and the quasiparticle properties of the attractive polaron, the repulsive polaron and the molecule were revisited. We showed that energy and quasiparticle width are in accordance with previous findings and the decay width of the attractive polaron does follow a scaling of $\Delta E^{9/2}$ with respect to the energy gap to the molecule. For the decay width of the molecule near the polaron-to-molecule transition, however, the applicability of the $\Delta E^{9/2}$ scaling is less clear and further research in this direction is necessary. One of the significant improvements of the method presented in this chapter is that it allows to investigate momentum-dependent decay widths which are small for states near the ground state. We find that both the attractive polaron and the molecule seem to be captured rather accurately within Fermi liquid theory.

The measurement of these quasiparticle properties is within experimental reach, using for instance Raman transfers of impurities to finite momentum states [9]. The decay of such states is then observable using Ramsey interferometry [334, 336]. Similarly, such properties may be accessed using implementations relying on a constantly driven many-body system [337]. This may be of particular relevance as momentum relaxation seems to play an important role in the decay of Rabi oscillations [338, 339].

As polarons may now be controlled so reliably that even induced interactions between polarons can be measured [340], extensions of our fRG method may be of

interest where for small impurity concentrations the interaction between polarons may be derived from an additional polaron-polaron scattering vertex. At larger impurity concentrations further modifications may be in order where some of the exact frequency integrations are replaced by contour integrals along horizontal lines above the real axis, which may prove as a promising method of self-consistently investigating strongly-coupled Bose-Fermi and Fermi-Fermi mixtures.

Chapter 6

Dispersion forces between weakly disordered van der Waals crystals

This chapter is based on the following publication:

[6] **J. von Milczewski**, J. R. Tolsma,
Dispersion forces between weakly disordered Van der Waals crystals,

Physical Review B 104, 125111 (2021).

In this chapter, we describe a many-body theory for interlayer dispersion forces between weakly disordered atomically thin crystals and we numerically investigate the role of disorder for different layer-separation distances and for different densities of induced electrons and holes. In contrast to the common wisdom that disorder tends to enhance the importance of Coulomb interactions in Fermi liquids, we show that short range disorder tends to *weaken* interlayer dispersion forces. This is in line with previous findings that suggest that transitioning from metallic to insulating propagation weakens interlayer dispersion forces. We demonstrate that disorder alters the scaling laws of dispersion forces and we comment on the role of the maximally crossed vertex-correction diagrams responsible for logarithmic divergences in the resistivity of two-dimensional metals.

6.1 Introduction

Even when two objects are each electrically neutral, forces between the two objects which are mediated by the electromagnetic field can still be present. These so-called *dispersion* forces were named by London in his theoretical investigation of forces between molecules [341]. Although each molecule has zero total charge, quantum fluctuations in the charge density of each molecule lead to an effective dipole-dipole intermolecular force. This mechanism was later generalized by Lifshitz [342, 343] to describe forces between solids, wherein he discovered a force which scales like $1/d^3$ when the distance d between two thick slabs becomes large. Depending on the context,

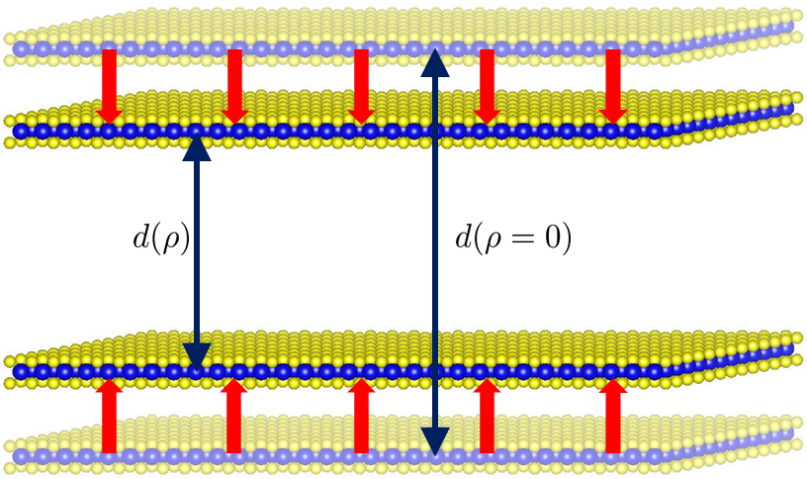

Figure 6.1. An illustration of the change in interlayer separation distance $d(\rho) - d(0)$, which results from the attractive forces between layers that are induced by creating a finite density of electrons and holes in each layer, ρ.

these forces also go under the name of van der Waals or Casimir forces, where the former (latter) often indicates that the force is mediated by the longitudinal (transverse) component of the electromagnetic gauge field [344].

Dispersion forces are relatively weak and short ranged compared to electrostatic forces, and thus are difficult to observe in experiments on solids. Recently however, advances in x-ray spectroscopy have allowed for atomic-level precision measurements of interlayer strain in thin films and atomically thin crystals [345, 346], and signatures consistent with interlayer dispersion forces among optically induced electrons and holes have been measured in transition-metal dichalcogenide multilayers [347]. This adds a new, experimentally measurable quantity to the class of phenomena which are sensitive to correlations among quasiparticles in neighboring layers of atomically thin crystals like transition-metal dichalcogenides, graphene, twisted bilayer graphene, and phosphorene. Coulomb drag [348] is a notable example of the type of phenomena which are sensitive to interlayer correlations. In these experiments a current is driven in one layer and as a result of interlayer Coulomb interactions an induced voltage drop appears in a second (otherwise passive) nearby layer. Drag experiments have led to a deeper understanding of the nature of the elementary excitations and ground state wavefunctions of complex phases of matter, from two-dimensional Fermi liquids to more exotic phases like exciton condensates [349, 350] and Luttinger liquids [351]. Just like Coulomb drag, the interlayer dispersion force between atomically thin crystals offers an interesting test bed for the various many-body theories describing the complex behavior of solids.

In this chapter we construct many-body approximations to explore the impact of weak disorder on the interlayer dispersion forces which act between layers of a bilayer heterostructure after a finite density of electrons and holes are induced in each layer as illustrated in Fig. 6.1. While *ab initio* methods for obtaining van der Waals con-

tributions to the ground state energy exist [352–357], the diagrammatic approach is sensitive to the exchange-correlation effects which density-functional theory usually deals with only on a mean-field level using variations of the local-density approximation; the approach discussed in this chapter is complementary to these existing tools and allows for the treatment of systems with strongly correlated ground states or, as we investigate in detail below, random disorder. Quasiparticle-impurity interactions are known to be responsible for a number of fascinating properties of metals, from weak-localization corrections to the longitudinal conductivity [358] to anomalies in the tunneling conductivity [359, 360], and we will make use of some of these well-developed many-body approximations in determining the role of weak disorder on interlayer dispersion forces.

To begin, in Section 6.2 we describe a many-body theory for the interlayer dispersion force based on a linked-cluster expansion for the correlation energy of a bilayer in the absence of disorder as discussed previously [361, 362]. Furthermore, we connect this approach to an equivalent treatment using the functional renormalization group. In the limit of high quasiparticle density and large separation distance d, one recovers a well-known $d^{-5/2}$ scaling behavior [362–364] in agreement with predictions from Quantum Monte Carlo methods [365]. Then, in Section 6.3 we describe a leading-order-in-$1/\varepsilon_{\rm F}\tau$ theory for interlayer forces. We demonstrate that disorder qualitatively alters the scaling laws and demonstrate that disorder tends to *reduce* the magnitude of interlayer forces. In Section 6.4 we discuss the impact on interlayer forces by a class of Feynman diagrams known to yield logarithmic divergences in the longitudinal resistivity of two-dimensional metals. Finally, in Section 6.5 we summarize the results and discuss interesting questions to be addressed in the future.

6.2 Induced dispersion forces in bilayer systems

Let us consider a system governed by the following Hamiltonian:

$$\hat{H} = \hat{H}_0 + \hat{H}_{\text{e-e}} + \hat{H}_{\text{e-imp}} \tag{6.1}$$

which describes the kinetic energy of electrons and holes, the Coulomb interaction, and the interaction of electrons and holes with impurities, respectively. We assume, as is often the case experimentally, that the density of induced electrons and holes (quasiparticles) is such that the kinetic energy of electrons and holes can be described by an effective mass approximation

$$\hat{H}_0 = \sum_{\boldsymbol{k}\alpha I} \varepsilon_\alpha(\boldsymbol{k})\, \hat{a}^\dagger_{\boldsymbol{k}\alpha I}\, \hat{a}_{\boldsymbol{k}\alpha I} \ , \tag{6.2}$$

where $\varepsilon_\alpha(\boldsymbol{k}) = \hbar^2 k^2/2m_\alpha$ and α is a composite index which labels the spin, valley, and band (e.g., valence vs conduction band) quantum numbers. In the following, we will consider the limit in which interlayer hopping is weak compared to the exchange-correlation energy per electron. Thus, the single-particle wavefunctions have a which-layer quantum number $I = 1, 2$, which denotes the two layers. Interlayer hybridization

of the conduction and valence bands is notoriously weak in van der Waals crystals (as the name suggests) and is often further weakened by rotational misalignment of neighboring layers.

The charged quasiparticles in the various layers of the system interact with each other via the Coulomb interaction

$$\hat{H}_{\text{e-e}} = \frac{1}{2L^2} \sum_{\substack{\boldsymbol{q}\, IJ \\ \boldsymbol{k}_1\boldsymbol{k}_2 \\ \alpha\beta}} V_{IJ}(\boldsymbol{q})\ \hat{a}^\dagger_{\boldsymbol{k}_1+\boldsymbol{q}\alpha I}\hat{a}^\dagger_{\boldsymbol{k}_2-\boldsymbol{q}\beta J}\hat{a}_{\boldsymbol{k}_2\beta J}\hat{a}_{\boldsymbol{k}_1\alpha I}\ , \tag{6.3}$$

where

$$V_{IJ}(\boldsymbol{q}) = \begin{cases} 2\pi e^2/(\kappa q), & I = J \\ 2\pi e^2 e^{-qd}/(\kappa q), & I \neq J. \end{cases} \tag{6.4}$$

The material-specific parameter κ describes the dielectric contributions of the elementary excitations outside of our model [e.g., phonons and propagation of electric field outside of the two-dimensional (2D) material]. The strength of Coulomb interactions is traditionally [366] described by the value of a parameter r_s which expresses the ratio of average interaction energy to average kinetic energy in a disorder-free two-dimensional electron gas (2DEG), $r_s \propto \langle \hat{H}_{\text{e-e}}\rangle/\langle \hat{H}_0\rangle$. The parameter depends on the total density of electrons (and holes) in each layer n_I and is larger when the density is lower, $r_s = \left[a_B^*\sqrt{\pi n_I}\right]^{-1}$. Here, $a_B^* = \kappa a_B/m_{eff}$ is the effective Bohr radius. When the system contains particle populations described by different effective masses it is useful to define a_B^* using the geometric mean of the masses $m_{eff} \to \sqrt{m_e m_h}$. Interactions of charged quasiparticles in different layers are ultimately responsible for the induced van der Waals forces we describe. In this chapter we consider densities of induced quasiparticles which are large enough to form electron liquids and hole liquids rather than excitons, as was recently demonstrated at room temperature [367].

The interaction between impurities of the crystal and electrons as well as holes is obtained by assuming that each impurity creates a deviation in the perfectly periodic scalar potential created by the underlying lattice. This scalar potential couples linearly to the density of electrons and holes,

$$\hat{H}_{\text{e-imp}} = \frac{1}{L^2}\sum_{\boldsymbol{Q},I} u_I(\boldsymbol{Q})\rho_I(\boldsymbol{Q}) \sum_{\boldsymbol{k}\alpha} \hat{a}^\dagger_{\boldsymbol{k}+\boldsymbol{Q}\alpha I}\,\hat{a}_{\boldsymbol{k}\alpha I}, \tag{6.5}$$

where $\rho_I(\boldsymbol{Q})$ is the Fourier transform of the density of impurities in layer I, and $u_I(\boldsymbol{Q})$ is the Fourier transform of the scalar potential of each impurity. We assume that electrons and holes only scatter off the impurity potential in the same layer, and we assume that the scalar potential is short ranged so that $u_I(\boldsymbol{Q})$ is actually independent of wave vector. The quasiparticle-impurity scattering time τ_k can be defined using the Born approximation for the self-energy [81] where $\Sigma(\boldsymbol{k},\omega) = -i\hbar/2\tau_{\boldsymbol{k}}$. In the presence of finite disorder, the scattering rate at the Fermi energy is used to define the small parameter of our perturbation theory $1/(\tau\varepsilon_{\text{F}}) \ll 1$, where we here (and will continue to) drop the subscript on τ.

Our method for evaluating the force between two atomically thin crystals consists of first calculating the ground state energy per layer as a function of interlayer

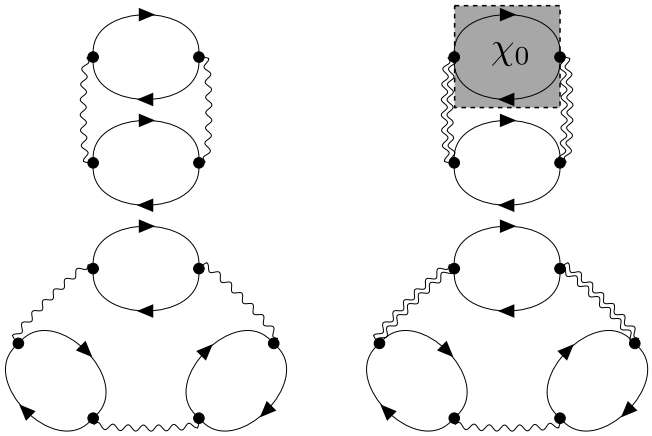

Figure 6.2. Feynman diagrams for the correlation energy of a bilayer system whose quasiparticles interact via intralayer Coulomb interactions (single wavy lines) and interlayer Coulomb interactions (double wavy lines). Only the four lowest-order diagrams are shown here. Solid lines with arrows represent noninteracting Green's functions of quasiparticles.

separation distance d, and then calculating the force by taking the first derivative

$$\mathcal{F} = -\frac{1}{2}\frac{\partial E}{\partial d} \ . \tag{6.6}$$

The ground state energy can be evaluated by taking the zero-temperature limit of the thermodynamic free energy Ω. The latter has a well-known perturbative formulation in the linked-cluster expansion [81]

$$\Omega - \Omega_0 = -\frac{1}{\beta}\sum_{\ell>0}\frac{1}{\ell!}\left(\frac{-1}{\hbar}\right)^{\ell}\int_0^{\hbar\beta} d\tau_1 \ldots \int_0^{\hbar\beta} d\tau_\ell \mathrm{tr}\left\{\rho_0 \mathrm{T}_\tau\left[\hat{V}(\tau_1)\ldots\hat{V}(\tau_\ell)\right]\right\}_0 \ , \tag{6.7}$$

where ρ_0 is the non-interacting density matrix, T_τ is the (imaginary) time-ordering operator, and $\hat{V}(\tau) = \hat{H}_{\text{e-imp}}(\tau) + \hat{H}_{\text{e-e}}(\tau)$ is the sum of the two interactions in our model within the interaction picture of time evolution [81]. By applying Wick's theorem, all contributions at order ℓ can be expressed in terms of integrals over noninteracting Green's functions, the Coulomb interaction V, and the electron-impurity interaction u_I. One can now make use of Feynman diagram techniques to efficiently calculate these contributions. We now have all the tools necessary to evaluate the interlayer force to any order in perturbation theory.

Before we consider the effects of weak disorder on the interlayer forces, we reproduce the well-known $d^{-5/2}$ scaling of energy [362–365, 368] by examining the force between two two-dimensional electron gases within the random-phase approximation (RPA) [369–372] and taking the limit of large interlayer distance d. We thus ignore disorder and take $\hat{V}(\tau) = \hat{H}_{\text{e-e}}(\tau)$ within Eq. (6.7). The RPA can be understood as an expansion of the ground state energy in powers of the small parameter r_s, and therefore gives a criterion for selecting which subset of Feynman diagrams at each

order in ℓ within Eq. (6.7) must be included in an approximation to a given order in r_s. The four lowest-order diagrams which contribute to the correlation energy are shown in Fig. 6.2. The full RPA approximation consists of summing all diagrams of this type, which at each order in ℓ contain ℓ bubble subdiagrams. The degeneracy of the diagrams in Fig. 6.2 is such that the infinite series of these types of diagrams can be resummed into a logarithm of a simple function of the single bubble diagram. After taking the derivative of the RPA approximation for the correlation energy [362], we obtain the following integral expression for the force per layer between a bilayer system containing a finite density of electrons and holes in each layer

$$\mathcal{F} = -\frac{\hbar L^2}{4\pi^2}\int_0^\infty dq \int_0^\infty d\omega \frac{q^2 V_{12}^2 \chi_0^2}{(1 - V_{11}\chi_0)(1 - V_{22}\chi_0) - V_{12}^2\chi_0^2} \ . \tag{6.8}$$

Here, χ_0 is represented by the bubble subdiagrams found in the four diagrams in Fig. 6.2 and describes the noninteracting density-density response function of each layer. The zero-temperature limit of χ_0 can be evaluated for parabolic-band effective mass models, and in the presence of both valence and conduction bands, $\chi_0 = \sum_\alpha \chi_0^\alpha$, where χ_0^α is the Lindhard function [373] of the $\alpha-$particle species. The integral over frequency in Eq. (6.8) is over the imaginary frequency axis, and the arguments of $\chi_0^\alpha(q, i\omega)$ have been omitted for brevity.

The application of Eq. (6.8) assumes that thermal equilibrium has been reached among the electrons and holes, which is usually several orders of magnitude faster than the electron-hole recombination time, and does not limit experimental observations. For arbitrary electron/hole densities and interlayer separation distances, Eq. (6.8) must be evaluated numerically. Furthermore, it should be mentioned that Eq. (6.8) leads to a nonvanishing force even in the absence of holes.

6.2.1 Derivation of ground state energy and force per layer from the fRG

Rather than using the linked cluster expansion and conducting Feynmann diagrammatics, the ground state energy and the force per layer can also be obtained using a two-channel model and the functional renormalization group, which we will sketch in the following. For simplicity, we consider only a single spin, valley and band quantum number in every layer, which can easily be generalized. In this case the Hamiltonian in Eqs. (6.2) and (6.3) can be used to generate a corresponding action

$$\begin{aligned} S = &\sum_I \int_Q \psi_I^*(Q)\left[-i\omega + \varepsilon(\mathbf{q}) - \mu_F\right]\psi_I(Q) \\ &+ \frac{1}{2}\sum_{IJ}\int_{QKK'} V_{IJ}(\mathbf{q})\psi_I^*(K+Q)\psi_J^*(K'-Q)\psi_J(K')\psi_I(K), \end{aligned} \tag{6.9}$$

where the ψ-field corresponds to the electron operators a. Using a Hubbard-Stratonovich transformation [49, 50] into a scalar bosonic field $m_I \propto \psi_I^*\psi_I$ this can then be rewritten

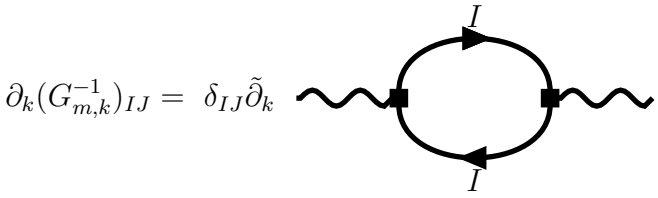

Figure 6.3. Feynman diagram of the flow of the m-field propagator shown in Eq. (6.11). Wiggly lines denote the m-field propagators, while solid lines denote electrons.

into an equivalent two-channel action

$$S_{2CH} = \sum_I \int_Q \psi^*_I(Q)\left[-i\omega + \varepsilon(\mathbf{q}) - \mu_F\right]\psi_I(Q) + \frac{1}{2}\sum_{IJ} m_I(Q)P_{IJ}(Q)m_J(-Q) + \lambda\sum_I \int_{QK} \psi^*_I(K+Q)\psi_I(K)m_I(Q), \tag{6.10}$$

where in the limit $\lambda \to \infty$ we have $-\lambda^2 P^{-1}_{IJ}(Q) = V_{IJ}(\mathbf{q})$. Note that while P_{IJ} formally is dependent on frequency (rendering m a dynamic field), in the limit $h \to \infty$ this dependence is asymptotically vanishing and as a result we will disregard this dependence. For simplicity, in the following we set $\lambda = 1$. Of course λ could be restored at anytime, but the results will not change.

Let us now, perform a two-step RG, where in the first RG we renormalize the self-energy of the m-field using a particle-hole bubble shown in Fig. 6.3. The first RG is conducted in a one-loop approximation such that after introducing a sharp regulator for the electrons (for details on this procedure see Section 2.3 and Chapter 5) the flow of the renormalized Green's function of the m particles takes the following form

$$\partial_k(G^{-1}_{m,k})_{IJ}(P) = -\delta_{IJ}\tilde{\partial}_k \int_Q \frac{\Theta(|\mathbf{q}| - k)}{-i\nu + \varepsilon(\mathbf{q}) - \mu_F}\frac{\Theta(|\mathbf{q}+\mathbf{p}| - k)}{-i(\nu+\omega) + \varepsilon(\mathbf{q}+\mathbf{p}) - \mu_F}, \tag{6.11}$$

where

$$(G^{-1}_{m,k=\Lambda})_{IJ}(P) = P_{IJ}(P) \tag{6.12}$$

such that

$$\begin{aligned}(G^{-1}_{m,k=0})_{IJ}(P) &= P_{IJ}(P) + \delta_{IJ}\int_Q \frac{1}{-i\nu + \varepsilon(\mathbf{q}) - \mu_F}\frac{1}{-i(\nu+\omega) + \varepsilon(\mathbf{q}+\mathbf{p}) - \mu_F} \\ &= P_{IJ}(P) + \delta_{IJ}\chi_0(P).\end{aligned} \tag{6.13}$$

Here χ_0 denotes the Lindhard function mentioned earlier and keeping the notation introduced before, its function argument contains Matsubara frequencies $i\omega$ rather than ω.

Thus, the resulting quantum effective action Γ_{2CH} which acts as an input classical action S' to the second RG is given by

$$\begin{aligned} S' = \Gamma_{2CH} = &\sum_I \int_Q \psi_I^*(Q)\left[-i\omega + \varepsilon(\mathbf{q}) - \mu_F\right]\psi_I(Q) \\ &+ \frac{1}{2}\sum_{IJ} m_I(Q)\left[P_{IJ}(Q) + \delta_{IJ}\chi_0(Q)\right]m_J(-Q) \\ &+ h\sum_I \int_{QK} \psi_I^*(K+Q)\psi_I(K)m_I(Q). \end{aligned} \tag{6.14}$$

Once again we can use the Wetterich equation in a one-loop approximation where on the left hand side of the flow equation no vertex flows. We then have that the effective action after a second RG process is given by

$$\Gamma'_{2CH} = S' + \frac{1}{2}\,\mathrm{STr}\log\left(\Gamma^{(2)}_{2CH}\right), \tag{6.15}$$

where

$$\begin{aligned} \left(\Gamma^{(2)}_{2CH}\right)_{\sigma\sigma'} &= \frac{\delta^2}{\delta\sigma\delta\sigma'}\Gamma_{2CH} \\ &= \begin{pmatrix} 0 & P_\psi & 0 & 0 \\ -P_\psi & 0 & 0 & 0 \\ 0 & 0 & P_{11}+\chi_0 & P_{12} \\ 0 & 0 & P_{12} & P_{22}+\chi_0 \end{pmatrix}_{\sigma\sigma'} \end{aligned} \tag{6.16}$$

and $P_\psi(\mathbf{p},\omega) = -i\omega + \varepsilon(\mathbf{q}) - \mu_F$. We thus arrive at

$$\begin{aligned} \Gamma'_{2CH} &= S' + \frac{1}{2}\int_P \log\left(\left[P_{11} - P_{12} + \chi_0\right]^2\left[P_{11} + P_{12} + \chi_0\right]^2\right) + (\text{terms involving } P_\psi) \\ &= S' + \frac{1}{2}\int_P \log\left(\frac{(1 - V_{11}\chi_0)(1 - V_{22}\chi_0) - (V_{12}\chi_0)^2}{V_{11}V_{22} - V_{12}^2}\right) + (\text{terms involving } P_\psi) \end{aligned} \tag{6.17}$$

and since the denominator in the logarithm does not hold a frequency dependence as mentioned in Section 2.3.4.2 this can be simplified to

$$\Gamma'_{2CH} = S' + \frac{1}{2}\int_P \log\left((1 - V_{11}\chi_0)(1 - V_{22}\chi_0) - (V_{12}\chi_0)^2\right) + (\text{terms involving } P_\psi). \tag{6.18}$$

As a result, the part of the energy density Γ'_{2CH} that depends on the interlayer distance is given by

$$\begin{aligned} E_{12}[d] = &\frac{1}{2}\frac{1}{(2\pi)^2}\int_0^\infty dqq\int_{-\infty}^\infty d\omega \\ &\times \log\left(\left[1 - V_{11}(q)\chi_0(q,i\omega)\right]\left[1 - V_{22}(q)\chi_0(q,i\omega)\right] - \left[V_{12}(q)\chi_0(q,i\omega)\right]^2\right), \end{aligned} \tag{6.19}$$

which after using that $\chi_0(q,i\omega) = \chi_0(q,-i\omega)$ and

$$-\frac{1}{2}\frac{\partial}{\partial d}E_{12}[d] = \frac{\mathcal{F}}{L^2}, \tag{6.20}$$

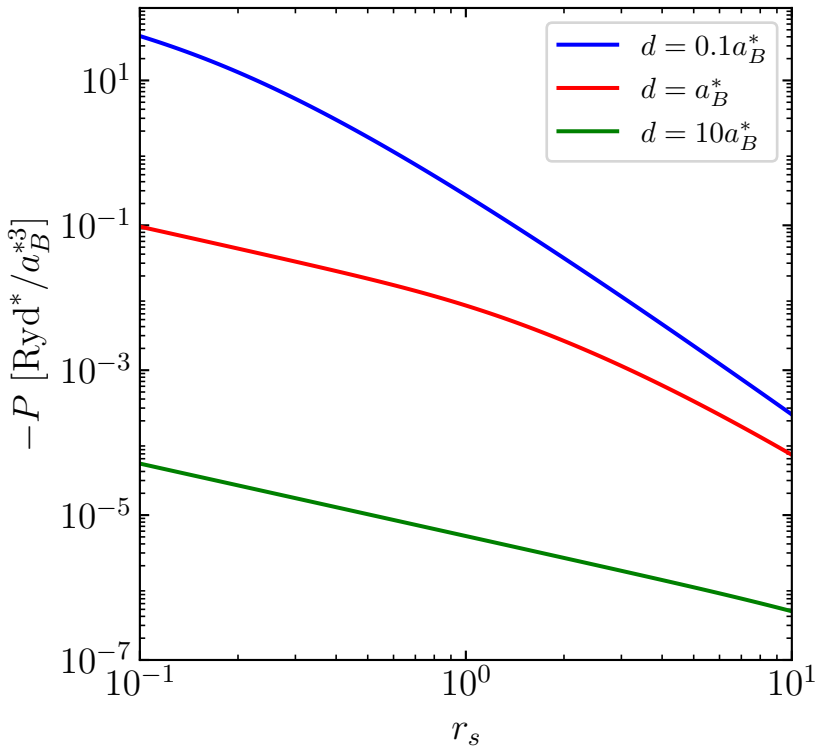

Figure 6.4. Interlayer forces as a function of the density of induced quasiparticles in a disorder-free bilayer system. On the vertical axis is the force per area in units of effective Rydbergs per effective Bohr radius cubed, where $\mathrm{Ryd}^* = e^2/\kappa a_B^*$. On the horizontal axis is the dimensionless parameter r_s which is inversely proportional to the square root of the density of induced quasiparticles.

reproduces Eq. (6.8).

This serves as a further example of how complicated diagrammatics within a single-channel model are surprisingly simple to derive in a two-channel model, as we saw already when comparing the diagrammatics in Section 2.2.2.2 and Chapter 4.

6.2.2 Numerical Results

In Fig. 6.4 we present the results of numerical calculations for the pressure (i.e., force per area) between two layers of atomically thin crystals with induced densities of electrons and holes parametrized by r_s. One immediately notices that the force between layers is attractive and that the magnitude varies dramatically with interlayer separation distance as V_{12} is dependent on d. This is a particular feature of the type of dispersion force that derives from the instantaneous Coulomb interaction (typically called van der Waals forces) instead of forces originating from the transverse and retarded parts of the electromagnetic field (typically called Casimir forces). While Casimir forces act at larger distances than van der Waals forces, they are significantly weaker and they are independent of the amount of impurities in the materials.

To demonstrate how the RPA theory obtains the known $d^{-5/2}$ scaling for the energy [362–365, 368], Eq. (6.8) is now evaluated in the limit of large interlayer separation to find the leading-order contribution to the interlayer force in the small parameter $1/(k_{\mathrm{F}}d)$, where $k_{\mathrm{F}} = \sqrt{k_{\mathrm{F}}^e k_{\mathrm{F}}^h}$ is the Fermi wave vector of the electron and hole Fermi seas which are present in each layer after excitation and thermalization. The presence of e^{-2qd} in the numerator of Eq. (6.8) restricts the relevant range of q in the integral to $q \lesssim 1/d$, which bears the physical interpretation that 2D in-plane charge perturbation waves at wavelengths which are short compared to the interlayer distance appear averaged out on the adjacent plate and thus will not contribute to forces. Long wavelengths, however, will not appear as averaged out and will therefore contribute to interlayer forces. In the limit $k_{\mathrm{F}}d \gg 1$, the dominant contribution to interlayer forces will then come from long in-plane wavelengths and this thus restricts the relevant part of phase space to small values of q. In this region of phase space one can approximate χ_0^α by its *dynamic* long-wavelength limit (i.e., $\omega > q$, $q \to 0$) which gives the leading-order contribution to the force. In the *dynamic* long-wavelength limit the noninteracting density-density response function of band α is given by

$$\chi_0^\alpha(q, i\omega) = -\frac{\rho_\alpha}{m_\alpha}\frac{q^2}{\omega^2} \ , \tag{6.21}$$

where ρ_α is the two-dimensional density of charged quasiparticles in band α. It is then straightforward to evaluate Eq. (6.8) analytically: using the dynamic long-wavelength of Eq. (6.21) within Eq. (6.8), one can carry out the frequency integral analytically and the momentum integral numerically to obtain the leading order in $1/(k_{\mathrm{F}}d)$:

$$\mathcal{F}_{7/2} = -\frac{\hbar e \xi_1 L^2}{8\sqrt{2\pi m}}\left(\frac{\sqrt{\rho}}{d^{7/2}}\right) \ , \tag{6.22}$$

which corresponds to the $d^{-5/2}$ scaling for the energy. Here,

$$\xi_1 \approx 0.315, \tag{6.23}$$

ρ is the total two-dimensional quasiparticle density in each layer, and we have taken $m_h = m_e = m$, and $\kappa = 1$ for simplicity. Interestingly, in the case of infinitely many parallel plates (superlattice), the scaling of force per layer is identical to Eq. (6.22) up to redefinition of ξ_1 [347]. By randomly choosing two adjacent plates and identifying the gap between them as the gap between two semi-infinite thick slabs separated by a distance d, one can connect this result to Lifshitz' theory for thick, semi-infinite slabs. Introducing the three-dimensional density $\rho_{3D} = \rho/d$ in Eq. (6.22) to compare with Lifshitz' theory, one immediately sees that we have reproduced the power law for the interlayer force in terms of interlayer separation and quasiparticle density (i.e., $\mathcal{F} \propto \sqrt{\rho_{3D}}d^{-3}$).

Despite the obvious utility of simple formulas like Eq. (6.22), the derivation demonstrates that only the long-wavelength excitations (i.e., plasmons) are accounted for, while finite q excitations (e.g., noncoherent particle-hole excitations) are neglected. Indeed, Eq. (6.22) is only reasonable in the limit $1/(k_{\mathrm{F}}d) \ll 1$, and outside of this

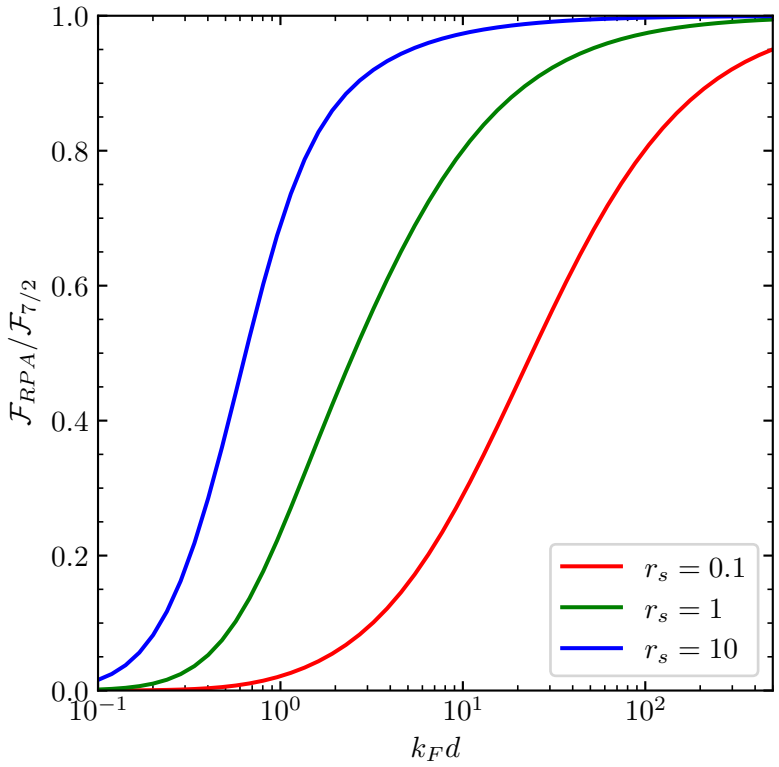

Figure 6.5. Ratio of the interlayer force in the random-phase approximation (RPA) $\mathcal{F}_{RPA}$, calculated numerically using Eq. (6.8), to the interlayer force in the leading-order-in-$(k_\mathrm{F}d)^{-1}$ approximation $\mathcal{F}_{7/2}$, given by Eq. (6.22). The more accurate RPA approximation predicts much smaller interlayer attraction unless $k_\mathrm{F}d \gg 1$, in which case both approximations yield the same result.

regime the interlayer forces are more accurately described by numerically evaluating Eq. (6.8). This is demonstrated in Fig. 6.5, where the ratio of pressure in the RPA approximation of Eq. (6.8) to the asymptotic form of Eq. (6.22) is shown. In the limit of $k_F d \gg 1$ the predictions coincide, while for smaller values of $k_F d$ the asymptotic form gives much higher interlayer attraction than the RPA form. In subsequent sections we will describe how these power law scalings are altered by the presence of impurities.

6.3 Impact of disorder on VdW forces: The 'Diffuson'

In this section we lay out the basic elements of a many-body theory for the impact of weak disorder on the interlayer van der Waals (VDW) forces between atomically thin crystals. Specifically, we begin by introducing the small parameter (i.e., $1/\varepsilon_\mathrm{F}\tau$) of the electron-impurity and hole-impurity interactions within the context of the first-order Born approximation (1BA) for the self-energy. We then identify the most relevant Feynman diagrams which contribute to interlayer dispersion forces within the regime of $r_s < 1/\varepsilon_\mathrm{F}\tau$. These diagrams contain an infinite series of ladder diagrams, and we discuss the solution of the Bethe-Salpeter equation for the vertex correction of the density-response function in the limit of short ranged impurity potentials. In contrast

to the effect of disorder on other phenomena which arise due to interlayer interactions (e.g., Coulomb drag [374]), one finds that disorder tends to *weaken* the magnitude of van der Waals forces.

The electron-impurity and hole-impurity scattering rates can be defined by the 1BA for the self-energy. In this approximation the self-energy is purely imaginary, $\Sigma(\boldsymbol{k},\omega) = -i\hbar/2\tau_{\boldsymbol{k}}$. For simplicity, we will take the hole's and electron's impurity scattering rates to be equal, although this condition is easily relaxed if required. The 1BA is given by the Feynman diagrams depicted in panel a) and b) of Fig. 6.6. Explicitly, the 1BA for the q-independent scattering rate at the Fermi energy is

$$\frac{1}{\tau} = \frac{\nu_\alpha}{2\hbar\pi}\rho^{imp}|u|^2, \tag{6.24}$$

where ν_α is the two-dimensional density of states at the Fermi surface of a single spin- and valley-resolved band, and $\rho^{imp} = \lim_{Q\to 0}[\rho_I(\boldsymbol{Q})]$. In obtaining Eq. (6.24) we have made two standard approximations for treating quenched disorder in solids [81]. First, we assume that the impurity potential is short ranged, such that the Fourier transform of the potential which appears in Eq. (6.5), $u_I(\boldsymbol{Q})$, becomes independent of wave vector. Second, the impurity potential at any two different points is uncorrelated, such that the average over the probability distribution governing the impurity potential leads to $\langle\rho_I(\boldsymbol{Q})\rho_I(-\boldsymbol{Q})\rangle_{imp} = N_{imp}$, where N_{imp} is the number of impurities in layer I.

Next, we consider how to incorporate quasiparticle-quasiparticle interaction diagrams *and* quasiparticle-impurity interaction diagrams into an approximation for the dispersion force between atomically thin crystals. In the previous section we identified the leading-order-in-r_s contribution to interlayer forces as the derivative of the RPA diagrams for the ground state energy. In order to work with a well-controlled perturbation theory we will restrict our selection of diagrams to the case when $r_s \ll 1/(\tau\varepsilon_{\rm F})$. This allows us to obtain a well-controlled theory in both small parameters. The key is to not alter the order in r_s of a diagram when adding any particular quasiparticle-impurity interaction line. We can accomplish this by adding to the RPA diagrams a nearly identical set of diagrams in which the noninteracting density-density response function bubble is *dressed* by quasiparticle-impurity interaction lines between the electron propagator and hole propagator which form each bubble. As long as these *vertex-correction* quasiparticle-impurity lines do not cross each other, they can be summed to infinite order and together they give the leading order in $1/(\tau\varepsilon_{\rm F})$. The sum of all ladder Feynman diagrams for the density-density response function of each layer I is represented in panels c) and d) of Fig. 6.6. The latter is the diagrammatic representation of the Bethe-Salpeter equation

$$\Gamma^{\rm D}_{\boldsymbol{k},\boldsymbol{k}'}(q,\omega) = \Gamma^0_{\boldsymbol{k},\boldsymbol{k}'} + \sum_{\boldsymbol{k}''}\Gamma^0_{\boldsymbol{k},\boldsymbol{k}''}\Pi_{\boldsymbol{k}''}(q,\omega)\Gamma^{\rm D}_{\boldsymbol{k}'',\boldsymbol{k}'}(q,\omega), \tag{6.25}$$

where

$$\Pi_{\boldsymbol{k}''}(q,\omega) = \frac{1}{\hbar^2 L^2}{\rm G}^{\rm R}(\boldsymbol{k}''+\boldsymbol{q},\varepsilon_{\rm F}+\omega){\rm G}^{\rm A}(\boldsymbol{k}'',\varepsilon_{\rm F}) \tag{6.26}$$

and where ${\rm G}^{\rm R/A}(\boldsymbol{k},\omega) = [\omega - \hbar^{-1}\xi_{\boldsymbol{k}\alpha} \pm i/2\tau]^{-1}$ and $\xi_{\boldsymbol{k}\alpha} = \varepsilon_{\boldsymbol{k}\alpha} - \varepsilon_{\rm F}$. The Bethe-Salpeter equation must usually be solved self-consistently for an arbitrary impurity

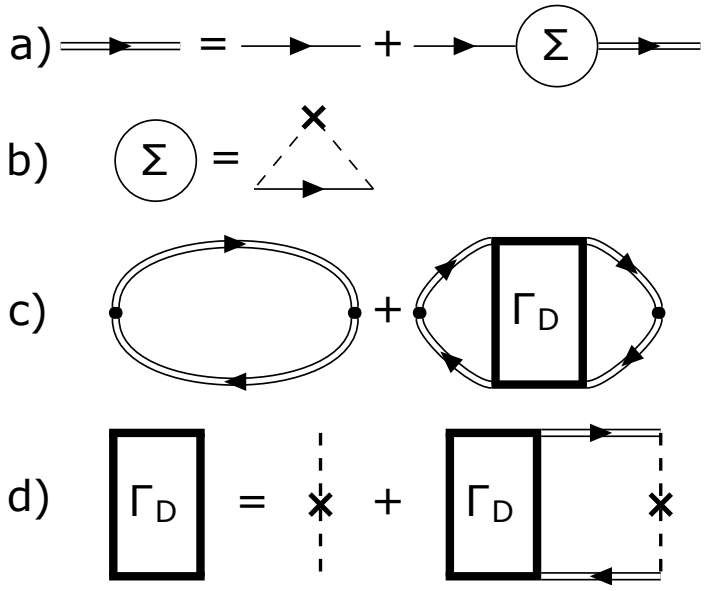

Figure 6.6. Feynman diagrams [375, 376] for the leading-order in $1/\varepsilon_{\rm F}\tau$ corrections to interlayer dispersion forces from impurity-quasiparticle interactions. Panel a) shows the diagrams for the Dyson equation for the self-energy. Single lines with arrows are noninteracting Green's functions and double lines with arrows are the noninteracting Green's functions dressed by scattering with impurities. Panel b) shows the proper self-energy in the first Born approximation. Each dashed line with a single cross represents the (disorder averaged) scattering off of the impurity potential. Panel c) shows the diagrams which contribute to the noninteracting density-response function in the leading-order in $1/\varepsilon_{\rm F}\tau$. Panel d) shows the diagrammatic representation of the Bethe-Salpeter equation for the *diffuson* contribution, *i.e.* the ladder-diagram vertex-correction $\Gamma_D(q,\omega)$

potential. However, here it can be solved directly as a result of the bare-scattering amplitude being independent of momentum $\Gamma^0_{\boldsymbol{k},\boldsymbol{k}'} = \rho^{imp}|u_I|^2$. In the regime where disorder gives significant contributions to the density-density response of a system, $\omega < 1/\tau$ and $q < 1/v_{\rm F}\tau$, it has been shown [377–379] that $\Gamma^{\rm D}(q,\omega) = \Gamma^0(q)/\left[-i\omega\tau + \tau {\rm D} q^2\right]$ where the diffusion constant is defined in two dimensions as ${\rm D} = v_{\rm F}^2\tau/2$. The diffusion pole present in $\Gamma^{\rm D}(q,\omega)$ at $\omega = -i{\rm D}q^2$ is also present in the disordered density-density response function of layer I that is obtained by summing the diagrams in panel c) of Fig. 6.6 and yields

$$\chi_D(q,\omega) = -\nu_0 \frac{{\rm D}q^2}{-i\omega + {\rm D}q^2}, \tag{6.27}$$

where ν_0 is the total density of states at the Fermi energy in layer I.

We can now evaluate the effect of weak disorder on the dispersion force between two atomically thin crystals by numerically evaluating Eq. (6.8) after replacing $\chi_0(q,i\omega)$ by $\chi_D(q,i\omega)$ in the region of phase space where $\omega < 1/\tau$ and $q < 1/v_{\rm F}\tau$. In Fig. 6.7 we plot the ratio of the interlayer force in the presence of disorder $\mathcal{F}_{dirty}$ to the force in the absence of disorder $\mathcal{F}_{clean}$. We find that the interlayer attraction is reduced

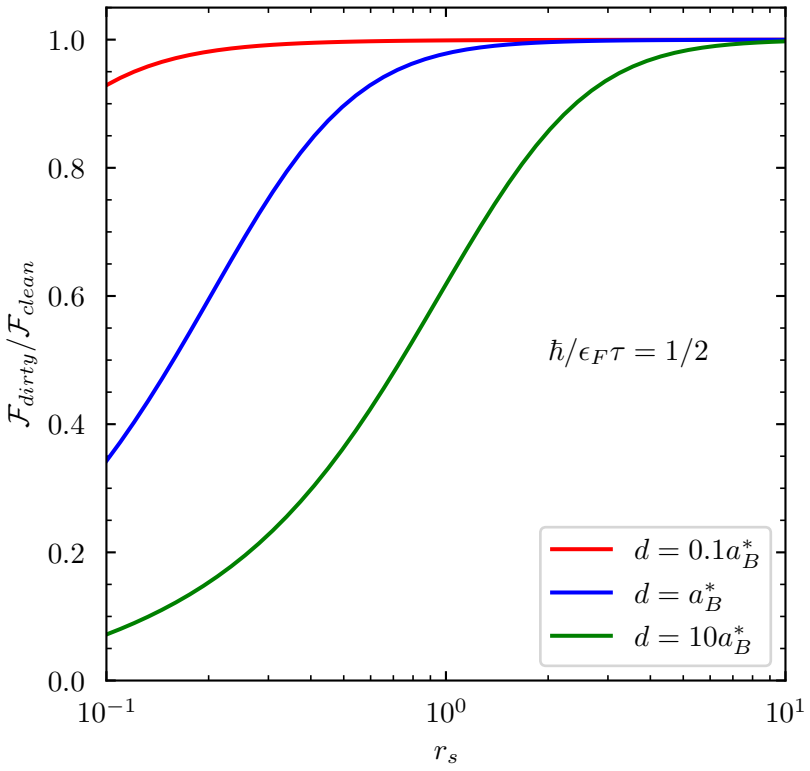

Figure 6.7. Ratio of the interlayer force in the presence of disorder $\mathcal{F}_{dirty}$ to the interlayer force with no disorder $\mathcal{F}_{clean}$, plotted against the interaction parameter r_s which is inversely proportional to the square root of the induced quasiparticle density in each layer of a bilayer. The three curves are for three different values of the interlayer separation distance d in units of the effective Bohr radius a_B^*. The degree of disorder is given by $\hbar/\epsilon_F\tau = 1/2$. The values of both $\mathcal{F}_{dirty}$ and $\mathcal{F}_{clean}$ are calculated numerically using Eq. (6.8). In $\mathcal{F}_{dirty}$, the density response is given by the disordered limit $\chi_D(q,\omega)$ for $\omega < 1/\tau$ and $q < 1/v_F\tau$.

in magnitude by the presence of quasiparticle-impurity interactions, which we will analyze in more detail below. We also find that $\mathcal{F}_{dirty}/\mathcal{F}_{clean}$ is reduced as d increases. This occurs due to the presence of e^{-2qd} in Eq. (6.8) which originates from the form of the 2D in-plane Fourier transform of the interlayer Coulomb interaction. This factor restricts the density fluctuations which contribute to interlayer forces to wave vectors $q \lesssim 1/2d$, and as d is increased, more of this region of phase space lies in the region governed by the disordered density-density response, $q < 1/v_F\tau$. We will now show that this phase space effect is also responsible for a change in the power-laws for the dispersion forces at large interlayer separation distances. In other words, in the presence of disorder, the asymptotic limit for forces between 2D planes presented in Eq. (6.22), $\mathcal{F} \propto d^{-7/2}$, is altered.

The numerical results presented in Fig. 6.7 show that disorder *decreases* the magnitude of interlayer forces. This is in contrast to the effect of disorder on other phenomena, like Coulomb drag [374], which also originates from interlayer quasiparticle-quasiparticle interactions. In the case of Coulomb drag, this conventional cartoon pic-

ture of the effect of disorder is that the change in the density-density response function from the noninteracting limit $\chi_0(q, i\omega)$ to the disordered limit $\chi_D(q, i\omega)$ represents a change from ballistic to diffusive motion of the quasiparticles. Indeed, the disordered density-density response function can be derived from semiclassical arguments using the diffusion equation [366], which is equivalent to the relaxation time approximation (RTA) [380] in the region $\omega < 1/\tau,\ q < 1/v_{\rm F}\tau$ in the *dynamic* limit. Since quasiparticles in neighboring layers which experience diffusive motion tend to spend longer periods of time near each other, they interact more strongly and this increases the Coulomb drag (i.e., disorder tends to enhance the transresistivity). However, since the interlayer forces are decreased in magnitude by the presence of disorder, we find that the cartoon picture of the effect of disorder cannot be imported to understand our case of interest. The reason why disorder decreases interlayer forces while increasing the interlayer Coulomb drag is most simply identified by again examining the large-d limit of the two quantities. Specifically, while both Coulomb drag and the interlayer force depend on the density-density response function, the leading-order-in-$1/(k_{\rm F}d)$ contribution to Coulomb drag comes from the *static* limit ($\omega < q,\ q \to 0$) of $\chi(q, i\omega)$ while the analogous contribution to the interlayer force comes from the *dynamic* limit ($\omega > q,\ q \to 0$) of $\chi(q, i\omega)$.

In the large-d limit our numerical results for the correlation energy per layer can be compared to previous investigations of disordered correlation energies within single-layer systems [381] where it was found that the introduction of disorder increases exchange energies in magnitude but decreases correlation energies in magnitude. Furthermore, by following similar steps as we took to derive the disorder-free expression presented in Eq. (6.22), we can also compute leading-order expression for the force. Plugging Eq. (6.27) into Eq. (6.8) and carrying out the frequency integral for $0 < \omega < 1/\tau$ we have

$$\begin{aligned}
\mathcal{F} &\approx -\frac{\hbar L^2}{4\pi^2}\int_0^\infty dq \int_0^{\frac{1}{\tau}} d\omega \frac{q^2 V_{12}^2 \chi_D(q,i\omega)^2}{(1-V_{11}\chi_D(q,i\omega))(1-V_{22}\chi_D(q,i\omega)) - V_{12}^2\chi_D(q,i\omega)^2} \\
&= -\int_0^\infty dq \frac{\hbar D V_{12} L^2 \nu_0 q^4}{4\pi^2}\left[\tanh^{-1}\left(\frac{1+\nu_0 V_{11}}{\nu_0 V_{12}}\right) - \tanh^{-1}\left(\frac{Dq^2(1+\nu_0 V_{11})+\frac{1}{\tau}}{Dq^2\nu_0 V_{12}}\right)\right] \\
&= -\int_0^\infty dq \frac{\hbar D V_{12} L^2 \nu_0 q^4}{4\pi^2}\log\left(\frac{\left[1+\frac{1+\nu_0 V_{11}}{\nu_0 V_{12}}\right]\left[1-\frac{Dq^2(1+\nu_0 V_{11})+\frac{1}{\tau}}{Dq^2\nu_0 V_{12}}\right]}{\left[1-\frac{1+\nu_0 V_{11}}{\nu_0 V_{12}}\right]\left[1+\frac{Dq^2(1+\nu_0 V_{11})+\frac{1}{\tau}}{Dq^2\nu_0 V_{12}}\right]}\right).
\end{aligned} \tag{6.28}$$

Keeping only the highest order in $k_F d$ term, this can then be simplified to

$$\begin{aligned}
&\approx -\frac{D^2 e^2 L^2 \nu_0 \hbar}{2\pi d^4}\int_0^\infty dx e^{-x} x^3 \log\left(\frac{1+e^x}{-1+e^x}\right) \\
&= -\frac{D^2 e^2 L^2 \nu_0 \hbar}{2\pi d^4}\xi_2 \\
&= -\frac{\hbar e^2 \xi_2 L^2 \tau}{4\pi m}\left(\frac{\rho}{d^4}\right),
\end{aligned} \tag{6.29}$$

where $\xi_2 \approx 0.768$ and ρ is the total two-dimensional density of quasiparticles in each layer and we have again taken $m_e = m_h = m$, $\kappa = 1$ for simplicity. Notice that the interlayer force now decays more quickly with distance than in the absence of disorder. This qualitative change is a direct result of the transition of electron and hole propagation from ballistic to diffusive.

While it might be surprising that the effect of disorder on the interlayer forces is opposite to its effect on interlayer Coulomb drag, this behavior actually fits nicely into a trend observed in other systems [382, 383]: the less metallic a system is, the faster its energy (and therefore its pressure) decreases with interlayer separation. Concretely, for a metallic sample, the energy scales as $d^{-5/2}$ [362–365, 368] while for a combination of a graphene and a metallic plate it scales as $\log(d)d^{-3}$ [382] and for two graphene plates is scales as d^{-3} [382]. Finally, for two insulator system it scales as d^{-4} [353]. The change of the scaling of the distance-dependent part of the correlation energy from $d^{-5/2}$ to d^{-3} upon changing from ballistic to diffusive propagation thus confirms this picture.

6.4 Quantum interference effects on VdW forces: The 'Cooperon'

In the previous section we developed a theory for interlayer dispersion forces between the layers of a bilayer system of atomically thin crystals which have uncorrelated and short ranged disorder. We summed an infinite set of Feynman diagrams by solving the Bethe-Salpeter equation and thus obtained the *diffuson* vertex correction of the density-density response function to leading-order in $1/(\epsilon_F \tau)$. In this section we will sum the class of diagrams which corresponds to the subleading-order terms for the interlayer dispersion force in powers of $1/\varepsilon_F \tau$. These diagrams are familiar from the theory of weak-localization and together they constitute the *cooperon* vertex-correction. Despite being of lower order in the small parameter governing the impurity-quasiparticle interaction, they are known to be responsible for a logarithmic divergence in the longitudinal resistivity of two-dimensional conductors [358], which is the motivation to consider them here as well.

The cooperon contributions to the density-density response function are obtained by summing the 'maximally crossed' vertex-correction; this infinite set of diagrams is illustrated in panel c) of Fig. 6.8. These diagrams represent the quantum interference of a wave packet of charge density which interferes with itself while traversing along the time-reversed path. This requires the system to have a time-reversal symmetry present in order for phase coherence to be maintained in-between collisions of the wave packet with different impurities. As previously mentioned, these diagrams give a logarithmic divergence in the resistivity (which is proportional to the current-density response function), and indeed a similar phenomenon happens in our case of interest. Specifically, the subleading-order contribution to the density-density response function yields a logarithmic divergence in the diffusion constant. When both the diffuson and cooperon contributions to the density-density response function are included [384], the

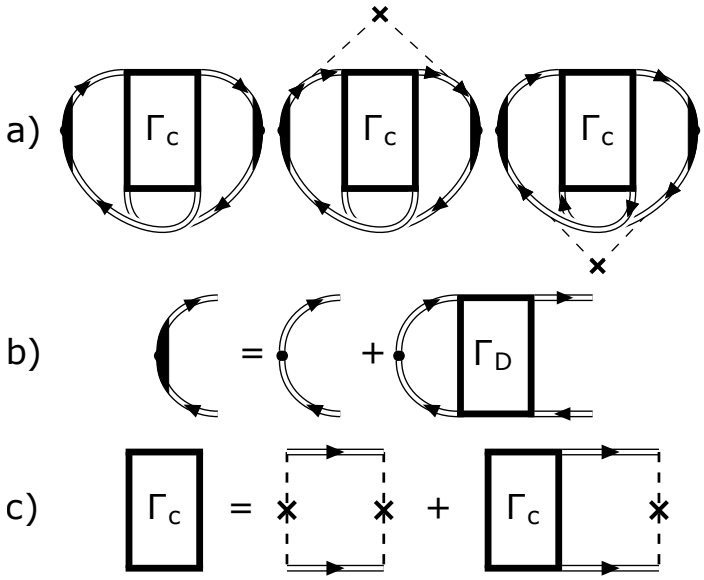

Figure 6.8. Feynman diagrams representing the *cooperon* contributions to the non-interacting density-response function from scattering of electron and holes off of the impurity potential. Panel a) shows the three diagrams that contribute at subleading order in $1/\varepsilon_{\rm F}\tau$. Panel b) shows the diagrams describing the *diffuson* dressing of the density-fluctuation operator. Panel c) shows the Bethe-Salpeter representation of the maximally crossed diagrams that represent the vertex-correction $\Gamma_C(q,\omega)$.

functional form of $\chi_D(q,\omega)$ remains the same as presented in the last section except that D gets an additional contribution which depends on frequency

$$\delta{\rm D}(\omega) = -\frac{1}{4\pi^2\hbar\nu_0}\log\left[\frac{1+2\tau\omega}{(\tau/\tau_0)^2+2\tau\omega}\right] , \tag{6.30}$$

where ν_0 is the total two-dimensional density of states of all quasiparticles in layer I. Just as in the case of the cooperon contribution to the longitudinal resistivity, the logarithmic divergence one obtains is cutoff at long distances, or small momenta, by the inelastic scattering time of the quasiparticles, τ_0. This time-scale is determined, for example, by the quasiparticle-quasiparticle scattering rate, and is responsible for destroying the phase coherence of the propagating (and time-reversed propagating) wave packet on very long time scales $\tau_0 > \tau$. This form of the disordered response function is only a reasonable approximation in the range where $\omega < 1/\tau$ and $q < 1/v_{\rm F}\tau$.

I numerically evaluate the interlayer dispersion forces using the disordered density-density response function including the renormalized diffusion constant ${\rm D} \to {\rm D} + \delta{\rm D}(\omega)$. The results are shown in Fig. 6.9. They demonstrate that the maximally crossed diagrams tend to further reduce the magnitude of interlayer forces. More surprisingly, perhaps, there is no logarithmic divergence in the interlayer force, in contrast to what happens when using the analogous approximation for the longitudinal conductivity. This is surprising in light of the well-known relationship $\sigma_{\rm dc} = \lim_{q\to 0}(q^2/\omega^2)\chi_D(q,\omega)$, which follows from the presence of global gauge symmetry.

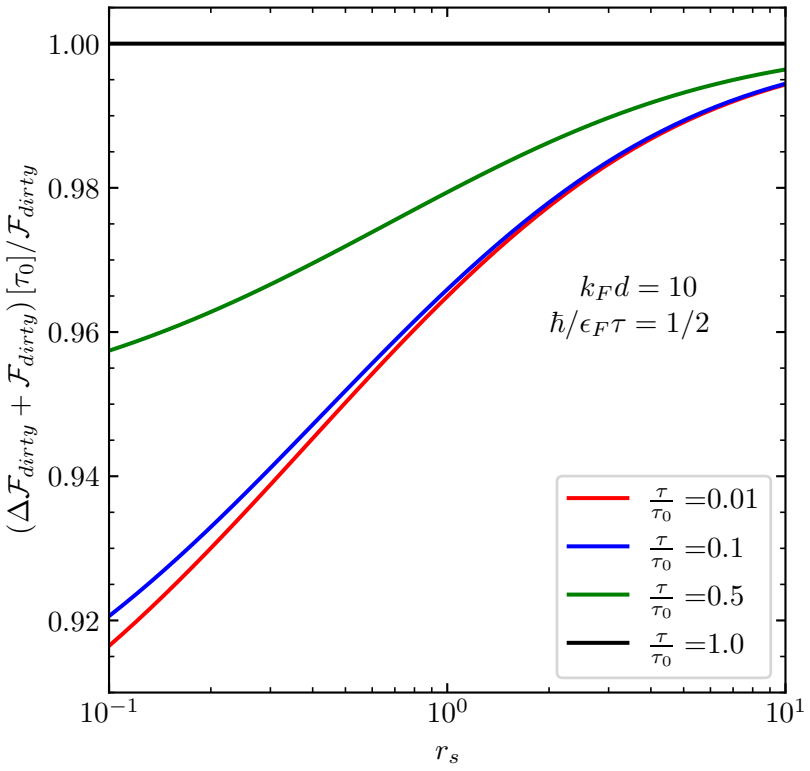

Figure 6.9. The fractional change in the interlayer dispersion force when the maximally crossed (i.e., weak-localization) diagrams are included. Notably, the logarithmic divergence which appears in the longitudinal resistivity of two-dimensional conductors is not present here. Instead, the *cooperon* diagrams have a similar, but weaker, effect as the *diffuson* diagrams, where both tend to reduce the magnitude of interlayer attractive forces. The fractional changes are shown at $\hbar/\epsilon_F\tau = 1/2$, $k_F d = 10$ as a function of r_s for different values of τ/τ_0.

However, while the conductivity is the response of the system to an external electric field whose frequency one can always fix to zero, in contrast, the interlayer dispersion force is an *integral over all frequencies* of density fluctuations in both layers (it is the Coulomb interaction between these density fluctuations which yields the dispersion force). And when the logarithmic divergence in $\chi_D(q,\omega)$ is integrated over frequency, it results simply in a finite reduction (on the order of $\lesssim 10$ percent) of the interlayer force's magnitude.

6.5 Summary And Discussion

I have presented a many-body theory for the dispersion forces between atomically thin crystals with weak disorder. Such systems can be realized within van der Waals crystals [385] (e.g., graphene, transition-metal dichalcogenides, etc.) which form multilayer systems with very weak interlayer hybridization, a property which has allowed for optically induced interlayer strain, originating from dispersion forces, to be observed recently [347]. In these systems *dispersion* forces arise due to Coulomb interactions

between fluctuations in the charge density of neighboring layers. The linked-cluster expansion as well as an equivalent renormalization group method was used to approximate the correlation energy of a bilayer system and the force between the layers of the bilayer system was obtained by taking a derivative of the correlation energy with respect to interlayer separation distance.

In the high-density limit, the random-phase approximation bubble diagrams give the leading-order contribution to the disorder-free interlayer dispersion force. To account for disorder, we have summed an infinite series of ladder diagrams by solving the Bethe-Salpeter equation. These ladder diagrams form the *diffuson* contribution to the vertex correction of the density-density response function (i.e., the bubble), and yield the leading-order-in-$1/(\varepsilon_{\mathrm{F}}\tau)$ theory. Numerical evaluation of the interlayer dispersion force shows that interlayer forces are *weakened* by disorder. On one hand, this is in contrast to the more conventional case [386] in which Coulomb interactions become more important when electron motion becomes diffusive rather than ballistic. On the other hand, this behavior is in accordance with previously observed changes in scaling laws as one transitions from metallic to insulating electron propagation.

This behavior is explained by considering the analytic structure of the density-response function in the small frequency and wave-vector limit. We find that the diffusive motion of electrons and holes leads to a qualitative change in the scaling laws for the interlayer dispersion force as a function of quasiparticle density and interlayer separation distance. Subsequently, the impact of the higher-order vertex-correction diagrams was investigated. Specifically, maximally crossed diagrams which are known to produce logarithmic divergences in the longitudinal resistivity of two-dimensional metals (i.e., weak localization diagrams) are found to be much less important for interlayer dispersion forces.

All the calculations shown in this chapter were carried out within a bilayer system consisting of two parallel plates. It should be mentioned, however, that the effects of the theories developed in this chapter were all at the level of "same-layer"-density-density response functions. As the theory of the bilayer system can easily be generalized to the theory of a superlattice system [347], the results of this chapter can easily be transferred to the superlattice system with similar effects (e.g., same power laws and qualitative effects).

Optical control of electron and hole populations yields a convenient control knob for manipulating the interlayer separation distance of van der Waals crystals. In future calculations one may investigate the possibility of inducing interlayer dispersion forces by doping heterostructures with electrostatic gates. While these systems include interlayer electrostatic forces which compete with dispersion forces, the latter are not reliant on equal populations of electrons and holes and can hopefully still be observed. Through electrostatic gating the role of the excitonic spectrum in the formation of strains could be differentiated from the induced strains presented in this chapter. In order to complement this investigation of the role of excitons, it would furthermore be interesting to study the qualitative changes in interlayer dispersion forces which are present in multilayer systems with more exotic ground state wavefunctions, such as are present in bilayer exciton condensates.

Chapter 7

Conclusion and Outlook

In this thesis we explored different aspects of the phase diagram and the quasiparticles found within strongly coupled Bose-Fermi mixtures. Employing a broad range of approaches such as quantum field theory/diagrammatics (see Chapters 4 and 6 and Ref. [7]), variational wavefunctions (see Section 1.7 and Refs. [8, 9]), stochastic variational methods (SVM) (see Chapter 3) and functional renormalization group approaches (fRG) (see Sections 2.2 and 2.3 and Chapter 5), where we have focused on utilizing analytical and physical insights to facilitate numerical implementations.

In Chapter 2 we studied the phase diagram of strongly coupled Bose-Fermi mixtures in two and three dimensions by combining the analysis of an experiment conducted in a three-dimensional ultracold quantum gas with an analysis from the functional renormalization group in two dimensions. Section 2.2 contains an analysis of the experimental data (along with a review of existing literature) and focuses on a characterization of the superfluid polaronic phase which transitions into a normal molecular phase. Section 2.3 on the other hand, employs an investigation in terms of the fRG and explores the molecular phase. The data obtained in the three-dimensional strongly interacting Bose-Fermi quantum gas mixtures with comparable densities (Section 2.2) suggest that at low temperatures where bosons commonly condense, strong boson-fermion interactions may induce a phase transition from a polaronic condensate to a molecular Fermi gas which connects to an underlying quantum phase transition (QPT) at $T = 0$ [98]. Signatures of this QPT were observed by producing a density-matched, double-degenerate Bose–Fermi mixture of ^{23}Na and ^{40}K. For vanishingly weak interactions, the bosons were unperturbed and thus condensed. As attractive interactions were increased, the bosonic condensate was dressed polaronically, and with increasing interaction strength, the condensate was eventually depleted, at which point a transition into a phase of quantum-degenerate fermionic molecules was observed. We found that this process of driving through the underlying QPT was highly efficient in associating Feshbach molecules, which allows for the creation of molecules with a large dipole moment, providing exciting opportunities to study strongly correlated dipolar quantum systems. Next, in Section 2.3 the phase diagram of strongly-coupled two-dimensional Bose-Fermi mixtures was studied theoretically for different boson and fermion densities. Connecting to the extreme limit of population-imbalance, the Fermi polaron problem, we developed a functional-renormalization-group approach

that by including three-body correlations reproduces the polaron-to-molecule transition in the two-dimensional Fermi polaron problem. By extending this approach to allow for a finite boson density, we found that beyond a critical bound state energy, the fermions and bosons can form a fermionic composite, with a well-defined Fermi surface. The physics described both in Sections 2.2 and 2.3 connects naturally to the polaron-to-molecule transition in the impurity limit, and key observables of both the experiment as well as the theoretical computations can be inferred from observables in the impurity limit, highlighting that the Fermi polaron problem captures key aspects of the strong coupling physics even in density-balanced Bose-Fermi mixtures.

In Chapter 3 we studied induced pairing between two identical fermions mediated by an attractively interacting quantum impurity in two-dimensional systems. Considering the two identical fermions as a small-scale Fermi sea in the few-body limit, we then went on to study the fate of the polaron-to-molecule transition within such few-body systems. Using a Stochastic Variational Method (SVM), in the first part of Chapter 3 we investigated the influence of confinement and finite interaction range effects on the mass ratio at which the ground state of this quantum three-particle system transitions from forming a three-particle bound state, a trimer, to a state containing a two-particle bound state between the impurity and a fermion along with the second fermion in a scattering state, an unbound dimer-fermion state. Both tighter confinement as well as longer interaction ranges favor trimer formation over dimer formation. The impurity induces strong coupling between the fermions, which can be so dominant that it can even outweigh Coulomb repulsion between the fermions. Furthermore, considering the confinement of the particles as an effective means to tune the density within the system, this suggests that Fermion-Fermion pairing may be stabilized in the presence of a Fermi sea, opening perspectives towards realizing novel forms of electron pairing in atomically-thin semiconductors beyond the conventional paradigm of Cooper pair formation. In the second part of the chapter, we then studied remnants of the polaron-to-molecule transition, to see how much of the many-body behavior transpires into the few-body limit. We showed that an analog of the transition occurs also in the few-body regime, exhibiting the same qualitative physics as its many-body relative.

In Chapter 4 we studied strong Bose-Fermi coupling as a means to induce superfluid pairing between fermions. To this end, we presented a mechanism to induce superconductivity in atomically thin semiconductors, where excitons mediate an effective attraction between electrons. Using the insights gained from the strong coupling physics described in Chapter 2, we devised a corresponding model that accounts for this and connects to the well-established limits of Bose and Fermi polarons. Using these ingredients, we showed that the system undergoes an emerging BCS-BEC crossover from weakly bound s-wave Cooper pairs to a superfluid of bipolarons with critical temperatures of up to 10% of the Fermi temperature. Given this scaling with Fermi temperature and given that the coupling physics within TMD is stable at high temperatures, we concluded that exciton-mediated pairing of electrons in doped, atomically thin semiconductor heterostructures offers a promising route towards realizing superconductivity at high critical temperatures.

Next, in Chapter 5 we revisited the Fermi polaron problem using a self-consistent, momentum- and frequency-resolved fRG approach. Leveraging the analytical structure of the impurity limit, we were able to compute Green's functions in the whole complex frequency plane using exact analytical continuation, circumventing a possibly unstable numerical analytical continuation. This came at a greatly reduced computation cost, allowing access to observables that were previously inaccessible due to a lack of numerical stability and precision. We used these improvements to study momentum-dependent decay widths of the attractive and repulsive polaron, as using Raman and Ramsey methods these observables are coming within experimental reach. Importantly, these decay widths are not accessible using conventional non-selfconsistent methods. Surprisingly, we found that both the attractive polaron and the molaron exhibit Fermi liquid-like behavior even deeply in the strongly interacting regime.

Finally, rather than studying dynamics originating from a particle-particle channel, in Chapter 6 we studied the effect of disorder on interlayer dispersion forces within TMD systems. These forces occur as a result of the dielectric density-density response of one layer to quantum fluctuations in the local charge distribution of the other layer. As the diffusive disorder we consider inhibits the coherent propagation of particles, the dielectric response of the system is inhibited, resulting in weaker Dispersion forces. Our results and the power laws we derived fit into this picture of force originating from dielectric response, as the diffusive results lie between insulting and metallic behavior.

Throughout this thesis, we have studied different aspects of strong coupling within Bose-Fermi mixtures from different angles and in different constellations. We have seen that large parts of the physics observed in these strongly coupled systems originate from the simplest of physics and the competition between simple states: Before even thinking of interactions, the first building block is the non-interacting ground state of a system and the intuition that sufficiently weak interactions merely perturb this state, but do not lead to a qualitatively different state. The second building block is the behavior of two-interacting particles, the two-body limit. These particles may bind together, forming a molecule, or they may remain unbound, likely expressing behavior similar to the non-interacting ground state. Moving from two particles of a different species to two particles of a fermionic species and a single particle of another species, it is clear that for sufficiently weak interactions, the ground state will be similar to the non-interacting ground state. For stronger interactions, it will be similar to the molecule state, along with a fermion in a non-interacting ground state. For even stronger interactions, a third building block becomes relevant: all three particles binding together. Moving from two particles of a fermionic species to a finite density of a fermionic species, the fundamental physics still remains a transition between the fundamental building blocks of a non-interacting ground state (dressed polaronically) and a molecule state (complemented with a Fermi sea). Now, going from a single impurity to a finite density of bosonic impurities, we can again make use of the building blocks to describe a quantum phase transition between a condensate of polarons (adiabatically connected to the non-interacting state) and a Fermi gas of molecules (connecting to the molaron, which in turn connects to the two-body bound

state). Finally, considering the induced pairing between fermions, the third building block reappears, albeit in a slightly modified version, as the induced pairing described in Chapter 4 is between electrons of different spin.

This benign comparison of different quasiparticles in different constellations serves to show that the fundamental physics studied in the course of this thesis consists of simple building blocks which reappear in different disguises. Their description may require advanced methods to be able to capture the qualitative physics at play, and even more sophisticated methods for these descriptions to be quantitatively correct. Their physical properties and their competition, however, may be explained in simple layperson's terms, giving rise to the beauty within the balancing act mentioned in the introduction.

Appendix A

Bose-Bose-Fermi coupling in the three-body limit and at finite density

The truncations considered in Section 2.3 neglect the emergence of a Bose-Bose-Fermi (BBF) coupling (and other higher-order couplings). In this Appendix we seek to explore the relevance of this coupling. From a physical standpoint, unlike the Fermi-Fermi-Bose (FFB) coupling λ_k, the BBF coupling does not suffer from Pauli blocking and may thus be considerably stronger, potentially resulting in the formation of bound states containing more than one boson.

First, we study the BBF coupling in the limit where two ϕ bosons and a single ψ fermion are present. We define the corresponding coupling vertex τ_k as

$$\tau_k \int_x \phi_x^* t_x^* t_x \phi_x \ . \tag{A.1}$$

The flow equations given in Eqs. (2.42) to (2.45) (excluding the flow of λ_k) are then complemented by the RG flow of τ_k

$$\begin{aligned}\partial_k \tau_k = &-\tau_k^2 \tilde{\partial}_k \int_Q G_{t,k}^c(Q) \left[G_{\phi,k}^c(Q) + G_{\phi,k}^c(-Q) \right] \\ &- h_k^4 \tilde{\partial}_k \int_Q G_{t,k}^c(Q) G_{\psi,k}^c(Q)^2 G_{\phi,k}^c(-Q) \\ &+ 2h_k^2 \tau_k \tilde{\partial}_k \int_Q G_{t,k}^c(Q) G_{\psi,k}^c(Q) G_{\phi,k}^c(-Q) \ .\end{aligned} \tag{A.2}$$

These equations are solved using the initial conditions of the two-body problem discussed in Section 2.3.2.6 where, unlike in Section 2.3.3.2, we consider the *on-mass-shell* scattering of a molecule and a quasi-free excess boson such that $\mu_\phi = 0^-$ and $\mu_\psi = -\epsilon_B - 0^-$. As in the previous section $G_{\phi,k}^{-1}$, $G_{\psi,k}^{-1}$ and h_k do not flow such that $m_{t,k}$ and $A_{t,k}$ are given by Eqs. (2.54) and (2.55), respectively. We find that τ_k flows from $\tau_{k=\Lambda} = 0$ to negative values before diverging at $k > 0$ and continuing to flow to $\tau_{k=0} = h^2/\epsilon_B$ at the end of the flow. The divergence indeed indicates the formation of three-body bound states in the vacuum limit as predicted in Refs. [177–179]. Our results show that these can, in principle, be captured using our fRG technique. We now demonstrate that this treatment can be extended to finite density.

To this end, we study the behavior of the BBF coupling at finite density. Thus, we apply the initial conditions used for Fig. 2.20 by tuning the binding energy and the

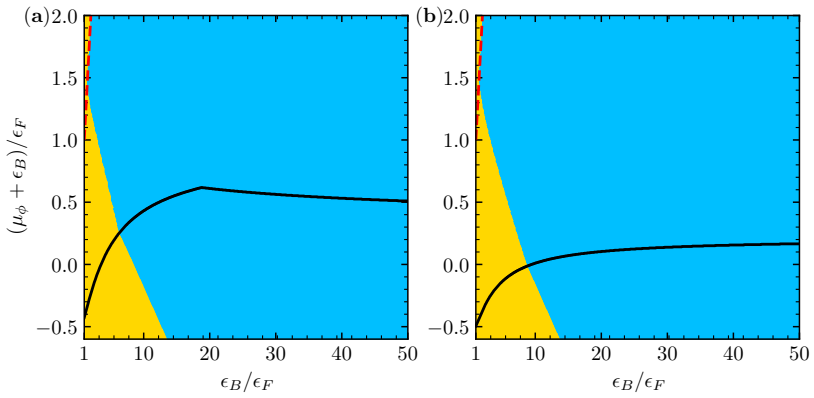

Figure A.1. Instability towards higher-order bound state formation. Indication of a divergence of τ_k for different ratios of μ_ϕ/ϵ_F and ϵ_B/ϵ_F using $\Gamma_{3,k}$ (a) and $\Gamma_{2,k}$ (b). The blue (dark gray) regions indicate the divergence of τ_k at finite k (thus resulting in a potential instability towards the formation of a Boson-Boson-Fermion bound state), while the yellow (light gray) regions indicate that τ_k had not diverged when the flow ended as discussed in Section 2.3.4. The solid black line shows the transition to the finite boson density regime, while the dashed red line indicates the path along which $\mu_\phi = 0$, as in Fig. 2.20.

boson chemical potential at a fixed Fermi energy. In order to simplify the calculation, however, here we do not choose a fully self-consistent calculation, but rather treat the BBF coupling as an observing flow that does not feed back into the renormalization of the other coupling constants. Hence, the flow of τ_k is influenced by the flow of λ_k (but not vice versa). In this framework at finite density the RG flow of τ_k picks up another term given by:

$$-h_k^2 \lambda_k \tilde{\partial}_k \int_Q G^c_{t,k}(Q) G^c_{\psi,k}(Q)^2 \ . \tag{A.3}$$

We now turn to the question under which conditions a divergence of τ_k occurs during the flow. The result of this calculation is shown in Fig. A.1. As can be seen, in both truncations, $\Gamma_{2,k}$ and $\Gamma_{3,k}$, the coupling constant τ_k diverges for most of the combinations of μ_ϕ/ϵ_B and ϵ_B shown in Fig. 2.20. Only at weaker interaction strengths when the boson is gapped strongly does the coupling constant remain finite. This shows the importance of 'non-Pauli-blocked' coupling channels such as τ_k which lead to bound states containing more than one boson, especially at a finite boson density where these are not suppressed.

Appendix B

Explicit flow equations for the functional renormalization group analysis of a strongly-coupled two-dimensional Bose-Fermi mixture

In this appendix we provide the explicit flow equations of parameters of the gradient expansion. These flows are obtained as described in Section 2.3.2.5, and for completeness we state them here explicitly. Note that we state the flow equations as used in Section 2.3.4. These are a generalization of the flow equations used in Section 2.3.3 and as such may also be used there.

B.1 Boson renormalization

$$\partial_k m_{\phi,k} = \frac{h_k^2 k}{\pi}\left[\Theta(\epsilon_F - 2k^2)\left(\frac{\Theta\left(\epsilon_F - k^2 + 2\frac{m_{t,k}}{A_{t,k}}\right)}{2m_{t,k} + A_{t,k}(k^2+\epsilon_F)} + \frac{\Theta\left(k^2 + 2\frac{m_{t,k}}{A_{t,k}}\right)}{2m_{t,k} - A_{t,k}(k^2 - 2\epsilon_F)}\right) + \frac{\Theta\left(-2\frac{m_{t,k}}{A_{t,k}} - (k^2+\epsilon_F)\right)}{-2m_{t,k} + A_{t,k}(k^2-\epsilon_F)}\right] \tag{B.1}$$

$$\partial_k A_{\phi,k} = \frac{2A_{t,k}h_k^2 k}{\pi}\left[\frac{\Theta\left(-2\frac{m_{t,k}}{A_{t,k}} - (k^2+\epsilon_F)\right)}{[-2m_{t,k} + A_{t,k}(k^2-\epsilon_F)]^2} - \Theta(\epsilon_F - 2k^2)\left(\frac{\Theta\left(\epsilon_F - k^2 + 2\frac{m_{t,k}}{A_{t,k}}\right)}{[2m_{t,k} + A_{t,k}(k^2+\epsilon_F)]^2} + \frac{\Theta\left(k^2 + 2\frac{m_{t,k}}{A_{t,k}}\right)}{[2m_{t,k} - A_{t,k}(k^2-2\epsilon_F)]^2}\right)\right] \tag{B.2}$$

B.2 Molecule renormalization

$$\partial_k m_{t,k} = \frac{h_k^2 k}{2\pi} \frac{\Theta\left(k^2 + \epsilon_F + \frac{m_{\phi,k}}{A_{\phi,k}}\right)}{A_{\phi,k}(2k^2 + \epsilon_F) + m_{\phi,k}} - \frac{\lambda k}{2\pi}\Theta(\epsilon_F - k^2) \tag{B.3}$$

$$\partial_k A_{t,k} = -\frac{h_k^2 k A_{\phi,k}}{2\pi} \frac{\Theta\left(k^2 + \epsilon_F + \frac{m_{\phi,k}}{A_{\phi,k}}\right)}{[A_{\phi,k}(2k^2 + \epsilon_F) + m_{\phi,k}]^2} \tag{B.4}$$

B.3 Three-body renormalization

B.3.1 Bubble

$$A_1 = \frac{\lambda_k^2 k}{\pi}\left[\frac{\Theta\left(k^2 + \frac{2m_{t,k}}{A_{t,k}} + \epsilon_F\right)}{A_{t,k}\left(3k^2 + \epsilon_F\right) + 2m_{t,k}} + \frac{\Theta\left(k^2 - \frac{2m_{t,k}}{A_{t,k}} - \epsilon_F\right)\Theta\left(\epsilon_F - 2k^2\right)}{3A_{t,k}k^2 - A_{t,k}\epsilon_F - 2m_{t,k}} - \frac{\Theta\left(-\frac{k^2}{2} - \frac{m_{t,k}}{A_{t,k}}\right)\Theta\left(\epsilon_F - 2k^2\right)}{3A_{t,k}k^2 - 2A_{t,k}\epsilon_F + 2m_{t,k}}\right] \tag{B.5}$$

B.3.2 Triangle

$$B_1 = \frac{2h_k^2 k\lambda_k \Theta\left(k^2 + \frac{2m_{t,k}}{A_{t,k}} + \epsilon_F\right)}{\pi\left(A_{\phi,k}\left(2k^2 + \epsilon_F\right) + m_{\phi,k}\right)\left(A_{t,k}\left(3k^2 + \epsilon_F\right) + 2m_{t,k}\right)} \tag{B.6}$$

$$B_2 = -\frac{2A_{\phi,k}h_k^2 k\lambda_k \Theta\left(-\frac{2m_{t,k} + A_{t,k}\left(k^2 + \epsilon_F\right)}{2A_{t,k}}\right)}{\pi\left(A_{\phi,k}\left(2k^2 + \epsilon_F\right) + m_{\phi,k}\right)\left(-2A_{\phi,k}m_{t,k} + A_{\phi,k}A_{t,k}\left(k^2 + \epsilon_F\right) + 2A_{t,k}m_{\phi,k}\right)} \tag{B.7}$$

$$B_3 = -\frac{4A_{t,k}h_k^2 k\lambda_k \Theta\left(-\frac{k^2}{2} - \frac{m_{t,k}}{A_{t,k}}\right)\Theta\left(\epsilon_F - 2k^2\right)}{\pi\left(3A_{t,k}k^2 - 2A_{t,k}\epsilon_F + 2m_{t,k}\right)\left(-2A_{\phi,k}m_{t,k} + A_{\phi,k}A_{t,k}k^2 + 2A_{t,k}m_{\phi,k}\right)} \tag{B.8}$$

$$B_4 = \frac{4A_{t,k}h_k^2 k\lambda_k \Theta\left(k^2 - \frac{2m_{t,k}}{A_{t,k}} - \epsilon_F\right)\Theta\left(\epsilon_F - 2k^2\right)}{\pi\left(A_{t,k}\left(\epsilon_F - 3k^2\right) + 2m_{t,k}\right)\left(2A_{\phi,k}m_{t,k} + A_{\phi,k}A_{t,k}\left(k^2 - \epsilon_F\right) - 2A_{t,k}m_{\phi,k}\right)} \tag{B.9}$$

B.3.3 Square

$$C_1 = \frac{h_k^4 k \Theta\left(k^2 + \frac{2m_{t,k}}{A_{t,k}} + \epsilon_F\right)}{\pi\left(A_{\phi,k}\left(2k^2+\epsilon_F\right)+m_{\phi,k}\right)^2\left(A_{t,k}\left(3k^2+\epsilon_F\right)+2m_{t,k}\right)} \tag{B.10}$$

$$C_2 = \frac{A_{\phi,k} h_k^4 k \Theta\left(-\frac{2m_{t,k}+A_{t,k}\left(k^2+\epsilon_F\right)}{2A_{t,k}}\right)\left(2A_{\phi,k}m_{t,k} - A_{t,k}\left[5A_{\phi,k}k^2 + 4m_{\phi,k} + 3A_{\phi,k}\epsilon_F\right]\right)}{\pi\left(A_{\phi,k}\left(2k^2+\epsilon_F\right)+m_{\phi,k}\right)^2\left(-2A_{\phi,k}m_{t,k} + A_{\phi,k}A_{t,k}\left(k^2+\epsilon_F\right)+2A_{t,k}m_{\phi,k}\right)^2} \tag{B.11}$$

$$C_3 = -\frac{4A_{t,k}^2 h_k^4 k \Theta\left(-\frac{k^2}{2} - \frac{m_{t,k}}{A_{t,k}}\right)\Theta\left(\epsilon_F - 2k^2\right)}{\pi\left(3A_{t,k}k^2 - 2A_{t,k}\epsilon_F + 2m_{t,k}\right)\left(-2A_{\phi,k}m_{t,k} + A_{\phi,k}A_{t,k}k^2 + 2A_{t,k}m_{\phi,k}\right)^2} \tag{B.12}$$

$$C_4 = -\frac{4A_{t,k}^2 h_k^4 k \Theta\left(k^2 - \frac{2m_{t,k}}{A_{t,k}} - \epsilon_F\right)\Theta\left(\epsilon_F - 2k^2\right)}{\pi\left(A_{t,k}\left(\epsilon_F - 3k^2\right)+2m_{t,k}\right)\left(2A_{\phi,k}m_{t,k} + A_{\phi,k}A_{t,k}\left(k^2-\epsilon_F\right) - 2A_{t,k}m_{\phi,k}\right)^2} \tag{B.13}$$

B.3.4 Total

$$\partial_k \lambda = -\frac{\lambda_k^2}{h_k^2}\partial_k m_{\phi,k} + A_1 + \sum_{i=1}^{4} B_i + \sum_{i=1}^{4} C_i \tag{B.14}$$

B.4 Fermion renormalization

$$\begin{aligned}\partial_k m_{\psi,k} = \frac{h_k^2 k}{A_{t,k}A_{\phi,k}}\Bigg(&\int_{-\pi}^{\pi}\frac{d\theta}{2\pi^2}\frac{\Theta\left(-k^2 - \frac{2m_{t,k}}{A_{t,k}}\right)\Theta\left(p^2 - 2kp\cos(\theta)\right)}{-k^2 + \frac{2m_{t,k}}{A_{t,k}} - \frac{2m_{\phi,k}}{A_{\phi,k}} - 2p^2 + 4kp\cos(\theta)}\Bigg|_{p=\sqrt{\epsilon_F}} \\ &+ \int_{-\pi}^{\pi}\frac{d\theta}{2\pi^2}\frac{\Theta\left(-k^2 - \frac{2m_{t,k}}{A_{t,k}} - p^2 - 2kp\cos(\theta)\right)\Theta\left(p^2 + 2kp\cos(\theta)\right)}{-k^2 + \frac{2m_{t,k}}{A_{t,k}} - \frac{2m_{\phi,k}}{A_{\phi,k}} + p^2 + 2kp\cos(\theta)}\Bigg|_{p=\sqrt{\epsilon_F}}\Bigg) \\ &- \frac{\lambda_k k}{2\pi A_\phi}\Theta\left(-k^2 - \frac{2m_{t,k}}{A_{t,k}}\right)\end{aligned} \tag{B.15}$$

$$\begin{aligned}\partial_k A_{\psi,k} = -\frac{2h_k^2 k}{A_{t,k}A_{\phi,k}\pi}\Bigg(&\int_{-\pi}^{\pi}\frac{d\theta}{2\pi}\frac{\Theta\left(-k^2 - \frac{2m_{t,k}}{A_{t,k}}\right)\Theta\left(p^2 - 2kp\cos(\theta)\right)}{\left(-k^2 + \frac{2m_{t,k}}{A_{t,k}} - \frac{2m_{\phi,k}}{A_{\phi,k}} - 2p^2 + 4kp\cos(\theta)\right)^2}\Bigg|_{p=\sqrt{\epsilon_F}} \\ &+ \int_{-\pi}^{\pi}\frac{d\theta}{2\pi}\frac{\Theta\left(-k^2 - \frac{2m_{t,k}}{A_{t,k}} - p^2 - 2kp\cos(\theta)\right)\Theta\left(p^2 + 2kp\cos(\theta)\right)}{\left(-k^2 + \frac{2m_{t,k}}{A_{t,k}} - \frac{2m_{\phi,k}}{A_{\phi,k}} + p^2 + 2kp\cos(\theta)\right)^2}\Bigg|_{p=\sqrt{\epsilon_F}}\Bigg)\end{aligned} \tag{B.16}$$

B.5 Effective potential

$$\begin{aligned}\partial_k U_k = &\frac{1}{4\pi}\left(\partial_k\frac{m_{t,k}}{A_{t,k}}\right)\min\left(k^2, -2\frac{m_{t,k}}{A_{t,k}}\Theta\left(-\frac{m_{t,k}}{A_{t,k}}\right)\right) \\ &+ \frac{1}{4\pi}\left(\partial_k\frac{m_{\psi,k}}{A_{\psi,k}}\right)\left(\max\left(\epsilon_F - \frac{m_{\psi,k}}{A_{\psi,k}}, 0\right) - \max\left(\epsilon_F - \frac{m_{\psi,k}}{A_{\psi,k}} - k^2, 0\right)\right)\end{aligned} \tag{B.17}$$

Appendix C

Two-body problem with confinement from the SVM

In this appendix, we show the influence of confinement on the solution of the two-body problem.

Let us consider a two-body system consisting of one impurity (with mass m_I) and one fermion (with mass m_F) in a 2D spherical box. The Hamiltonian then reads

$$H = -\frac{\hbar^2}{2m_I}\nabla_1^2 - \frac{\hbar^2}{2m_F}\nabla_2^2 + \sum_{i=1}^{2} V_{\text{conf}}(\mathbf{r}_i) + V_{\text{FI}}(\mathbf{r}_1 - \mathbf{r}_2), \tag{C.1}$$

where we have used the same notation as in Section 3.4.1. To solve this two-body problem, we employ the SVM as described in Section 3.2.

In Fig. C.1, we show the two-body as well as the three-body ground state energy as a function of α for $r_0/r_B = 1.2$ and different values of R. The dimer energies lie slightly higher than $-E_{2B}^{\infty}$ due to the confinement, while for larger system sizes the energies approach $-E_{2B}^{\infty}$. Additionally, a close to linear increase of the energies with the mass ratio α is visible, which decreases as R increases. This observation is in line with the interpretation of a decrease of the two-body confinement energy, given by

$$E_{\text{conf}} = \frac{z_{01}^2}{2m_I R^2} + \frac{z_{01}^2}{2m_F R^2} = \frac{z_{01}^2(\alpha+1)}{2m_F R^2}, \tag{C.2}$$

where z_{01} is the first zero of the Bessel function J_0.

Comparing the three-body energy with the two-body energy, one can see that, below the critical mass ratio, the three-body energy also increases linearly with α, and that the increase is larger for smaller box size. Additionally, especially for smaller system sizes, the three-body energies below the critical mass ratio lie considerably higher than their two-body counterparts. This is caused by the confinement energy of the fermion in a scattering state, as expected from our analysis in Section 3.4.2.

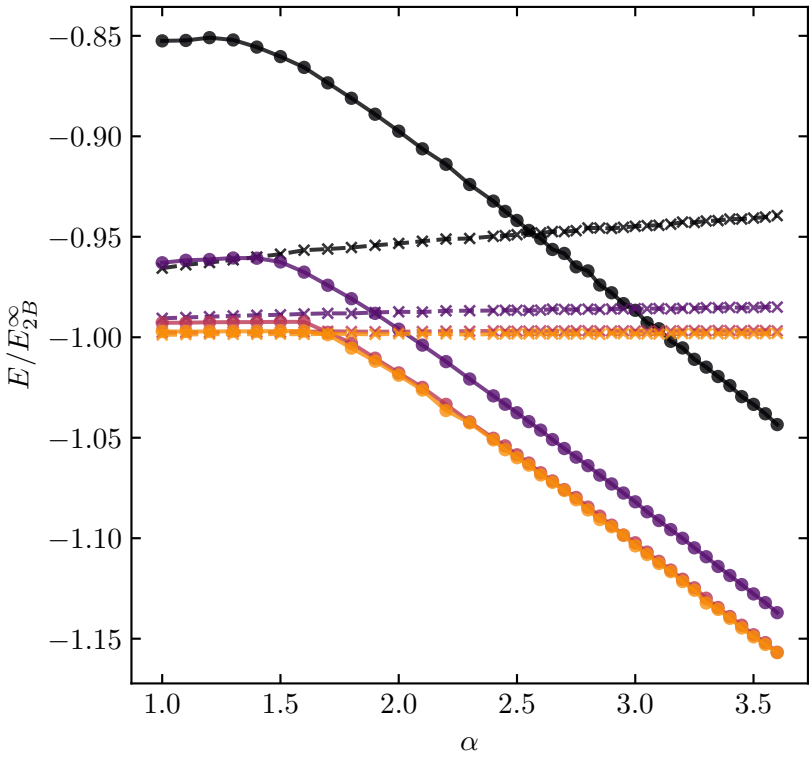

Figure C.1. Ground state energy of the two- (crosses, dashed lines, described n this appendix) and three-body system (dots, solid lines, described in Section 3.4 for $R/r_B = 10$ (black), 20 (purple), 50 (red) and 100 (orange), and a fixed value $r_0/r_B = 1.2$. The two-body ground state energy increases linearly with mass ratio α, which coincides with the behavior of the three-body ground state energy below the critical mass ratio.

Appendix D

Convergence Analysis of SVM method

In this appendix, we analyze the convergence of the results shown in Fig. 3.2, which is followed by a study with regards to the number of wavefunctions sampled in every expansion step.

There are two aspects in which the SVM algorithm needs to achieve convergence in:

1. The number of basis states needs to be sufficiently large to describe the ground state accurately.

2. A sufficient number of samples have to be drawn from the ECG manifold in every basis expansion step in order to ensure stable results.

The number of basis states and the number of samplings necessary to obtain accurate results varies depending on the nature of the ground state and the energy gap to the first excited state. Additionally, there are ranges of R/r_B and r_0/r_B that are more challenging to achieve convergence in. That is, when the confinement length R is large and the interaction range r_0 is small, the manifold of wavefunctions that respect the confinement-imposed boundary conditions increases in size. In contrast, the subset of wavefunctions resolving the box potential is quite small. Combining both arguments, one sees that a larger number of sampling steps is required. Additionally, when the energy gap between the dimer and the trimer state becomes small near the transition, the numerically-determined ground state can be a varying admixture of dimer and trimer state, resulting in angular momentum scatter.

To study the convergence of the results shown in Fig. 3.2, we have performed a convergence analysis of select data points. The results are shown in Appendix D.1 (Figs. D.1 and D.2), and they serve to investigate the behavior of the energy and the angular momentum of the ground state as the number of basis states N is increased. To further study the role of the number of sampling steps, in Appendix D.2 a similar analysis was performed in which, for varying numbers of sampling steps, the ground state properties were tracked, again, as a function of the number of basis states N. These results are shown in Figs. D.3 and D.4.

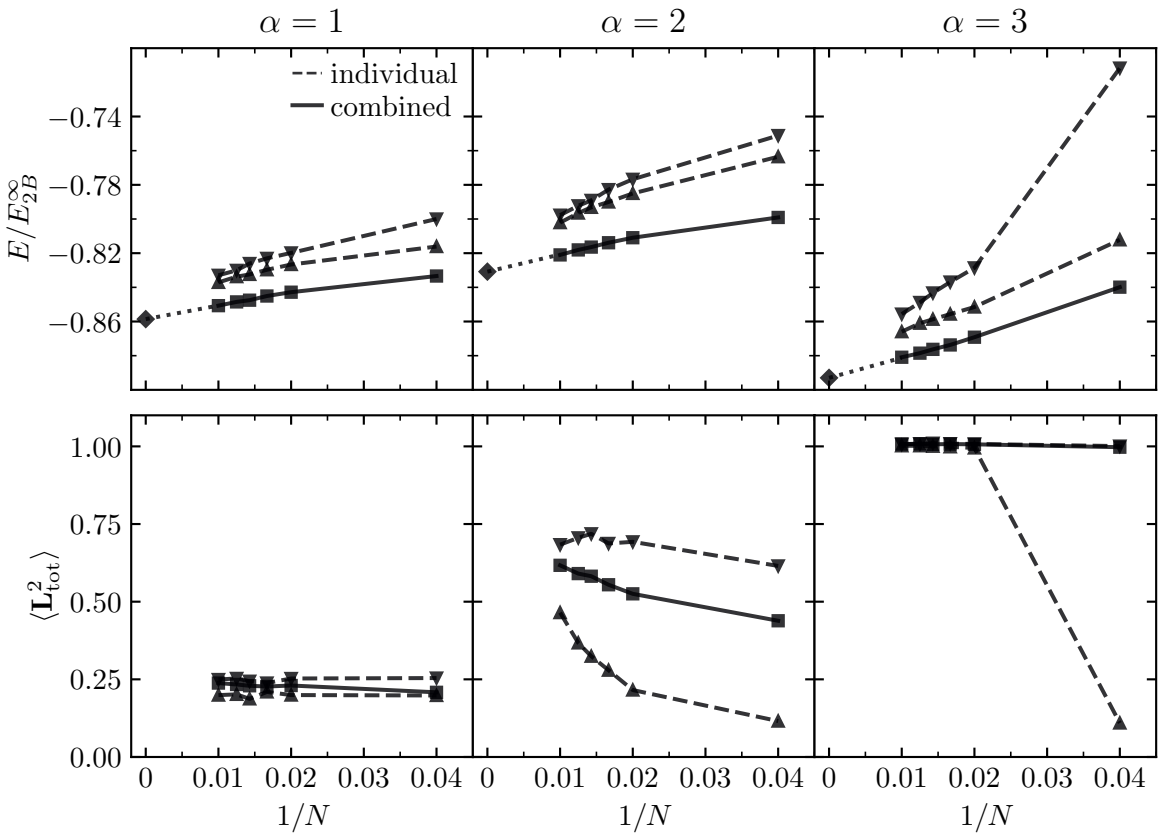

Figure D.1. Analysis of convergence with increasing number of basis states N, for parameters $R/r_B = 10$, $r_0/r_B = 0.8$ that yield a critical mass ratio of around $\alpha_c = 2$. The analysis is conducted for mass ratios well before (left, $\alpha = 1$), close to (center, $\alpha = 2$) and well after (right, $\alpha = 3$) the dimer-to-trimer transition. For every data point (α, R/r_B, r_0/r_B), shown in Fig. 3.2, 10 independent runs with up to 100 basis states were conducted. For the present figure, the ground state in each of these 10 independent runs was tracked as the number of basis states N increased from 1 to 100, and the energies and angular momentum expectation values $\langle \mathbf{L}^2_{\mathrm{tot}} \rangle$ of these states were computed. In the upper row, the down-(up-)facing triangles, connected by dashed lines, mark the highest (lowest)-lying ground state energies of these ten runs at $1/N = 1/25, 1/50, 1/60, 1/70, 1/80$ and $1/100$. In the lower panels, the $\langle \mathbf{L}^2_{\mathrm{tot}} \rangle$ values are shown in the same way. The energy ($\langle \mathbf{L}^2_{\mathrm{tot}} \rangle$ values) obtained by combining the bases of the 10 individual runs into a single basis of $10 \times N$ states is shown as a solid line. From the relation between energy and $1/N$, we estimate the energy at $N = \infty$ (diamond marker) by extrapolation (dotted line). The difference between the obtained extrapolation and the combined energy of $10 \times 100 = 1000$ basis states is given by $0.0079 E^{\infty}_{2B}$ ($\alpha = 1$), $0.0098 E^{\infty}_{2B}$ ($\alpha = 2$), and $0.0121 E^{\infty}_{2B}$ ($\alpha = 3$), and it can be regarded as an estimated basis set extrapolation error.

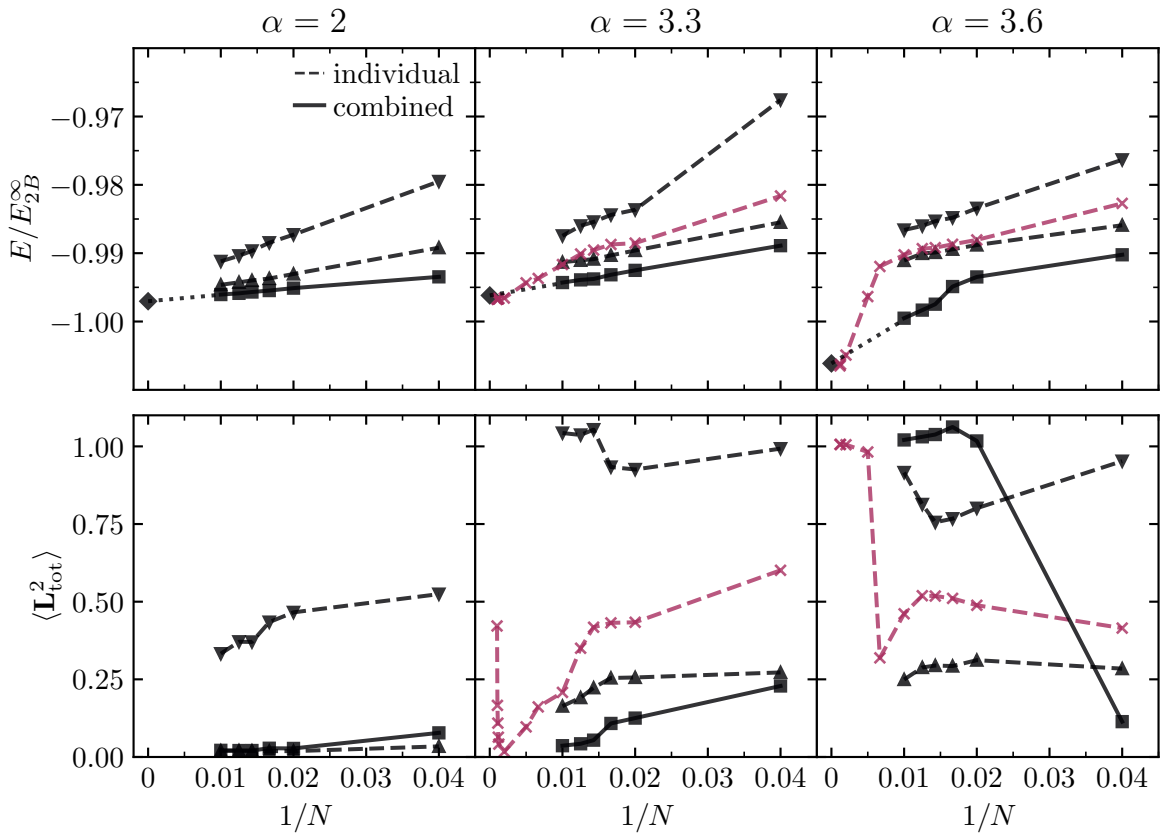

Figure D.2. Analysis of convergence with increasing number of basis states N, for parameters $R/r_B = 100$, $r_0/r_B = 0.2$ that yield a critical mass ratio of around $\alpha_c = 3.3$ (see also Fig. 3.9). In the same manner as the analysis shown in Fig. D.1, the analysis is conducted for mass ratios well before (left, $\alpha = 2$), close to (middle, $\alpha = 3.3$) and well after (right, $\alpha = 3.6$) the dimer-to-trimer transition. Additionally, for $\alpha = 3.3$ and $\alpha = 3.6$, energies and angular momentum expectation values obtained in a single run with up to $N = 1000$ basis states are shown (crosses, dashed, purple). The difference between the combined energy of $10 \times 100 = 1000$ basis states and the extrapolation is given by $0.00098 E_{2B}^{\infty}$ ($\alpha = 2$), $0.0019 E_{2B}^{\infty}$ ($\alpha = 3.3$) and $0.0066 E_{2B}^{\infty}$ ($\alpha = 3.6$), and it can be regarded as an estimated basis set extrapolation error. The results obtained from the extrapolated energy (diamond) and the single run with $N = 1000$ basis states are consistent.

D.1 Convergence analysis of the number of basis states N

In Fig. D.1, values of $R/r_B = 10$, $r_0/r_B = 0.8$ were chosen as representing parameters for which it is easier to achieve convergence. In contrast, the values $R/r_B = 100$, $r_0/r_B = 0.2$ chosen for Fig. D.2 represent parameters more challenging for the algorithm. For each of these sets of parameters, mass ratios before the transition, in the transition region, and beyond the transition were chosen to show the effect of the

closing energy gap between the trimer and dimer states. A detailed description of the data presented in the figures can be found in the respective figure captions.

As mandated by the variational principle, the energies found are upper bounds for the true energy of the ground state. Moreover, as the number of basis states is increased, the variational energy must be lowered. In Fig. D.1, it can be seen that away from the transition ($\alpha = 1$, $\alpha = 3$) the 10 individual energies and angular momenta have a tight grouping, indicating that the number of sampling steps is sufficient. At the transition, the individual energies are also grouped tightly, but because the energy gap to the first excited state is small, the angular momentum expectation values have a significant spread and a stabilization of the observable comes from the combination of individual runs. Fig. D.2, on the other hand, is obtained for a larger system size, making the dimer-to-trimer crossover much more narrow. As a consequence, the spread of energies relative to the energy gap to $-E_{2B}^{\infty}$ is much larger than in Fig. D.1. Highlighting the challenge in describing such parameter regimes, even away from the transition, stabilization of the results is achieved only after the combination of basis states of the individual runs, and not by a sheer increase of the number of sampling steps as in Fig. D.1.

Away from the transition, no qualitative changes in the angular momentum expectation value are observed once around 50 states have been taken into account. This holds true even when comparing with a run in which the basis states are derived from a single run of up to 1000 basis states (see also Fig. 3.9), rather than from 10 independent runs of up to 100 basis states. Close to the transition, however, a larger number of basis states is required to achieve convergence, as both the ground and the first excited state need to be resolved with a sufficiently large number of basis states. As a result, the single run of up to 1000 basis states shows different results than the combined runs at $\alpha = 3.3$ shown in Fig. D.2, see also the discussion in Section 3.4.4.

For the data shown in Figs. D.1 and D.2 we estimate the uncertainties of our energies as the energy difference between the combined energies at $N = 100$, and the extrapolated energies at $1/N = 0$. The resulting uncertainties are given in the captions of Figs. D.1 and D.2. We note that these estimated uncertainties are of the order of $\sim 0.01 E_{2B}^{\infty}$ in Fig. D.1, and, in Fig. D.2, they are of the order $\sim 0.001 E_{2B}^{\infty}$ before the transition and about $\sim 0.007 E_{2B}^{\infty}$ beyond the transition. As such, they are much smaller than the actual gap between the ground state and $-E_{2B}^{\infty}$. Furthermore, we note that, as can be seen in Fig. D.2, the extrapolated energies are very close to the energies obtained from a single run of 1000 basis states.

D.2 Convergence analysis of the number of sampling steps

Finally, we investigate the impact of the number of sampling steps on convergence. To this end, we show in Fig. D.3 an analysis of the convergence with the number of basis states for relatively low numbers of sampling steps obtained for $R/r_B = 10$ and $r_0/r_B = 0.8$. In Fig. D.4, the same analysis is performed for $R/r_B = 100$ and $r_0/r_B = 0.2$. In the case of $R/r_B = 10$ and $r_0/r_B = 0.8$, the energies and angular

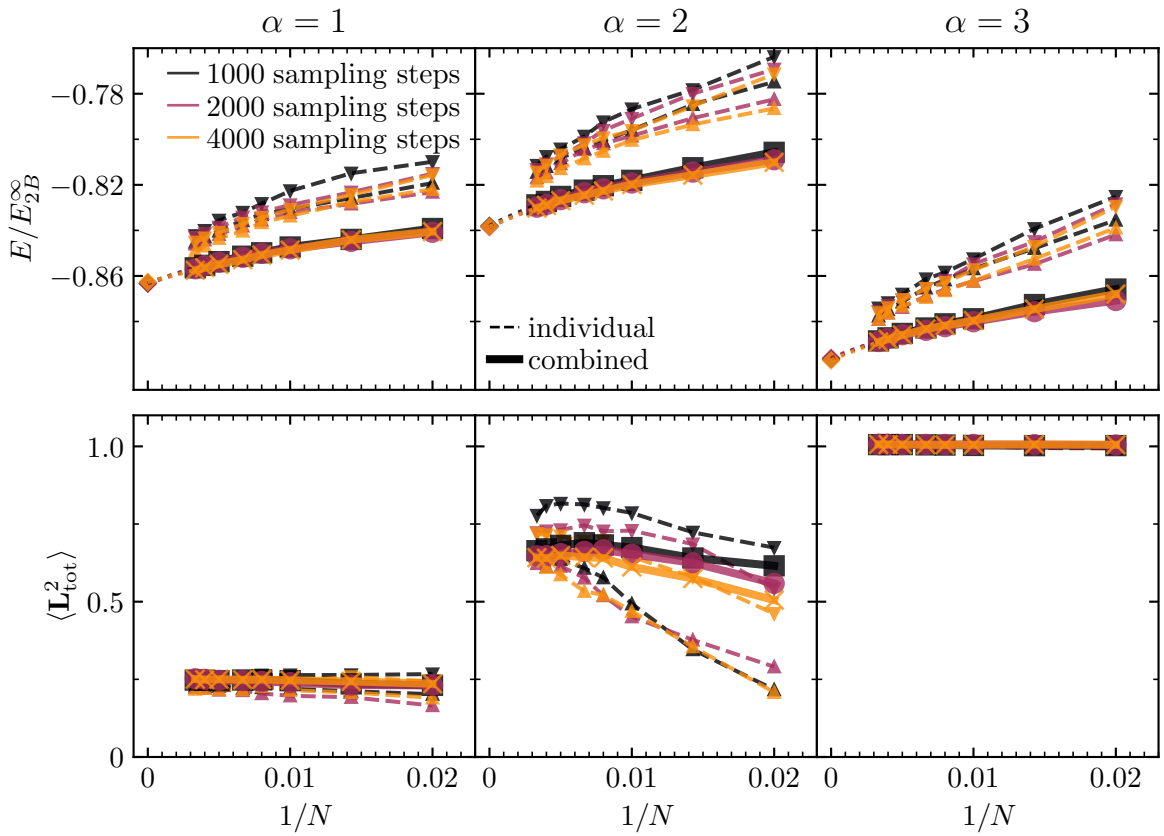

Figure D.3. Analysis of convergence as function of the number of basis states N and increasing numbers of sampling steps. The analysis is conducted for the parameters $R/r_B = 10$, $r_0/r_B = 0.8$ and for mass ratios well before (left, $\alpha = 1$), close to (middle, $\alpha = 2$) and well after (right, $\alpha = 3$) the transition region. 10 independent runs with up to 300 basis states using 1000 (black), 2000 (purple) and 4000 (yellow) sampling steps in every basis expansion step were conducted and the resulting ground states were tracked as a function of the number of basis states N for $1/N = 1/300, 1/250, 1/200, 1/150, 1/125, 1/100, 1/70$ and $1/50$. Ground state energies and angular momentum expectation values are shown in the same manner as in Figs. D.1 and D.2, with different colours representing different numbers of sampling steps.

momenta are, along with their spreads, comparable to those shown in Fig. D.1, even though the former results were obtained for a significantly lower number of sampling steps. In contrast, in the case of $R/r_B = 100$ and $r_0/r_B = 0.2$, shown in Fig. D.4, one can see that, by increasing the number of sampling steps, one obtains a much tighter grouping in energy, which differs from the results shown in Fig. D.2. The estimated uncertainties obtained from the data given in Figs. D.3 and D.4 are shown in Table D.1. This illustrates further the requirements different parameter ranges of r_0/r_B and R/r_B pose on the number of sampling steps.

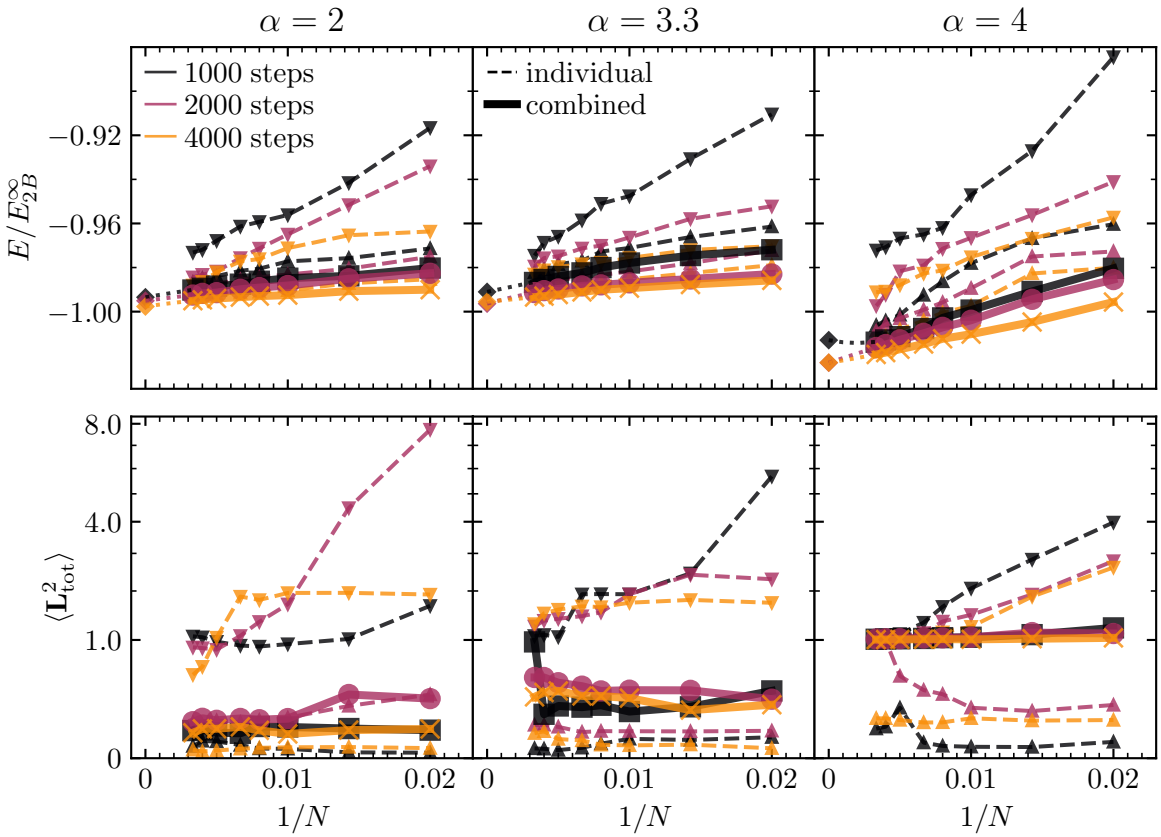

Figure D.4. Analysis of convergence with increasing number of basis states N for $R/r_B = 100$, $r_0/r_B = 0.2$, and different numbers of sampling steps. In the same manner as the analysis shown in Fig. D.3, the analysis is conducted for mass ratios well before (left,$\alpha = 2$), close to (middle,$\alpha = 3.3$), and well after (right, $\alpha = 4$) the transition region.

extrapolation error $[E^{\infty}_{2B}]$

	$R/r_B = 10,\ r_0/r_B = 0.8$			$R/r_B = 100, r_0/r_B = 0.2$		
	$\alpha = 1$	$\alpha = 2$	$\alpha = 3$	$\alpha = 2$	$\alpha = 3.3$	$\alpha = 4$
1000 sampling steps	0.0068	0.0092	0.0079	0.0033	0.0043	0.0009
2000 sampling steps	0.0065	0.0087	0.0072	0.0026	0.0050	0.0069
4000 sampling steps	0.0051	0.0081	0.0081	0.0026	0.0021	0.0037

Table D.1. Estimated extrapolation error of the ground state energy in units of E^{∞}_{2B} in dependence of the number of sampling steps, for different system parameters. The uncertainty is obtained by comparing the extrapolated energy and the energy obtained by a combination of 10×100 basis states, shown in Fig. D.3 and Fig. D.4.

Bibliography

[1] J. von Milczewski, F. Rose, and R. Schmidt, *Functional-renormalization-group approach to strongly coupled Bose-Fermi mixtures in two dimensions*, Phys. Rev. A **105**, 013317 (2022).

[2] M. Duda, X.-Y. Chen, A. Schindewolf, R. Bause, J. von Milczewski, R. Schmidt, I. Bloch, and X.-Y. Luo, *Transition from a polaronic condensate to a degenerate fermi gas of heteronuclear molecules*, Nature Physics **19**, 720–725 (2023).

[3] R. Li*, J. von Milczewski*, A. Imamoglu, R. Odziejewski, and R. Schmidt, *Impurity-induced pairing in two-dimensional fermi gases*, Phys. Rev. B **107**, 155135 (2023).

[4] J. von Milczewski, X. Chen, A. Imamoglu, and R. Schmidt, *Superconductivity induced by strong electron-exciton coupling in doped atomically thin semiconductor heterostructures*, arXiv: 2310.10726, (2023).

[5] J. von Milczewski and R. Schmidt, *Momentum-dependent quasiparticle properties of the fermi polaron from the functional renormalization group*, arXiv: 2312.05318, (2023).

[6] J. von Milczewski and J. R. Tolsma, *Dispersion forces between weakly disordered van der waals crystals*, Phys. Rev. B **104**, 125111 (2021).

[7] A. Nikolaenko, J. von Milczewski, D. G. Joshi, and S. Sachdev, *Spin density wave, fermi liquid, and fractionalized phases in a theory of antiferromagnetic metals using paramagnons and bosonic spinons*, Phys. Rev. B **108**, 045123 (2023).

[8] O. K. Diessel, J. von Milczewski, A. Christianen, and R. Schmidt, *Probing molecular spectral functions and unconventional pairing using raman spectroscopy*, arXiv:2209.11758, (2022).

[9] G. Ness, C. Shkedrov, Y. Florshaim, O. K. Diessel, J. von Milczewski, R. Schmidt, and Y. Sagi, *Observation of a Smooth Polaron-Molecule Transition in a Degenerate Fermi Gas*, Phys. Rev. X **10**, 041019 (2020).

[10] H. J. Metcalf and P. Van der Straten, *Laser cooling and trapping* (Springer Science & Business Media, 1999).

[11] W. Ketterle and M. W. Zwierlein, *Making, probing and understanding ultracold fermi gases*, La Rivista del Nuovo Cimento **31**, 247–422 (2008).

[12] C. C. Bradley, C. A. Sackett, J. J. Tollett, and R. G. Hulet, *Evidence of bose-einstein condensation in an atomic gas with attractive interactions*, Phys. Rev. Lett. **75**, 1687–1690 (1995).

[13] M. H. Anderson, J. R. Ensher, M. R. Matthews, C. E. Wieman, and E. A. Cornell, *Observation of bose-einstein condensation in a dilute atomic vapor*, Science **269**, 198–201 (1995).

[14] K. B. Davis, M.-O. Mewes, M. R. Andrews, N. J. van Druten, D. S. Durfee, D. M. Kurn, and W. Ketterle, *Bose-einstein condensation in a gas of sodium atoms*, Phys. Rev. Lett. **75**, 3969–3973 (1995).

[15] B. DeMarco and D. S. Jin, *Onset of fermi degeneracy in a trapped atomic gas*, Science **285**, 1703–1706 (1999).

[16] F. Schreck, L. Khaykovich, K. L. Corwin, G. Ferrari, T. Bourdel, J. Cubizolles, and C. Salomon, *Quasipure bose-einstein condensate immersed in a fermi sea*, Phys. Rev. Lett. **87**, 080403 (2001).

[17] A. G. Truscott, K. E. Strecker, W. I. McAlexander, G. B. Partridge, and R. G. Hulet, *Observation of fermi pressure in a gas of trapped atoms*, Science **291**, 2570–2572 (2001).

[18] S. Inouye, M. R. Andrews, J. Stenger, H.-J. Miesner, D. M. Stamper-Kurn, and W. Ketterle, *Observation of feshbach resonances in a boseeinstein condensate*, Nature **392**, 151–154 (1998).

[19] P. Courteille, R. S. Freeland, D. J. Heinzen, F. A. van Abeelen, and B. J. Verhaar, *Observation of a feshbach resonance in cold atom scattering*, Phys. Rev. Lett. **81**, 69–72 (1998).

[20] C. Chin, R. Grimm, P. Julienne, and E. Tiesinga, *Feshbach resonances in ultracold gases*, Rev. Mod. Phys. **82**, 1225–1286 (2010).

[21] Wikipedia, *Transition metal dichalcogenide monolayers — Wikipedia, the free encyclopedia*, Link, [Online; accessed 05-December-2023], 2023.

[22] G. Wang, A. Chernikov, M. M. Glazov, T. F. Heinz, X. Marie, T. Amand, and B. Urbaszek, *Colloquium: excitons in atomically thin transition metal dichalcogenides*, Rev. Mod. Phys. **90**, 021001 (2018).

[23] D. R. Cooper, B. DAnjou, N. Ghattamaneni, B. Harack, M. Hilke, A. Horth, N. Majlis, M. Massicotte, L. Vandsburger, E. Whiteway, and V. Yu, *Experimental review of graphene*, ISRN Condensed Matter Physics **2012**, 1–56 (2012).

[24] K. F. Mak, C. Lee, J. Hone, J. Shan, and T. F. Heinz, *Atomically thin* MoS_2*: a new direct-gap semiconductor*, Phys. Rev. Lett. **105**, 136805 (2010).

[25] A. Splendiani, L. Sun, Y. Zhang, T. Li, J. Kim, C.-Y. Chim, G. Galli, and F. Wang, *Emerging photoluminescence in monolayer mos2*, Nano Letters **10**, 1271–1275 (2010).

[26] O. Lopez-Sanchez, D. Lembke, M. Kayci, A. Radenovic, and A. Kis, *Ultrasensitive photodetectors based on monolayer mos2*, Nature Nanotechnology **8**, 497–501 (2013).

[27] F. K. Perkins, A. L. Friedman, E. Cobas, P. M. Campbell, G. G. Jernigan, and B. T. Jonker, *Chemical vapor sensing with monolayer mos2*, Nano Letters **13**, 668–673 (2013).

[28] B. Radisavljevic, M. B. Whitwick, and A. Kis, *Integrated circuits and logic operations based on single-layer mos2*, ACS Nano **5**, 9934–9938 (2011).

[29] R. Cheng, D. Li, H. Zhou, C. Wang, A. Yin, S. Jiang, Y. Liu, Y. Chen, Y. Huang, and X. Duan, *Electroluminescence and photocurrent generation from atomically sharp wse2/mos2 heterojunction pn diodes*, Nano Letters **14**, 5590–5597 (2014).

[30] T. Cao, G. Wang, W. Han, H. Ye, C. Zhu, J. Shi, Q. Niu, P. Tan, E. Wang, B. Liu, and J. Feng, *Valley-selective circular dichroism of monolayer molybdenum disulphide*, Nature Communications **3**, 887 (2012).

[31] D. Xiao, G.-B. Liu, W. Feng, X. Xu, and W. Yao, *Coupled spin and valley physics in monolayers of* MoS_2 *and other group-vi dichalcogenides*, Phys. Rev. Lett. **108**, 196802 (2012).

[32] M. Van der Donck, M. Zarenia, and F. M. Peeters, *Excitons and trions in monolayer transition metal dichalcogenides: a comparative study between the multiband model and the quadratic single-band model*, Phys. Rev. B **96**, 035131 (2017).

[33] M. Sidler, P. Back, O. Cotlet, A. Srivastava, T. Fink, M. Kroner, E. Demler, and A. Imamoglu, *Fermi polaron-polaritons in charge-tunable atomically thin semiconductors*, Nat. Phys. **13**, 255–261 (2017).

[34] L. B. Tan, O. K. Diessel, A. Popert, R. Schmidt, A. Imamoglu, and M. Kroner, *Bose polaron interactions in a cavity-coupled monolayer semiconductor*, Phys. Rev. X **13**, 031036 (2023).

[35] E. V. Calman, M. M. Fogler, L. V. Butov, S. Hu, A. Mishchenko, and A. K. Geim, *Indirect excitons in van der waals heterostructures at room temperature*, Nature Communications **9**, 1895 (2018).

[36] L. Wang et al., *Correlated electronic phases in twisted bilayer transition metal dichalcogenides*, Nat. Mat. **19**, 861–866 (2020).

[37] L. Ma, P. X. Nguyen, Z. Wang, Y. Zeng, K. Watanabe, T. Taniguchi, A. H. MacDonald, K. F. Mak, and J. Shan, *Strongly correlated excitonic insulator in atomic double layers*, Nature **598**, 585–589 (2021).

[38] Z. Zhang et al., *Correlated interlayer exciton insulator in heterostructures of monolayer WSe2 and moiré WS2/WSe2*, Nat. Phys. **18**, 1214–1220 (2022).

[39] I. Amelio, N. D. Drummond, E. Demler, R. Schmidt, and A. Imamoglu, *Polaron spectroscopy of a bilayer excitonic insulator*, Phys. Rev. B **107**, 155303 (2023).

[40] S. Giorgini, L. P. Pitaevskii, and S. Stringari, *Theory of ultracold atomic fermi gases*, Rev. Mod. Phys. **80**, 1215–1274 (2008).

[41] M. Macêdo-Lima and L. Madeira, *Scattering length and effective range of microscopic two-body potentials*, Revista Brasileira de Ensino de Física **45**, 1 (2023).

[42] E. Timmermans, P. Tommasini, M. Hussein, and A. Kerman, *Feshbach resonances in atomic boseeinstein condensates*, Physics Reports **315**, 199–230 (1999).

[43] M. Holland, S. J. J. M. F. Kokkelmans, M. L. Chiofalo, and R. Walser, *Resonance Superfluidity in a Quantum Degenerate Fermi Gas*, Phys. Rev. Lett. **87**, 120406 (2001).

[44] E. Timmermans, K. Furuya, P. W. Milonni, and A. K. Kerman, *Prospect of creating a composite Fermi-Bose superfluid*, Phys. Lett. A **285**, 228–233 (2001).

[45] R. A. Duine and H. T. C. Stoof, *Microscopic many-body theory of atomic bose gases near a feshbach resonance*, Journal of Optics B: Quantum and Semiclassical Optics **5**, S212 (2003).

[46] R. Duine and H. Stoof, *Atommolecule coherence in bose gases*, Physics Reports **396**, 115–195 (2004).

[47] G. M. Bruun and C. J. Pethick, *Effective theory of feshbach resonances and many-body properties of fermi gases*, Phys. Rev. Lett. **92**, 140404 (2004).

[48] I. Bloch, J. Dalibard, and W. Zwerger, *Many-body physics with ultracold gases*, Rev. Mod. Phys. **80**, 885–964 (2008).

[49] D. Lurié and A. J. Macfarlane, *Equivalence between four-fermion and yukawa coupling, and the $Z_3 = 0$ condition for composite bosons*, Phys. Rev. **136**, B816–B829 (1964).

[50] P. Nikolic and S. Sachdev, *Renormalization-group fixed points, universal phase diagram, and $1/N$ expansion for quantum liquids with interactions near the unitarity limit*, Phys. Rev. A **75**, 033608 (2007).

[51] A. L. Fetter and J. D. Walecka, *Quantum theory of many-particle systems* - (Courier Corporation, New York, 2012).

[52] A. Altland and B. D. Simons, *Condensed matter field theory* (Cambridge University Press, Mar. 2010).

[53] S. K. Adhikari, *Quantum scattering in two dimensions*, Am. J Phys. **54**, 362–367 (1986).

[54] F. Chevy, *Universal phase diagram of a strongly interacting Fermi gas with unbalanced spin populations*, Phys. Rev. A **74**, 063628 (2006).

[55] C. Trefzger and Y. Castin, *Impurity in a fermi sea on a narrow feshbach resonance: a variational study of the polaronic and dimeronic branches*, Phys. Rev. A **85**, 053612 (2012).

[56] M. Punk, P. T. Dumitrescu, and W. Zwerger, *Polaron-to-molecule transition in a strongly imbalanced fermi gas*, Phys. Rev. A **80**, 053605 (2009).

[57] C. Mora and F. Chevy, *Ground state of a tightly bound composite dimer immersed in a fermi sea*, Phys. Rev. A **80**, 033607 (2009).

[58] P. Massignan and G. M. Bruun, *Repulsive polarons and itinerant ferromagnetism in strongly polarized fermi gases*, The European Physical Journal D **65**, 83–89 (2011).

[59] R. Combescot, A. Recati, C. Lobo, and F. Chevy, *Normal state of highly polarized fermi gases: simple many-body approaches*, Phys. Rev. Lett. **98**, 180402 (2007).

[60] E. Courtade et al., *Charged excitons in monolayer* WSe_2*: experiment and theory*, Phys. Rev. B **96**, 085302 (2017).

[61] C. Fey, P. Schmelcher, A. Imamoglu, and R. Schmidt, *Theory of exciton-electron scattering in atomically thin semiconductors*, Phys. Rev. B **101**, 195417 (2020).

[62] A. Imamoglu, O. Cotlet, and R. Schmidt, *Excitonpolarons in two-dimensional semiconductors and the taviscummings model*, Comptes Rendus. Physique **22**, 1–8 (2021).

[63] A. Raja et al., *Coulomb engineering of the bandgap and excitons in two-dimensional materials*, Nat. Comm. **8**, 15251 (2017).

[64] J. Berges, N. Tetradis, and C. Wetterich, *Non-perturbative renormalization flow in quantum field theory and statistical physics*, Physics Reports **363**, 223–386 (2002).

[65] H. Gies, *Introduction to the functional RG and applications to gauge theories*, in *Renormalization group and effective field theory approaches to many-body systems* (Springer Berlin Heidelberg, 2012), pp. 287–348.

[66] B. Delamotte, *An introduction to the nonperturbative renormalization group*, in *Renormalization group and effective field theory approaches to many-body systems* (Springer Berlin Heidelberg, 2012), pp. 49–132.

[67] N. Dupuis, L. Canet, A. Eichhorn, W. Metzner, J. Pawlowski, M. Tissier, and N. Wschebor, *The nonperturbative functional renormalization group and its applications*, Phys. Rep. **910**, 1–114 (2021).

[68] M. Reuter, *Nonperturbative evolution equation for quantum gravity*, Phys. Rev. D **57**, 971–985 (1998).

[69] A. Eichhorn, *Status of the Asymptotic Safety Paradigm for Quantum Gravity and Matter*, Found. Phys. **48**, 1407–1429 (2018).

[70] J. M. Pawlowski and M. Reichert, *Quantum gravity: a fluctuating point of view*, Frontiers in Physics **8**, 527 (2021).

[71] J. M. Pawlowski, *Equation of state and phase diagram of strongly interacting matter*, Nucl. Phys. A **931**, 113–124 (2014).

[72] N. Strodthoff, *Phase Structure and Dynamics of QCD-A Functional Perspective*, Journal of Physics: Conference Series **832**, 012040 (2017).

[73] B. Delamotte, D. Mouhanna, and M. Tissier, *Nonperturbative renormalization group approach to frustrated magnets*, Phys. Rev. B **69**, 134413 (2004).

[74] F. Benitez, J.-P. Blaizot, H. Chaté, B. Delamotte, R. Méndez-Galain, and N. Wschebor, *Nonperturbative renormalization group preserving full-momentum dependence: Implementation and quantitative evaluation*, Phys. Rev. E **85**, 026707 (2012).

[75] G. Tarjus and M. Tissier, *Random-field Ising and $O(N)$ models: theoretical description through the functional renormalization group*, Eur. Phys. J. B **93**, 50 (2020).

[76] J.-P. Blaizot, R. Mendez Galain, and N. Wschebor, *Non-Perturbative Renormalization Group calculation of the transition temperature of the weakly interacting Bose gas*, Europhys. Lett. **72**, 705–711 (2005).

[77] A. Rançon and N. Dupuis, *Nonperturbative renormalization group approach to strongly correlated lattice bosons*, Phys. Rev. B **84**, 174513 (2011).

[78] J. Reuther and R. Thomale, *Functional renormalization group for the anisotropic triangular antiferromagnet*, Phys. Rev. B **83**, 024402 (2011).

[79] W. Metzner, M. Salmhofer, C. Honerkamp, V. Meden, and K. Schönhammer, *Functional renormalization group approach to correlated fermion systems*, Rev. Mod. Phys. **84**, 299–352 (2012).

[80] F. Rose and N. Dupuis, *Superuniversal transport near a $(2+1)$-dimensional quantum critical point*, Phys. Rev. B **96**, 100501 (2017).

[81] G. D. Mahan, *Many-particle physics* (Springer, Mar. 31, 1990), 1032 pp.

[82] C. Wetterich, *Exact evolution equation for the effective potential*, Phys. Lett. B **301**, 90–94 (1993).

[83] J. Bardeen, L. N. Cooper, and J. R. Schrieffer, *Microscopic theory of superconductivity*, Phys. Rev. **106**, 162–164 (1957).

[84] J. Bardeen, L. N. Cooper, and J. R. Schrieffer, *Theory of superconductivity*, Phys. Rev. **108**, 1175–1204 (1957).

[85] K.-K. Ni, S. Ospelkaus, M. H. G. de Miranda, A. Pe'er, B. Neyenhuis, J. J. Zirbel, S. Kotochigova, P. S. Julienne, D. S. Jin, and J. Ye, *A high phase-space-density gas of polar molecules*, Science **322**, 231–235 (2008).

[86] J. W. Park, S. A. Will, and M. W. Zwierlein, *Ultracold dipolar gas of fermionic* ^{23}Na^{40}K *molecules in their absolute ground state*, Phys. Rev. Lett. **114**, 205302 (2015).

[87] T. M. Rvachov, H. Son, A. T. Sommer, S. Ebadi, J. J. Park, M. W. Zwierlein, W. Ketterle, and A. O. Jamison, *Long-Lived Ultracold Molecules with Electric and Magnetic Dipole Moments*, Phys. Rev. Lett. **119**, 143001 (2017).

[88] F. Seesselberg, N. Buchheim, Z.-K. Lu, T. Schneider, X.-Y. Luo, E. Tiemann, I. Bloch, and C. Gohle, *Modeling the adiabatic creation of ultracold polar* ^{23}Na^{40}K *molecules*, Phys. Rev. A **97**, 013405 (2018).

[89] H. Yang, D.-C. Zhang, L. Liu, Y.-X. Liu, J. Nan, B. Zhao, and J.-W. Pan, *Observation of magnetically tunable Feshbach resonances in ultracold* ^{23}Na^{40}K+^{40}K *collisions*, Science **363**, 261–264 (2019).

[90] K. F. Mak, K. He, C. Lee, G. H. Lee, J. Hone, T. F. Heinz, and J. Shan, *Tightly bound trions in monolayer mos2*, Nature Materials **12**, 207–211 (2012).

[91] L. De Marco, G. Valtolina, K. Matsuda, W. G. Tobias, J. P. Covey, and J. Ye, *A degenerate Fermi gas of polar molecules*, Science **363**, 853–856 (2019).

[92] T. Enss and W. Zwerger, *Superfluidity near phase separation in bose-fermi mixtures*, EPJ B **68**, 383–389 (2009).

[93] M. Matuszewski, T. Taylor, and A. V. Kavokin, *Exciton supersolidity in hybrid Bose-Fermi systems*, Phys. Rev. Lett. **108**, 060401 (2012).

[94] I. A. Shelykh, T. Taylor, and A. V. Kavokin, *Rotons in a hybrid bose-fermi system*, Phys. Rev. Lett. **105**, 140402 (2010).

[95] O. Cotlet, S. Zeytinoglu, M. Sigrist, E. Demler, and A. Imamoglu, *Superconductivity and other collective phenomena in a hybrid bose-fermi mixture formed by a polariton condensate and an electron system in two dimensions*, Phys. Rev. B **93**, 054510 (2016).

[96] S. Powell, S. Sachdev, and H. P. Büchler, *Depletion of the Bose-Einstein condensate in Bose-Fermi mixtures*, Phys. Rev. B **72**, 024534 (2005).

[97] K. Suzuki, T. Miyakawa, and T. Suzuki, *p-wave superfluid and phase separation in atomic Bose-Fermi mixtures*, Phys. Rev. A **77**, 043629 (2008).

[98] E. Fratini and P. Pieri, *Pairing and condensation in a resonant Bose-Fermi mixture*, Phys. Rev. A **81**, 051605 (2010).

[99] D. Ludwig, S. Floerchinger, S. Moroz, and C. Wetterich, *Quantum phase transition in bose-fermi mixtures*, Phys. Rev. A **84**, 033629 (2011).

[100] A. Guidini, G. Bertaina, D. E. Galli, and P. Pieri, *Condensed phase of Bose-Fermi mixtures with a pairing interaction*, Phys. Rev. A **91**, 023603 (2015).

[101] J. J. Kinnunen, Z. Wu, and G. M. Bruun, *Induced p-wave pairing in bose-fermi mixtures*, Phys. Rev. Lett. **121**, 253402 (2018).

[102] F. P. Laussy, A. V. Kavokin, and I. A. Shelykh, *Exciton-polariton mediated superconductivity*, Phys. Rev. Lett. **104**, 106402 (2010).

[103] S. P. Rath and R. Schmidt, *Field-theoretical study of the bose polaron*, Phys. Rev. A **88**, 053632 (2013).

[104] H. Fröhlich, *Electrons in lattice fields*, Advances in Physics **3**, 325–361 (1954).

[105] T. Holstein, *Studies of polaron motion*, Annals of Physics **8**, 325–342 (1959).

[106] M.-G. Hu, M. J. Van de Graaff, D. Kedar, J. P. Corson, E. A. Cornell, and D. S. Jin, *Bose polarons in the strongly interacting regime*, Phys. Rev. Lett. **117**, 055301 (2016).

[107] N. B. Jørgensen, L. Wacker, K. T. Skalmstang, M. M. Parish, J. Levinsen, R. S. Christensen, G. M. Bruun, and J. J. Arlt, *Observation of attractive and repulsive polarons in a bose-einstein condensate*, Phys. Rev. Lett. **117**, 055302 (2016).

[108] Z. Z. Yan, Y. Ni, C. Robens, and M. W. Zwierlein, *Bose polarons near quantum criticality*, Science **368**, 190–194 (2020).

[109] F. Camargo, R. Schmidt, J. D. Whalen, R. Ding, G. Woehl, S. Yoshida, J. Burgdörfer, F. B. Dunning, H. R. Sadeghpour, E. Demler, and T. C. Killian, *Creation of Rydberg Polarons in a Bose Gas*, Phys. Rev. Lett. **120**, 083401 (2018).

[110] J. Tempere, W. Casteels, M. K. Oberthaler, S. Knoop, E. Timmermans, and J. T. Devreese, *Feynman path-integral treatment of the BEC-impurity polaron*, Phys. Rev. B **80**, 184504 (2009).

[111] W. Casteels, T. Cauteren, J. Tempere, and J. T. Devreese, *Strong coupling treatment of the polaronic system consisting of an impurity in a condensate*, Laser Physics **21**, 1480–1485 (2011).

[112] A. Shashi, F. Grusdt, D. A. Abanin, and E. Demler, *Radio-frequency spectroscopy of polarons in ultracold bose gases*, Phys. Rev. A **89**, 053617 (2014).

[113] V. Ginzburg, *On surface superconductivity*, Phys. Lett. **13**, 101–102 (1964).

[114] F. P. Laussy, *Superconductivity with excitons and polaritons: review and extension*, Journal of Nanophotonics **6**, 064502 (2012).

[115] E. Cherotchenko, T. Espinosa-Ortega, A. Nalitov, I. Shelykh, and A. Kavokin, *Superconductivity in semiconductor structures: the excitonic mechanism*, Superlattices and Microstructures **90**, 170–175 (2016).

[116] L. Viverit, C. J. Pethick, and H. Smith, *Zero-temperature phase diagram of binary boson-fermion mixtures*, Phys. Rev. A **61**, 053605 (2000).

[117] D. V. Efremov and L. Viverit, *p-wave cooper pairing of fermions in mixtures of dilute fermi and bose gases*, Phys. Rev. B **65**, 134519 (2002).

[118] R. Roth and H. Feldmeier, *Mean-field instability of trapped dilute boson-fermion mixtures*, Phys. Rev. A **65**, 021603 (2002).

[119] R. Roth, *Structure and stability of trapped atomic boson-fermion mixtures*, Phys. Rev. A **66**, 013614 (2002).

[120] A. P. Albus, S. A. Gardiner, F. Illuminati, and M. Wilkens, *Quantum field theory of dilute homogeneous bose-fermi mixtures at zero temperature: general formalism and beyond mean-field corrections*, Phys. Rev. A **65**, 053607 (2002).

[121] H. Hu and X.-J. Liu, *Thermodynamics of a trapped bose-fermi mixture*, Phys. Rev. A **68**, 023608 (2003).

[122] T. Watanabe, T. Suzuki, and P. Schuck, *Bose-fermi pair correlations in attractively interacting bose-fermi atomic mixtures*, Phys. Rev. A **78**, 033601 (2008).

[123] Z.-Q. Yu, S. Zhang, and H. Zhai, *Stability condition of a strongly interacting boson-fermion mixture across an interspecies Feshbach resonance*, Phys. Rev. A **83**, 041603 (2011).

[124] G. Bertaina, E. Fratini, S. Giorgini, and P. Pieri, *Quantum Monte Carlo Study of a Resonant Bose-Fermi Mixture*, Phys. Rev. Lett. **110**, 115303 (2013).

[125] A. Guidini, G. Bertaina, E. Fratini, and P. Pieri, *Bose-fermi mixtures in the molecular limit*, Phys. Rev. A **89**, 023634 (2014).

[126] D. K. Efimkin, E. K. Laird, J. Levinsen, M. M. Parish, and A. H. MacDonald, *Electron-exciton interactions in the exciton-polaron problem*, Phys. Rev. B **103**, 075417 (2021).

[127] A. Camacho-Guardian, L. A. Peña Ardila, T. Pohl, and G. M. Bruun, *Bipolarons in a bose-einstein condensate*, Phys. Rev. Lett. **121**, 013401 (2018).

[128] A. Schirotzek, C.-H. Wu, A. Sommer, and M. W. Zwierlein, *Observation of fermi polarons in a tunable fermi liquid of ultracold atoms*, Phys. Rev. Lett. **102**, 230402 (2009).

[129] M. Koschorreck, D. Pertot, E. Vogt, B. Fröhlich, M. Feld, and M. Köhl, *Attractive and repulsive fermi polarons in two dimensions*, Nature **485**, 619–622 (2012).

[130] I. Fritsche, C. Baroni, E. Dobler, E. Kirilov, B. Huang, R. Grimm, G. M. Bruun, and P. Massignan, *Stability and breakdown of Fermi polarons in a strongly interacting Fermi-Bose mixture*, Phys. Rev. A **103**, 053314 (2021).

[131] L. D. Carr, D. DeMille, R. V. Krems, and J. Ye, *Cold and ultracold molecules: science, technology and applications*, New J. Phys. **11**, 055049 (2009).

[132] J. L. Bohn, A. M. Rey, and J. Ye, *Cold molecules: progress in quantum engineering of chemistry and quantum matter*, Science **357**, 1002–1010 (2017).

[133] F. M. Marchetti, C. J. M. Mathy, D. A. Huse, and M. M. Parish, *Phase separation and collapse in Bose-Fermi mixtures with a Feshbach resonance*, Phys. Rev. B **78**, 134517 (2008).

[134] W. Zwerger, *The bcs-bec crossover and the unitary Fermi gas*, Vol. 836 (Springer Science & Business Media, 2011).

[135] R. Haussmann, W. Rantner, S. Cerrito, and W. Zwerger, *Thermodynamics of the bcs-bec crossover*, Phys. Rev. A **75**, 023610 (2007).

[136] K. V. Houcke, F. Werner, E. Kozik, N. Prokof'ev, B. Svistunov, M. J. H. Ku, A. T. Sommer, L. W. Cheuk, A. Schirotzek, and M. W. Zwierlein, *Feynman diagrams versus Fermi-gas Feynman emulator*, Nat. Phys. **8**, 366–370 (2012).

[137] R. Schmidt and T. Enss, *Excitation spectra and rf response near the polaron-to-molecule transition from the functional renormalization group*, Phys. Rev. A **83**, 063620 (2011).

[138] M. M. Parish, H. S. Adlong, W. E. Liu, and J. Levinsen, *Thermodynamic signatures of the polaron-molecule transition in a Fermi gas*, Phys. Rev. A **103**, 023312 (2021).

[139] D. J. Thouless, *Perturbation theory in statistical mechanics and the theory of superconductivity*, Annals of Physics **10**, 553–588 (1960).

[140] N. M. Hugenholtz and D. Pines, *Ground-state energy and excitation spectrum of a system of interacting bosons*, Phys. Rev. **116**, 489–506 (1959).

[141] C. Lobo, A. Recati, S. Giorgini, and S. Stringari, *Normal state of a polarized Fermi gas at unitarity*, Phys. Rev. Lett. **97**, 200403 (2006).

[142] N. Prokof'ev and B. Svistunov, *Fermi-polaron problem: diagrammatic Monte Carlo method for divergent sign-alternating series*, Phys. Rev. B **77**, 020408 (2008).

[143] N. V. Prokof'ev and B. V. Svistunov, *Bold diagrammatic Monte Carlo: a generic sign-problem tolerant technique for polaron models and possibly interacting many-body problems*, Phys. Rev. B **77**, 125101 (2008).

[144] A. Viel and A. Simoni, *Feshbach resonances and weakly bound molecular states of boson-boson and boson-fermion NaK pairs*, Phys. Rev. A **93**, 042701 (2016).

[145] X.-Y. Chen, M. Duda, A. Schindewolf, R. Bause, I. Bloch, and X.-Y. Luo, *Suppression of unitary three-body loss in a degenerate Bose-Fermi mixture*, Phys. Rev. Lett. **128**, 153401 (2022).

[146] K. Mølmer, *Bose Condensates and Fermi Gases at Zero Temperature*, Phys. Rev. Lett. **80**, 1804–1807 (1998).

[147] M. Zaccanti, C. DErrico, F. Ferlaino, G. Roati, M. Inguscio, and G. Modugno, *Control of the interaction in a Fermi-Bose mixture*, Phys. Rev. A **74**, 041605 (2006).

[148] C. Ospelkaus, S. Ospelkaus, K. Sengstock, and K. Bongs, *Interaction-driven dynamics of* ^{40}K–^{87}Rb *fermion-boson gas mixtures in the large-particle-number limit*, Phys. Rev. Lett. **96**, 020401 (2006).

[149] R. S. Bloom, M.-G. Hu, T. D. Cumby, and D. S. Jin, *Tests of universal three-body physics in an ultracold Bose-Fermi mixture*, Phys. Rev. Lett. **111**, 105301 (2013).

[150] M. Pini, P. Pieri, M. Jäger, J. H. Denschlag, and G. C. Strinati, *Pair correlations in the normal phase of an attractive Fermi gas*, New J. Phys. **22**, 083008 (2020).

[151] Z. Zhang, L. Chen, K.-X. Yao, and C. Chin, *Transition from an atomic to a molecular Bose–Einstein condensate*, Nature **592**, 708–711 (2021).

[152] W. Witczak-Krempa, E. S. Sørensen, and S. Sachdev, *The dynamics of quantum criticality revealed by quantum Monte Carlo and holography*, Nat. Phys. **10**, 361–366 (2014).

[153] T. Takekoshi, L. Reichsöllner, A. Schindewolf, J. M. Hutson, C. R. Le Sueur, O. Dulieu, F. Ferlaino, R. Grimm, and H.-C. Nägerl, *Ultracold dense samples of dipolar rbcs molecules in the rovibrational and hyperfine ground state*, Phys. Rev. Lett. **113**, 205301 (2014).

[154] P. K. Molony, P. D. Gregory, Z. Ji, B. Lu, M. P. Köppinger, C. R. Le Sueur, C. L. Blackley, J. M. Hutson, and S. L. Cornish, *Creation of ultracold* ^{87}Rb^{133}Cs *molecules in the rovibrational ground state*, Phys. Rev. Lett. **113**, 255301 (2014).

[155] M. Guo, B. Zhu, B. Lu, X. Ye, F. Wang, R. Vexiau, N. Bouloufa-Maafa, G. Quéméner, O. Dulieu, and D. Wang, *Creation of an ultracold gas of ground-state dipolar* ^{23}Na^{87}Rb *molecules*, Phys. Rev. Lett. **116**, 205303 (2016).

[156] K. K. Voges, P. Gersema, M. Meyer zum Alten Borgloh, T. A. Schulze, T. Hartmann, A. Zenesini, and S. Ospelkaus, *Ultracold gas of bosonic* ^{23}Na^{39}K *ground-state molecules*, Phys. Rev. Lett. **125**, 083401 (2020).

[157] W. B. Cairncross, J. T. Zhang, L. R. B. Picard, Y. Yu, K. Wang, and K.-K. Ni, *Assembly of a rovibrational ground state molecule in an optical tweezer*, Phys. Rev. Lett. **126**, 123402 (2021).

[158] C. Warner, A. Z. Lam, N. Bigagli, H. C. Liu, I. Stevenson, and S. Will, *Overlapping Bose-Einstein condensates of* ^{23}Na *and* ^{133}Cs, Phys. Rev. A **104**, 033302 (2021).

[159] G. Valtolina, K. Matsuda, W. G. Tobias, J.-R. Li, L. D. Marco, and J. Ye, *Dipolar evaporation of reactive molecules to below the Fermi temperature*, Nature **588**, 239–243 (2020).

[160] J.-R. Li, W. G. Tobias, K. Matsuda, C. Miller, G. Valtolina, L. D. Marco, R. R. W. Wang, L. Lassablière, G. Quéméner, J. L. Bohn, and J. Ye, *Tuning of dipolar interactions and evaporative cooling in a three-dimensional molecular quantum gas*, Nat. Phys. **17**, 1144–1148 (2021).

[161] A. Schindewolf, R. Bause, X.-Y. Chen, M. Duda, T. Karman, I. Bloch, and X.-Y. Luo, *Evaporation of microwave-shielded polar molecules to quantum degeneracy*, Nature **607**, 677–681 (2022).

[162] M. A. Baranov, M. Dalmonte, G. Pupillo, and P. Zoller, *Condensed Matter Theory of Dipolar Quantum Gases*, Chem. Rev. **112**, 5012–5061 (2012).

[163] V. Velji, A. Pelster, and A. Bala, *Stability of quantum degenerate Fermi gases of tilted polar molecules*, Phys. Rev. Res. **1**, 012009 (2019).

[164] D. Peter, S. Müller, S. Wessel, and H. P. Büchler, *Anomalous behavior of spin systems with dipolar interactions*, Phys. Rev. Lett. **109**, 025303 (2012).

[165] A.-L. Gadsbølle and G. M. Bruun, *Dipolar fermions in a two-dimensional lattice at nonzero temperature*, Phys. Rev. A **86**, 033623 (2012).

[166] R. Combescot, S. Giraud, and X. Leyronas, *Analytical theory of the dressed bound state in highly polarized fermi gases*, EPL **88**, 60007 (2009).

[167] G. M. Bruun and P. Massignan, *Decay of polarons and molecules in a strongly polarized fermi gas*, Phys. Rev. Lett. **105**, 020403 (2010).

[168] K. B. Gubbels and H. T. C. Stoof, *Renormalization group theory for the imbalanced fermi gas*, Phys. Rev. Lett. **100**, 140407 (2008).

[169] R. Combescot and S. Giraud, *Normal state of highly polarized fermi gases: full many-body treatment*, Phys. Rev. Lett. **101**, 050404 (2008).

[170] S. Zöllner, G. M. Bruun, and C. J. Pethick, *Polarons and molecules in a two-dimensional fermi gas*, Phys. Rev. A **83**, 021603 (2011).

[171] M. M. Parish, *Polaron-molecule transitions in a two-dimensional fermi gas*, Phys. Rev. A **83**, 051603 (2011).

[172] R. Schmidt, T. Enss, V. Pietilä, and E. Demler, *Fermi polarons in two dimensions*, Phys. Rev. A **85**, 021602 (2012).

[173] G. Bertaina, *BCS-BEC crossover in two dimensions: a quantum monte carlo study*, AIP Conference Proceedings **1485**, 286–290 (2012).

[174] M. M. Parish and J. Levinsen, *Highly polarized fermi gases in two dimensions*, Phys. Rev. A **87**, 033616 (2013).

[175] P. Kroiss and L. Pollet, *Diagrammatic monte carlo study of quasi-two-dimensional fermi polarons*, Phys. Rev. B **90**, 104510 (2014).

[176] J. Vlietinck, J. Ryckebusch, and K. Van Houcke, *Diagrammatic monte carlo study of the fermi polaron in two dimensions*, Phys. Rev. B **89**, 085119 (2014).

[177] L. Pricoupenko and P. Pedri, *Universal $(1+2)$-body bound states in planar atomic waveguides*, Phys. Rev. A **82**, 033625 (2010).

[178] J. Levinsen, P. Massignan, and M. M. Parish, *Efimov trimers under strong confinement*, Phys. Rev. X **4**, 031020 (2014).

[179] P. Naidon and S. Endo, *Efimov physics: a review*, Rep. Prog. Phys. **80**, 056001 (2017).

[180] C. Shkedrov, Y. Florshaim, G. Ness, A. Gandman, and Y. Sagi, *High-sensitivity rf spectroscopy of a strongly interacting fermi gas*, Phys. Rev. Lett. **121**, 093402 (2018).

[181] C. Shkedrov, G. Ness, Y. Florshaim, and Y. Sagi, *In situ momentum-distribution measurement of a quantum degenerate fermi gas using raman spectroscopy*, Phys. Rev. A **101**, 013609 (2020).

[182] R. Combescot, X. Leyronas, and M. Y. Kagan, *Self-consistent theory for molecular instabilities in a normal degenerate fermi gas in the BEC-BCS crossover*, Phys. Rev. A **73**, 023618 (2006).

[183] M. Randeria, J.-M. Duan, and L.-Y. Shieh, *Superconductivity in a two-dimensional fermi gas: evolution from cooper pairing to bose condensation*, Phys. Rev. B **41**, 327–343 (1990).

[184] K. Kamikado, T. Kanazawa, and S. Uchino, *Mobile impurity in a fermi sea from the functional renormalization group analytically continued to real time*, Phys. Rev. A **95**, 013612 (2017).

[185] J. M. Pawlowski, M. M. Scherer, R. Schmidt, and S. J. Wetzel, *Physics and the choice of regulators in functional renormalisation group flows*, Annals of Physics **384**, 165–197 (2017).

[186] J. Levinsen and M. M. Parish, *Bound states in a quasi-two-dimensional fermi gas*, Phys. Rev. Lett. **110**, 055304 (2013).

[187] S. Floerchinger, M. M. Scherer, and C. Wetterich, *Modified fermi sphere, pairing gap, and critical temperature for the BCS-BEC crossover*, Phys. Rev. A **81**, 063619 (2010).

[188] M. Q. Huber and J. Braun, *Algorithmic derivation of functional renormalization group equations and dysonschwinger equations*, Computer Physics Communications **183**, 1290–1320 (2012).

[189] M. Q. Huber, A. K. Cyrol, and J. M. Pawlowski, *DoFun 3.0: functional equations in mathematica*, Computer Physics Communications **248**, 107058 (2020).

[190] L. Gor'kov and T. Melik-Barkhudarov, *Contribution to the theory of superfluidity in an imperfect fermi gas*, Sov. Phys. JETP **13**, 1018 (1961).

[191] C. J. Pethick and H. Smith, *Boseeinstein condensation in dilute gases* (Cambridge University Press, Nov. 2001).

[192] S. Floerchinger, M. Scherer, S. Diehl, and C. Wetterich, *Particle-hole fluctuations in BCS-BEC crossover*, Phys. Rev. B **78**, 174528 (2008).

[193] M. Köhl, in (2012).

[194] H. Yabu, Y. Takayama, and T. Suzuki, *Bosefermi mixed condensates of atomic gas with bosonfermion quasi-bound state*, Physica B: Condensed Matter **329**, 25–27 (2003).

[195] A. A. Abrikosov, *Methods of quantum field theory in statistical physics* (Dover Publications, New York, 1975).

[196] S. Floerchinger, *Analytic continuation of functional renormalization group equations*, Journal of High Energy Physics **2012**, 21 (2012).

[197] J. M. Pawlowski and N. Strodthoff, *Real time correlation functions and the functional renormalization group*, Phys. Rev. D **92**, 094009 (2015).

[198] K. Kamikado, N. Strodthoff, L. von Smekal, and J. Wambach, *Fluctuations in the quark-meson model for QCD with isospin chemical potential*, Phys. Lett. B **718**, 1044–1053 (2013).

[199] J.-P. Blaizot, R. Méndez-Galain, and N. Wschebor, *A new method to solve the non-perturbative renormalization group equations*, Phys. Lett. B **632**, 571–578 (2006).

[200] K. Kamikado, N. Strodthoff, L. von Smekal, and J. Wambach, *Real-time correlation functions in the o(n) o (n) model from the functional renormalization group*, The European Physical Journal C **74**, 1–10 (2014).

[201] R.-A. Tripolt, N. Strodthoff, L. von Smekal, and J. Wambach, *Spectral functions for the quark-meson model phase diagram from the functional renormalization group*, Phys. Rev. D **89**, 034010 (2014).

[202] R.-A. Tripolt, L. von Smekal, and J. Wambach, *Flow equations for spectral functions at finite external momenta*, Phys. Rev. D **90**, 074031 (2014).

[203] X. Cui, *Fermi polaron revisited: polaron-molecule transition and coexistence*, Phys. Rev. A **102**, 061301 (2020).

[204] S. Sachdev, *Topological order, emergent gauge fields, and Fermi surface reconstruction*, Reports on Progress in Physics **82**, 014001 (2018).

[205] P. Fulde and R. A. Ferrell, *Superconductivity in a strong spin-exchange field*, Phys. Rev. **135**, A550–A563 (1964).

[206] A. Larkin and Y. N. Ovchinnikov, *Zh. é ksp. teor. fiz. 47, 1136 1964 sov. phys*, JETP **20**, 762 (1965).

[207] L. N. Cooper, *Bound electron pairs in a degenerate fermi gas*, Phys. Rev. **104**, 1189–1190 (1956).

[208] J. B. Ketterson and S. N. Song, *Superconductivity* (Cambridge University Press, 1999).

[209] B. W. H. Baugher, H. O. H. Churchill, Y. Yang, and P. Jarillo-Herrero, *Optoelectronic devices based on electrically tunable pn diodes in a monolayer dichalcogenide*, Nat. Nano. **9**, 262–267 (2014).

[210] D. J. Scalapino, *A common thread: the pairing interaction for unconventional superconductors*, Rev. Mod. Phys. **84**, 1383–1417 (2012).

[211] A. Mackenzie and Y. Maeno, *P-wave superconductivity*, Physica B: Condensed Matter **280**, 148–153 (2000).

[212] O. Viyuela, L. Fu, and M. A. Martin-Delgado, *Chiral topological superconductors enhanced by long-range interactions*, Phys. Rev. Lett. **120**, 017001 (2018).

[213] J. R. Kirtley, C. C. Tsuei, J. Z. Sun, C. C. Chi, L. S. Yu-Jahnes, A. Gupta, M. Rupp, and M. B. Ketchen, *Symmetry of the order parameter in the high-tc superconductor YBa2cu3o7- δ*, Nature **373**, 225–228 (1995).

[214] S. A. Kivelson, V. J. Emery, and H. Q. Lin, *Doped antiferromagnets in the weak-hopping limit*, Phys. Rev. B **42**, 6523–6530 (1990).

[215] S.-K. Jian, Y. Huang, and H. Yao, *Charge-4e superconductivity from nematic superconductors in two and three dimensions*, Phys. Rev. Lett. **127**, 227001 (2021).

[216] B. Uchoa and A. H. Castro Neto, *Superconducting states of pure and doped graphene*, Phys. Rev. Lett. **98**, 146801 (2007).

[217] R. Nandkishore, L. S. Levitov, and A. V. Chubukov, *Chiral superconductivity from repulsive interactions in doped graphene*, Nat. Phys. **8**, 158–163 (2012).

[218] J. C. Wheatley, *Experimental properties of superfluid* ^{3}He, Rev. Mod. Phys. **47**, 415–470 (1975).

[219] A. J. Leggett, *A theoretical description of the new phases of liquid* ^{3}He, Rev. Mod. Phys. **47**, 331–414 (1975).

[220] D. Vollhardt and P. Wolfle, *The superfluid phases of helium 3*, (1990).

[221] G. R. Stewart, *Unconventional superconductivity*, Advances in Physics **66**, 75–196 (2017).

[222] D. S. Petrov, *Three-body problem in fermi gases with short-range interparticle interaction*, Phys. Rev. A **67**, 010703 (2003).

[223] J. Levinsen and M. M. Parish, *Strongly interacting two-dimensional fermi gases*, Ann. Rev. C. At. Mol., 1–75 (2015).

[224] B. Bazak and D. S. Petrov, *Five-body efimov effect and universal pentamer in fermionic mixtures*, Phys. Rev. Lett. **118**, 083002 (2017).

[225] B. Bazak and D. S. Petrov, *Stable p-wave resonant two-dimensional fermi-bose dimers*, Phys. Rev. Lett. **121**, 263001 (2018).

[226] V. Efimov, *Energy levels of three resonantly interacting particles*, Nucl. Phys. A **210**, 157–188 (1973).

[227] O. I. Kartavtsev and A. V. Malykh, *Low-energy three-body dynamics in binary quantum gases*, J Phys. B **40**, 1429 (2007).

[228] S. Giorgini, L. P. Pitaevskii, and S. Stringari, *Theory of ultracold atomic fermi gases*, Rev. Mod. Phys. **80**, 1215–1274 (2008).

[229] J. Levinsen, T. G. Tiecke, J. T. M. Walraven, and D. S. Petrov, *Atom-dimer scattering and long-lived trimers in fermionic mixtures*, Phys. Rev. Lett. **103**, 153202 (2009).

[230] Y. Castin, C. Mora, and L. Pricoupenko, *Four-body efimov effect for three fermions and a lighter particle*, Phys. Rev. Lett. **105**, 223201 (2010).

[231] D. Blume, *Universal four-body states in heavy-light mixtures with a positive scattering length*, Phys. Rev. Lett. **109**, 230404 (2012).

[232] P. Massignan, M. Zaccanti, and G. M. Bruun, *Polarons, dressed molecules and itinerant ferromagnetism in ultracold fermi gases*, Rep. Prog. Phys. **77**, 034401 (2014).

[233] C. Kohstall, M. Zaccanti, M. Jag, A. Trenkwalder, P. Massignan, G. M. Bruun, F. Schreck, and R. Grimm, *Metastability and coherence of repulsive polarons in a strongly interacting fermi mixture*, Nature **485**, 615–618 (2012).

[234] M. Cetina, M. Jag, R. S. Lous, I. Fritsche, J. T. M. Walraven, R. Grimm, J. Levinsen, M. M. Parish, R. Schmidt, M. Knap, and E. Demler, *Ultrafast many-body interferometry of impurities coupled to a Fermi sea*, Science **354**, 96–99 (2016).

[235] R. Liu, C. Peng, and X. Cui, *Universal tetramer and pentamer bound states in two-dimensional fermionic mixtures*, Phys. Rev. Lett. **129**, 073401 (2022).

[236] Y. Shimazaki, C. Kuhlenkamp, I. Schwartz, T. Smolenski, K. Watanabe, T. Taniguchi, M. Kroner, R. Schmidt, M. Knap, and A. Imamoglu, *Optical signatures of periodic charge distribution in a mott-like correlated insulator state*, Phys. Rev. X **11**, 021027 (2021).

[237] A. Popert, Y. Shimazaki, M. Kroner, K. Watanabe, T. Taniguchi, A. Imamoglu, and T. Smolenski, *Optical sensing of fractional quantum hall effect in graphene*, Nano Lett. **22**, 7363–7369 (2022).

[238] T. Smoleski et al., *Signatures of Wigner crystal of electrons in a monolayer semiconductor*, Nature **595**, 53–57 (2021).

[239] Y. Zhou et al., *Bilayer Wigner crystals in a transition metal dichalcogenide heterostructure*, Nature **595**, 48–52 (2021).

[240] N. Navon, R. P. Smith, and Z. Hadzibabic, *Quantum gases in optical boxes*, Nat. Phys. **17**, 1334–1341 (2021).

[241] Y. Xu, X. Wang, W. L. Zhang, F. Lv, and S. Guo, *Recent progress in two-dimensional inorganic quantum dots*, Chem. Soc. Rev. **47**, 586–625 (2018).

[242] L. Bayha, M. Holten, R. Klemt, K. Subramanian, J. Bjerlin, S. M. Reimann, G. M. Bruun, P. M. Preiss, and S. Jochim, *Observing the emergence of a quantum phase transition shell by shell*, Nature **587**, 583–587 (2020).

[243] M. Holten, L. Bayha, K. Subramanian, C. Heintze, P. M. Preiss, and S. Jochim, *Observation of pauli crystals*, Phys. Rev. Lett. **126**, 020401 (2021).

[244] M. Holten, L. Bayha, K. Subramanian, S. Brandstetter, C. Heintze, P. Lunt, P. M. Preiss, and S. Jochim, *Observation of cooper pairs in a mesoscopic two-dimensional fermi gas*, Nature **606**, 287–291 (2022).

[245] A. N. Wenz, G. Zürn, S. Murmann, I. Brouzos, T. Lompe, and S. Jochim, *From few to many: observing the formation of a fermi sea one atom at a time*, Science **342**, 457–460 (2013).

[246] N. S. Rytova, *The screened potential of a point charge in a thin film*, MSU Phys. Bulletin **3**, 18 (1967).

[247] L. V. Keldysh, *Coulomb interaction in thin semiconductor and semimetal films*, JETP Lett. **29**, 658 (1979).

[248] M. Suzuki, Y. Suzuki, and K. Varga, *Stochastic variational approach to quantum-mechanical few-body problems*, Vol. 54 (Springer Science & Business Media, Nov. 1998), 332 pp.

[249] J. Mitroy, S. Bubin, W. Horiuchi, Y. Suzuki, L. Adamowicz, W. Cencek, K. Szalewicz, J. Komasa, D. Blume, and K. Varga, *Theory and application of explicitly correlated gaussians*, Rev. Mod. Phys. **85**, 693–749 (2013).

[250] K. Varga, *Solution of few-body problems with the stochastic variational method ii: two-dimensional systems*, Comp. Phys. Comm. **179**, 591–596 (2008).

[251] Y. Cho, S. M. Greene, and T. C. Berkelbach, *Simulations of trions and biexcitons in layered hybrid organic-inorganic lead halide perovskites*, Phys. Rev. Lett. **126**, 216402 (2021).

[252] J. Yan and K. Varga, *Excited-state trions in two-dimensional materials*, Phys. Rev. B **101**, 235435 (2020).

[253] M. Van der Donck, M. Zarenia, and F. M. Peeters, *Excitons, trions, and biexcitons in transition-metal dichalcogenides: magnetic-field dependence*, Phys. Rev. B **97**, 195408 (2018).

[254] D. W. Kidd, D. K. Zhang, and K. Varga, *Binding energies and structures of two-dimensional excitonic complexes in transition metal dichalcogenides*, Phys. Rev. B **93**, 125423 (2016).

[255] D. V. Fedorov, *Analytic matrix elements and gradients with shifted correlated gaussians*, Few-Body Systems **58**, 21 (2016).

[256] T. M. Whitehead, L. M. Schonenberg, N. Kongsuwan, R. J. Needs, and G. J. Conduit, *Pseudopotential for the two-dimensional contact interaction*, Phys. Rev. A **93**, 042702 (2016).

[257] S. Becker, A. Michelangeli, and A. Ottolini, *Spectral analysis of the 2+1 fermionic trimer with contact interactions*, Math. Phys. Anal. Geom. **21**, 35 (2018).

[258] P. Steinleitner et al., *Dielectric engineering of electronic correlations in a van der waals heterostructure*, Nano Lett. **18**, 1402–1409 (2018).

[259] S. A. Moses, J. P. Covey, M. T. Miecnikowski, D. S. Jin, and J. Ye, *New frontiers for quantum gases of polar molecules*, Nat. Phys. **13**, 13–20 (2016).

[260] L. Chomaz, I. Ferrier-Barbut, F. Ferlaino, B. Laburthe-Tolra, B. L. Lev, and T. Pfau, *Dipolar physics: a review of experiments with magnetic quantum gases*, Rep. Prog. Phys. **86**, 026401 (2022).

[261] E. C. Regan et al., *Mott and generalized wigner crystal states in WSe2/WS2 moiré superlattices*, Nature **579**, 359–363 (2020).

[262] M. Serlin, C. L. Tschirhart, H. Polshyn, Y. Zhang, J. Zhu, K. Watanabe, T. Taniguchi, L. Balents, and A. F. Young, *Intrinsic quantized anomalous hall effect in a moiré heterostructure*, Science **367**, 900–903 (2020).

[263] Y.-M. Xie, C.-P. Zhang, J.-X. Hu, K. F. Mak, and K. T. Law, *Valley-polarized quantum anomalous hall state in moiré* $MoTe_2/WSe_2$ *heterobilayers*, Phys. Rev. Lett. **128**, 026402 (2022).

[264] J. Cai et al., *Signatures of fractional quantum anomalous hall states in twisted MoTe2*, Nature **622**, 63–68 (2023).

[265] Y. Cao, V. Fatemi, A. Demir, S. Fang, S. L. Tomarken, J. Y. Luo, J. D. Sanchez-Yamagishi, K. Watanabe, T. Taniguchi, E. Kaxiras, R. C. Ashoori, and P. Jarillo-Herrero, *Correlated insulator behaviour at half-filling in magic-angle graphene superlattices*, Nature **556**, 80–84 (2018).

[266] A. L. Sharpe, E. J. Fox, A. W. Barnard, J. Finney, K. Watanabe, T. Taniguchi, M. A. Kastner, and D. Goldhaber-Gordon, *Emergent ferromagnetism near three-quarters filling in twisted bilayer graphene*, Science **365**, 605–608 (2019).

[267] X. Liu, Z. Hao, E. Khalaf, J. Y. Lee, Y. Ronen, H. Yoo, D. H. Najafabadi, K. Watanabe, T. Taniguchi, A. Vishwanath, and P. Kim, *Tunable spin-polarized correlated states in twisted double bilayer graphene*, Nature **583**, 221–225 (2020).

[268] X. Xi, Z. Wang, W. Zhao, J.-H. Park, K. T. Law, H. Berger, L. Forró, J. Shan, and K. F. Mak, *Ising pairing in superconducting NbSe2 atomic layers*, Nat. Phys. **12**, 139–143 (2015).

[269] Y. Cao, V. Fatemi, S. Fang, K. Watanabe, T. Taniguchi, E. Kaxiras, and P. Jarillo-Herrero, *Unconventional superconductivity in magic-angle graphene superlattices*, Nature **556**, 43–50 (2018).

[270] M. Yankowitz, S. Chen, H. Polshyn, Y. Zhang, K. Watanabe, T. Taniguchi, D. Graf, A. F. Young, and C. R. Dean, *Tuning superconductivity in twisted bilayer graphene*, Science **363**, 1059–1064 (2019).

[271] V. Crépel, D. Guerci, J. Cano, J. H. Pixley, and A. Millis, *Topological superconductivity in doped magnetic moiré semiconductors*, Phys. Rev. Lett. **131**, 056001 (2023).

[272] Z. Sun, J. Beaumariage, Q. Wan, H. Alnatah, N. Hougland, J. Chisholm, Q. Cao, K. Watanabe, T. Taniguchi, B. M. Hunt, I. V. Bondarev, and D. Snoke,

Charged bosons made of fermions in bilayer structures with strong metallic screening, Nano Lett. **21**, 7669–7675 (2021).

[273] K. Slagle and L. Fu, *Charge transfer excitations, pair density waves, and superconductivity in moiré materials*, Phys. Rev. B **102**, 235423 (2020).

[274] V. Crépel and L. Fu, *New mechanism and exact theory of superconductivity from strong repulsive interaction*, Science Advances **7**, eabh2233 (2021).

[275] V. Crépel and L. Fu, *Spin-triplet superconductivity from excitonic effect in doped insulators*, Proceedings of the National Academy of Sciences **119**, 17735119 (2022).

[276] V. Crépel, T. Cea, L. Fu, and F. Guinea, *Unconventional superconductivity due to interband polarization*, Phys. Rev. B **105**, 094506 (2022).

[277] Y. He, K. Yang, J. B. Hauck, E. J. Bergholtz, and D. M. Kennes, *Superconductivity of repulsive spinless fermions with sublattice potentials*, Phys. Rev. Res. **5**, L012009 (2023).

[278] A. Julku, J. J. Kinnunen, A. Camacho-Guardian, and G. M. Bruun, *Light-induced topological superconductivity in transition metal dichalcogenide monolayers*, Phys. Rev. B **106**, 134510 (2022).

[279] S. Jochim, M. Bartenstein, A. Altmeyer, G. Hendl, S. Riedl, C. Chin, J. H. Denschlag, and R. Grimm, *Bose-einstein condensation of molecules*, Science **302**, 2101–2103 (2003).

[280] M. W. Zwierlein, C. H. Schunck, A. Schirotzek, and W. Ketterle, *Direct observation of the superfluid phase transition in ultracold fermi gases*, Nature **442**, 54–58 (2006).

[281] M. J. H. Ku, A. T. Sommer, L. W. Cheuk, and M. W. Zwierlein, *Revealing the superfluid lambda transition in the universal thermodynamics of a unitary fermi gas*, Science **335**, 563–567 (2012).

[282] M. Feld, B. Fröhlich, E. Vogt, M. Koschorreck, and M. Köhl, *Observation of a pairing pseudogap in a two-dimensional fermi gas*, Nature **480**, 75–78 (2011).

[283] A. T. Sommer, L. W. Cheuk, M. J. H. Ku, W. S. Bakr, and M. W. Zwierlein, *Evolution of fermion pairing from three to two dimensions*, Phys. Rev. Lett. **108**, 045302 (2012).

[284] M. G. Ries, A. N. Wenz, G. Zürn, L. Bayha, I. Boettcher, D. Kedar, P. A. Murthy, M. Neidig, T. Lompe, and S. Jochim, *Observation of pair condensation in the quasi-2d bec-bcs crossover*, Phys. Rev. Lett. **114**, 230401 (2015).

[285] P. A. Murthy, M. Neidig, R. Klemt, L. Bayha, I. Boettcher, T. Enss, M. Holten, G. Zürn, P. M. Preiss, and S. Jochim, *High-temperature pairing in a strongly interacting two-dimensional fermi gas*, Science **359**, 452–455 (2018).

[286] L. Sobirey, N. Luick, M. Bohlen, H. Biss, H. Moritz, and T. Lompe, *Observation of superfluidity in a strongly correlated two-dimensional fermi gas*, Science **372**, 844–846 (2021).

[287] M. Greiner, C. A. Regal, and D. S. Jin, *Emergence of a molecular boseeinstein condensate from a fermi gas*, Nature **426**, 537–540 (2003).

[288] M. W. Zwierlein, C. A. Stan, C. H. Schunck, S. M. F. Raupach, S. Gupta, Z. Hadzibabic, and W. Ketterle, *Observation of bose-einstein condensation of molecules*, Phys. Rev. Lett. **91**, 250401 (2003).

[289] C. A. Regal, M. Greiner, and D. S. Jin, *Observation of resonance condensation of fermionic atom pairs*, Phys. Rev. Lett. **92**, 040403 (2004).

[290] M. W. Zwierlein, C. A. Stan, C. H. Schunck, S. M. F. Raupach, A. J. Kerman, and W. Ketterle, *Condensation of pairs of fermionic atoms near a feshbach resonance*, Phys. Rev. Lett. **92**, 120403 (2004).

[291] C. Chin, M. Bartenstein, A. Altmeyer, S. Riedl, S. Jochim, J. H. Denschlag, and R. Grimm, *Observation of the pairing gap in a strongly interacting fermi gas*, Science **305**, 1128–1130 (2004).

[292] J. Kinast, S. L. Hemmer, M. E. Gehm, A. Turlapov, and J. E. Thomas, *Evidence for superfluidity in a resonantly interacting fermi gas*, Phys. Rev. Lett. **92**, 150402 (2004).

[293] T. Bourdel, L. Khaykovich, J. Cubizolles, J. Zhang, F. Chevy, M. Teichmann, L. Tarruell, S. J. J. M. F. Kokkelmans, and C. Salomon, *Experimental study of the bec-bcs crossover region in lithium 6*, Phys. Rev. Lett. **93**, 050401 (2004).

[294] K. E. Strecker, G. B. Partridge, and R. G. Hulet, *Conversion of an atomic fermi gas to a long-lived molecular bose gas*, Phys. Rev. Lett. **91**, 080406 (2003).

[295] M. Randeria, J.-M. Duan, and L.-Y. Shieh, *Bound states, cooper pairing, and bose condensation in two dimensions*, Phys. Rev. Lett. **62**, 981–984 (1989).

[296] N. D. Mermin and H. Wagner, *Absence of ferromagnetism or antiferromagnetism in one- or two-dimensional isotropic heisenberg models*, Phys. Rev. Lett. **17**, 1133–1136 (1966).

[297] P. C. Hohenberg, *Existence of long-range order in one and two dimensions*, Phys. Rev. **158**, 383–386 (1967).

[298] V. L. Berezinsky, *Destruction of Long-range Order in One-dimensional and Two-dimensional Systems Possessing a Continuous Symmetry Group. II. Quantum Systems.* Sov. Phys. JETP **34**, 610 (1972).

[299] J. M. Kosterlitz and D. J. Thouless, *Ordering, metastability and phase transitions in two-dimensional systems*, J Phys. C **6**, 1181 (1973).

[300] D. S. Petrov, M. A. Baranov, and G. V. Shlyapnikov, *Superfluid transition in quasi-two-dimensional fermi gases*, Phys. Rev. A **67**, 031601 (2003).

[301] F. Isaule, I. Morera, P. Massignan, and B. Juliá-Daz, *Renormalization-group study of bose polarons*, Phys. Rev. A **104**, 023317 (2021).

[302] T. Goldstein, Y.-C. Wu, S.-Y. Chen, T. Taniguchi, K. Watanabe, K. Varga, and J. Yan, *Ground and excited state exciton polarons in monolayer MoSe2*, J Chem. Phys. **153**, 070401 (2020).

[303] K. Xiao, T. Yan, Q. Liu, S. Yang, C. Kan, R. Duan, Z. Liu, and X. Cui, *Many-body effect on optical properties of monolayer molybdenum diselenide*, J Phys. Chem. Lett. **12**, 2555–2561 (2021).

[304] E. Liu, J. van Baren, Z. Lu, T. Taniguchi, K. Watanabe, D. Smirnov, Y.-C. Chang, and C. H. Lui, *Exciton-polaron rydberg states in monolayer MoSe2 and WSe2*, Nat. Comm. **12**, 6131 (2021).

[305] J. Zipfel, K. Wagner, M. A. Semina, J. D. Ziegler, T. Taniguchi, K. Watanabe, M. M. Glazov, and A. Chernikov, *Electron recoil effect in electrically tunable* $MoSe_2$ *monolayers*, Phys. Rev. B **105**, 075311 (2022).

[306] K. Miyake, *Fermi Liquid Theory of Dilute Submonolayer 3He on Thin 4He II Film: Dimer Bound State and Cooper Pairs*, Prog. Theor. Phys. **69**, 1794–1797 (1983).

[307] S. Maiti and A. V. Chubukov, *Superconductivity from repulsive interaction*, AIP Conference Proceedings **1550**, 3–73 (2013).

[308] D. S. Fisher and P. C. Hohenberg, *Dilute bose gas in two dimensions*, Phys. Rev. B **37**, 4936–4943 (1988).

[309] N. Prokof'ev, O. Ruebenacker, and B. Svistunov, *Critical point of a weakly interacting two-dimensional bose gas*, Phys. Rev. Lett. **87**, 270402 (2001).

[310] N. Prokof'ev and B. Svistunov, *Two-dimensional weakly interacting bose gas in the fluctuation region*, Phys. Rev. A **66**, 043608 (2002).

[311] J. Sous, M. Chakraborty, R. V. Krems, and M. Berciu, *Light bipolarons stabilized by peierls electron-phonon coupling*, Phys. Rev. Lett. **121**, 247001 (2018).

[312] M. R. Carbone, A. J. Millis, D. R. Reichman, and J. Sous, *Bond-peierls polaron: moderate mass enhancement and current-carrying ground state*, Phys. Rev. B **104**, L140307 (2021).

[313] D. M. Eagles, *Possible pairing without superconductivity at low carrier concentrations in bulk and thin-film superconducting semiconductors*, Phys. Rev. **186**, 456–463 (1969).

[314] S. S. Botelho and C. A. R. Sá de Melo, *Vortex-antivortex lattice in ultracold fermionic gases*, Phys. Rev. Lett. **96**, 040404 (2006).

[315] A. J. Leggett, *Diatomic molecules and cooper pairs*, in Modern trends in the theory of condensed matter, edited by A. Pkalski and J. A. Przystawa (1980), pp. 13–27.

[316] P. Nozières and S. Schmitt-Rink, *Bose condensation in an attractive fermion gas: from weak to strong coupling superconductivity*, J Low Temp. Phys. **59**, 195–211 (1985).

[317] S. Schmitt-Rink, C. M. Varma, and A. E. Ruckenstein, *Pairing in two dimensions*, Phys. Rev. Lett. **63**, 445–448 (1989).

[318] M. Drechsler and W. Zwerger, *Crossover from BCS-superconductivity to bose-condensation*, Ann. Phys. **504**, 15–23 (1992).

[319] A. Gezerlis and J. Carlson, *Strongly paired fermions: cold atoms and neutron matter*, Phys. Rev. C **77**, 032801 (2008).

[320] M. M. Forbes, A. Gezerlis, K. Hebeler, T. Lesinski, and A. Schwenk, *Neutron polaron as a constraint on nuclear density functionals*, Phys. Rev. C **89**, 041301 (2014).

[321] L. D. Landau, *Electron motion in crystal lattices*, Phys. Z. Sowjet. **3**, 664 (1933).

[322] C. Zerba, C. Kuhlenkamp, A. Imamoglu, and M. Knap, *Realizing topological superconductivity in tunable bose-fermi mixtures with transition metal dichalcogenide heterostructures*, arXiv:2310.10720, (2023).

[323] M. M. Parish, H. S. Adlong, W. E. Liu, and J. Levinsen, *Thermodynamic signatures of the polaron-molecule transition in a fermi gas*, Phys. Rev. A **103**, 023312 (2021).

[324] H. Tajima and S. Uchino, *Many fermi polarons at nonzero temperature*, NJP **20**, 073048 (2018).

[325] H. S. Adlong, W. E. Liu, F. Scazza, M. Zaccanti, N. D. Oppong, S. Fölling, M. M. Parish, and J. Levinsen, *Quasiparticle lifetime of the repulsive fermi polaron*, Phys. Rev. Lett. **125**, 133401 (2020).

[326] H. Hu, B. C. Mulkerin, J. Wang, and X.-J. Liu, *Attractive fermi polarons at nonzero temperatures with a finite impurity concentration*, Phys. Rev. A **98**, 013626 (2018).

[327] H. Hu and X.-J. Liu, *Fermi polarons at finite temperature: spectral function and rf spectroscopy*, Phys. Rev. A **105**, 043303 (2022).

[328] H. Hu and X.-J. Liu, *Spectral function of fermi polarons at finite temperature from a self-consistent many-body T-matrix approach in real frequency*, arXiv:2311.11554, (2023).

[329] G. Baym and C. Pethick, *Landau fermi-liquid theory* (Wiley, Dec. 1991).

[330] G. M. Bruun, A. Recati, C. J. Pethick, H. Smith, and S. Stringari, *Collisional properties of a polarized fermi gas with resonant interactions*, Phys. Rev. Lett. **100**, 240406 (2008).

[331] K. Sadeghzadeh, G. M. Bruun, C. Lobo, P. Massignan, and A. Recati, *Metastability in spin-polarized fermi gases and quasiparticle decays*, NJP **13**, 055011 (2011).

[332] V. Ngampruetikorn, J. Levinsen, and M. M. Parish, *Repulsive polarons in two-dimensional fermi gases*, EPL **98**, 30005 (2012).

[333] C. Trefzger and Y. Castin, *Self-energy of an impurity in an ideal fermi gas to second order in the interaction strength*, Phys. Rev. A **90**, 033619 (2014).

[334] M. Cetina, M. Jag, R. S. Lous, J. T. M. Walraven, R. Grimm, R. S. Christensen, and G. M. Bruun, *Decoherence of impurities in a fermi sea of ultracold atoms*, Phys. Rev. Lett. **115**, 135302 (2015).

[335] R. Schmidt and T. Enss, private communication, 2022.

[336] M. Cetina, M. Jag, R. S. Lous, I. Fritsche, J. T. M. Walraven, R. Grimm, J. Levinsen, M. M. Parish, R. Schmidt, M. Knap, and E. Demler, *Ultrafast many-body interferometry of impurities coupled to a fermi sea*, Science **354**, 96–99 (2016).

[337] F. J. Vivanco, A. Schuckert, S. Huang, G. L. Schumacher, G. G. Assumpção, Y. Ji, J. Chen, M. Knap, and N. Navon, *The strongly driven fermi polaron*, arXiv:2308.05746, (2023).

[338] F. Scazza, G. Valtolina, P. Massignan, A. Recati, A. Amico, A. Burchianti, C. Fort, M. Inguscio, M. Zaccanti, and G. Roati, *Repulsive fermi polarons in a resonant mixture of ultracold* ^{6}Li *atoms*, Phys. Rev. Lett. **118**, 083602 (2017).

[339] B. C. Mulkerin, J. Levinsen, and M. M. Parish, *Rabi oscillations and magnetization of a mobile spin-1/2 impurity in a fermi sea*, arXiv:2308.06659, (2023).

[340] C. Baroni, B. Huang, I. Fritsche, E. Dobler, G. Anich, E. Kirilov, R. Grimm, M. A. Bastarrachea-Magnani, P. Massignan, and G. M. Bruun, *Mediated interactions between fermi polarons and the role of impurity quantum statistics*, Nat Phys., 1–6 (2023).

[341] R. Eisenschitz and F. London, *Über das verhältnis der van der waalsschen kräfte zu den homöopolaren bindungskräften*, Z. Phys. **60**, 491–527 (1930).

[342] E. M. Lifshitz, *The theory of molecular attractive forces between solids*, Sov. Phys. JETP **2**, [Zh. Eksp. Teor. Fiz. **29**, 94 (1956)], 73–83 (1956).

[343] I. Dzyaloshinskii, E. Lifshitz, and L. Pitaevskii, *The general theory of van der waals forces*, Adv. Phys. **10**, 165–209 (1961).

[344] J. D. Jackson, *Classical electrodynamics* (Wiley, July 27, 1998), 832 pp.

[345] M. Kozina et al., *Measurement of transient atomic displacements in thin films with picosecond and femtometer resolution*, Struct. Dyn. **1**, 034301 (2014).

[346] I.-C. Tung et al., *Anisotropic structural dynamics of monolayer crystals revealed by femtosecond surface x-ray scattering*, Nat. Photonics **13**, 425–430 (2019).

[347] E. M. Mannebach et al., *Dynamic optical tuning of interlayer interactions in the transition metal dichalcogenides*, Nano Lett. **17**, 7761–7766 (2017).

[348] B. N. Narozhny and A. Levchenko, *Coulomb drag*, Rev. Mod. Phys. **88**, 025003 (2016).

[349] J. P. Eisenstein and A. H. MacDonald, *Boseeinstein condensation of excitons in bilayer electron systems*, Nature **432**, 691–694 (2004).

[350] M. Kellogg, I. B. Spielman, J. P. Eisenstein, L. N. Pfeiffer, and K. W. West, *Observation of quantized hall drag in a strongly correlated bilayer electron system*, Phys. Rev. Lett. **88**, 126804 (2002).

[351] D. Laroche, G. Gervais, M. P. Lilly, and J. L. Reno, *1d-1d coulomb drag signature of a luttinger liquid*, Science **343**, 631–634 (2014).

[352] Y. Andersson, D. C. Langreth, and B. I. Lundqvist, *Van der waals interactions in density-functional theory*, Phys. Rev. Lett. **76**, 102–105 (1996).

[353] H. Rydberg, M. Dion, N. Jacobson, E. Schröder, P. Hyldgaard, S. I. Simak, D. C. Langreth, and B. I. Lundqvist, *Van der waals density functional for layered structures*, Phys. Rev. Lett. **91**, 126402 (2003).

[354] J. Antony and S. Grimme, *Density functional theory including dispersion corrections for intermolecular interactions in a large benchmark set of biologically relevant molecules*, Phys. Chem. Chem. Phys. **8**, 5287–5293 (2006).

[355] S. Grimme, J. Antony, T. Schwabe, and C. Mück-Lichtenfeld, *Density functional theory with dispersion corrections for supramolecular structures, aggregates, and complexes of (bio)organic molecules*, Org. Biomol. Chem. **5**, 741–758 (2007).

[356] A. Tkatchenko and M. Scheffler, *Accurate molecular van der waals interactions from ground-state electron density and free-atom reference data*, Phys. Rev. Lett. **102**, 073005 (2009).

[357] A. Tkatchenko, R. A. DiStasio, R. Car, and M. Scheffler, *Accurate and efficient method for many-body van der waals interactions*, Phys. Rev. Lett. **108**, 236402 (2012).

[358] L. P. Gor'kov, A. I. Larkin, and D. E. Khmelnitski, *Particle conductivity in a two-dimensional random potential*, JETP Lett. **30**, [Pisma Zh.Eksp. Teor. Fiz. **30**, 248 (1979)], 228 (1979).

[359] B. Altshuler and A. Aronov, *Contribution to the theory of disordered metals in strongly doped semiconductors*, Zh. Eksp. Teor. Fiz **77**, [Sov. Phys. JETP **50**, 968 (1979)], 2028–2044 (1979).

[360] B. Altshuler and A. Aronov, *Zero bias anomaly in tunnel resistance and electron-electron interaction*, Solid State Commun. **30**, 115–117 (1979).

[361] T. J. Gramila, J. P. Eisenstein, A. H. MacDonald, L. N. Pfeiffer, and K. W. West, *Mutual friction between parallel two-dimensional electron systems*, Phys. Rev. Lett. **66**, 1216–1219 (1991).

[362] B. E. Sernelius and P. Björk, *Interaction energy for a pair of quantum wells*, Phys. Rev. B **57**, 6592–6601 (1998).

[363] M. Boström and B. E. Sernelius, *Fractional van der waals interaction between thin metallic films*, Phys. Rev. B **61**, 2204–2210 (2000).

[364] J. F. Dobson, K. McLennan, A. Rubio, J. Wang, T. Gould, H. M. Le, and B. P. Dinte, *Prediction of dispersion forces: is there a problem?*, Aust. J. Chem. **54**, 513 (2001).

[365] N. D. Drummond and R. J. Needs, *Van der waals interactions between thin metallic wires and layers*, Phys. Rev. Lett. **99**, 166401 (2007).

[366] G. Giuliani and G. Vignale, *Quantum theory of the electron liquid* (Cambridge University Press, 2005).

[367] T. B. Arp, D. Pleskot, V. Aji, and N. M. Gabor, *Electronhole liquid in a van der waals heterostructure photocell at room temperature*, Nat. Photonics **13**, 245–250 (2019).

[368] S. Lian Tan and P. Anderson, *Long-range van der waals forces between restricted-dimensional metals*, Chem. Phys. Lett. **97**, 23–25 (1983).

[369] D. Bohm and D. Pines, *A collective description of electron interactions. i. magnetic interactions*, Phys. Rev. **82**, 625–634 (1951).

[370] D. Pines and D. Bohm, *A collective description of electron interactions: ii. collective* vs *individual particle aspects of the interactions*, Phys. Rev. **85**, 338–353 (1952).

[371] D. Bohm and D. Pines, *A collective description of electron interactions: iii. coulomb interactions in a degenerate electron gas*, Phys. Rev. **92**, 609–625 (1953).

[372] D. Pines, *A collective description of electron interactions: iv. electron interaction in metals*, Phys. Rev. **92**, 626–636 (1953).

[373] J. Lindhard, *On the properties of a gas of charged particles*, Dan. Mat. Fys. Medd. **28**, 8 (1954).

[374] L. Zheng and A. H. MacDonald, *Coulomb drag between disordered two-dimensional electron-gas layers*, Phys. Rev. B **48**, 8203–8209 (1993).

[375] J. P. Ellis, *Tikz-feynman: feynman diagrams with tikz*, Comp. Phys. Comm. **210**, 103–123 (2017).

[376] M. Dohse, *Tikz-feynhand: basic user guide*, (2018).

[377] D. Vollhardt and P. Wölfle, *Diagrammatic, self-consistent treatment of the anderson localization problem in $d \leq 2$ dimensions*, Phys. Rev. B **22**, 4666–4679 (1980).

[378] E. Akkermans and G. Montambaux, *Mesoscopic physics of electrons and photons* (Cambridge University Press, 2007).

[379] M. V. Sadovskii, *Diagrammatics* (World Scientific, Aug. 2019).

[380] N. D. Mermin, *Lindhard dielectric function in the relaxation-time approximation*, Phys. Rev. B **1**, 2362–2363 (1970).

[381] R. Asgari and B. Tanatar, *Effects of disorder on the ground-state energy of a two-dimensional electron gas*, Phys. Rev. B **65**, 085311 (2002).

[382] J. F. Dobson, A. White, and A. Rubio, *Asymptotics of the dispersion interaction: analytic benchmarks for van der waals energy functionals*, Phys. Rev. Lett. **96**, 073201 (2006).

[383] J. F. Dobson and T. Gould, *Calculation of dispersion energies*, J Phys. Cond. Matt. **24**, 073201 (2012).

[384] C. D. Castro and R. Raimondi, *Statistical mechanics and applications in condensed matter* (Cambridge University Press, 2015).

[385] A. K. Geim and I. V. Grigorieva, *Van der waals heterostructures*, Nature **499**, 419–425 (2013).

[386] P. A. Lee and T. V. Ramakrishnan, *Disordered electronic systems*, Rev. Mod. Phys. **57**, 287–337 (1985).

Acknowledgements

The work presented in this thesis would not be would be without the great amount of support, guidance, supervision, encouragement, care and trust I have received throughout my life and during this dissertation.

To begin, I would like to thank my supervisor Richard Schmidt for his continued support and trust throughout the years. It is challenging to put into words how much I have been able to learn from him, both in physics and in life, and how valuable his insights and ideas have been. He has the unique talent of speaking the language of his conversation partners, whether they are experimentalists or theorists, seasoned professors or incoming bachelor students. This great talent meant that the valuable advice I received from him was always accessible to me, allowing me to benefit from it. He was dedicated to help me succeed and showed great commitment in that with, sometimes with unconventional solutions, sometimes at unconventional times and sometimes within unconventional time frames. Having the professional support of a great scientist *and* a great person is more than I could reasonably ask for.

Along the way, I had the great privilege of discussing and collaborating with a series of excellent scientists and exceptional persons. Among these are Marcel Duda, Oriana Diessel, Rafał Ołdziejewski, Ruipeng Li, Aileen Durst, Felix Rose, Gal Ness, Arthur Christianen, Darshan Joshi, Keerthan Subramanian and Xin Chen. Aside from the physics we explored, a whole lot of laughter was shared and many intriguing conversations were lead.

Furthermore, I would like to thank Immanuel Bloch, Atac Imamoglu and Yoav Sagi for the fruitful discussions and collaborations we had. I would further like to thank Subir Sachdev for the opportunity to spend time in his research group at Harvard University and the opportunity to contribute to his research.

During my time as a PhD student, I had the opportunity to devote significant efforts to my passion, Ultimate Frisbee. I am grateful for the great experiences this sport has provided me, the people I have had the honor of getting to know and play with, and the many places I got to visit in the process. I thank my team mates from MUC, the german men's beach national team, MINT, Super Swimsuits 3000 and Unicorn Butts for all the great times we got to spend together.

I would like to thank my dear friends for the friendships we share and all the joy they have brought into my life.

Finally, I would like to thank my parents, Dr. Christine von Milczewski and Driss Denguir, and my grandparents, Frauke von Milczewski and Dr. Karl-Ernst von

Milczewski. I am deeply grateful for the continuous support I have received from them.